MPM SCIENTIFIC JOURNAL

ISSN 1605-2730
E-ISSN 1605-8119

MATERIALS PHYSICS AND MECHANICS

Vol. 52, No. 2, 2024

125

MATERIALS PHYSICS AND MECHANICS

"Materials Physics and Mechanics" Editorial Office:
Phone: +7(812)552 77 78, ext. 224 **E-mail:** mpmjournal@spbstu.ru **Web-site:** http://www.mpm.spbstu.ru

International scientific journal "**Materials Physics and Mechanics**" is published by Peter the Great St. Petersburg Polytechnic University in collaboration with Institute for Problems for Mechanical Engineering in the Russian Academy of Sciences in both hard copy and electronic versions. The journal provides an international medium for the publication of reviews and original research papers written in English and focused on the following topics:

- Mechanics of composite and nanostructured materials.
- Physics of strength and plasticity of composite and nanostructured materials.
- Mechanics of deformation and fracture processes in conventional materials (solids).
- Physics of strength and plasticity of conventional materials (solids).
- Physics and mechanics of defects in composite, nanostructured, and conventional materials.
- Mechanics and physics of materials in coupled fields.

Owner organizations: Peter the Great St. Petersburg Polytechnic University; Institute of Problems of Mechanical Engineering RAS.

Materials Physics and Mechanics is indexed in Chemical Abstracts, Cambridge Scientific Abstracts, Web of Science Emerging Sources Citation Index (ESCI) and Elsevier Bibliographic Databases (in particular, SCOPUS).

МЕХАНИКА И ФИЗИКА МАТЕРИАЛОВ

Materials Physics and Mechanics

Том 52, номер 2, 2024 год

Учредители:
ФГАОУ ВО «Санкт-Петербургский политехнический университет Петра Великого»
ФГБУН «Институт проблем машиноведения Российской академии наук»

Тел.: +7(812)552 77 78, доб. 224 **E-mail:** mpmjournal@spbstu.ru **Web-site:** http://www.mpm.spbstu.ru

Тематика журнала

Международный научный журнал "Materials Physics and Mechanics" издается Санкт-Петербургским политехническим университетом Петра Великого в сотрудничестве с Институтом проблем машиноведения Российской академии наук в печатном виде и электронной форме. Журнал публикует обзорные и оригинальные научные статьи на английском языке по следующим тематикам:

- Механика композиционных и наноструктурированных материалов.
- Физика прочности и пластичности композиционных и наноструктурированных материалов.
- Механика процессов деформации и разрушения в традиционных материалах (твердых телах).
- Физика прочности и пластичности традиционных материалов (твердых тел).
- Физика и механика дефектов в композиционных, наноструктурированных и традиционных материалах.
- Механика и физика материалов в связанных полях.

Редколлегия принимает статьи, которые нигде ранее не опубликованы и не направлены для опубликования в другие научные издания. Все представляемые в редакцию журнала "Механика и физика материалов" статьи рецензируются. Статьи могут отправляться авторам на доработку. Не принятые к опубликованию статьи авторам не возвращаются.

Журнал "Механика и физика материалов" ("Materials Physics and Mechanics") включен в систему цитирования Web of Science Emerging Sources Citation Index (ESCI), SCOPUS и РИНЦ.

Contents

Submitted: July 10, 2023 Revised: October 6, 2023 Accepted: December 25, 2023

Optimizing processing parameters for semi-solid casting: a comprehensive review

D.P. Singh [1]✉, V.K. Dwivedi [1], M. Agarwal [3],

[1] GLA University, Mathura, India

[2] Dr. Ram Manohar Lohia Avadh University, Ayodhya, India

✉ devendraps.research@gmail.com

ABSTRACT

Semi-solid processing has gained popularity in the casting industry due to its significant advantages, offering a net shape single or multistep flexible process. This study aims to establish an evaluation criterion to understand the relationship between processability and its impact on outcomes. Pouring temperature and fluidity emerge as primary factors, while solidification and viscosity demonstrate secondary importance in the processing. Through a multi-angle evaluatory approach, the flexibility of all semi-solid casting process parameters can be assessed based on alloying elements, temperature gradient, fluidity, heat transfer, and solidification.

KEYWORDS

semi-solid casting • pouring temperature • solidification • temperature gradient • MMC

Citation: Singh DP, Dwivedi VK, Agarwal M. Optimizing processing parameters for semi-solid casting: a comprehensive review. *Materials Physics and Mechanics*. 2024;52(2): 1–10.
http://dx.doi.org/10.18149/MPM.5222024_1

Introduction

Semi-solid metal (SSM) processing is highly regarded as an attractive technique for manufacturing near-net-shape components with improved mechanical properties compared to traditional methods [1]. The concept of SSM processing emerged in the early 1970s, but its full understanding was achieved in later years, particularly after the 1990s. Initially, the understanding of SSM processing was limited, but it has now been linked to key processing parameters such as deformation rate, material fluidity, rheology (pseudo-plasticity and thixotropy), and pouring temperature [2]. Among these factors, fluidity, commonly expressed as fluidity length (L_f), plays a crucial role. L_f is defined as the distance covered by molten metal during forced flow in a small cross-section until solidification. It significantly influences the suggested solidification microstructures, which depend on the cooling rate [3,4]. Furthermore, during the semi-solid stage of liquid metallurgy, several other processing parameters come into play, including stirring action, squeeze pressure, pouring temperature, and pressurized solidification [5–11]. A semi-solid state is characterized by a higher fraction of solid than liquid within the melt, while a mushy state occurs just above the solidus line, where liquid metal is present during cooling. The liquid fraction is higher than the solid fraction in the semi-solid state. In both states, the behavior of the slurry resembles a thick (low viscous) material, depending on the presence of solidified grains within the melt [12]. The solid fraction affects the viscosity of the slurry, which is considered a suspension with dispersed solid particles exhibiting unique rheological properties such as pseudo-plasticity and thixotropy [13–28]. The melt temperature in liquid metallurgy plays a crucial role in determining the formation of states

such as semi-solid and mushy, which are determined by the solidus line of the parent material [29–31]. Intensive research has focused on the effects of semi-solid liquid metallurgy, as it offers improved properties with secondary parameters to control the pouring temperature of the melt. Figure 1 provides a summary of the organization of processing parameters and their effects. It has been identified that: fluidity and pouring temperature are vital processing parameters for controlling the solidification rate of the melt, inhibiting grain growth, promoting incomplete re-crystallization, and resulting in the formation of micro-fine grains.

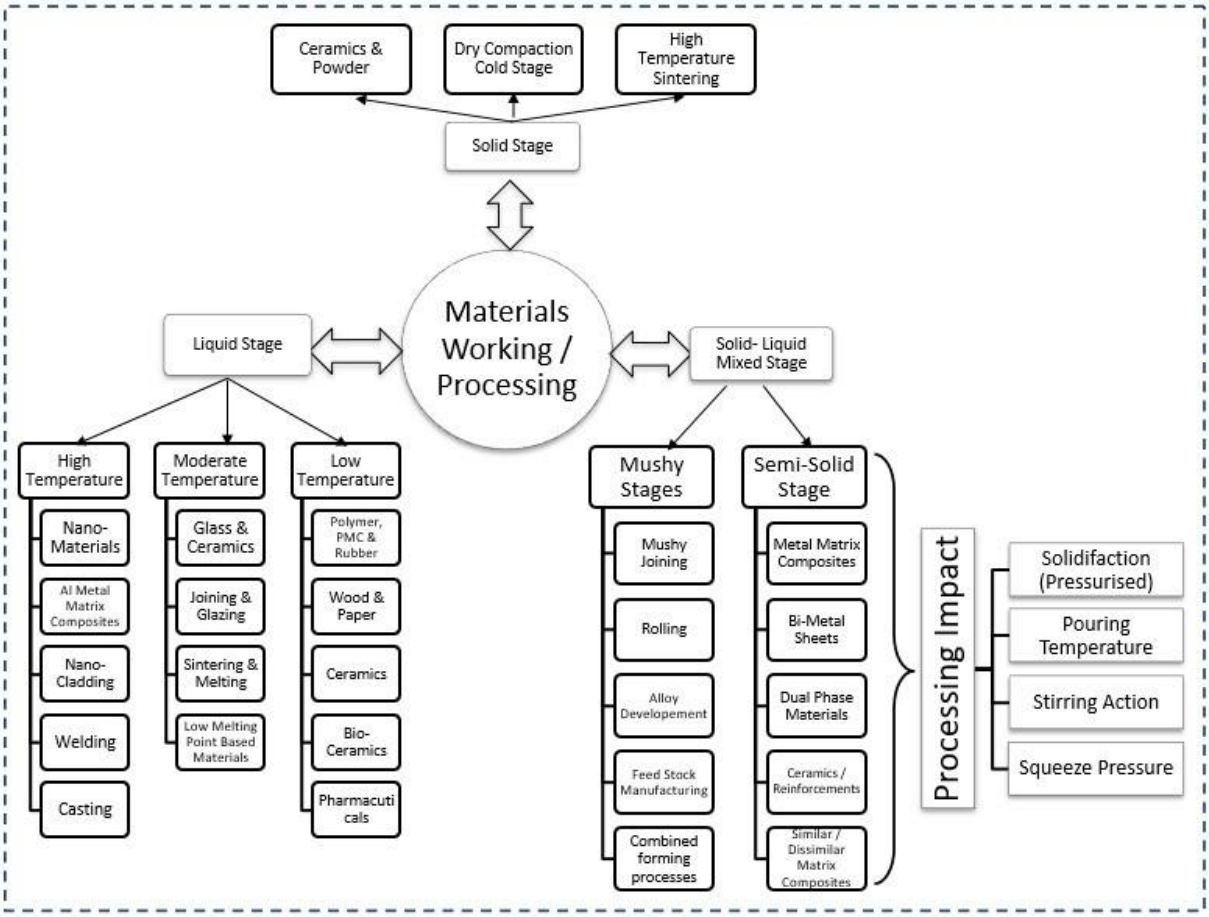

Fig. 1. Development of mushy/semi-solid material processing, parameters and application areas

These parameters can be controlled with the assistance of various associated parameters such as stirring action, reinforcement type, and squeeze pressure. However, this paper specifically discusses the effects of fluidity and pouring temperature on cast material properties and microstructure.

Impact of reinforcement on the fluidity and temperature

In the semi-solid casting process, a major challenge often encountered is achieving a high flow rate of semi-solid paste through thin sections and complex geometries [14]. Therefore, fluidity, which refers to the ability of the liquid metal to fill a mold, becomes a critical process parameter. Several factors contribute to fluidity determination, including molten metal characteristics such as viscosity, surface tension, suspended inclusions, mold design and material, pouring rate, superheat, and metal composition

[24–62]. Fluidity is inversely proportional to viscosity, viscosity index (sensitivity of viscosity to temperature), and freezing range. As these factors increase, fluidity decreases. Pure metals and eutectics with shorter freezing ranges exhibit higher fluidity, while alloys with longer freezing ranges tend to have lower fluidity [19,48]. The presence of high surface tension and oxide films on the liquid metal also reduces fluidity. Additionally, the inclusion of insoluble particles significantly affects fluidity, as they increase viscosity [20,51]. The dimensions of the runner, riser, and sprue in the mold also influence fluidity. Higher surface roughness of the mold and higher thermal conductivity of the mold material tend to decrease fluidity. Moreover, a slow pouring rate leads to reduced fluidity due to a higher cooling rate during slow pouring [21,40]. However, the most influential parameters governing fluidity are superheating, as higher temperature in the metal promotes greater flow in the mold, and metal composition, which impacts the mechanical and physical properties of the molten metal based on different alloying elements and their weight percentages [15–17,34–43].

Table 1. Effect of various alloying elements in Al-Base alloy

S. No.	Alloy	Alloying element	Effect of alloying on fluidity and temperature
1	A357	Copper	In the solid state the solubility of Cu in Al increases from less than 0.50 % at room temperature to 5.65 % at 821 K. Fluidity decreases along with ductility but also results better mechanical properties (hardness & strength) as Cu content increases. Thus, to have optimum ductility limited % of Cu (2 to 5 %) is beneficial and do not exceed 12 % in most Al-Cu based alloys [22].
2	Al-6Ni-3Si	Silicon	As an alloying element Si is used up to 14 % in amount. The solubility in Al, the α phase of Si is limited up to 1.65 % at 851 K and less than 0.05 % at room temperature. Up to eutectic % of Si, strength of Al-Si alloy increased by increasing Si% while ductility decreases. Like Mn and Ni, Si also do not confer response to solution heat treatment [23].
3	AZ91D and Mg–3Nd–0.2Zn–Zr	Magnesium	Magnesium behaves similar to copper when alloyed with aluminium. Solid-solubility change of the α phase with temperature reflects in alloy system. Solubility of Mg at 724 K is 14.9 % while at room temperature it is less than 2.90 %. If the solid-solubility limit is exceeded, A second, harder β phase exists. Aging and solution heat treatment can be done on this binary system which normally contain 4, 8, and 10 % of magnesium [24].
4	AlSi9Mg	Magnesium - Silicon	Some important alloying effects are reflected in aluminium by combination of Mg-Si which form the metallic compound Mg_2Si and produce a quasi-binary alloy system. Due to excess of Silicon present in Ternary alloys results improved casting properties like enhanced fluidity [25].
5	A357	Zinc	One of the principal alloying elements with major advantage that it makes possible to get maximum mechanical properties in the as-cast conditions but when it exceeds 0.1 to 0.3 %, it reduces corrosion resistance properties of alloy [22].
6	A356/TiB_2 + RE + Sn	Iron (as impurity)	Iron as impurity, omnipresent in amount of 0.8 to 2 % because iron can dissolve from ladles or from furnace pots and form Fe-Al phase which results embrittlement, reduced corrosion resistance ability & coarsening of as-cast grain size of metal [26].

Aluminum-based alloys, for example, are eutectic systems with various intermetallic compounds. Due to the lower solubility of most alloying elements in aluminum, these alloys exhibit multiple metallic phases with complex compositions [14,41]. Table 1 provides an overview of the effect of some key alloying elements such as Cu, Si, Mg, Zn, Cr, Mn, Sn, and Ti in aluminum-based casting alloys on fluidity and temperature.

Solidification and mechanism

After pouring, the solidification behavior of semi-solid slurry differs from conventional casting in the following aspects: the temperature gradient of the surrounding environment, the presence of constituent or alloying elements in the slurry, the mode of heat transfer [10,51].

These three conditions give rise to a solidification range, known as the freezing range, which is determined by the solidus and liquidus temperatures. Within this range, both primary and secondary solidification occur. Primary solidification initiates just before the liquidus temperature, while secondary solidification takes place over time. Figures 2 and 3 illustrate the time-dependent temperature curves.

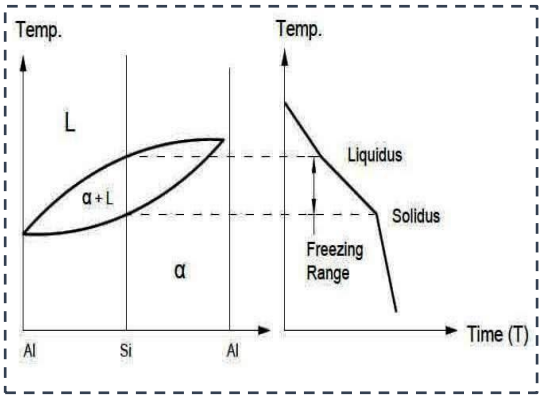

Fig. 2. Variations in temperature vs time for semi solid processing

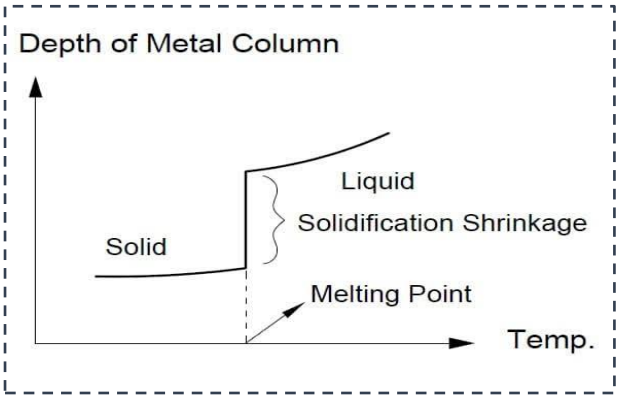

Fig. 3. Variations in depth of metal column vs temperature for semi solid processing

Above the liquidus temperature, the fluidity of the slurry is influenced by gravitational and convection effects and is affected by the thermal conductivity of the mold. In this temperature range, the primary solidification range is narrower compared to the secondary solidification range. This phenomenon, known as liquid solidification shrinkage (Fig. 4), is influenced by the presence of unmelted solid particles, such as reinforcement ceramics, hindering the movement of silicon particulates in the α-Al melt. A thermal mismatch between the solid particles and the liquid melt enhances the temperature gradient, leading to a decrease in solidification time. Gravitational and convection effects contribute to the formation of columnar grains and equiaxed grains during the tertiary solidification zone, which is primarily observed in liquid-liquid solidification. The formation of these grains is influenced by factors such as the depth of the metal column, temperature gradient, and available solidification time [10]. Local solidification, governed by the secondary solidification zone (Fig. 5), is also affected. The

total solidification time depends on the pouring temperature of the melt, which is governed by the α-cooling rate [10,40–42]. Figure 5 illustrates the "semi-solid pouring zone" (AB) as part of the total solidification time. In the actual solidification time, local solidification is influenced by alloying particulates/elements, leading to a decrease in the secondary solidification range and an increase in the primary solidification range due to a higher thermal gradient (A'B'). However, the total solidification time is less hindered in conventional slurry melts, where the time zone mostly increases for tertiary solidification (CD C'D', Fig. 5). This is referred to as the "thermal arrest zone", where sensible heat transfer is higher compared to latent heat transfer, resulting in a difference between secondary solidification and tertiary solidification. Figure 4 represents the effect of fluidity, showing the solidification starting range, phase transition range, and secondary solidification range. The solidification process after the phase transition, up to the solidification temperature, involves latent heat transfer and takes more time compared to primary and tertiary solidification [10,62].

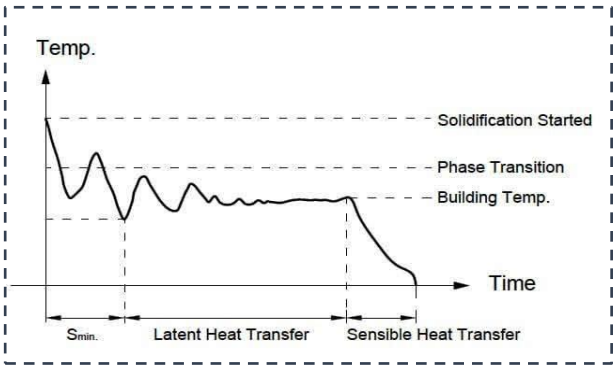

Fig. 4. Variations showing for temperature and time for heat transfer and phase transformation

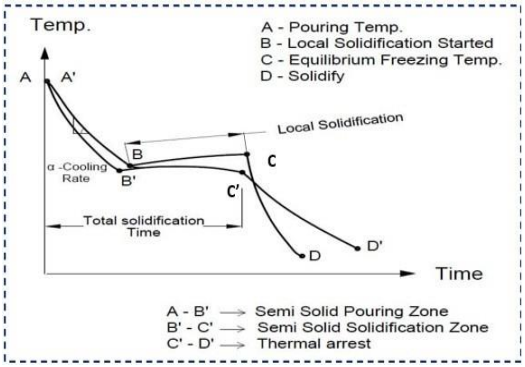

Fig. 5. Variations showing for temperature and time for effect of pouring temperature and solidification

Thermodynamic- equilibrium, interface and solidification

Thermodynamics plays a crucial role in analyzing the solidification phase composition and the resulting interfacial effects [6,10,39]. The slopes of liquidus variations, solidus phase boundaries, and solidification paths are correlated with the constituent temperature of the melt during solidification. The degree of undercooling, which is related to the type of matrix and reinforcement, directly impacts interface formation. Different types of interfaces can be formed, including: local interface equilibrium, interface non-equilibrium, equilibrium departure, and pressurized undercooling.

These interfaces are influenced by the solidus and liquidus phenomena of the pouring temperature, with Gibbs' free energy directly linked to the formation of interfaces at various stages. The correlation between solidification and interfaces can be determined by examining the steps involved in the solidification process.

Well known Gibb's free energy:

$$G = H - T.S \tag{1}$$

where $H = E + Pv$ (enthalpy of phase neutral alloy).

Considering three steps of the semi-solid melt before solidification:
(1) Liquidus stage (G_1);
(2) Liquidus/Solidus stage (liquid in majority) (G_2);
(3) Solidus/Liquidus stage (solid in majority) (G_3).

Difference of Gibb's free energy from initial to final stage:

$$\Delta G = (G_1 - G_2) + G_2' - G_3 \quad , \tag{2}$$

where G_2'- the Gibb's free energy due to the impact of reinforcement. Generally,

$$G_2' > G_2 - \Delta G_2 = G_l - G_s. \tag{3}$$

However, $G_2 > \Delta G_2 > G_2'$:

$$\Delta G_2 = (H_l - H_s) - T_e(S_l - S_s) = 0 \text{ (for pure metal)}, \tag{4}$$

$$\Delta G_2 = (H_l - H_s) - T_e(S_l - S_s) \neq 0 \text{ (for reinforced metal)}. \tag{5}$$

Further,

$$\Delta H = (\Delta S_f)T_e \tag{6}$$

where, ΔH is change in enthalpy during the melting, ΔS_f entropy of the fused solidus particle, T_e is equivalent temperature (mean value).

Now, as T_e decreases:

$$\Delta G_2 = \Delta H_f \left(\frac{T_e - T'}{T_e}\right), \tag{7}$$

where $T'$is temperature at a particular stage. As T' decreases solidification increases:

$$\Delta G_2 = \Delta H_f \left(\frac{\Delta T'}{T_e}\right) \tag{8}$$

$$\Delta G_2 = \Delta S_f \Delta T', \tag{9}$$

where $\Delta T'$is considered for undercooling.

According to the above equations, liquid in majority is considered for the liquidus stage for Gibb's free energy G_2 used in the above equations. Further, this stage is variable and changes appears due to the type and amount of reinforcement incorporation for which Gibb's free energy is much higher as compare to the unmodified liquid conditions as shown in Eq. (3). Generally, change in Gibb's free energy due to the incorporation of reinforcement is increases in initial stage, whereas this can be considerable as 'zero' for the pure metal and ideal condition as shown in Eqs. (4) and (5).

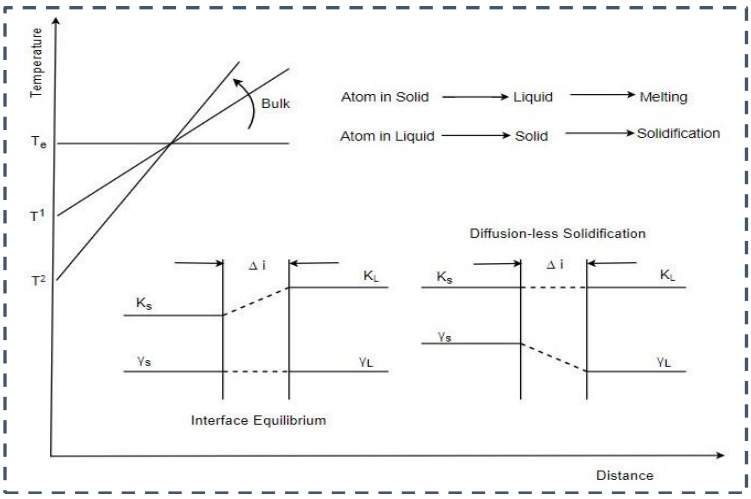

Fig. 6. Relation between temperature and distance for Interfacial and diffusion-less solidification

Equations (6-9) and (10) show the correlation between enthalpy and entropy with the equilibrium temperature, as shown in Fig. 6. Here, according to Fig. 6 and Eqs. (6-9) and (10), change in enthalpy and entropy for the fused solid particles is a potential candidate and parameter for the equilibrium temperature under pressurized solidification [59]. Generally, equilibrium temperature is a function of a particular stage (T) in which solidification started. T is dependent on the type of reinforcement and its incorporation, while ΔH_f is the change in enthalpy for the liquid melt. As the amount of reinforcement increases T decreases solidification rate increases which is an obvious phenomenon [7,24,40,51]. This shows the condition of undercooling according to Eq. (10) while as under undercooling condition, ΔT becomes positive and solidification rate is considered as a function of enthalpy and entropy. Moreover, for no undercooling condition:

$$\Delta T = 0 \text{ however } \Delta G = 0. \tag{10}$$

System is in equilibrium and no transformation is existed. This is the general and possible condition of self-pouring temperature under gravity of melt.

Free energy under pressurized cooling $\Delta F_{l|_s} = \Delta F_l - \Delta F_s$

$$\Delta F_l = \Delta P(v_l - v_s) - \Delta T(S_l - S_s) \tag{11}$$

The change in equilibrium temperature due to applied pressure:

$$\Delta TP = \frac{\Delta v}{\Delta S_f}\Delta P. \tag{12}$$

This pressure is the function of temperature. As the temperature of the slurry decreases, pressurized solidification increases. As $\Delta P > 0$ result is increase in undercooling. This is converted to kinetic undercooling for solid to liquid interface. Generally, solidification velocity depends on the rate of solidification and rate of melting [10,62]. However,

$$v = v_s - v_s e^{\left(\frac{\Delta G}{RT_i}\right)}, \tag{13}$$

where ΔG is in J/mole and $\boldsymbol{v_s}$ is the hypothetical maximum growth of the velocity.

Table 2. Effect of the increment in undercooling or solidification

Diffusional equilibrium	Interfacial equilibrium	Interfacial non-equilibrium
Absence of temperature gradient	Liquid-solid interface for temperature	Arbitrary impact of temperature gradient
Uniform phase composition	Metastable phase condition	Phase diagram fails to evaluate the compositions on local interface zone

Equations (11-13) describe the thermodynamic equilibrium conditions for undercooling and interfacial stages, involving ΔG (change in Gibbs free energy) and the growth velocity of solidification [10]. Equation (11) represents pressurized solidification, where interface equilibrium occurs when the thermal conductivity of the reinforcement is the dominant factor [39,46,59]. At this stage, interface formation increases, and interface equilibrium is sustained, as depicted in Fig. 6 and described by Eqs. (11), (12). After a certain point, incomplete recrystallization occurs due to these interfaces, and diffusion solidification begins [10,60]. Diffusion solidification leads to the transformation of micro level reinforcement particles near the interface boundaries, causing an increase in the growth of solid particles. As a result, there is a drop in solidification velocity, as shown in Fig. 6. In the semi-solid stage, the temperature conditions T1 and T2 represent

the solid and liquid candidates present in the slurry, respectively. These conditions give rise to several thermally dependent stages, including: constitutional undercooling, Conditional and unconditional undercooling, and interfacial thermal undercooling.

Undercooling plays a dominant role in the solidification process in the semi-solid stage and contributes to the formation of different thermal interfaces and undercooling conditions, as summarized in Table 2.

Conclusions

This review primarily focuses on the research findings related to semi-solid casting, specifically exploring the impact of processing temperature, alloying elements, and fluidity as crucial parameters. The solidification rate, considered a secondary parameter, is also influenced by factors such as pouring temperature, holding time, and stirring action, which are essential for controlling the slurry. Moreover, restricted grain growth plays a significant role in the solidification behavior, influenced by the solid-liquid fraction and viscosity of the slurry. This correlation between rheological properties and processing parameters establishes the cohesion within the system. Additionally, the temperature gradient, as an associated processing parameter, affects the heat transfer mode during solidification and is influenced by the alloying elements, resulting in different types of solidification shrinkage. In summary, all the selected criteria are interconnected, playing a crucial role in the overall processing, phase transition, and solidification processes.

References

1. Kirkwood DH. Semi-solid metal processing. *International Materials Reviews*. 1994;39(5): 173–189.
2. Fan Z. Semi-solid metal processing. *International Materials Review*. 2002;47: 249–285.
3. Morando C, Fornaro O, Garbellini O, Palacio H. Fluidity on metallic eutectic alloys. *Procedia Materals Science*. 2015;8: 959–967.
4. Alrobei H. Effect of different parameters and aging time on wear resistance and hardness of SiC-B4C reinforced AA6061 alloy. *Journal of Mechanical Science and Technology*. 2020;34: 2027–2034.
5. Singh DP, Dwivedi VK, Agarwal M. The key attributes of processing parameters on semi-solid metal casting: An Overview. *E3S Web of Conferences*. 2021;309: 01089.
6. Miazga A, Konopka K, Gizowska M, Szafran M. Alumina matrix ceramic-nickel composites formed by gel-casting method. *Composites Theory and Practice*. 2012;12(2): 138–141.
7. Agarwal M, Srivastava R. Influence of processing parameters on microstructure and mechanical response of a high-pressure die cast aluminum alloy. *Materials and Manufacturing Processes*. 2019;34(4): 462–472.
8. Agarwal M, Srivastava R. Influence of fine Al2O3 and aluminium nano-particles on the 6061 aluminium alloy near the grain boundary of the semisolid cast microstructure. *Transactions of the Indian Ceramic Society*. 2019;78(2): 94–100.
9. Agarwal M, Srivastava R. Effect of thick slurry and stepped deformation on mechanical properties of AA6061 alloys. *Emerging Materials Research*. 2019;8(3): 394-403.
10. Agarwal M, Dixit NK, Dixit M, Srivastava R. Interfacial study for the effect of Al2O3 addition on the microstructure and micro-hardness of the Al2O3/AA6061 semi-solid cast composite. *Phase Transitions*. 2021;94(12): 899–909.
11. Chen S, Chang G, Yue X, Li Q. Solidification process and microstructure of transition layer of Cu–Al composite cast prepared by method of pouring molten aluminum. *Transactions of Nonferrous Metals Society of China*. 2016;26(8): 2247–256.
12. Deev VB, Ponomareva KV, Kutsenko AI, Prikhodko OG, Smetanyuk SV. Influence of temperatures of melt overheating and pouring on the quality of aluminum alloy lost foam castings. *Russian Journal of Non-Ferrous Metals*. 2017;58: 373–377. (In Russian)
13. Sui Y, Feng K, Cheng C, Chen X, Qi J, He Y, Meng Q, Wei F, Sun Z. Effects of pouring temperature on interfacial reaction between Ti-47.5Al-2.5V-1Cr alloy and mold during centrifugal casting. *Journal of Wuhan University of Technology-Mater. Sci. Ed.* 2016;31: 1105–1108.
14. Heo M, Jin CK, Roh JS, Kang CG. Investigating the micro-structures of A356 semi-solids based on electromagnetic stirring currents and crucible materials. *Journal of Mechanical Science and Technology*. 2020;34: 3807–3813.

15. Kim JH, Yasukawa A, Yonezawa S. Enhanced dispersion stability and fluidity of rutile TiO_2 particles using surface fluorination. *Materials Today: Proceedings*. 2020;20: 311–319.
16. Sang-Su N, Yong-Ho K, Hyeon-Taek S, Seong-Hee L. Effect of Sc addition on microstructure, electrical conductivity, thermal conductivity and mechanical properties of Al-2Zn-1Cu-0.3Mg based Alloy. *Korean Journal of Materials Research*. 2020;30(10): 542–549.
17. Mishra RR, Sharma AK. Microwave heating characteristics of bulk metallic materials and role of oxides. *Journal of Materials Science*. 2018;53: 16567–16584.
18. Olszówka-Myalska A, Myalski J, Wrzała K. Fabrication of magnesium matrix composite with glassy carbon particles by pressure die casting. *Composites Theory and Practice*. 2014;14(2): 101–105.
19. Motoyama Y, Tokunaga H, Yoshida M, Maruyama T, Okane T. Measuring the interfacial heat transfer coefficient between flowing molten alloy and sand mold using fluidity tests. *Journal of Materials Processing Technology*. 2019;11: 6394.
20. Fu Y, Wang H, Zhang C, Hao H. Effects of minor Sr additions on the as-cast microstructure, fluidity and mechanical properties of Mg-4.2Zn-1.7RE-0.8Zr-0.2Ca (wt%) alloy. *Materials Science and Engineering: A*. 2018;723: 118–125.
21. Birru AK, Kumar BP. Influence of fluidity of Al-Cu alloy with fly ash reinforcement by single spiral fluidity test. *Materials Today: Proceedings*. 2015;24(5): 2776–2783.
22. Mao G, Liu D, Gao W, Liu S, Zhong L. The effects of copper (Cu) or zinc (Zn) on fluidity of A357 alloy. *Materials Letters*. 2021;304: 130733.
23. Yang L, Li W, Du J, Wang K, Tang P. Effect of Si and Ni contents on the fluidity of Al-Ni-Si alloys evaluated by using thermal analysis. *Thermochimica Acta*. 2016;6: 457–415.
24. Huang H, Wang YX, Fu PH, Peng LM, Jiang HY, Xu WY. Fluidity of AZ91D and Mg–3Nd–0·2Zn–Zr (wt-%) magnesium alloys: response to pouring and mould temperature. *International Journal of Cast Metals Research*. 2013;26(4): 213–219.
25. Qi Z, Miao C, Jin C. AlSi9Mg aluminum alloy semi-solid slurry preparation by intermediate frequency electromagnetic oscillation process. *Journal of Materials Processing Technology*. 2015;215: 42–49.
26. Rathod N, Menghani J. Detrimental effect of Fe as impurity on A356/TiB2 + RE + Sn alloy fabricate via in situ route. *Materials Today: Proceedings*. 2021;44(1): 1326–1330.
27. Ragab KA, Bouaicha A, Bouazara M. Optimization of casting design parameters on fabrication of reliable semi-solid aluminum suspension control arm. *Journal of Materials Engineering and Performance*. 2017;26: 4450–4461.
28. Liu Z, Mao W, Wang W, et al. Investigation of rheo-diecasting mold filling of semi-solid A380 aluminum alloy slurry. *International Journal of Minerals, Metallurgy and Materials*. 2017;24: 691–700.
29. Srivastava A, Shaikh KA, Bopanna S. Microstructural Characterization of SiC reinforced Ti–6Al–4V metal matrix composites fabricated through powder metallurgy route. *Materials Physics and Mechanics*. 2023;51(3): 29–37.
30. Zemtsova EG, Smirnov VM, Kozlova LA, Morozov PE, Yurchuk DV, Semenov BN, Morozov NF. Development of aluminum-based composite with two reinforcing modifiers (TiC/Ni, CNTs/Ni) with improved mechanical properties. *Materials Physics and Mechanics*. 2023;51(3): 9–19.
31. Ravikumar M, Naik R, Vinod BR, Chethana KY, Rammohan YS. Study on nanosized Al2O3 and Al2O3-SiC on mechanical, wear and fracture surface of Al7075 composites for soil anchoring applications. *Materials Physics and Mechanics*. 2023;51(6): 24–41.
32. Prasad KS, Mukhopadhyay AK, Majumdar B, Akhtar D. Nature and stability of phases present in a rapidly solidified aluminium alloy 7010 containing scandium. *Materials and Manufacturing Processes*. 2008;23(7): 658–664.
33. Ragab KA, Bouazara M, Bouaicha A, Allaoui O. Microstructural and mechanical features of aluminium semi-solid alloys made by rheocasting technique. *Materials Science and Technology*. 2017;33(6): 646–655.
34. Kolahdooz A, Aminian S. Effects of important parameters in the production of Al-A356 alloy by semi-solid forming process. *Journal of Materials Research and Technology*. 2019;8(1): 189–198.
35. Ansari MHS, Aghaie-Khafri M. Predicting flow localization in semi-solid deformation. *International Journal of Material Forming*. 2018;11: 165–173.
36. Simlandi S, Barman N, Chattopadhyay H. Study on rheological behavior of semisolid A356 alloy during solidification. *Transactions of the Indian Institute of Metals*. 2012;65: 809–814.
37. Nikanorov SP, Osipov VN, Regel LI. Structural and mechanical properties of directionally solidified Al-Si alloys. *Journal of Materials Engineering and Performance*. 2019;28: 7302–7323.
38. Li M, Li Y, Bi G, Huang X, Chen T, Ma Y. Effects of melt treatment temperature and isothermal holding parameter on water-quenched microstructures of A356 aluminum alloy semisolid slurry. *Transactions of Nonferrous Metals Society of China*. 2018;28(3): 393–403.
39. Pang S, Wu G, Liu W, Zhang L, Zhang Y, Conrad H, Ding W. Influence of pouring temperature on solidification behavior, microstructure and mechanical properties of sand-cast Mg-10Gd-3Y-0.4Zr alloy. *Transactions of Nonferrous Metals Society of China*. 2015;25(2): 363–374.
40. Birol Y. A357 thixoforming feedstock produced by cooling slope casting. *Journal of Materials Processing Technology*. 2007;186(1-3): 94–101.
41. Alhejazi HJ, Maijer DM, Macht JP, Phillion AB. Comparison of semi-solid contraction of aluminum alloys during solidification quantified by a combined numerical-experimental approach. *Metals and Materials International*. 2022;28: 1783–1793.

42. Birol Y. Semi-solid processing of the primary aluminium die casting alloy A365. *Journal of Alloys and Compounds*. 2009;473(1-2): 133–138.
43. Pulivarti SR, Birru AK. Effect of mould coatings and pouring temperature on the fluidity of different thin cross-sections of A206 Alloy by sand casting. *Transactions of the Indian Institute of Metals*. 2018;71: 1735–1745.
44. Zou GT, Zhang HH, Yang YT, Lu FM, Yu ZT, Wang C. Effects of pouring and mold temperatures on the fluidity and hot tearing susceptibility of Al–3.5Si–0.5Mg–0.4Cu alloy. *Transactions of the Indian Institute of Metals*. 2020;73: 2511–2517.
45. Shehata MM, El-Hadad S, Moussa ME, El-Shennawy M. Optimizing the pouring temperature for semisolid casting of a hypereutectic Al–Si alloy using the cooling slope plate method. *Inter Metalcast*. 2021;15: 488–499.
46. Liu G, Wang Q, Zhang L, Ye B, Jiang H, Ding W. Effects of melt-to-solid volume ratio and pouring temperature on microstructures and mechanical properties of Cu/Al bimetals in compound casting process. *Metall Mater Trans A*. 2019;50: 401–414.
47. Fehlbier M, Klaassen O, Salun PR. Semi-solid-metal casting/thixocasting: determination of the flow characteristics of semi-solid aluminium alloys. In: Winkler PJ. (ed.) *Materials for Transportation Technology*. Weinheim, Germany: Wiley-VCH Verlag GmbH; 2000. p.124–128.
48. Balitchev E, Hallstedt B, Neuschütz D. Thermodynamic criteria for the selection of alloys suitable for semi-solid processing. *Steel Research International*. 2005;76(2-3): 92–98.
49. Li L, Li D, Feng J, Zhang Y, Kang Y. Effect of cooling rates on the microstructure and mechanical property of La modified Al7SiMg alloys processed by gravity die casting and semi-solid die casting. *Metals*. 2020;10(4): 549.
50. Talangkun S, Potisawang C, Saenpong P. Thixoforming and rheo-die-casting of A356/SiC composite. *Metals*. 2020;10(2): 251.
51. Stefanescu DM. Equilibrium and non-equilibrium during solidification. In: *Science and Engineering of Casting Solidification*. Second Edition. Boston, MA: Springer; 2009. p.1–20.
52. Cao Fx, Deng KK, Wang CJ, Nie K, Liang W, Fan J. Synergistic enhancement of the strength-ductility for stir casting SiCp/2024 Al composites by two-step deformation. *Metals and Materials International*. 2021;27: 5450–5461.
53. Samavedam S, Sakri SB, Hanumantha RD, Sundarrajan S. Estimation of porosity and shrinkage in a cast eutectic Al–Si alloy. *Canadian Metallurgical Quarterly*. 2014; 53(1): 55–64.
54. Birol Y. Cooling slope casting and thixoforming of hypereutectic A390 alloy. *Journal of Materials Processing Technology*. 2008;207(1-3): 200–203.
55. Aguilar J, Fehlbier M, Grimmig T, Bramann H, Afrath C, Bührig AP. Semi-solid processing of metal alloys. *Steel Research International*. 2004;75: 492–505.
56. Mishra RR, Sharma AK. Microwave–material interaction phenomena: heating mechanisms, challenges and opportunities in material processing. *Composites Part A: Applied Science and Manufacturing*. 2016;81: 78–97.
57. Han J, Liu Z, Jia Y, Wang T, Zhao L, Guo J, Chen Y. Effect of TiB2 addition on microstructure and fluidity of cast Ti-Al alloy. *Vacuum*. 2020;174: 109210.
58. Mao J, Liu W, Wu G, et al. Semi-solid slurry preparation, rheo-die casting and rheo-squeeze casting of an AZ91–2Ca–1.5Ce ignition-proof magnesium alloy by gas-bubbling process. *Journal of Materials Research*. 2017;32: 677–686.
59. Moustafa SF. Casting of particulate Al-base composites. *International Journal of Materials Research*. 1997;88(3): 209–216.
60. Tuan NA, Van LD, Giang LD. Optimization of Processing Parameters of Primary Phase Particle Size of Cooling Slope Process for Semi-solid Casting of ADC 12 Al Alloy. In: Bui TQ, Cuong LT, Khatir S. (eds.) *Structural Health Monitoring and Engineering Structures. Lecture Notes in Civil Engineering*. Singapore: Springer; 2021. p.49–61.
61. Midson SP. Using micro-CT scanning to quantitative characterizes porosity in high pressure die castings and semi-solid castings. *In: Solid State Phenomena*. 2022;327: 33–44.
62. Yumi K, Youngchan K, Seweon C. Effect of precipitation and dissolution of Si on the thermal diffusivity in the Al-Si alloy system. *Korean Journal of Materials Research*. 2020;30(9): 474–479.

About Authors

Devendra Pratap Singh Sc
Research Scholar, GLA University, Mathura, India

Dwivedi Vijay Kumar Sc
Professor, GLA University, Mathura, India

Mayank Agarwal Sc
PhD, Associate Professor, Dr. RML Avadh University, Faizabad, India

MATERIALS PHYSICS AND MECHANICS RESEACH ARTICLE

Submitted: May 30, 2023 Revised: November 14, 2023 Accepted: March 14, 2024

Effect on annealing on the micro-structural behavior of spray deposited Al-6Si-10Pb alloys

R. Mittal ✉, I. Choudhary, R. Sehrawat, R. Dhawan, P.S. Singh,

Maharishi Markandeshwar University, Mullana, India

✉ rashmimittal3@gmail.com

ABSTRACT

In the present work, the microstructural features of spray deposited Al-6Si-10Pb alloys before and after annealing at different locations of the preform have been compared with each other. XRD confirms the presence of all elements present in the Al-6Si-10Pb alloy. The optical micrographs were taken at three different regions of the preform before and after annealing predicts that the grain size is lower at the peripheral region as compared to central region. Equiaxed grain structure was observed in SEM images, with a uniform distribution of Pb and Si phase in an Al-matrix. Further, grain refinement and reduction of porosity was observed after annealing.

KEYWORDS

Al-alloys • microstructure • spray deposition • annealing

Citation: Mittal R, Choudhary I, Sehrawat R, Dhawan R, Singh PS. Subcritical growth of repolarization nuclei in polycrystalline ferroelectric films. *Materials Physics and Mechanics*. 2024;52(2): 11–18. http://dx.doi.org/10.18149/MPM.5222024_2

Introduction

Manufacturing industry such as construction, aerospace, and automobile demand metals/alloys which possess high strength, high corrosion resistance, high stiffness, light-weight, and low thermal expansion coefficients [1–4]. Contrary, these materials should have excellent wear and abrasive resistance for their use in bearings and gear boxes [5,6]. These properties of the materials have direct impact on the performance and efficiency of the constructed machines parts. However, attaining high strength along with good ductility is still a great challenge in the metallurgy. In steel industry, achieving this objective require a complex and time-consuming process of nitriding and carburizing. Aluminum (Al) due to its superior properties and ease of casting can be suitable alternative for iron (Fe). However, casting Al alone offers new challenges of high shrinkage, low fluidity and hot tearing. Recent studies predict that alloying aluminum (Al) with various metals such as silicon (Si), manganese (Mn), magnesium (Mg), copper (Cu) and magnesium-silicide (Mg_2Si) can resolve these casting problems. For example, Al-Si alloys offer good fluidity of molten metal at lower casting temperatures in comparison to the pure metal [7–9]. However, during conventional casting the ductility of the aluminum is compromised simultaneously as the coarse silicon particles gets embedded in the Al metal. To compensate for ductility soft elements such as lead (Pb), indium (In), and tin (Sn) can be added the mixture [10]. However, due to large density differences these elements are not miscible with Al and can't be casted using simple conventional casting techniques. Alternatively, advanced casting techniques such as spray forming [11,12] can lead to the homogeneous dispersion of soft elements in Al matrix. This technique utilizes

high velocity gas jets to disintegrate the molten metal into droplets of submicron size. These small droplets contain partially solidified particles in molten metal, which acts as nucleating sites. Consequently, rapid solidification takes place which leads to homogeneous microstructures with negligible agglomeration. In case of Al-Si alloys, earlier reports suggests that size and shape of Si particles plays major role in obtaining a fine grain structure, which can be controlled by adjusting the cooling rate during solidification. Usually, faster cooling rates lead to fine microstructure. Thus, use of spray forming technique for the production of good quality Al-Si alloy is a good choice. However, due to the non-uniform gaussian distribution of the mass in the spray droplets, the obtained preform contains high level of porosity. Thus, requires further heat treatments to reduce the porosity [13,14].

The objectives of our work are (1) to obtain fully miscible Al-6Si-10Pb alloy with no segregation using spray forming technique, and (2) to study the effect of annealing on the microstructure of Al-6Si-10Pb alloy taken at different locations of the preform.

Materials and Methods

Figure 1 represents the experimental setup and the process mechanism of the spray forming technique used for the deposition of Al-6Si-10Pb alloy on a substrate. The material processing involves heating a mixture of 900 g commercially available Al–6Si alloy (see Table 1 for the detail composition) and 100 g Pb at 1123K in the crucible kept over the nozzle of the atomizer unit.

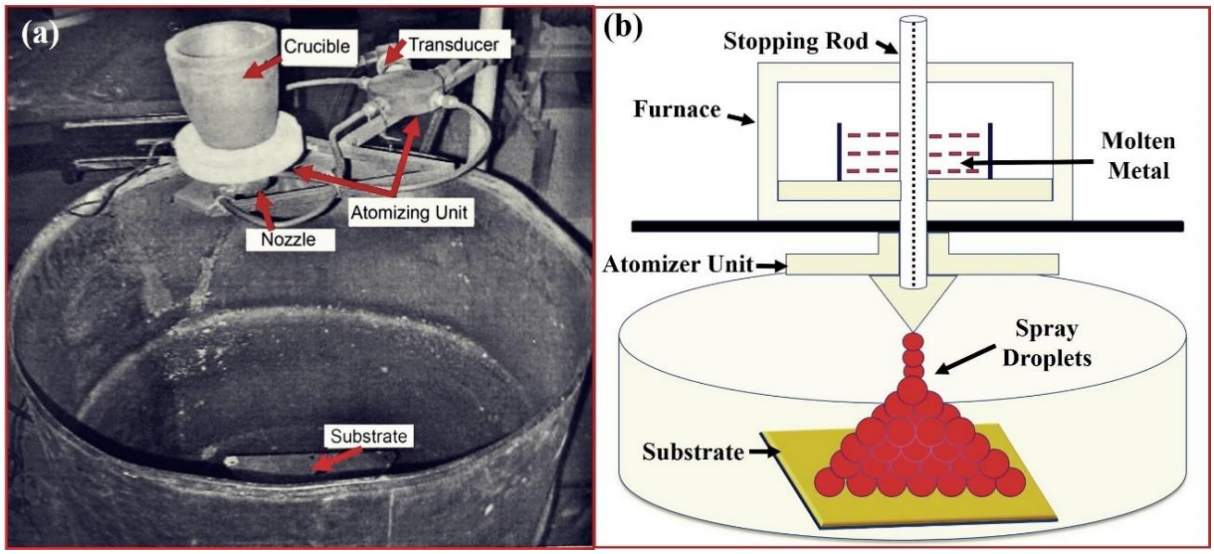

Fig. 1. (a) Photograph of the apparatus used for experimental work and (b) the process mechanism of the spray forming

Table 1. Chemical composition of Al-Si alloy

Si	Fe	Mn	Zn	Ti	Pb	Sn	Mg	Ni	Al
6.0	0.41	0.21	0.29	0.06	0.04	0.12	0.13	0.12	balance

A stopper rod at the entrance of delivery tube prevents the melt flow through it prior to its atomization. Nitrogen was supplied for atomization prior to melt flowing through the delivery tube. Atomization of melt resulted in a spray of wide range of micron size droplets. These droplets were then allowed to deposit over a copper substrate. The obtained preform was taken out of the substrate after deposition. The deposition was carried out for the alloy of composition Al-6Si-10Pb at 1123 K temperature and 1 MPa pressure of nitrogen gas. The details of the various process parameters have been listed in the Table 2.

Table 2. Process parameters used during the casting

Process parameter	Value
Melt temperature, K	1123
Atomizing gas	Nitrogen
Gas pressure, MPa	1.0
Nozzle to substrate distance, cm	35.0
Nozzle type	Convergent-divergent
Throat diameter, mm	16 (inner), 18 (outer)
Throat width, mm	1.0
Throat angle, º	5.0
Melt delivery tube diameter, mm	5.0
Substrate	Copper
Substrate diameter, mm	200.0

The spray deposited-Al-6Si-10Pb alloy was further processed through cold rolling and annealing process. The rolling operation was performed using rolling mill consisting of rollers having diameter of 110 mm and speed of 8 rpm. Several numbers of passes were applied on spray deposited Al-6Si-10Pb alloys through the rolls to achieve 40 % thickness reduction. Afterward, these samples were processed through annealing at temperature 250 °C for 1 hour. The obtained spray formed preform was characterized using X-ray diffraction (XRD), optical microscopy (OM) and scanning electron microscopy (SEM) to understand the structural and morphological properties of the Al-6Si-10Pb alloy before and after annealing. The XRD measurements Al-6Si-10Pb alloy was performed using Bruker AXS D8 Advance X-Ray Diffractometer, having Cu as target and Ni filter material. The diffraction angle (2ϑ) was varied from 20 to 100° with a step-size of 0.05°. The goniometer speed was kept at 2°/minute. For the observation of the microstructures, samples from the different parts of the spray formed deposits were cut down and first polished using emery paper of 1/0, 2/0, 3/0 and 4/0 specifications. Later, the samples were polished on wheel cloth polishing machine using an emulsion of alumina (Al_2O_3) particles suspended in water. Afterward, these samples were polished by kerosene oil. Lastly, these samples were etched with Keller's reagent (composition: 1 % vol. HF, 1.5 % vol. HCl, 2.5 % vol. HNO_3 and remaining water). The microstructures of samples were examined under optical microscope (Leica) and SEM (Leo-435-VP).

Results and Discussion

Structural analysis

First, the structural properties of the casted Al-6Si-10Pb alloy using XRD has been investigated. Sharp and high intensity XRD peaks (see Fig. 2) observed at diffraction angles of 38.47, 44.74, 65.13, 78.23, 82.48, and 99.08° belong to cubic lattice structure of aluminum (JCPDS card no. 04-0787) and corresponds to (111), (200), (220), (311), (222), and (400) lattice planes, respectively.

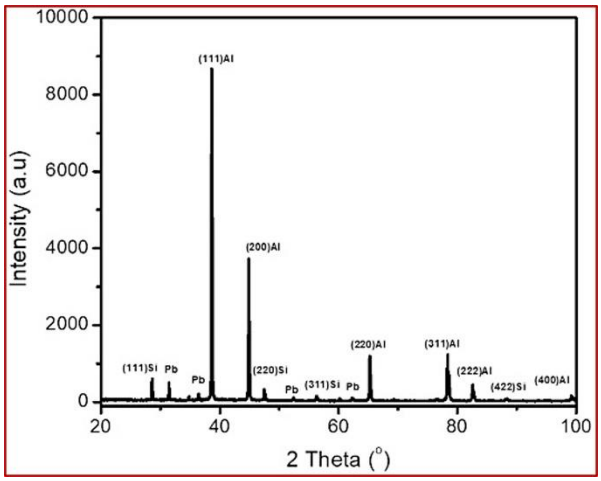

Fig. 2. XRD pattern of spray deposited Al-6Si-10Pb alloy

XRD peaks with small intensity observed at 31.31, 36.27, 52.23, and 62.12° belong to the cubic lattice structure of lead (JCPDS card no. 04-0686) and corresponds to the (111), (200), (220), and (311) lattice planes respectively. The rest of the small intensity peaks at diffraction angles of 28.44, 47.30, 56.12, and 88.03° belong to cubic silicon (JCPDS card no. 27-1402) and corresponds to the (111), (220), (311) and (422) lattice planes, respectively. This confirms the formation of Al-6Si-10Pb alloy.

Morphological analysis

Optical microscopy

Figure 3 shows the typical microstructures of the spray deposited Al-6Si-10Pb alloy, observed by optical microscopy. It is possible to recognize an equiaxial Al matrix and near-uniform distributed silicon and lead particles surrounding the Al matrix (Fig. 3(a,c,e)). The average grain size of Al is 40 μm for center and middle region (Fig. 3(a,c)) while it is lower (around 30 μm) for peripheral region (Fig. 3(e)). One of the reasons for lower grain size at peripheral region is high rate of heat transfer due to small thickness at this region reported by other researchers also [15]. Some noticeable pores are also observed in these micrographs (Fig. 3(a,c,e)). The pore size is 5-10 μm. Porosity occurs due to the high velocity gas entrapment during solidification process. However, after rolling and annealing, the porosity gets almost eliminated as can be depicted from the microstructures (Fig. 3(b,d,f)).

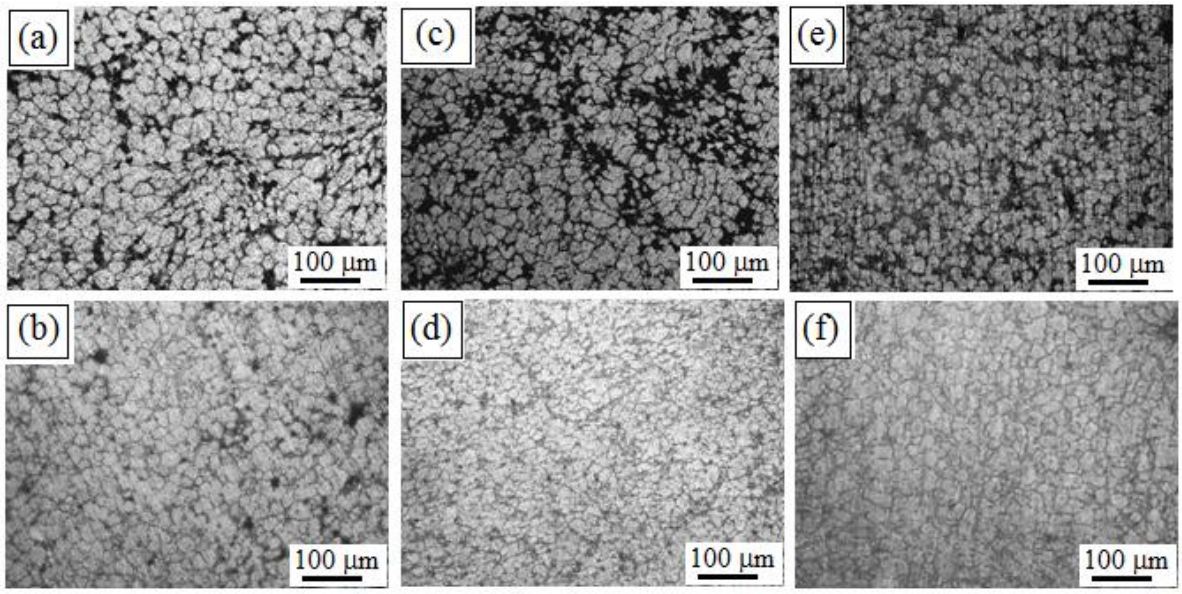

Fig. 3. Microstructure of spray deposited Al-6Si-10Pbat center region (a,b), middle region (c,d) and peripheral region (e,f) before annealing (a,c,e) and after annealing (b,d,f)

Scanning electron microscopy

Figure 4 shows SEM microstructure of the as sprayed deposit. Mostly pores are noticed at the grain boundaries. The grain boundaries due to presence of porosity have quite strained structure. The white phase shown in SEM micrograph is of silicon and grey grains are of Al matrix. The observed grain structure was homogeneous through the deposit, indicating that a good compromise between heat extraction and deposition rate was attained during deposit build-up. In addition, no banded microstructure was observed in these deposits as described by Cantor [16]. Equiaxial morphology of the Al phase was a remarkable feature of this structure and is ascribed to the extensive fragmentation and coarsening of solid phases during the build-up of the deposit. It has been assumed that during this stage of the process the solid, semisolid and fully liquid droplets impacting the surface of the deposit provide a great quantity of nuclei that coarsen due to the vigorous agitation and the cooling conditions at this solidifying layer, resulting in an equiaxial form. Concerning silicon and the intermetallic phases there are still greater differences to the conventionally cast material. In contrast to a typical eutectic as well as in spray formed hypoeutectic Al–Si alloys of others works [17,18], the silicon was identified without the appearance of a eutectic structure in this work, but as isolated particles similar to primary silicon in hypereutectic alloys. The presence of these particulate silicon has been documented by other investigators working on spray forming of eutectic and hypereutectic aluminum–silicon alloys [19,20]. The formation of the microstructure in the spray forming is frequently correlated to the situation occurring in rheo-casting because both processes show strong agitation in semi-solid state [21]. However, the rheo-cast hypoeutectic Al–Si alloys always show eutectic silicon, while the spray formed material of this work did not. The reason for this could be the significant differences between the two processes, respectively, to the cooling rate and the situation of the materials before “agitation” in semisolid state. The rheo-casting has no step which suffers rapid solidification as the atomized droplets do, it says, the solidified droplets

impact the deposit with a very fine structure and play a very important role in the subsequent microstructural development. In addition, the reheating of the deposit due to the release of latent heat is another factor in existent in rheo-casting. Indeed, the solidification conditions by spray forming of long-range freezing alloys such as A380 are difficult to be explained by classical theories of solidification, even of rapid solidification.

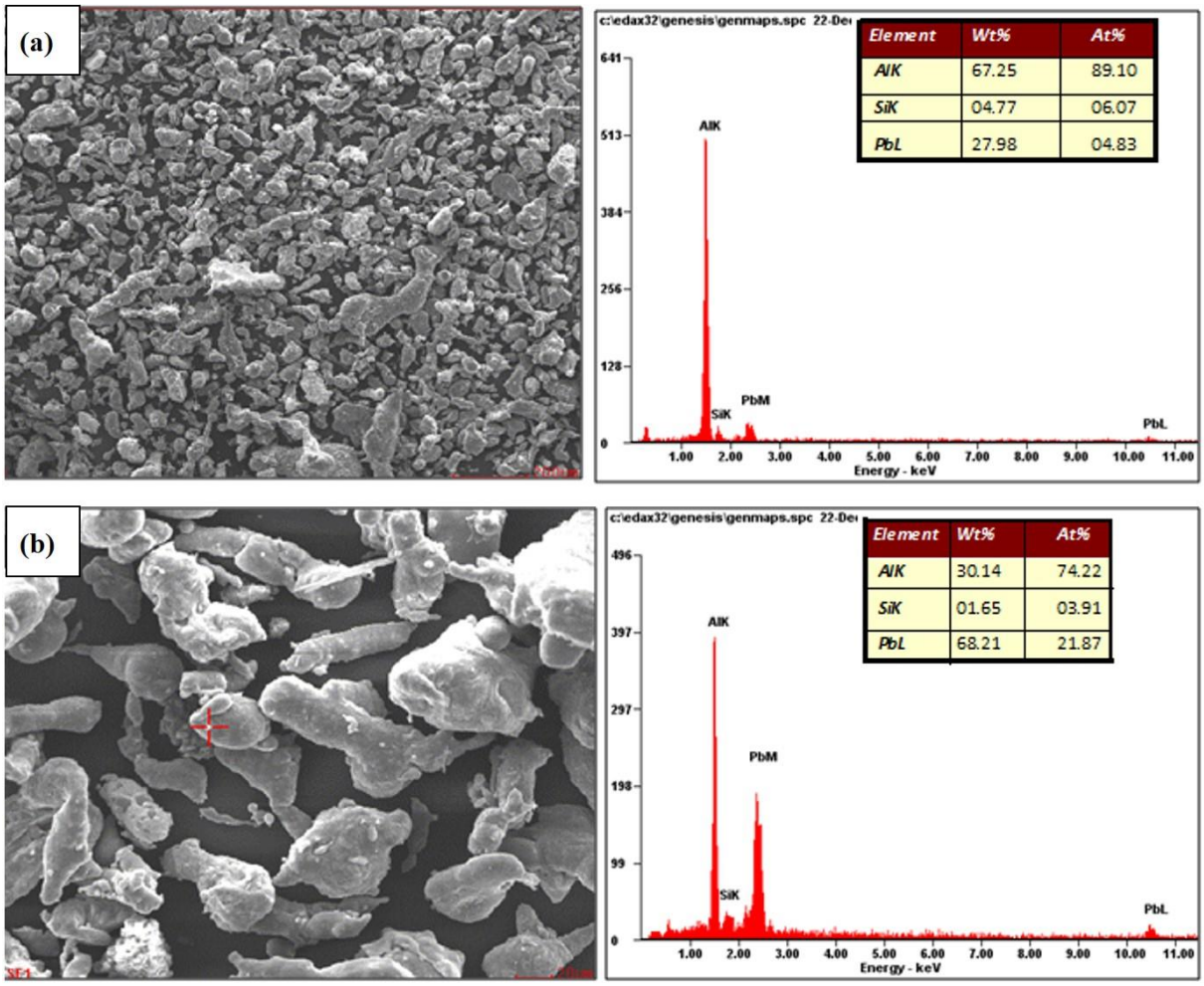

Fig. 4.SEM with EDS spectrum (a) analyzed whole region; (b) analyzed bright region, indicating Pb and Si phases in spray deposited Al-6Si-10Pb alloy

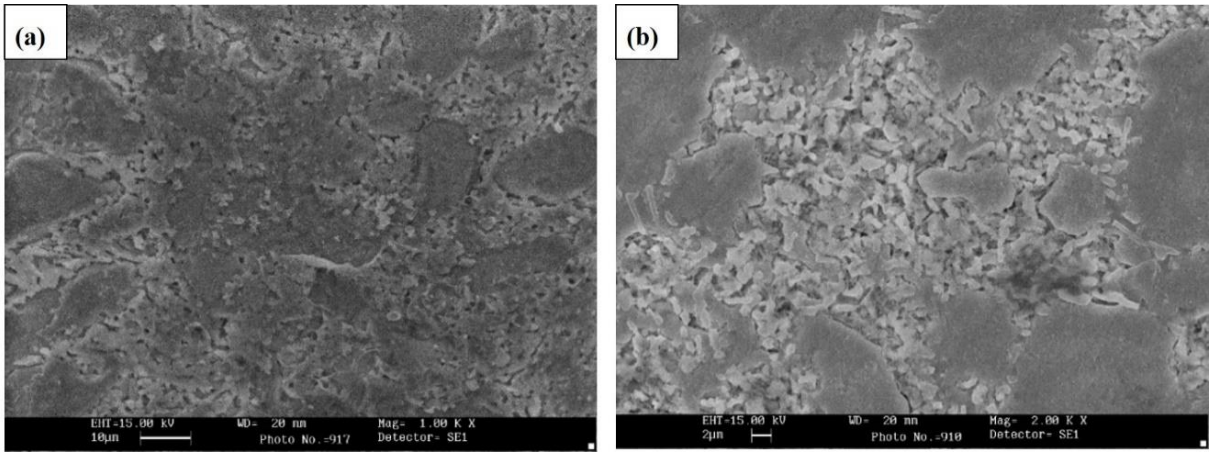

Fig. 5. SEM micrographs showing porosity at (a) 2000x; (b)1000x

SEM micrographs showing porosity are shown in Fig. 5. The porosity formation can take place due to gas entrapment, insufficient melt to fill the porosity and solidification shrinkage. The decrease in porosity from center to periphery could be explained on the basis of decrease in gas velocity from center to periphery of the deposit. Higher gas velocity would lead to higher particle velocity at center as compared to periphery. Semi-solid particle impacting the substrate or preform at higher sped would undergo greater deformation and thus lead to lesser pores as compared to periphery where the particles would undergo less deformation leading to existence of more pores.

Conclusions

1. Al-6Si-10Pb alloy with fine equiaxed grain structure of aluminum was casted using spray forming technique.
2. Uniformly spread needle shaped silicon particles surrounding the aluminum grains were observed in the microstructure ofAl-6Si-10Pb alloy.
3. The preforms at different location shows different grain size with larger grains at the center and smaller grains along the periphery. Further, high porosity was observed for the as casted preforms due to gas entrapment, and insufficient melt.
3. Rolling treatment reduces the porosity, but simultaneously generate cracks due to the applied stress. The developed stress can be reduced by using an additional annealing treatment to the Al-6Si-10Pb alloy.

References

1. Mauduit D, Dusserre G, Cutard T. Influence of temperature cycles on strength and microstructure of spray-deposited Si–Al CE9F alloy. *Mechanics of Materials*. 2019;131: 93–101.
2. Wang Y, Zhao G, Xu X, Chen X, Zhang C. Constitutive modeling, processing map establishment and microstructure analysis of spray deposited Al-Cu-Li alloy 2195. *Journal of Alloys and Compounds*. 2019;779: 735–751.
3. Goudar DM, Srivastava VC, Rudrakshi GB, Raju K, Ojha SN. Effect of Tin on the Wear Properties of Spray Formed Al–17Si Alloy. *Transactions of the Indian Institute of Metals*. 2015;68: 3–7.
4. Ramana Reddy BV, Mittal R, Maity SR, Pandey KM. Investigation on metallurgical, tribological, hardness properties of spray deposited and warm rolled Al-18Pb, Al-22Pb alloys. *Journal of Materials Research and Technology*. 2019;8: 5687–5697.
5. Milhorato FR, Mazzer EM. Effects of aging on a spray-formed Cu-Al-Ni-Mn-Nb high temperature shape memory alloy. *Materials Science and Engineering: A*. 2019;753: 232–237.
6. Ran G, Zhou J-E, Xi S, Li P. Microstructure and morphology of Al–Pb bearing alloy synthesized by mechanical alloying and hot extrusion. *Journal of Alloys and Compounds*. 2006;419: 66–70.
7. Srivastava VC, Surreddi KB, Scudino S, Schowalter M, Uhlenwinkel V, Schulz A, Rosenauer A, Zoch HW, Eckert J. Spray forming of bulk Al85Y8Ni5Co2 with co-existing amorphous, nano- and micro-crystalline structures. *Transactions of the Indian Institute of Metals*. 2009;62: 331–335.
8. Raju K, Harsha AP, Ojha SN. Microstructural Features, Wear, and Corrosion Behaviour of Spray Cast Al—Si Alloys. *Proceedings of the Institution of Mechanical Engineers, Part J: Journal of Engineering Tribology*. 2011;225: 151–160.
9. Sheinerman AG. Strengthening of nanocrystalline alloys by grain boundary segregations. *Materials Physics and Mechanics*. 2022;50(2): 193–199.
10. Mittal R, Singh D. Tribology Characteristics of Cold Rolled Spray Cast Al–6Si–20Pb Alloy. In: Patel HC, Deheri G, Patel HS. (eds.) *Proceedings of International Conference on Advances in Tribology and Engineering Systems 2014*. New Delhi, India: Springer; 2014. p.431–439.

11. Wang X, Pan Q, Liu L, Xiong S, Wang W, Lai J, Sun Y, Huang Z. Characterization of hot extrusion and heat treatment on mechanical properties in a spray formed ultra-high strength Al-Zn-Mg-Cu alloy. *Materials Characterization*. 2018;144: 131–140.
12. Mittal R, Moon AP. Effect of Rolling on the Electrochemical Corrosion Behavior of Spray Deposited Al-6Si Alloys with Different Pb Content. *Journal of Materials Engineering and Performance*. 2023;2: 7969–7979.
13. Tomar A, Mittal R, Singh D. Strength and elongation of spray formed Al-Si-Pb alloys. *International Journal of Minerals, Metallurgy, and Materials*. 2014;21: 1222–1227.
14. Singh D, Dangwal S. Effects of process parameters on surface morphology of metal powders produced by free fall gas atomization. *Journal of Materials Science*. 2006;41: 3853–3860.
15. Mittal R, Reddy BVR. Studying the Influence of Rolling Deformation Degree and Pb Content on the Hardness of Spray Deposited Al–6Si Alloy Using Linear Regression Analysis. *Powder Metallurgy and Metal Ceramics*. 2021;60: 164–173.
16. Underhill RP, Grant PS, Cantor B. Microstructure of spray-formed Al alloy 2618. *Materials & Design*. 1993;14: 45–47.
17. Gupta M, Ling S. Microstructure and mechanical properties of hypo/hyper-eutectic Al–Si alloys synthesized using a near-net shape forming technique. *Journal of Alloys and Compounds*. 1999;287: 284–294.
18. Srivastava AK, Anandani RC, Dhar A, Gupta AK. Effect of thermal conditions on microstructural features during spray forming. *Materials Science and Engineering: A*. 2001;304-306: 587–591.
19. Anand S, Srivatsan TS, Wu Y, Lavernia EJ. Processing, microstructure and fracture behaviour of a spray atomized and deposited aluminium–silicon alloy. *Journal of Materials Science*. 1997;32: 2835–2848.
20. Evstifeev AD, Chevrychkina AA, Petrov YV. Dynamic strength properties of an ultra-fine-grained aluminum alloy under tension conditions. *Materials Physics and Mechanics*. 2017;32(3): 258–261.
21. Fuxiao Y, Jianzhong C, Ranganathan S, Dwarakadasa ES. Fundamental differences between spray forming and other semisolid processes. *Materials Science and Engineering: A*. 2001;304-306: 621–626.

About Author

Rashmi Mittal Sc
PhD, Associate Professor (Maharishi Markandeshwar University, Mullana, India)

Ishan Choudhary Sc
PhD, Assistant Professor (Maharishi Markandeshwar University, Mullana, India)

Rajeev Sehrawat Sc
PhD, Assistant Professor (Maharishi Markandeshwar University, Mullana, India)

Rajat Dhawan Sc
PhD, Assistant Professor (Maharishi Markandeshwar University, Mullana, India)

Prabh Simranjit Singh Sc
Research Scholar (Maharishi Markandeshwar University, Mullana, India)

MATERIALS PHYSICS AND MECHANICS RESEACH ARTICLE

Submitted: May 30, 2023 Revised: October 9, 2023 Accepted: February 6, 2024

Effect of extrusion ratio on the grain refinement and properties of copper prepared by powder metallurgy route

A. Mehdi[1], M. Dixit [1], M. Agarwal [2]✉,

[1] B.N. College of Engineering and Technology, Lucknow, India

[2] Dr. RML Avadh University, Faizabad, India

✉ manish.dixit39@gmail.com

ABSTRACT

The present study emphasizes determining the optimum value of the extrusion ratio for superior microstructure and mechanical properties of copper via the synergistic effect of powder metallurgy and extrusion process. In this study, sintered Cu is hot extruded for different extrusion ratios, from 2.8 to 11.1. During extrusion treatment, copper experiences high compressive and shear stress, which enhances the nucleation rate and recrystallization. It also breaks the oxide precipitates into tiny pieces with uniform dispersion. Experimental evaluation of the extruded copper pallets analyzes the effect of extrusion ratio on compressive stress, density, micro-indentation hardness, and electrical conductivity for extruded copper components. These properties show a combined effect of grain refinement and compaction as a function and potential candidate for extrusion ratio. The impact of grain refinement as a function of extrusion ratio and compressive deformation is analyzed according to microstructural analysis and different phase identification.

KEYWORDS

copper • hot extrusion • powder metallurgy • microstructure • metallurgical properties

Acknowledgements. *The authors would like to acknowledge Sarda Metal Industries Jaipur for the powder materials used in the experiments. The authors also like to thank Mr. Abhilash Bajpai Center of Nano-sciences IIT Kanpur for their assistance during the work.*

Citation: MehdiA, DixitM, AgarwalM. Effect of extrusion ratio on the grain refinement and properties of copper prepared by powder metallurgy route. 2024;52(2): 19–29.
http://dx.doi.org/10.18149/MPM.5222024_3

Introduction

Copper is a highly sought-after standout material in electrical applications including current-conducting wires, heat sinks, automotive, electric appliances, electronic devices, and other power transmission devices [1]. The high electrical conductivity, thermal conductivity, and corrosion resistance of copper make it useful in power transmission and heating applications [2,3]. The copper synthesized by the powder metallurgy route exhibits large porosity content [4,5]. It may adversely affect the physical properties of copper.

Thus, secondary processing techniques such as hot extrusion and forging may overcome these limitations. These may considerably enhance mechanical properties. In hot extrusion, sintered metal is heated to 50-75 % of its melting temperature [4]. To avoid metal seizing, the extrusion die is heated near the metal temperature. Then, heated metal billets are extruded in a shaped extrusion die by applying an appropriate pressure. It makes the die of the conversing shape. The ratio of in to out the cross-section area of the extrusion die is known as the extrusion ratio. During the extrusion process, the material passes through a narrow opening; It suffers compressive and rheological shear loading. It axially

aligns the randomly oriented reinforced particulates and decreases the porosity content. It may facilitate densification, which significantly enhances the microstructure and mechanical properties [6]. According to the literature, extrusion ratios affect the microstructure and mechanical properties of AZ91D magnesium alloy undergoing the hot extrusion process [7,8]. It also depicts that grain refinement and interfacial adhesion have a great influence on the extrusion ratio.

Extrusion of materials through the die depends on the profile parameters and complexity of the die opening. The factor of complexity is also controlled by the applied resultant forces in the direction of flow during the process, which is variable and increases with the rise in temperature and gravitational force [1–15]. Nevertheless, complexity decreases with an increase in the profile perimeter of the die opening but also depends on the force/pressure of extrusion as well as on the ductile behavior of the material. For pure copper, the combined effect of experimental parameters such as profile of the die opening, rise in temperature, extrusion force, extrusion ratio, etc., might be the reason behind the excellent level of grain refinement and metallurgical properties [1–17].

The present work evaluated the effect of different extrusion ratios on the microstructure of sintered copper prepared by the hot extrusion process. The Cu specimens were prepared by two routes, i.e. (1) powder metallurgy route and (2) powder metallurgy route followed by hot extrusion for different extrusion ratios. Synthesized copper specimens were analyzed according to a function of extrusion ratio and metallurgical characteristics. In this work, a synergetic effect of the two-processing techniques (powder metallurgy and extrusion) has been used to improve the grain refinement and properties of pure copper specimens. This work is mostly suitable and recommended for the essential utilization of copper-based components, where the inclusion of ceramic and any type of reinforcement is not preferred.

Materials and Methods

The present study used an electrolytic copper powder, Loba Chemicals Pvt. of an average size of 40 μm and 99.9 % purity. The copper powder was preheated at 120 °C for 1.5 h to remove the moisture content from the powder and milled at 300 rpm for 1 h in a planetary ball mill.

The steps involved in the fabrication process are described in Fig. 1. Hardened steel balls were used with a ratio of 5:1 for the ball-to-powder weight ratio. In Fig. 2(a), copper powder particles are represented with some sharp edges followed by the ball milling process shown in Fig. 2(b). After milling, the copper powder was cold compacted at 700 MPa with a 3-min dwell time in a custom-made two-piece compaction die shown in Fig. 2(c), with the use of zinc stearate as the die lubricant. The green compact was sintered at 900 °C for 1.5 h in a three-stage diffusion furnace (Fig. 2(c)).

To reduce the porosity content of copper, hot extrusion was used as a secondary process after sintering (Fig. 2(d)). For the hot extrusion process, sintered billets of size 20 mm in diameter and 30 mm in height were heated up to 750 °C for 20 mins. Complex die for the extrusion consists of several parts or the load sustaining and hold for the constant die cavity space. The most important part of the extruded die part shown in Fig. 2(d) for which the dimensions of the extruded bar are 20 mm in diameter at the inlet while 7.14, 3.17, and 1.8 mm at the outlet. With this different extruded ratio, bars were

obtained. The sintered copper pallets were extruded in a preheated extrusion die, which was maintained at 700 °C. The extrusion of the copper was done for three extrusion ratios of 2.8:1, 6.3:1, and 11.1:1 with a punch speed of 1 mm/s. The purpose of using different extrusion ratios was to analyze its effect on microstructure. Graphite was duly applied to the punch and die before each experiment to carry out the extrusion process in the dedicated extrusion die. FESEM (Field Emission Scanning Electron Microscopy), EDX (Energy Dispersive X-ray), and XRD (X-ray Diffraction) analyses were conducted to identify the surface morphology, phase formation, and physical properties of the extruded specimens.

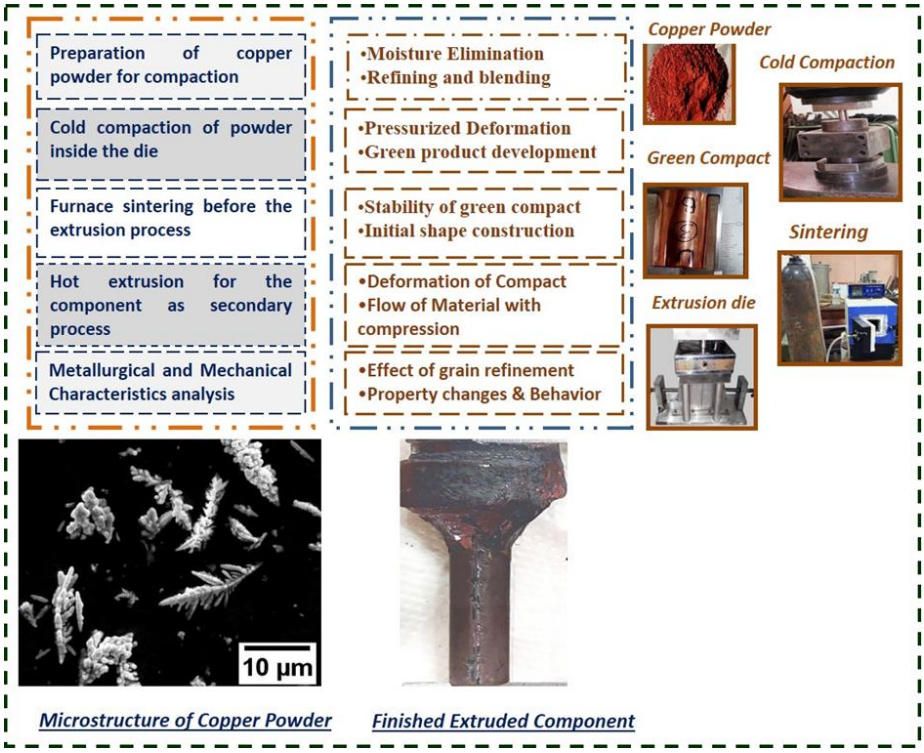

Fig. 1. Synthesis steps of Extruded copper component

The ball milling was performed at room temperature with volume size ((π/4) 862 × 80 mm^3, RETSCH PM-100). Compressive stress evaluation was performed by the prepared sample of extruded specimens according to the ASTM E9-19 standard. For this purpose, the diameter to length ratio was maintained at 0.8. The compression test was done with the help of a UTM (Universal Testing Machine) until the first crack was developed along the lateral dimension of the specimen. It was considered the rate of the load increases constant with a value of 0.25 MPa/s. It was observed that for a limited value of load between 250 and 280 KN first fracture on the lateral surface appeared and obtained data has been reported for this work. To examine the performance of the prepared composite, well-polished samples (roughness below 0.05 µm) were used with the help of EDX attached FESEM (ZEISS, SUPRA 40 P). XRD analysis was conducted by using (PAN AlyticalXpert, K-Alpha1 wavelength: 1.540598 nm radian intensity up to 26000 a.u.) scanning range of 10-90° with a step size 0.02°/sec.

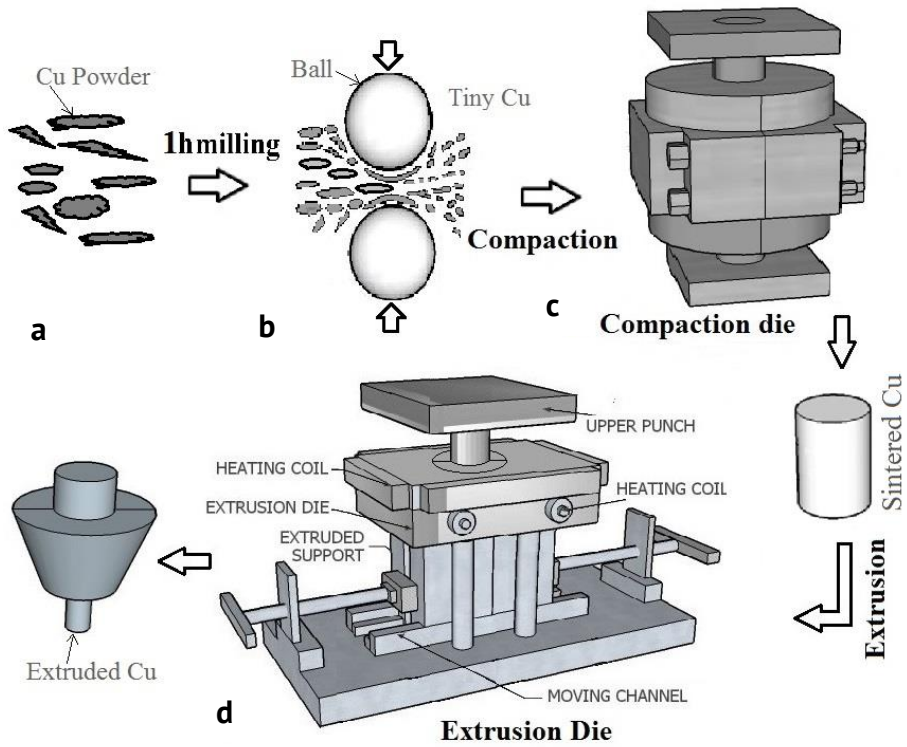

Fig. 2. Processing sequence for the synthesis of copper extruded specimen (a) Cu powder particles; (b) Ball milling process; (c) Powder compaction inside the die and sintering process; (d) representation of extrusion die process

Vicker's microindentation hardness tester (VI diamond indenter, CSM Instruments, Singapore) was used for the measurement of microhardness of the extruded pallets on different locations by a maximum load of 2000 mN with a pause time of 10-20 seconds. To the accuracy of the results, a minimum of 5 tests for each phase were conducted for different locations, and an average of the obtained values was reported. Moreover, for each indentation, a minimum indentation distance of 2.5*d* (*d* is indentation diameter) was maintained in each phase and experiment. For FESEM analysis, the specimens were prepared by grinding the samples with 2000-grade silicon grit paper followed by polishing with fine alumina powder. Finally, the specimens were etched with a solution of 5g FeCl3 in 15 ml HCl and 90 C2H6OH to observe the grain morphology.

Results and Discussion

The density of all copper specimens is determined by the Archimedes method. Table 1 shows the value of actual density, sintered density, and relative density of copper for different extrusion ratios. Figure 3(a) shows the density of Cu and extruded Cu with different extrusion ratios. The general trend shows that the sintered density increases with increasing extrusion ratio. The narrow opening of the extrusion die may increase compressive and shear stress, which significantly increases the particle-to-particle contact and results in the close packing of the Cu particles. It may increase the density of Cu by increasing the extrusion ratio. The theoretical density of the copper is 8.96 g/cm^3 [3]. The relative density of the Cu increases with increasing the extrusion ratio and achieves its

maximum value (8.66 g/cm^3) of 96.65 % at an 11.1 extrusion ratio, which is 4.9 % higher than that without the extrusion process. The micrograph shown in Fig. 4 (microstructural evaluation) also depicts that the high extrusion ratio considerably reduces the pores and voids, which increase the sintered density [3]. With increasing the extrusion ratio, dynamic recrystallization of the Cu particles increases at elevated temperatures, which results in the reduction of the oxide formation and enhances the sintered density [16].

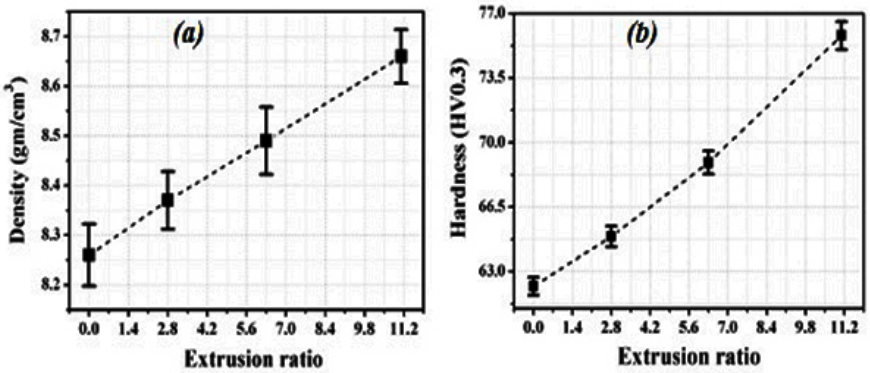

Fig. 3. (a) Variation of density with extrusion ratio, and (b) variation of hardness with extrusion ratio

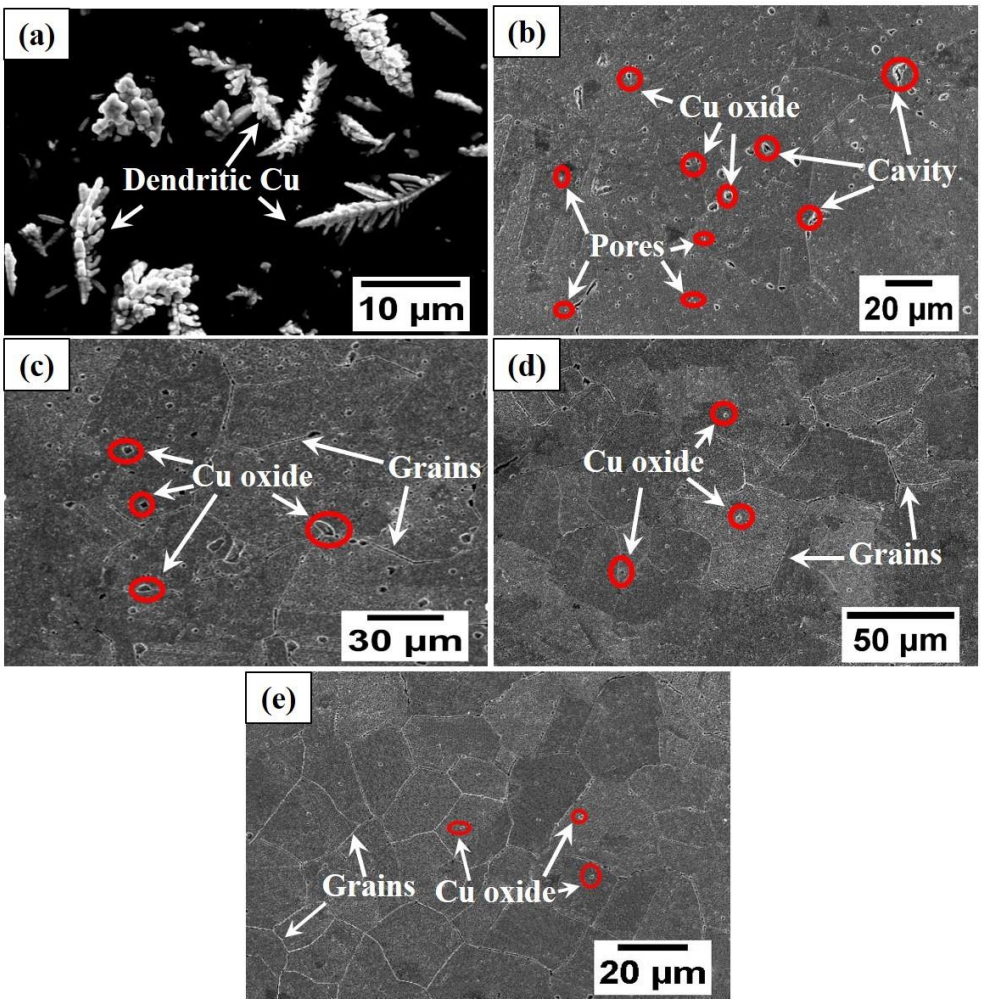

Fig. 4. FESEM images of (a) as received dendritic copper powder, (b) Cu without extrusion, (c) Cu extruded with a 2.8:1 extrusion ratio, (d) Cu with a 6.3:1 extrusion ratio, (e) Cu with an 11.1:1 extrusion ratio

Figure 3(b) shows the value of the microhardness of the Cu for different extrusion ratios. It illustrates that the value of hardness increases with increasing extrusion ratios. The hardness depends on the porosity content, interface bonding, and plastic deformation of the material at the point of indentation [15]. The micrograph (Fig. 4) shows that the porosity of the copper decreases with an increase in the extrusion ratio, with a reduction in the amount of pores.

Table 1. Relation of actual density, theoretical density, and relative density with respect to extrusion ratio

S. No.	Extruded Alloy	Actual density, g/cm^3	Theoretical density, g/cm^3	Relative density, %
1	Cu	8.26	8.96	92.12
2	Cu (2.8 ext. ratio)	8.37	8.96	93.41
3	Cu (6.3 ext. ratio)	8.49	8.96	94.75
4	Cu (11.1 ext. ratio)	8.66	8.96	96.65

It may be attributed to the strong bonding and close particle packing of Cu at a higher extrusion ratio [18–23]. With an increasing extrusion ratio, the oxide precipitate is broken into small pieces and homogeneously dispersed. A higher nucleation rate leads to dynamic recrystallization, which further leads to grain refinement [20,24–26]. In hardness tests, fine grain structure and uniform dispersion of oxide content create an obstacle in displacing the copper during the indentation of the diamond ball. This strengthening mechanism increases the hardness of the extruded copper. The hardness value of sintered copper is 62.2 HV. The value increases with the extrusion ratio and achieves its maximum value of 75.8 HV for an 11.1 extrusion ratio. Thus, the study reported a 21.9 % increase in the microhardness of Cu with an extrusion ratio of 11.1 than of without extrusion. Authors [4,12] have reported a similar result of microhardness. It was found that the value of microhardness increases from 66.2 to 77.2 VHN with an increasing extrusion ratio from 4:1 to 15:1. Generally, hardness value is a dependent parameter on the types of material such as abrasive and matrix-based material. As, in this experimental work, no abrasive has been used but due to compaction and dual sintering process, synthesized copper alloy has been denser. This results in the reduction in porosity as discussed, which also affects the micro-indentation hardness. This is a simple phenomenon for the different phases generated due to sintering and reduction of porosity [7,16].

Figure 5(a) shows the micrograph of extruded Cu for a 2.8:1 extrusion ratio. Several numbers of pores with interfaces of Cu and Cu-oxide phases are identified in Fig. 5(a). These interfaces are variable according to the size and dominated by the copper due to which variable density and porosity have been obtained as discussed earlier. For this, Fig. 5(b) shows the EDX spectra of extruded Cu with the elemental analysis. The elemental analysis of EDX spectra shows oxygen content, which may confirm the formation of copper oxide. It may be attributed to the involvement of atmospheric oxygen during the sintering and hot extrusion process [15,16]. The corresponding micrograph for the hardness test at the copper extruded surface is represented in Figs. 5(c,d) related to copper and its interfaces. These micrographs are directly affected by the elemental involvement and interfaces as observed in the EDX spectrum. Both the phases shown in Fig. 5(a,b) are different from each other according to indentation. Indentation for pure copper (Fig. 5(a)) is more uniform than the indentation in the oxide phase of copper (Fig. 5(b)).

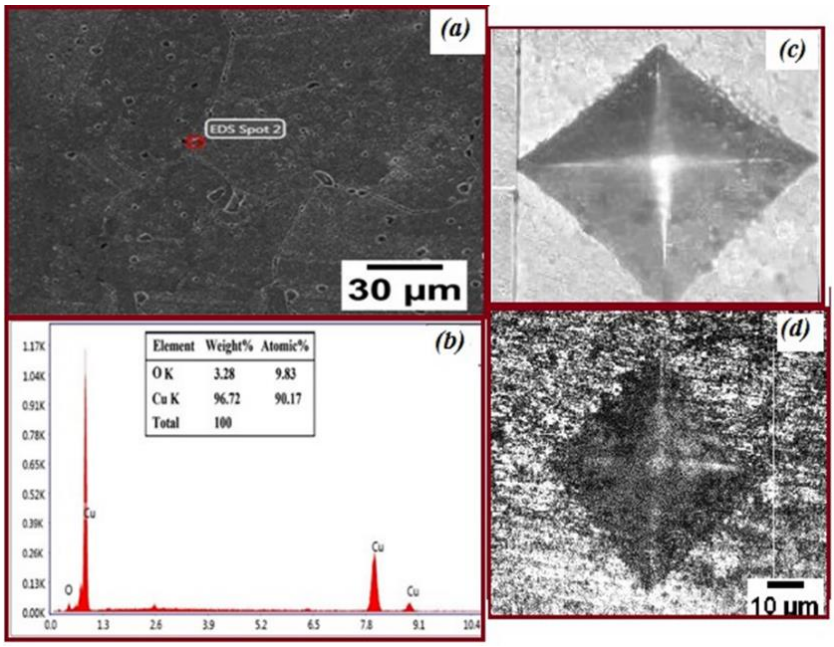

Fig. 5. (a) Micrograph of Cu extruded with the extrusion ratio of 2.8:1; (b) EDX spectrum with the elemental analysis; (c) microindentation on pure copper phase; (d) microindentation on the interface of Cu-oxide phase

The general trend in Fig. 6 depicts that electrical conductivity increases with increasing the extrusion ratio. It shows the highest value of electrical conductivity (94.9 % IACS) for the extrusion ratio of 11.1 which is 8.11 % greater than that of the Cu without extrusion. The increase in the electrical conductivity may be attributed to the reduction in porosity content with increasing the extrusion ratio. The synergetic effect of pores elimination and strong interface adhesion may remarkably enhance the electrical conductivity by increasing the extrusion ratio.

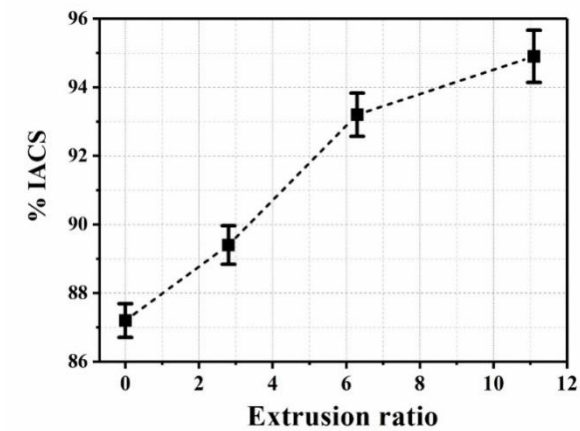

Fig. 6. Variation of electrical conductivity (% IACS) with extrusion ratio (%)

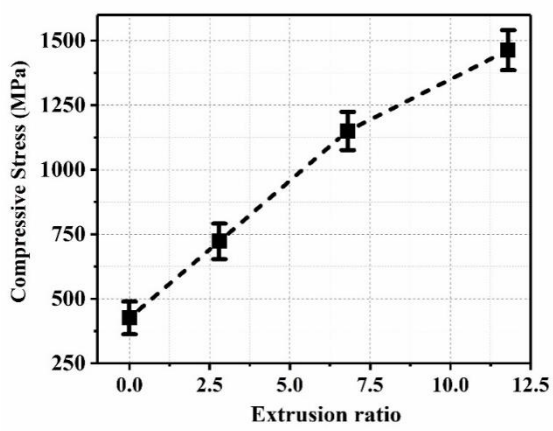

Fig. 7. Variation of compressive strength (MPa) with extrusion ratio (%)

The electrical conductivity of any material depends on several factors, including: (1) number of free electrons present; (2) porosity and cavity content; (3) interfacial adhesion of the material.

It may refer to the ease in the movement of free electrons, as the presence of pores and cavities may act as an obstacle in the motion of free electrons. It may also be attributed to strong interface adhesion with increasing the extrusion ratio, which may refer to the high plastic deformation of the Cu under high compression and shear stress at elevated temperatures [7,16]. However, the 1.79 % increase in electrical conductivity (93.2 to 94.9 % IACS) with increasing the extrusion ratio from 6.3 to 11.1 depicts less increment in the electrical at high extrusion ratio. It refers to the excellent interface adhesion and low porosity content at a 6.3 extrusion ratio, therefore less improvement is depicted in interface adhesion, and porosity content may be depicted with increasing further extrusion ratio.

The size and shape of the particles in the specimens have an impact on the compression behavior, which varies. Energy is stored in the extruded copper pallets before any first cracking and is distributed among the contact particles with the compaction surface [13,15,16,27]. As represented in Fig. 7, it seems that compressive stress values for the copper extruded billets increase with the increase in extrusion ratio. A maximum value for the compressive stress before fracture is obtained about 1442 MPa (for 11.1 extrusion ratio) which is approx. 277 % higher than the non-compressed extrusion pallets. Moreover, for the extrusion ratio of 2.8 and 6.3, the value of compressive stress reached 742 and 1156 MPa, respectively. These obtained results show the combined effect of extrusion ratio and initial companion with grain refinement for copper pallets. When a compressive force is applied, internal fracture (dislocation) initiation for copper billets is always started within grains, moving toward the grain boundary. As Copper has a high work hardening exponent and these dislocations pile up and immediately form a dislocation forest (Frank–Read source). These dislocation forests may accumulate at the grain boundaries. As interaction of the two dislocations are repulsive in nature. Therefore, more compressive stress is required to propagate the dislocation from the grain boundaries, as the dislocation forest present at the grain boundary may create obstacles in the movement of dislocation. A high extrusion ratio increases the number of grains present in the same region, which leads to more compressive stress to propagate the dislocation from these grain boundaries [16]. In the compression test, dislocations (cracks) are initiated within the material and progressively moved towards the outer direction. At an optimum value of compressive stress, these dislocations (cracks) may come out from the material surface and cause the first fracture on the specimen's outer lateral surface. Therefore, grain refinement may increase the compressive strength of the extruded copper by increasing the extrusion ratio.

Figure 4 shows the micrographs of the sintered Cu and the sintered Cu extruded for different extrusion ratios. The metallographic images are taken perpendicular to the extrusion direction. With an increasing extrusion ratio, the micrograph in Fig. 4 shows the recrystallization of Cu with a more refined and homogeneous grain structure and size. Figure 4(a) depicts the dendritic shape of received the copper. It shows an extended facet of dendritic copper. Figure 4(b) illustrates the micrograph of copper sintered at 900 °C. It shows non-uniform grains of large size along with the formation of copper oxide (CuO). The micrograph shows some tiny pores [16,27,28].

Figure 4(c) shows the micrograph of extruded Cu with the 2.8:1 extrusion ratio. It shows the partial recrystallization with a non-uniform grain structure. It confirms that grains are suppressed however, the formation of copper oxide is observed. These oxides are marked in the micrographs (Fig. 4), mostly white phases, and settled on the spaces available between

grains and pores. The reduction in grain size may refer to densification during extrusion [27]. The micrograph in Fig. 4(d) shows the extruded Cu with the 6.3:1 extrusion ratio. It shows the recrystallization along with the non-uniform grain structure. Figure 4(d) shows that the grains are considerably suppressed along with partial grain refinement. During the extrusion process, the Cu particles pass through the confined narrow opening, which leads to achieving close particle packing [15]. It may reduce the porosity and grain size. Here, in different magnifications of the micrographs, pores size is also variable with the grain size. It can be observed from these images that the number of available pores is also variable and reduces with the increase of the extrusion ratio. The micrograph also confirms the reduction in the size of copper oxide. It may be attributed to the compressive and shear stress developed during hot extrusion, which breaks the copper oxide into small pieces [10]. Figure 7(e) shows the micrograph of extruded Cu with the 11.1:1 extrusion ratio. A high extrusion ratio may rearrange particles that may cause high plastic deformation [16].

The severe plastic deformation at elevated temperatures may store the internal energy and the system becomes thermodynamically unstable [28–30]. The micrograph in Fig. 4(d,e) shows that the porosity and cavity content decreases with increasing the extrusion ratio, concerning Fig. 4(b,c). It may lead to dynamic recrystallization and refine grain structure [1,31,32]. It may lead to a considerable reduction in grain size. Figure 4(e) shows the tiny copper oxide along with fine grain boundaries. It may refer to the development of high compressive and shear stress at a high extrusion ratio. It may break the large-size CuO into small pieces [10]. The high extrusion ratio enhances the high plastic deformation, which increases the nucleation rate [11,15,32,33]. It may be attributed to the fine grain structure at 11.1 extrusion ratio. It may eliminate porosity and enhance densification behavior.

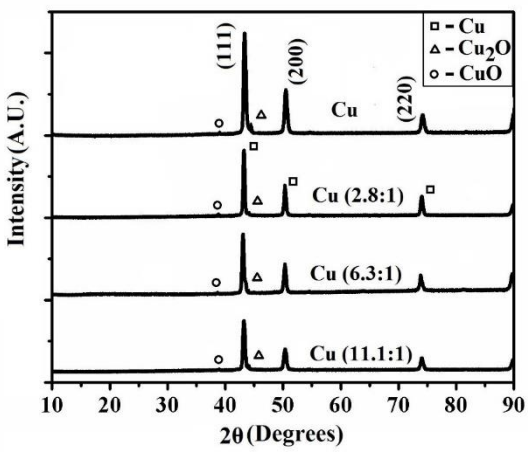

Fig. 8. XRD pattern for sintered Cu and Cu extruded with different (2.8:1, 6.3:1, and 11.1:1) extrusion ratios

Figure 8 shows the XRD pattern of Cu and extruded Cu with different extrusion ratios. XRD spectra show the intensity peaks of Cu. The interlayer lattice spacings of the Cu specimens for different extrusion ratios were determined by Bragg's law ($d = n\lambda/2\sin\vartheta$), where n=1, wavelength λ=1.5406 Å for Cu Ka, and ϑ is the Bragg angle. Figure 5 depicts the high-intensity diffraction peaks of Cu at the 2ϑ angle of 43.20 ± 0.04, 50.26 ± 0.06, and 73.98 ± 0.6° which corresponds to the lattice spacing 2.094, 1.814, and 1.28 Å, respectively. This lattice spacing refer to the (111), (200), and (220) planes of the fcc Cu.

It also confirms the low-intensity peaks of CuO and Cu_2O. It may be because of the involvement of atmospheric air during sintering and the hot extrusion process. Not only that, but it reacts with the amount of oxygen present in the air with the copper at elevated temperatures and forms copper oxide [16]. The XRD pattern shows that the intensity of oxide peaks decreases with increasing the extrusion ratio. It may be attributed to grain refinement and breaking of copper oxide under high compressive and shear stress [9].

Conclusions

The sintered copper specimens were successfully extruded for 2.8, 6.3, and 11.1 extrusion ratios by hot extrusion route. Microstructure and phase formation of Cu specimens are characterized by FESEM, EDX, and XRD techniques.

The micrograph of the sintered copper shows the large grain size. It also shows oxide participation and porosity content. For a high extrusion ratio of 11.1:1, the micrograph confirms the refined and uniform grain structure with reduced oxide precipitate.

It might be attributed to high nucleation rate and dynamic recrystallization because of high compressive and shear stress at elevated temperatures. Thus, the test results recommend that the 11:1 extrusion ratio is suitable for achieving superior grain structure and mechanical properties.

The strengthening of Cu is the coordination of dynamic recrystallization, grain refinement, and homogeneous dispersion of oxide precipitates.

Obtained results for the density, compressive strength, microhardness, and electrical conductivity confirm an appreciable increase due to the effect of compression and as a function of extrusion ratio.

References

1. Liang C, Ma M, Zhang D. Microstructures and Tensile Mechanical Properties of Consolidated Copper. *Materials Research*. 2015;18: 158–163.
2. Tuncer N, Bose A. Solid-State Metal Additive Manufacturing: A Review. *JOM*. 2020;72(9): 3090–3111.
3. Yang Y, Tang S, Wang Y, Yang L, Fan Z. Process optimization of porous Al2O3 filter via layered extrusion forming. *Materials and Manufacturing Processes*. 2022;37(14): 1630–1641.
4. Romero C, Yang F, Raynova S, Bolzoni L. Thermomechanically processed powder metallurgy Ti-5Fe alloy: Effect of microstructure, texture, Fe partitioning and residual porosity on tensile and fatigue behaviour. *Materialia*. 2021;20: 101254.
5. Ramesh C, Hirianiah A, Harishanad KS, Noronha NP. A review on hot extrusion of Metal Matrix Composites (MMC's). *Research Inventory: International Journal of Engineering Science*. 2012;1(10): 30–35.
6. Gonzalez-Gutierrez J, Cano S, Ecker JV, Kitzmantel M, Arbeiter F, Kukla C, Holzer C. Bending Properties of Lightweight Copper Specimens with Different Infill Patterns Produced by Material Extrusion Additive Manufacturing, Solvent Debinding and Sintering. *Applied Sciences*. 2021;11(16): 7262.
7. Xin L, Yang W, Zhao Q, Dong R, Liang X, Xiu Z, Hussain M, Wu G. Effect of extrusion treatment on the microstructure and mechanical behavior of SiC nanowires reinforced Al matrix composites. *Materials Science and Engineering A*. 2017;682: 38–44.
8. Kumar P, Panda SS. A review on properties and microstructure of micro-extruded product using SPD and as-cast material. *Sādhanā*. 2018;43(5): 77.
9. Torralba JM, Alvaredo P, García-Junceda A. High-entropy alloys fabricated via powder metallurgy. A critical review. *Powder Metallurgy*. 2019;62(2): 84–114.
10. Hu M, Ji Z, Chen X. Effect of extrusion ratio on microstructure and mechanical properties of AZ91D magnesium alloy recycled from scraps by hot extrusion. *Transactions of Nonferrous Metals Society of China*. 2010;20(6): 987–991.
11. Ebrahimi R, Rahimzadeh Lotfabad F. Simple shear extrusion as an efficient severe plastic deformation technique: a review. *Materials Science and Technology*. 2022;39(3): 259–282.
12. Ramesh CS, Keshavamurthy R, Naveen G.J. Effect of extrusion ratio on wear behaviour of hot extruded

Al6061–SiCp (Ni–P coated) composites. *Wear*. 2011;271(9-10): 1868–1877.
13. Wilson MF, Donaldson IW, Bishop DP. Sinter-swage processing of an Al-Si-Mg-Cu powder metallurgy alloy. *Canadian Metallurgical Quarterly*. 2022;61(1): 94–107.
14. Zhang T, Ji Z, Wu S. Effect of extrusion ratio on mechanical and corrosion properties of AZ31B alloys prepared by a solid recycling process. *Materials in Engineering*. 2011;32(5): 2742–2748.
15. Qamar SZ. Shape Complexity, Metal Flow, and Dead Metal Zone in Cold Extrusion. Materials and Manufacturing Processes. 2010;25(12): 1454–1461.
16. Dixit M, Srivastava R. The effect of copper granules on interfacial bonding and properties of the copper-graphite composite prepared by flake powder metallurgy. *Advanced Powder Technology*. 2019;30(12): 3067–3078.
17. Pilz F, Merklein M. Influence of component design on extrusion processes in sheet-bulk metal forming. *International Journal of Material Forming*. 2019;13: 981–992.
18. Ji X, Zhang H, Luo S, Jiang F, Fu D. Microstructures and properties of Al–Mg–SI alloy overhead conductor by horizontal continuous casting and continuous extrusion forming process. *Materials Science and Engineering: A*. 2016;649: 128–134.
19. Basinski ZS, Dugdale JS, Howie A. The electrical resistivity of dislocations. *Philosophical Magazine*. 1963;8(96): 1989–1997.
20. Dixit M, Srivastava R. Effect of compaction pressure on microstructure, density and hardness of Copper prepared by Powder Metallurgy route. *IOP Conference Series: Materials Science and Engineering*. 2018;377: 012209.
21. Wu Y, Li Y, Lu J, Tan S, Jiang F, Sun J. Correlations between microstructures and properties of Cu-Ni-Si-Cr alloy. *Materials Science and Engineering: A*. 2018;731: 403–412.
22. Liu Y, Cai S, Xu F, Wang Y, Dai L. Enhancing strength without compromising ductility in copper by combining extrusion machining and heat treatment. *Journal of Materials Processing Technology*. 2019;267: 52–60.
23. Wang J, Feng Z. Manufacturing of surface features from extrusion forging and extrusion rolling of sheet metals. *Manufacturing Letters*. 2018;15: 42–45.
24. Geißdörfer S, Rosochowski A, Olejnik L, Engel U, Richert M. Micro-extrusion of ultrafine grained copper. *International Journal of Material Forming*. 2008;1: 455–458.
25. Wu Y, Huang S, Chen Q, Feng B, Shu D, Huang Z. Microstructure and Mechanical Properties of Copper Billets Fabricated by the Repetitive Extrusion and Free Forging Process. *Journal of Materials Engineering and Performance*. 2019;28(4): 2063–2070.
26. Wang M, Averback RS, Bellon P, Dillon S. Chemical mixing and self-organization of Nb precipitates in Cu during severe plastic deformation. *Acta Materialia*. 2014;62: 276–285.
27. Selmi O, Hamza Bouzid, Saidi H, Abdelaziz Bouazizi. The effect of copper doping on the optical and electrical properties of nickel oxide thin films deposited by spin coating technique. *Emergent Materials*. 2021;5(4): 1033–1038.
28. Agarwal M, Srivastava R. Effect of thick slurry and stepped deformation on mechanical properties of AA6061 alloy. *Emerging Materials Research*. 2019;8(3):394–403.
29. Agarwal M, Dixit NK, Dixit M, Srivastava R. Interfacial study for the effect of Al2O3 addition on the microstructure and micro-hardness of the Al2O3/AA6061 semi-solid cast composite. *Phase Transitions*. 2021;94(12): 899–909.
30. Meignanamoorthy M, Ravichandran M. Synthesis, properties and microstructure of sintered and hot extruded boron carbide reinforced AA8079 (Al-Cu-Fe-Si-Zn) matrix composites. *Materials Research Express*. 2018;5(11): 116508.
31. Musabirov II, Safarov IM, Galeyev RM, Afonichev DD, Koledov VV, Rudskoy A, Mulyukov RR,Plastic deformation of the Ni-Mn-Ga alloy by multiple isothernal forging. *Materials Physics and Mechanics*. 2017;57(1): 124–136.
32. Chen J, Yang CL, Yan W, Xia F, Fan X. Effect of Transverse Grain Boundary on Microstructure, Texture and Mechanical Properties of Drawn Copper Wires. *Journal of Materials Science and Technology*. 2014;30(2): 184–191.
33. Andreev AP, Andreeva SI, Shibakov VG, Pankratov DL, The heterogeneity of the stress-strain state during severe plastic deformation by multiple extrusion. *Materials Physics and Mechanics*. 2015;22(2): 170-175.

About Authors

Abbas Mehdi
M. Tech Scholar (B.N. College of Engineering and Technology, Lucknow, India)

Manish Dixit Sc
PhD, Associate Professor (B.N. College of Engineering and Technology, Lucknow, India)

Mayank Agarwal Sc
PhD, Associate Professor (Dr. RML Avadh University, Faizabad, India)

MATERIALS PHYSICS AND MECHANICS RESEACH ARTICLE

Submitted: March 4, 2024 **Revised: March 19, 2024** **Accepted: April 8, 2024**

Martensite stabilization effect after high strain rate loading

E.S. Ostropiko [1] ✉, **A.Yu. Konstantinov** [2],

[1] St. Petersburg State University, St. Petersburg, Russia

[2] Lobachevsky State University of Nizhny Novgorod, Nizhny Novgorod, Russia

✉ es-ostropiko@mail.ru

ABSTRACT

The behavior of shape memory alloys depends on the deformation technique and strain rate. This paper aims to demonstrate the martensite stabilization effect in equiatomic NiTi shape memory alloy after high strain rate loading. The high strain rate deformation at different rates and temperatures was performed using the Kolsky method modified for tension. Quasistatic deformation tests were conducted on a universal testing machine at identical temperatures up to the same residual strains. After tests, the samples were heated through reverse martensitic transformation temperature range in a thermomechanical analyzer with a temperature measurement accuracy of 0.3 °C. It is shown that the martensite stabilization effect depends on the loading rate in martensitic, premartensitic, and mixed phase states. An increase in the loading rate in the martensitic state results in a greater stabilization effect. High strain rate loading in the premartensitic and mixed-phase states does not lead to martensite stabilization, unlike in the quasi-static case. The results are consistent with the those of other authors and can be explained by hypotheses referenced in the paper.

KEYWORDS

shape memory alloys • nickel titanium • martensite stabilization effect • high-strain rate loading

Acknowledgements. *Research was performed using the Centre for Thermogravimetric and Calorimetric Research of the Research Park of St Petersburg State University. The work was supported by Russian Science Foundation (project no. 22-79-00068).*

Citation: Ostropiko ES, Konstantinov AYu. Martensite stabilization effect after high strain rate loading. *Materials Physics and Mechanics*. 2024;52(2): 30–36.
http://dx.doi.org/10.18149/MPM.5222024_4

Introduction

Shape memory alloys (SMAs) are the special type of smart materials [1]. They have been used in various fields, including engineering [2–5], medicine [6–8], and aerospace technology [9–12]. The NiTi (Nickel Titanium) alloy is the most well-known and studied SMA due to its superior properties, including high strength, biocompatibility, corrosion resistance, and most importantly, the superior shape memory effect (SME). SME is the ability of a deformed alloy to return to its "remembered" pre-deformed shape when heated. The mechanism of the SME is due to the thermoelastic reversible martensitic phase transformation that can be activated by temperature change and loading/unloading [13].

The mechanical and functional behavior of the material depends on the deformation technique and on the strain rate. Researchers have long been interested in the influence of strain rate on the SMAs, and research has focused on their mechanical properties, structures and functional behavior [14–21]. The reason for the high interest in the behavior under the high strain rate loading is clear. For example, SMAs have a high damping capacity due to stress-induced martensite phase transformation or martensite

reorientation, which makes them ideal for use in damping devices [22]. However, the phase transformation is not perfectly thermoelastic and is sensitive to the strain rate. Moreover, the thermoelastic martensitic transformation itself has a unique property known as the martensite stabilization effect (MSE). After deformation, the reverse martensitic transformation start temperature (A_s) increases, according to the Clausius-Claiperon equation. This effect has been widely studied for various compositions [23], and prestrain methods [24]. The microstructural approach was used to model the martensite stabilization effect [25]. However, no clear explanation for this phenomenon has appeared, although there are several hypotheses. For instance, in [26], the authors proposed the following hypothesis to explain the effect. They proposed a new mechanism for the MSE, suggesting that damage to the martensite boundaries during pre-strain decreases their mobility. As a result, a greater thermodynamic force (overheating) is required to move the interfaces during the reverse martensitic transformation.

Although the stabilization effect has been extensively studied, there are no works demonstrating this phenomenon after high strain rate loading. This work shows the peculiarities of the martensite stabilization effect after deformation at various rates and temperatures. It was discovered that the realization of this effect, as well as functional and mechanical behavior, is also dependent on the loading rate. The presented results are consistent with the hypothesis mentioned above.

Methods

Equiatomic NiTi, the most popular shape memory alloy, was selected for the investigation. Samples with a working part's height and diameter of 8 mm were manufactured using a CNC machine. Residual stresses were removed by subsequent aging at 500 °C for 1 hour, followed by cooling in a furnace. After heat treatment, the material demonstrated a single-step B2-B19' transformation with characteristic temperatures of M_s = 78 °C, M_f = 55 °C, A_s = 89 °C and A_f°= 110 °C. The results of different scanning calorimetry are shown in Fig. 1.

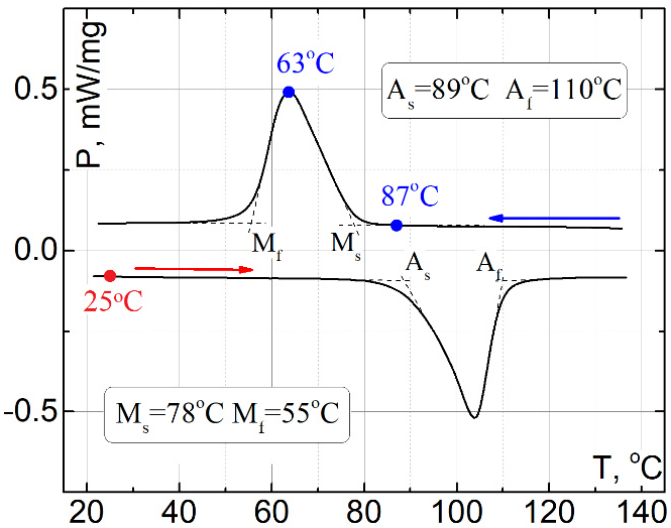

Fig. 1. Calorimetric curve of the material (●, ● - test temperatures)

The following test temperatures were chosen: 25, 87, 63 °C (marked with dots in Fig. 1). The temperatures of 87 and 63 °C were achieved by cooling from the high-temperature austenitic state, from 140 °C. At 87 °C the material was in the "pre-martensitic" state, close to the martensite start temperature M_s. At 63 °C, which corresponds to the peak in the calorimetric curve, the material was in the mixed-phase state. At room temperature (25 °C) the material was in a pure martensitic state.

High strain rate loading was performed using a Kolsky method for a split Hopkinson pressure bar [27] modified for tension mode [28,29]. Figure 2 illustrates the experimental setup. To conduct tests at elevated temperatures, a small tubular oven was placed at the edges of the bars with the specimen in between, and temperature control was provided by a thermocouple. Test parameters (stress, strain in the specimen, load, strain rate, loading time) were automatically calculated using the Kolsky formulae based on data obtained from low-base foil strain gauges placed on the surfaces of the bars. Further details can be found in [29].

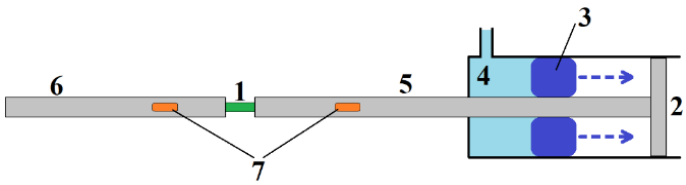

Fig. 2. Scheme of Kolsky method modified for tension: 1 – specimen; 2 – anvil; 3 – striker; 4 – compressed air; 5,6 – measuring bars; 7 – strain gauge

Residual strains were measured after the deformation and cooling to room temperature. Due to the peculiarities and limitations of the loading method, achieving higher strain rates resulted in higher residual strains in the specimens. Residual strains were approximately 5, 10 and 15 % after deformation at strain rates of ≈ 500, 1000, and 1500 sec^{-1}, respectively.

The universal testing machine equipped with a thermal chamber was used to perform quasistatic deformation up to the residual strains at the test temperatures.

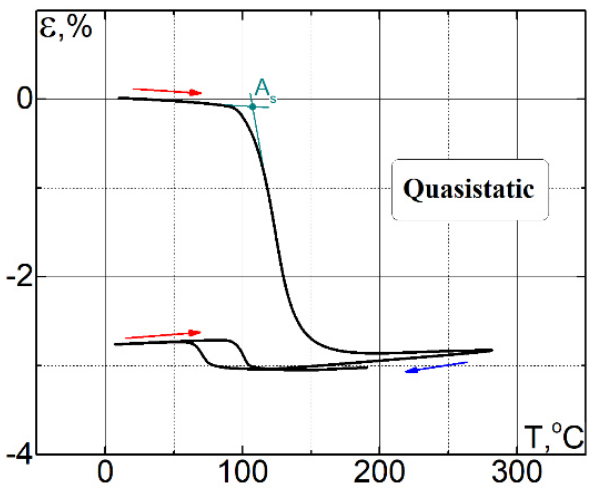

Fig. 3. Determination of reverse martensitic transformation start temperature A_s. As an example, a specimen deformed quasistatically to 5 % residual strain at a strain rate of 500 s^{-1} is shown

After tests, the specimens were thermocycled through the temperature range of the direct and reverse martensitic transformation in a thermomechanical analyzer with a temperature measurement accuracy of 0.3 °C. The rate of temperature change was about 1.5 °C per minute. The reverse martensitic transformation start temperatures A_s were measured by the tangent method, at the moment when the strain recovery curves on heating deviated from a straight trajectory, as shown in the example in Fig. 3. The paper focuses on the A_s, without considering the mechanical and functional features that appear with high-strain rate loading.

Results and Discussion

At room temperature, the material is in the martensitic state. When subjected to external load, the material accumulates reversible strain due to martensite reorientation and irreversible plastic strain. However, the increase of loading rate in the martensitic state leads to the increase of irreversible strain and decrease of reversible strain [30]. From the experimental data presented in Fig. 4, it can be seen that in both cases, the martensite stabilization effect increases as the total residual strain $\boldsymbol{\varepsilon_{res}}$ increases, but the difference in the proportions of reversible and irreversible strains in the quasi-static and dynamic cases leads to a difference in the stabilization effect. The higher loading rate results in a higher proportion of irreversible strain compared to the quasistatic case, which leads to a greater difference in the stabilization effect. According to results a stronger MSE is correlated with an increase in irreversible plastic deformation. Higher plastic strain leads to an increase in strain inconsistency, which reduces the mobility of martensitic boundaries. As a result, a greater thermodynamic force is required for the reverse martensitic transformation to occur.

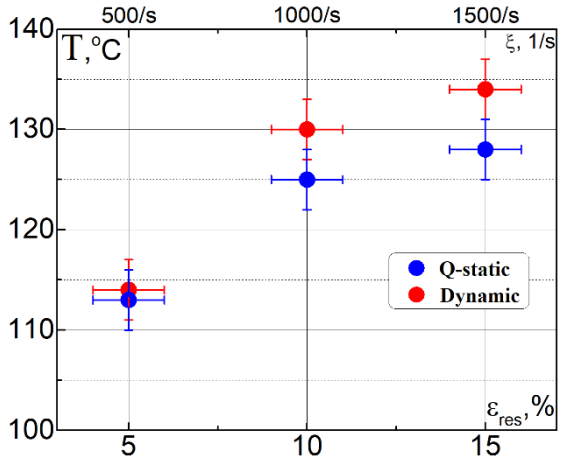

Fig. 4. The values of As in the first heating after tests at room temperature in the martensitic state depend on the strain rate ξ and the residual strain ε_{res} (● – after quasistatic deformation; ● – after high strain rate loading)

As mentioned above, martensitic transformation in shape memory alloys can be activated not only by temperature change but also by loading/unloading. The transition from one phase to another is accompanied by the absorption or release of heat (as shown in Fig. 1). This fact was addressed in [31] where the authors studied the temperature evolution of a TiNi alloy during dynamic loading. Among other things, they suggested

that higher strain rates bring the stress-induced direct martensitic transformation conditions closer to adiabatic conditions. This phenomenon gives rise to peculiarities shown in Fig. 5.

Quasi-static loading in the mixed phase state at 63 °C (Fig. 5(a)) and in the premartensitic state at 87 °C (Fig. 5(b)) is followed by the usual behavior - the martensite stabilization effect is observed (recall that these test temperatures were reached by cooling from the high-temperature state). The bigger the residual strain, the stronger the stabilization effect. However, the higher the test temperature is from the martensitic state, the weaker is the stabilization effect, which is fully consistent with results in [24,26] and the damaged boundary hypothesis described above. In this case, the martensite boundaries are less damaged, compared to active deformation in the martensitic state. The martensite appears and grows oriented in the same direction as the load, exhibiting so-called transformation plasticity effect. Active deformation in the martensitic state has a more "aggressive" influence on the martensite boundaries, compared to transformation plasticity effect.

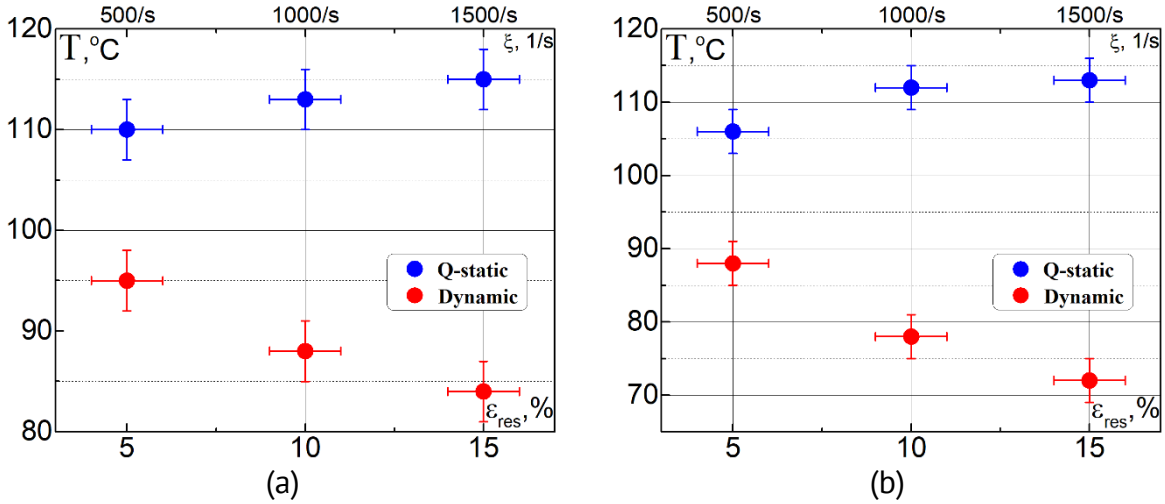

Fig. 5. The values of As in the first heating after tests at 63°C (a) and 87°C(b) depend on the strain rate ξ and the residual strain ε_{res} (● – after quasistatic deformation; ● – after high strain rate loading)

MSE is not observed after high strain rate loading. The temperature of the reverse martensitic transformation A_s during the first heating does not increase despite the growing residual strain. This feature can be explained by a combination of the both hypotheses mentioned above [26,31]. If higher strain rates bring the conditions of stress-induced martensitic transformation closer to adiabatic conditions, the martensite formation does not occur under high strain rate loading (at least it is significantly less than in the quasistatic case). This is because the transformation heat does not have opportunity to be distributed and dissipated in the environment under adiabatic condition. Thus, the only way is to accumulate the strain in the austenitic phase rather than through martensite formation. If the martensite remains undeformed, its boundaries will not be damaged, and therefore the martensite stabilization effect cannot occur.

The martensite stabilization effect depends on the loading rate in martensitic, premartensitic, and mixed phase states. The results are consistent with the results of other authors and can be explained by hypotheses presented in the literature.

Conclusions

The loading rate has a significant impact on the properties of NiTi shape memory alloy, including the martensite stabilization effect. An increase in the loading rate in the martensitic state results in a higher stabilization effect. However, high strain rate loading in the premartensitic and mixed-phase states does not lead to martensite stabilization, unlike in the quasi-static case. This behavior is consistent with the results and the hypotheses of other authors. The hypothesis that the conditions of stress-induced martensite formation are close to adiabatic in the dynamic case, as well as the idea that martensite boundaries are damaged under load, can explain the features presented.

References

1. Naresh C, Bose PSC, Rao C S P. Shape memory alloys: a state of art review. *IOP Conference Series: Materials Science and Engineering*. 2016;149: 012054.
2. Wilson JC, Wesolowsky MJ. Shape Memory Alloys for Seismic Response Modification: A State-of-the-Art Review. *Earthquake Spectra*. 2005;21(2): 569–601.
3. Priadko AI, Pulnev SA, Kovalev OO, Ilin IA. Rotary actuator control based on tensile force elements made of shape memory Cu-Al-Ni crystals when operated in a cyclic mode. *Materials Physics and Mechanics*. 2019;42: 407–414.
4. Priadko AI, Nikolaev VI, Pulnev SA, Stepanov SI, Rogov AV, Chikiryaka AV, Shmakov OA. Shape memory Cu-Al-Ni single crystals for application in rotary actuators. *Materials Physics and Mechanics*. 2017;32(1): 83–87.
5. Costanza G, Radwan N, Tata ME, Varone E. Design and characterization of linear shape memory alloy actuator with modular stroke. *Procedia Structural Integrity*. 2019;18: 223–230.
6. Petrini L, Migliavacca F. Biomedical Applications of Shape Memory Alloys. *Journal of Metallurgy*. 2011;1: 501483.
7. Morgan NB. Medical shape memory alloy applications – the market and its products. *Materials Science and Engineering: A*. 2004;378(1–2): 16–23.
8. Wen C, Yu X, Zeng W, Zhao S, Wang L, Wan G, Huang S, Grover H, Chen Z. Mechanical behaviors and biomedical applications of shape memory materials: A review. *AIMS Materials Science*. 2018;5(4): 559–590.
9. Hartl DJ, Lagoudas DC. Aerospace applications of shape memory alloys. *Proceedings of the Institution of Mechanical Engineers, Part G: Journal of Aerospace Engineering*. 2007;221(4): 535–552.
10. Barbarino S, Saavedra Flores EI, Ajaj RM, Dayyani I, Friswell MI. A review on shape memory alloys with applications to morphing aircraft. *Smart Materials and Structures*. 2014;23(6): 063001.
11. Brailovski V, Terriault P, Georges T, Coutu D. SMA actuators for morphing wings. *Physics Procedia*. 2010;10: 197–203.
12. Wanhill RJH, Ashok B. Shape Memory Alloys (SMAs) for Aerospace Applications. In: Prasad N, Wanhill R. (Eds.) *Aerospace Materials and Material Technologies*. Singapore; Springer: 2017.
13. Otsuka K, Ren X. Physical Metallurgy of Ti-Ni-Based Shape Memory Alloys. *Progress in Materials Science*. 2005;50(5): 511–678.
14. Liu Y, Li Y, Ramesh KT, Humbeeck JV. High strain rate deformation of martensitic NiTi shape memory alloy. *Scripta Materialia*. 1999;41(1): 89–95.
15. Liu Y, Li Y, Xie Z, Ramesh KT. Dynamic deformation of shape-memory alloys: Evidence of domino detwinning? *Philosophical Magazine Letters*. 2002;82(9): 511–517.
16. Belyaev S, Petrov A, Razov A, Volkov A. Mechanical properties of titanium nickelide at high strain rate loading. *Materials Science and Engineering: A*. 2004;378(1–2): 122–124.
17. Nemat-Nasser S, Choi JY. Thermomechanical response of an Ni–Ti–Cr shape-memory alloy at low and high strain rates. *Philosophical Magazine*. 2006;86(9): 1173–1187.
18. Nemat-Nasser S, Choi JY. Strain rate dependence of deformation mechanisms in a Ni–Ti–Cr shape-memory alloy. *Acta Materialia*. 2005 ;53(2): 449–454.
19. Adharapurapu RR, Jiang F, Vecchio KS, Gray III GT. Response of NiTi shape memory alloy at high strain rate: A systematic investigation of temperature effects on tension–compression asymmetry. *Acta Materialia*. 2006;54(17): 4609–4620.
20. Qiu Y, Young ML, Nie X. High Strain Rate Compression of Martensitic NiTi Shape Memory Alloy at Different Temperatures. *Metallurgical and Materials Transactions A*. 2017;48: 601–608.

21. Ostropiko E, Magazinov S, Krivosheev S. Uniaxial Magnetic Pulse Tension of TiNi Alloy with Experimental Strain Rate Evaluation. *Experimental Mechanics*. 2022;62: 1027–1036.
22. San Juan J, No ML. Damping behavior during martensitic transformation in shape memory alloys. *Journal of Alloys and Compounds*. 2003:355(1–2): 65–71.
23. Belyaev S, Resnina N, Iaparova E, Ivanova A, Rakhimov T, Andreev V. Influence of chemical composition of NiTi alloy on the martensite stabilization effect. *Journal of Alloys and Compounds*. 2019;787: 1365–1371.
24. Belyaev S, Resnina N, Ivanova A, Ponikarova I, Iaparova E. Martensite Stabilization Effect in the Ni50Ti50 Alloy After Preliminary Deformation by Cooling Under Constant Stress. *Shape Memory and Superelasticity*. 2020;6: 223–231.
25. Belyayev FS, Volkov AE, Volkova NA, Vukolov EA, Evard ME, Rebrov TV. Simulation of the effect of martensite stabilizationin titanium nickelide after deformationin the martensitic state. *Mechanics of Composite Materials and Structures*. 2023:29(4): 470–482. (In-Russian)
26. Belyaev S, Resnina N, Ponikarova I, Iaparova E, Rakhimov T, Ivanova A, Tabachkova N, Andreev V. Damage of the martensite interfaces as the mechanism of the martensite stabilization effect in the NiTi shape memory alloys. *Journal of Alloys and Compounds*. 2022;921: 166189.
27. Kolsky H. An Investigation of Mechanical Properties of Materials at Very High Rates of Loading. *Proceedings of the Physical Society. Section B*. 1949;62: 676.
28. Nicholas T. Tensile Testing of Materials at High Rates of Strain. *Experimental Mechanics*. 1981;21: 177–185.
29. Bragov AM, Igumnov LA, Konstantinov AY, Lomunov AK. Deformation and Fracture of Titanium Alloys Under Dynamic Loading. In: Aizikovich S, Altenbach H, Eremeyev V, Swain M, Galybin A. (eds.) *Modeling, Synthesis and Fracture of Advanced Materials for Industrial and Medical Applications. Advanced Structured Materials*. Cham: Springer; 2020.
30. Ostropiko E, Konstantinov AY. Functional behavior of TiNi shape memory alloy after high strain rate deformation. *Materials Science and Technology*. 2021;37(8): 794–804.
31. Yonggui L, Lingyan S, Junfang S, Mengmeng H. Experimental study on temperature evolution and strain rate effect on phase transformation of TiNi shape memory alloy under shock loading. *International Journal of Mechanical Sciences*. 2019;156: 342–354.

About Author

Eugeny S. Ostropiko Sc
Candidate of Physical and Mathematical Sciences
Associate Professor (St. Petersburg State University, St. Petersburg, Russia)

Alexander Yu. Konstantinov c Sc
Doctor of Physical and Mathematical Sciences
Professor (Lobachevsky State University of Nizhny Novgorod, Nizhny Novgorod, Russia)

MATERIALS PHYSICS AND MECHANICS RESEACH ARTICLE

Submitted: August 17, 2023 Revised: September 1, 2023 Accepted: October 14, 2023

Formation and stability of β-Si_3N_4 and Si_2N_2O phases in composite materials during mechanochemical treatment of powder mixtures including silicon, Taunite-M and nitrogen-containing components

I.S. Zherebtsov [1] ✉, V.V. Savin [1], L.A. Savina [1], A.V. Osadchy [2],

[1] Immanuil Kant Baltic Federal University, Kaliningrad, Russia

[2] Prokhorov General Physics Institute of the Russian Academy of Sciences, Moscow, Russia

✉ zheredcov@mail.ru

ABSTRACT

Scientific research and exploratory work on the creation of new technologies are continuing, the purpose of which is to increase the level of mechanical and high temperature properties of materials. A multicomponent carbon composite material (MCCM) containing silicon nitride and oxynitride was synthesized by the method of sequential stepwise high-energy mechanochemical treatment (MCT) and isothermal annealing at 1100 °C of powder mixtures of Taunite-M, silicon, g-C_3N_4 phase and melamine. Using X-ray diffraction analysis, IR spectroscopy and Raman spectroscopy, it was proved that β-Si_3N_4 and Si_2N_2O phases are present in the MCCM. Their crystallographic characteristics and crystal lattice parameters were determined. A crystal chemical explanation of the formation and stability of these phases in the realized synthesis is proposed. The synthesized MCCM is a promising material for high-temperature heat-resistant ceramics.

KEYWORDS

subcritical growth multicomponent carbon composite material • IR spectroscopy • Raman spectroscopy X-ray diffractometry • silicon nitride • silicon oxynitride

Acknowledgements. *The study was carried out with the financial support of the IKBFU. I. Kant within the framework of scientific project No. 197-L-21.*

Citation: Zherebtsov IS, Chayka VA, Savin VV, Savina LA, Osadchy AV. Formation and stability of β-Si_3N_4 and Si_2N_2O phases in composite materials during mechanochemical treatment of powder mixtures including silicon, Taunite-M and nitrogen-containing components. *Materials Physics and Mechanics*. 2024;52(2): 37–44. http://dx.doi.org/10.18149/MPM.5222024_5

Introduction

Formation of silicon nitride and oxynitride phases in a carbon matrix significantly changes the properties of carbon composite materials. This is due to their high hardness, shape morphology and distribution pattern in the composite. With standard technologies [1], the formation of these phases is achieved through prolonged high-temperature treatment and/or at elevated pressure. We implemented a different approach in our research. The technology of mechanochemical treatment (MCT) of multicomponent polyphase powder mixtures is used [2]. The elemental, phase and fractional compositions of the components of the initial powder mixture and the gas composition of the technological atmosphere undergo changes in the process of sample preparation and the initial stage of MCT. This is necessary for the subsequent mechanochemical alloying of the components in a high-energy planetary mill, the formation of nonequilibrium structural-phase states. The presence of fine single-crystalline silicon particles in the processed powder mixture promotes the synthesis on such a substrate with its random favorable crystallographic orientation in the carbon matrix and the real technological atmosphere of the desired

phases: silicon nitride and oxynitride. The resulting state was stabilized by isothermal annealing. Varying the parameters and conditions of the MCT technological process provides the necessary set of types of impact action (of the balls on the powder mixture), their energy and kinetic patterns. This includes the duration and nature of the interaction, the gas composition of the technological environment in which local impact processes and various physical and chemical processes occur during subsequent mixing of the powder in the working volume [3]. Alternating the above technological parameters makes it possible to form micro- and nano-particles of powder material of various shapes. The use of subsequent isothermal annealing makes it possible to detect the formation of silicon nitride and oxynitride phases and ensures the formation of the required phase composition in the synthesized multicomponent carbon composite material (MCCM). Since the formation and distribution of phases in the volume of the synthesized MCCM is significantly influenced by the form factor of the initial carbon material, we used Taunite-M type nanostructured carbon material in the work. When using high-energy ball mills for synthesis, it is necessary to create a protective or reducing environment. At the level of micro- and nano-processes, the composition of the technological atmosphere in the local volume of direct impact interaction comes to the fore. For these purposes, a component (melamine) was added to the processed powder mixture, which, upon decomposition during the synthesis process, released nitrogen-containing gas components (including ammonia), forming a reducing or protective environment, both in the local interaction volume and in the entire working volume [4]. In addition, at all subsequent repeating stages of MCT and stepwise heat treatment (SHT), the factor of the reducing atmosphere of nitrogen-containing compounds formed at the first stage of synthesis is continuously enhanced by the active (atomic) carbon of working environment in the local volume of impact interaction, which primarily binds technological oxygen residues to form carbon monoxide.

Therefore, the purpose of the performed work was to use diffraction and spectral research methods to prove the synthesized MCCM contains such phase components as silicon nitride (Si_3N_4) and silicon oxynitride (Si_2N_2O).

Methods

The considered multicomponent carbon composite material (MCCM) was obtained by synthesis using mechanochemical treatment (MCT) in a PM-100 planetary ball mill (Retsch Technology, Hamburg, Germany) and subsequent stepwise isothermal annealing in a vacuum furnace at a temperature not exceeding 1100 °C and vacuum of $1 \cdot 10^{-3}$ mbar for at least three hours.

To obtain MCCM, we used carbon nanostructured material Taunite-M as a basis: quasi-one-dimensional, nano-sized, thread-like formations of polycrystalline graphite, predominantly cylindrical in shape with an internal channel compliant with TU 2166-001-77074291-2012 produced by LLC NanoTechCenter (Tambov, Russia).

In order to accelerate the process of phase formation, powder material obtained using the technology described in [4] was added to the mixture together with Taunite-M. This technology involves the thermal decomposition of carbamide (in our case, melamine) to graphite-like carbon nitride. The presence of the g-C_3N_4 phase in the processed mixture

is a necessary condition for the formation of β-Si_3N_4 during synthesis. The weight proportionality of the charge components of powder mixtures corresponds to the requirement of substance balance during synthesis.

The mixture included four components of optimal proportional weight composition and homogeneous fractional composition: Taunite-M; g-C_3N_4; silicon (KR0 GOST 2169-69); melamine (GOST 7579-76). The total mass of the powder mixture did not exceed 4 g and was controlled at all stages of the synthesis with an accuracy of ± 0.002 g. All components used were fractions of ⩽ 56 μm composition.

At the first stage, mechanochemical synthesis was carried out in a PM-100 planetary mill at 600 rpm in an agate jar with agate balls in ethanol. The processing time was 10 hours, while the mode included stopping the process every 2 hours for 0.5 hours. This mode maximizes phase formation in the processed carbon material. The ratio of the mass of the balls to the mass of the load was 18:1.

Next, the resulting material was dried at a temperature of (60 ± 2) °C for 4 hours and pressed into tablets with a diameter of 6 mm at a pressure of 1.5 tons (hydraulic press with a maximum force of 10 tons). The mass of the samples was (0.060 ± 0.001) g. At the third stage, multi-stage annealing was carried out in vacuum: at 360 ± 5 °C for 1 hour; at 450 ± 5 °C for 1 hour; at 1100 ± 5°C for 3 hours.

The first two stages of heat treatment are carried out to decompose the melamine and thereby create a protective atmosphere.

The phase composition of the resulting MCCM was studied by X-ray diffractometry using a DRON-3M diffractometer and Co Kα filtered radiation. The shooting was carried out according to the Bragg–Brentano setup (ϑ–2ϑ) in the angle range of 2ϑ = (10 ÷ 90) angular degrees with a scanning step of 0.05° and exposure at a point of 3 s. At least three samples synthesized under the same conditions were analyzed. The ratio of the min-max total set of pulses at a point provided a statistical error of 0.05/0.005.

IR spectroscopy was performed on a Shimadzu IRPrestige-21 infrared spectrometer with Fourier transform, standard measurement parameters, spectral range of 7800–350 cm^{-1}, ceramic radiation source, KBr beamsplitter, DLATGS detector.

Raman spectra were taken on a Centaur scientific research complex, including a Renishaw Virsa spectrometer with excitation wavelength of 785 nm, 5 s exposure time, without radiation attenuation.

Results and Discussion

The X-ray studies had increased accuracy: we increased the number of samples examined (up to three per analysis); used analytical slits of reduced sizes and Soller slits to limit the axial deflection of the X-ray beam; increased shooting time per point by 3 times; reduced the scanning step; installed an iron β-filter for Co-radiation. Figure 1 shows the results of X-ray diffraction studies of the synthesized MCCM. The analysis proves, with a high degree of reliability, the presence of β-Si_3N_4 and Si_2N_2O phases in the synthesized material. When decoding the identified diffraction maxima, we used the data from our previous studies [5]. The fundamental factor in the studies performed is the fact of the existence of diffraction maxima that belong exclusively to the β-Si_3N_4 and Si_2N_2O phases

(see Fig. 1). Thus, X-ray studies indeed indicate that the proposed hybrid technology of MCCM synthesis produces silicon nitride and oxynitride.

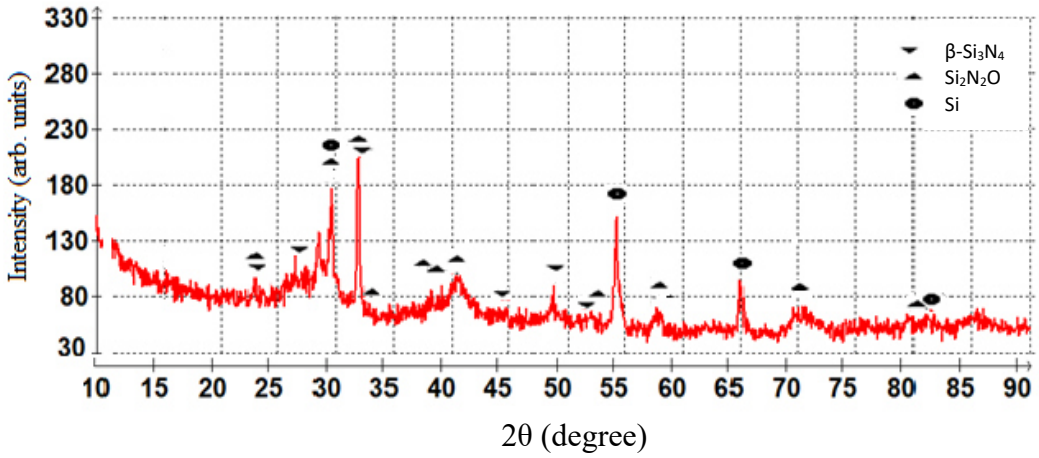

Fig. 1. X-ray diffraction pattern of MCCM obtained using the hybrid technology

However, since the synthesized MCCM has a multiphase state (four phases), as a consequence all diffraction patterns obtained from X-ray analysis are complex: many diffraction peaks belonging to different phases, often closely spaced and often overlapping with each other [5]. In such cases, the results of phase analysis require clarification by other methods. For this purpose, in order to confirm that β-Si_3N_4 and Si_2N_2O phases formed during synthesis, we performed spectral studies of the MCCM samples using infrared spectroscopy (IR) and Raman spectroscopy (RS). This choice of spectral analysis methods is due to their increased sensitivity to the type of interatomic (intermolecular) interaction. The research results are shown in Figs. 2 and 3 and in Tables 1 and 2.

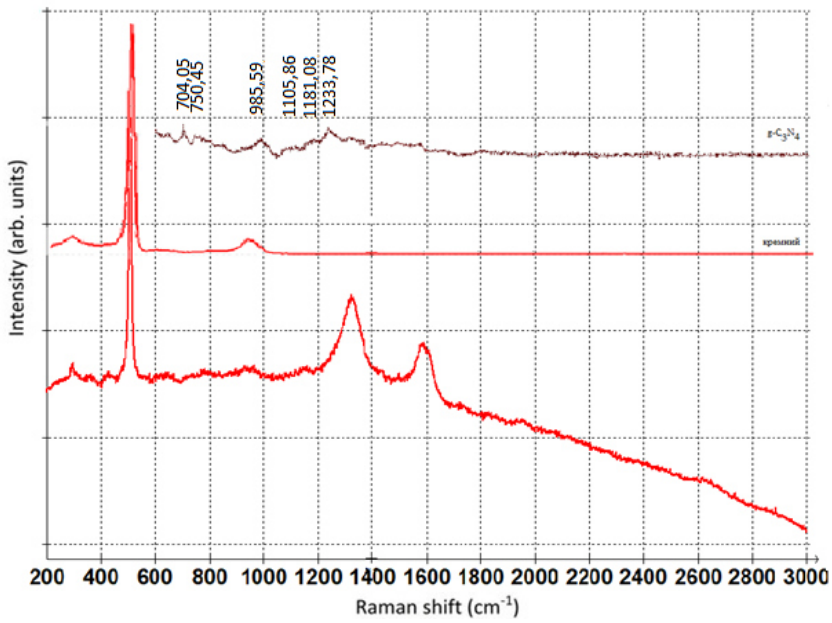

Fig. 2. Results of Raman scattering by samples of the synthesized MCCM (lower graph) and mixture components used for synthesis (Si and g-C_3N_4)

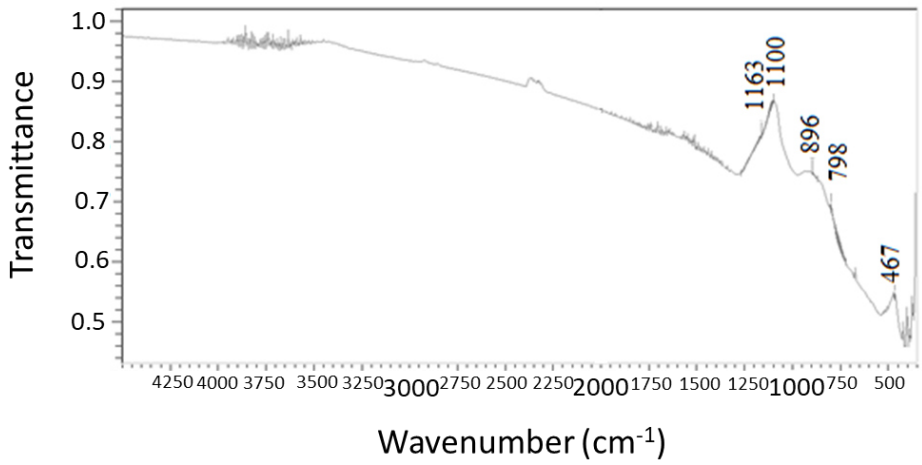

Fig. 3. Results of IR spectroscopy of the synthesized MCCM samples

Table 1. Interpretation of Raman scattering data for the synthesized MCCM samples (Raman spectroscopy)

Experimentally obtained peaks, cm^{-1}	Literature data	Phases
296.53	259; 365 α-Si_3N_4 [8] 303.24 Si experiment	α-Si_3N_4
411.75	400 Si-N [9]	Si-N
440.55	480 Crystalline Si [10]	Crystalline Si
505.23	515 α-Si_3N_4 [8] 520 amorphous Si [10] 518.08 Si experiment	α-Si_3N_4 amorphous Si
656.24	668 α-Si_3N_4 [8]	α-Si_3N_4
704.05	g-C_3N_4 experiment	g-C_3N_4
750.45	g-C_3N_4 experiment	g-C_3N_4
800.44	804 heptazine rings [11] 800 Si-C [10] 800 Si-N [12]	heptazine rings Si-C Si-N
809.84	810 [13] melamine degradation	melon
849.01	~860 Si-N [14]	Si-N
925.76	915 α-Si_3N_4 [8] 946,81 Si experiment	α-Si_3N_4
962.19	975 α-Si_3N_4 [6]	α-Si_3N_4
1034	1034 α-Si_3N_4 [6]	α-Si_3N_4
1100-1700	1.3.5-s-triazine rings [12]	1.3.5-s- triazine
1105.86	g-C_3N_4 experiment	g-C_3N_4
1181.08	g-C_3N_4 experiment	g-C_3N_4
1350		D-graphite
1582		G-graphite
1620		D'-graphite
2100-2300	~2200 Si-H [11]	Si-H
2700		2D-graphite
~3250	~3300 N-H [11]	N-H

Figure 2 shows the results of Raman scattering studies for the synthesized MCCM samples. Note the shift of the silicon peak towards lower values. The authors of [6,7] proved that a shift of the silicon peak to lower values occurs upon heating due to a change

in the thermal conductivity of silicon, which is covered with an oxide film. In our studies, a bond between silicon and nitrogen is formed, which can also change the thermal conductivity of the sample material and cause a change in the position of the Raman peak and its half-width.

Table 1 shows the interpretation of the Raman spectra indicating the sources that served as justification for the adoption of the phases. For silicon and g-C_3N_4, experimental data were taken, obtained by recording the initial components of the mixture. The results presented in the table clearly confirm the fact of the formation of silicon nitride.

However, note that although the silicon peak shifted, there are no peaks characteristic of the Si-O bond. In this case, the well-known peaks of amorphous disordered graphite are present. This result somewhat contradicts the known fact of graphitization at 700 °C. In our opinion, this is due to the formation of open and closed pores in the material. Closed pores presumably prevent graphitization at higher temperatures.

As the graph demonstrates, there are three areas of low-intensity bands (noise), which can be attributed to the result of the melamine degradation and the formation of the g- C_3N_4 phase, the formation of CO_2 and thin graphene films. Table 2 shows the interpretation of the IR spectra indicating the sources that confirmed the presence of specific bonds between atoms in the phases existing in the synthesized MCCM samples.

Table 2. Interpretation of IR spectroscopy data for the synthesized MCCM samples

Experimental data, cm^{-1}	Literature data	Bonds
467	470 Si-N [16,19] 480 Si-Si [9,10] 457 Si-O rocking bands [10]	Si-N
798	814 Si-O bending bands [10]	Si-O
896	875 Si-N stretching bonds [15] 865 Si-N [10] >850 Si-N [16]	Si-N
1100	1100 HN-H [17] 1080 Si-O [15] 1069↑t 1080 Si-O [10]	HN-H, Si-O
1163	1170 N-H [16] 1175 N-H [10]	N-H
1300-1700 ('noise')	Low-intensity absorption bands with maxima at wavenumbers from 1554 to 1234 cm^{-1} correspond to bending and stretching vibrations of the C-N bonds of the heptazine ring [11]	C-N heptazine rings
2300-2400 ('noise')	2260-2300 CO_2[11]	CO_2
2350	2200 Si-H [9]	Si-H
2851	Graphene [18]	
2924	Graphene [18]	
3350	3340 Si-N [16,19]	Si-N

As can be seen from the table, the samples contain a Si-O bond. However, X-ray studies do not confirm the formation of silicon oxide [20]. Therefore, the Si-O and Si-N bond can be rightfully attributed to the silicon oxynitride phase.

Conclusion

The non-equilibrium of the processes and the structural-phase states during mechanochemical treatment, the degradation of metastable phases and structural formations when the technological process is interrupted, and the use of stepwise heat treatment, form multicomponent carbon composite materials with a very complex phase composition, both in the type (set) of phases, and in their chemical composition and structural (defective) condition. The phase composition of a composite primarily determines its physical and chemical properties and the range of possible applications. The production of carbon composites (MCCM) containing phases of silicon nitride and oxynitride by mechanochemical treatment and stepwise heat treatment opens up new prospects for their use as a functional material, including for microelectronics.

Based on the results of X-ray and spectral studies, it can be stated that the proposed hybrid technology of MCCM synthesis induces β-Si_3N_4 and Si_2N_2O phases. Their formation and stability are determined by the weight proportions and composition (set of components) of the mixture and the physicochemical laws of the processes in the system during hybrid synthesis by high-energy mechanochemical treatment and subsequent isothermal vacuum annealing at a temperature of 1100 °C.

References

1. Garishin OK, Svistkov AL, Voznyakovskii AP, Tchypkina IM, Neverovskaya AY, Shadrin VV. Anisotropic mechanical properties of elastomeric nanocomposites filled by carbon black, few-layer graphene, and carbon nanotubes. *Materials Physics and Mechanics*. 2022;50(3): 495-508.
2. Aminikia B, Youzbashi AA. Effect of milling time on mechanochemical synthesis of nanocrystalline zirconium diboride. *Materials Physics and Mechanics*. 2013;17(1): 1-5.
3. Lapshin OV. Modeling of mechanochemical and structural transformations in a binary powder mixture. *Theoretical Foundations of Chemical Technology*. 2020;54(2): 236-243.
4. Chebanenko MI, Zakharova NV, Popkov VI. Synthesis and Visible-Light Photocatalytic Activity of Graphite-like Carbon Nitride Nanopowders. *Russian Journal of Applied Chemistry*. 2020;93: 494-501.
5. Zherebtcov IS, Osadchy AV, Savin VV, Savina LA, Chaika VA. Synthesis of powder functional composite materials containing g-C3N4, β-Si3N4 and Si2N2O phases. *Journal of Physics: Conference Series*. 2022;2388: 012013.
6. Sahoo S, Mallik SK, Sahu MC, Joseph A, Rout B, Pradhan GK, Sahoo S. Thermal conductivity of free-standing silicon nanowire using Raman spectroscopy. *Nanotechnology*. 2020;31(50): 505701.
7. Giura P, Bonini N, Creff G, Brubach JB, Roy P, Lazzeri M. Temperature evolution of infrared- and Raman-active phonons in graphite. *Physical Review*. 2012;86(12): 121404(R).
8. Kuzuba T, Kijima K, Bando Y. Raman-active modes of alpha silicon nitride. *J. Chem. Phys*. 1978;69: 40.
9. Ahmed N, Bhal Singh C, Bhattacharya S, Dhara S, Balaji Bhargav P. Raman and FTIR Studies on PECVD Grown Ammonia-Free Amorphous Silicon Nitride Thin Films for Solar Cell Applications. *Conference Papers in Energy*. 2013;2013: 837676.
10. Osip H, Czosnek C, Janik JF, Marchewka J, Sitarz M. Amorphous Silicon Oxynitride-Based Powders Produced by Spray Pyrolysis from Liquid Organosilicon Compounds. *Materials*. 2021;14(2): 386.
11. Xu J, Li Y, Peng Sh, Lu G, Li Sh, Eosin Y. Sensitized graphitic carbon nitride fabricated by heating urea for visible light photocatalytic hydrogen evolution The effect of the pyrolysis temperature of urea. *Phys. Chem*. 2013;15(20): 7657.
12. Liu R, Canonico M. Applications of UV—Raman Spectroscopy to Microelectronic Materials and Devices. *Proceedings of the AIP Conference*. 2003;683(1): 738–743.
13. Zhao YC, Yu DL, Zhou HW, Tian YJ, Yanagisawa O. Turbostratic carbon nitride prepared by pyrolysis of melamine. *Journal of Materials Science*. 2005;4: 2645–2647.

14. Bucio TD, Khokhar AZ, Lacava C, Stankovic S, Mashanovich GZ, Petropoulos P, Gardes FY. Material and optical properties of low-temperature NH3-free PECVD SiNx layers for photonic applications. *J. Phys. D: Appl. Phys*. 2017;50(2): 025106.
15. Yamazaki H, Ishikawa Y, Fujil M, Ueoka Y. The influence of fluorinated silicon nitride gate insulator on positive bias stability toward highly reliable amorphous InGaZnO transistors. *ECS Journal of Solid Science and Technology*. 2014;3(2): Q20.
16. Kobayashi S. IR Spectroscopic Study of Silicon Nitride Films Grown at a Low Substrate Temperature Using Very High Frequency Plasma-Enhanced Chemical Vapor Deposition. *World Journal of Condensed Matter Physics*. 2016;6: 287-293.
17. Jafari S, Hirsch J, Lausch D, John M, Bernhard N, Meyer S. Composition limited hydrogen effusion rate of a-SiNx:H passivation stack. *AIP Conference Proceedings*. 2019;2147: 050004.
18. Malard LM, Pimenta MA, Dresselhaus G, Dresselhaus MS. Raman spectroscopy in grapheme. *Physics Reports*. 2009;473(5-6): 51-87.
19. Dhruva K, Bibhu P. Swain. Investigation of structural and mechanical properties of silicon carbonitride thin films. *Journal of Alloys and Compounds*. 2019;789: 295-302.
20. Mofa NN, Zhapekova AO, Sadykov BS, Bakkara AE, Sakhan MG, Bekentaeva AD, Mansurov ZA. Complex use of mechanochemical and ultrasonic processing for obtaining highly dispersed silicon dioxide for special purposes. *Gorenje and Plasmo Chemistry*. 2019;17(2): 123-132. (In-Russian)

About Author

Ivan S. Zherebtsov Sc
Engineer (Immanuil Kant Baltic Federal University, Kaliningrad, Russia)

Valeriy V. Savin Sc
Doctor of Physical and Mathematical Sciences, Professor
Head of the Laboratory of Physical Materials Science (Albert Einstein Gymnasium, Bratislava, Slovakia)

Lyudmila A. Savina Sc
Candidate of Technical Sciences
Senior Researcher (Albert Einstein Gymnasium, Bratislava, Slovakia)

Alexander V. Osadchy Sc
Candidate of Physical and Mathematical Sciences
Senior Researcher (Prokhorov General Physics Institute of the Russian Academy of Sciences, Moscow, Russia)

MATERIALS PHYSICS AND MECHANICS RESEACH ARTICLE

Submitted: October 30, 2023 Revised: November 7, 2023 Accepted: December 8, 2023

In-situ high-temperature bending strength measurement of YSZ ceramics manufactured using novel B_2O_3-based glass binder

P. Maniakin [1], S.G. Shalagaev [2], I.Yu. Archakov [3] ✉, Ya.V. Konakov [1,3], O.Yu. Kurapova [3,4], V.G. Konakov [1-3],

[1] Peter the Great St. Petersburg Polytechnic University, St. Petersburg, Russia

[2] Glass and Ceramics, LTD, St. Petersburg, Russia

[3] Institute for Problems in Mechanical Engineering RAS, St. Petersburg, Russia

[4] Saint Petersburg State University, St Petersburg, Russia

✉ ivan.archakov@gmail.com

ABSTRACT

Stabilized zirconia ceramics are in high demand for various high temperature applications as fuel cells, oxygen sensors or protective barriers in aircraft. The use of additive manufacturing with polymeric binders do not allow the application of manufactured zirconia ceramics units at high temperature. The present research highlights the manufacturing of cubic yttria stabilized zirconia (YSZ) using Co_3O_4-doped MgO-BaO-B_2O_3 glass as a novel high-temperature binder. In order to produce ceramics, YSZ powder with 4 wt. % of glass binder was milled in a planetary mill, compacted using isostatic cold pressing and annealed at 1500 °C for 2 hours. Sol-gel co-precipitated YSZ powder with average particle size of 290 nm was used as a precursor. The structure of ceramics was investigated via HR-SEM, EDS, XRD, hydrostatic weighting. In situ 3-point bending strength measurement showed that the ultimate bending strength is 104 ±10 MPa at room temperature. Temperature increase induces the linear decrease of bending strength value. Fractography tests revealed that the glass binder plays a key role in the mechanical behavior of the ceramics. The ways to improve the mechanical behavior of ceramics are suggested.

KEYWORDS

yttria stabilized zirconia • bending strength • glass binder • high temperature ceramics• in-situ measurements

Acknowledgements. *This work was supported by Russian science foundation (RSF #23-19-00236). SEM and EDS data of the powders and consolidated ceramics as well as fracture of specimens after mechanical tests were obtained at the Research park of St. Petersburg State University" Interdisciplinary Center for Nanotechnology".*

Citation: Maniakin P, Shalagaev SG, Archakov IYu, Konakov YaV, Kurapova OYu, Konakov VG. In-situ high-temperature bending strength measurement of YSZ ceramics manufactured using novel B_2O_3-based glass binder. *Materials Physics and Mechanics*. 2024;52(2): 45–56.
http://dx.doi.org/10.18149/MPM.5222024_6

Introduction

Due to a set of its unique characteristics, Yttria Stabilized Zirconia (YSZ) ceramics is considered as one of the most perspective materials of XXI century. Depending on the type of zirconia allotrope it is widely used in the various fields of modern industry: cubic zirconia is utilized in solid oxide fuel cells [1–5], high-temperature oxygen sensors [6,7], optical sensors [8], tetragonal zirconia is used as a biomaterial for dentistry and orthopedy [9,10], as thermal barriers coatings for aircraft [11], etc. The available literature data on the YSZ mechanical properties mainly concerns the behavior of the tetragonal phase of

zirconia or partially stabilized zirconia at room temperature or at presence of a moisture [9,12–15]. Paper by L. Zhou et al. [16] reports the properties of yttria-stabilized zirconia computed by molecular dynamics simulations depending on the crystal orientation. YSZ structure here was obtained by random replacement of Zr^{4+} in ZrO_2 by Y^{3+}; in order to save the charge neutrality, one oxygen atom was removed for every two Zr^{4+} replacements. Rather high values of the Young's modulus (325-400 GPa at room temperature and ~ 325 GPa at 1000 °C) and Poisson's ratio (0.45 and 0.4 at 25 and 1000 °C, respectively) were obtained; note that the authors consider the temperature dependence of the mechanical properties to be rather low. Authors of [17] performed a set of computations for a wide range of zirconia-based objects: cubit, tetragonal and monoclinic ZrO_2, pure cubic YSZ and cubic YSZ (c-YSZ) doped by some metal oxides; density functional theory was used for this task. In contract to [16], the difference in the mechanical properties attributed to the different crystal orientation is considered to be quite significant: the strain strength in the [100] direction is ~ 2.8 times higher than in the [110] one. The high value of Young's modulus (277 GPa), bulk modulus (239 GPa), shear modulus (106 GPa) and Poisson's ratio of 0.307 at room temperature are reported for cubic YSZ. The experimental work [18] reports the study of the spark plasma sintered YSZ mechanical properties. It should be noted that the obtained ceramics was quite porous, the best porosity obtained at higher temperature and pressure values exceeds 10 % for tetragonal YSZ. The drastic porosity effect on the YSZ mechanical properties is discussed: as an example, Young's modulus at minimal porosity is ~ 170 GPa, while at a maximal one (40 %) it decreases down to ~5 GPa. Similar effect was also shown for the Vickers hardness (~ 1050 and ~ 200 $HV_{0.3}$, respectively) and for the flexural strength (~ 320 and ~ 40 MPa, respectively). YSZ (8 % yttria) Young's modulus as a function of temperature was studied by S. Giraud and J. Canel [19], ceramics here were synthesized from powders by cold pressing at 250 MPa with a further annealing at 1350 °C for 3 h in air. The following data were obtained for Young's modulus, modulus of rigidity and Poisson's ratio at room temperature: 205, 78 GPa and 0.31, respectively. The authors report the complicated Young's modulus dependence on the temperature: it slowly decreases in the temperature range up to 150 °C; this decrease is more evident at 150-550 °C. However, an increase in the Young's modulus value was observed at temperatures higher than 600 °C. Finally, rather high Young's modulus value is reported for the maximal temperature of 1000 °C – ~ 150 GPa. The work by T. Kushi et al. [20] deals with the temperature effect of the elastic modulus and the internal friction of YSZ itself ($Zr_{0.85}Y_{0.15}O_{1.93}$) and YSZ doped by a number of metal oxides; specimens under study were produced within the traditional ceramic approach (cold pressing at 150 MPa with further sintering at 1350 °C). The mechanical properties of the specimens were investigated in an oxidizing and a reducing atmosphere (O_2 and H_2 additions to Ar) in the temperature range from room to 1300 K. It was shown that the temperature behavior of the Young's modulus is similar to that reported in [19], the difference between the values typical for both atmospheres seems to be rather low. Young's modulus demonstrated some decrease from ~210 GPa at room temperature to ~ 160 GPa at 1023 °C; the decrease in the shear modulus was not so distinctive (~ 75 and 55 GPa, respectively), while the Poisson's ratio was not linear and demonstrated some increase from ~ 0.38 to ~ 0.4. A recent paper [21] discusses the yttria contents effect of on the YSZ microstructure and mechanical

properties. A conventional approach (sintering at 1550 °C for 2 h in argon) was used to prepare the specimens, it should be noted that the obtained specimens were the mixture of monoclinic, tetragonal, and cubic phases. The flexural strength of the studied materials varied from 900 to 500 MPa depending on the yttria contents, the highest values were obtained for the compositions with 3, 7, and 8 % of yttria. The authors stated that the variations in the flexural strength value coincide with the variations in the monoclinic phase contents. The work by X. Ren and W. Pan [22] considers the changes in the mechanical properties of 8 wt. % yttria-stabilized zirconia ceramics due to the thermal degradation of the metastable tetragonal phase. The specimens for the study were manufactured using the powder air spraying to obtain metastable T' phase powders which were then ball milled and sintered at 1450 °C for 5 min under a unidirectional pressure of 50 MPa by the SPS method. Note that the samples cut for the mechanical testing were additionally hardened by an annealing at 1300 °C for 1–24 h. The authors report the following typical values for the samples depending on the metastable phase contents: Vickers hardness in the range from 13 to 14 GPa, elastic modulus of ~ 229 GPa, bending strength from 220 to 500 MPa, and fracture toughness from 4.0 to 5.4 MPa $m^{1/2}$. The effect of carbon nanotubes on the YSZ (3 % yttria) mechanical properties was investigated in [23], SPS approach (60 MPa with a maximum sintering temperature of 1450 °C) was used for the specimens production. The Young's modulus of ~ 290 GPa, the shear modulus of ~ 215 GPa, and the fracture toughness value of 4.1 MPa $m^{1/2}$ were reported for the pure 3YSZ samples at room temperature. The effect of the phase composition is discussed. The effect of the thermal cycling on the mechanical properties of the tetragonal polycrystalline YSZ is reported in [24]. Rather high flexural strength value of 776 MPa is stated. The obtained values of the Young's modulus demonstrated an evident decrease with temperature from 206 GPa at room temperature to ~ 165 GPa at 850 °C, the thermal cycling seems to produce fairly low effect on the Young's modulus temperature behavior.

In summary, it can be stated that YSZ itself possesses rather high values of Young's and shear moduli, along with the bending (flexural) strength values. However, the mechanical properties of the exact specimen are highly affected by a lot of material characteristics: yttria contents, phase composition, synthesis approach, porosity, grain size, thermal prehistory, etc.

One of the main problems, hindering the comfortable YSZ usage, is the well-known difficulties dealing with manufacturing of the complex geometry pieces within the traditional ceramic approaches. Despite the traditional approaches to allow the fabrication of YSZ ceramics, they are often not cost-effective and often require the use of the additional machining tools. Additive technologies providing the automated production of the pieces with a precision geometry seems to be the evident decision of this problem; it is especially effective for the units with a highly developed system of internal surfaces – channels and cavities [12,25]. However, the use of the additive technologies for the production of ceramic units is characterized by a number of serious limitations, the detailed analysis of such limitations can be found in our recent work, see e.g. [26].

Modern approaches of the YSZ ceramic pieces production via additive manufacturing include stereolithography, ink jet-printing, tape casting, selective laser sintering (SLS), and selective laser melting (SLM) [25]. They are usually based on the use of organic or inorganic binders. Typically, organic binders are rather universal for all

ceramic materials including YSZ, asphotoreactive organic mixture provided by 3D CERAM Sinto, France [12], various acrylate derivatives, as 1,6-hexanediol diacrylate (HDDA) [27], 2-hydroxyethyl methacrylate (HEMA) [28] or polyvinylpyrrolidone (PVP) binder. Regretfully, the exploitation of the materials with such binders is usually restricted by temperatures below 250-300 °C. In turn, such inorganic colloid binders as TiO_2 [29], Ti_3SiC_2, $CoAl_2O_4$ and ZrO_2 [30] provide higher exploitation temperatures. In [30], a zirconium basic carbonate was used as a binder to print zirconia based ceramic parts. Aqueoustetragonal zirconia-based inks with solid contents of 22 and 27 vol. % were used in [31] to fabricate three-dimensional ceramic parts by the ink-jet printing. The sintered ceramics reached up to ~ 97 % of the theoretical density. In both works, the focus was made on the rheological properties of slurries. The effects of the structure, sintering parameters on bending strength, compressive strength, and pore structure architecture were not studied. It should be noted that to produce the part having high mechanical properties, the binder should be matched with the ceramic matrix material according to the Coefficient of Thermal Expansion (CTE) [32]. The use of the glass binder with the same CTE as zirconia is prospective as such matching prevents the material destruction upon heating. Thus, the present work aims he the possibility of the use of Cobalt oxide-doped MgO-BaO-B_2O_3 glass (here and after Co-MBB glass) as a binder for the production of YSZ matrix pieces by additive technologies. Model specimens produced using the traditional ceramic approach were used for in-situ evaluation of the high-temperature bending strength of such a material. The result obtained is the decisive for the whole complex of further research – the possibility of the significant increase of the material exploitation temperature range is shown comparing with 250-300 °C limit typical for the materials produced using organic binders.

Methods

YSZ powders synthesis

The synthesis of $9Y_2O_3$-$91ZrO_2$ (YSZ) powders with the mean particle size of 290 nm was carried out using the co-precipitation approach followed by freeze-drying described in details in [33,34]. Yttrium and zirconyl nitrates hydrates $Y(NO_3)_3{\times}6H_2O$ (Acros organics, Geel, Belgium, 99.9 %) and $ZrO(NO_3)_2{\times}6H_2O$ (Acros organics, Geel, Belgium, 99.5 %) were utilized to prepare a 0.1 M aqueous mixed salt solution. A resulted salt solution was added dropwise to 1 M aqueous ammonia solution (LenReactiv Ltd, St. Petersburg, Russia, c.p.) at a rate of ~1–2 mL/min. The precipitation was performed at ~1–2 °C in an ice bath; the pH of the solution was controlled to be ~ 9–10 during the synthesis. To remove reaction byproducts, the obtained gel was filtered and rinsed by distilled water until the neutral pH was reached. The precipitate of mixed hydroxides was then freeze-dried (Labconco, 1L-chamber, Kansas City, MO, USA; 20 ºC, 24 h, P = 0.018 mm Hg). The obtained powder was annealed at 650 °C for 3 hours, and then it was milled in a planerary mill (400 rpm, 12 reverse cycles of 5 minutes each, Pulverisette 6, Fritsch, Germany).

Co-MBB glass

A glass with 30MgO-35BaO-35B_2O_3 (mol.%) composition (further, MBB glass) was produced as follows: the starting reagents MgO, $Ba(OH)_2 \times 8H_2O$, and H_3BO_3 (all LenReactiv Ltd, St. Petersburg, Russia, 99.98 %) were mixed in the required proportions; the mixture was ground in a porcelain mortar to a homogeneous powder (typical particle mean size ~ 15-25 μm, maximal < 40 μm). The obtained powder was kept in an alundum crucible at 1100 °C for about ~ 3 hours until the end of the gases release. The temperature was then increased up to 1250 °C, the glass was exposed at that temperature for 1.5 hours and then poured on a steel plate. As it was shown in [35], CTE of such glass in the temperature range from room to 1000 °C is close to that of YSZ [32]. Unfortunately, the obtained glass was fairly colorless and transparent making it quite inefficient as a binder in additive manufacturing, as Selective Laser Synthesis and Selective Laser Melting (SLS and SLM) approaches. To overcome this problem, MBB glass was doped by cobalt oxide Co_3O_4 as follows. Commercially available Co_3O_4 powder (mean size 18 μm, maximal particle size < 40 μm) was added to MBB glass powder in the ratio 100 g MBB glass powder / 4 g Co_3O_4 powder, the resulting powder was thoroughly mixed, the technology of glass baking was the same. The resulting glass has an evident blue color (Fig. 1) making it suitable for SLS / SLM approaches. At that, the relatively small addition of the cobalt oxide should not noticeably change the glass CTE.

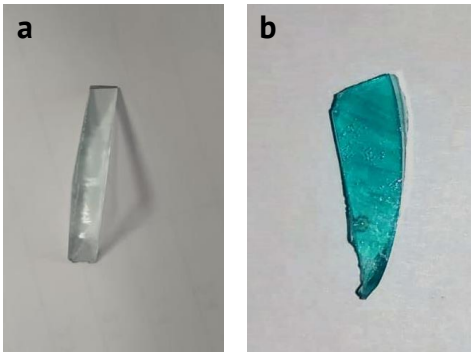

Fig. 1. Comparison of MBB glass (a) and Co-doped MBB glass (b)

In order to use the manufactured Co-MBB glass as a binder for ceramics manufacturing, the obtained material was crushed into powder using mortar and pestel. The high resolution scanning electron microscopy (HR-SEM) photos obtained in the scattered electron (SE) mode and back-scattered electron (BSE) mode of the resulted powder for a better contrast are presented in Fig. 2.

As seen, glass powder after crushing consists of the coarse particles with the sizes up to ~ 200 μm. However, due to the fragility of glass, individual particles of 10-20 μm are also present in the powder (see Fig. 2(b)). The BSE mode allows better phase contrast. The typical particles are non-porous with the glassy-like fracture surface. The use of the MBB powder as a binder requires additional milling in a planetary mill. According to the EDS spectra obtained for the glass powder, the chemical composition of obtained glass corresponds to the MgO:BaO = 1.28 and differs from the initial mixture. Surely, long-term annealing is accompanied by the change of the glass binder composition due to intensive $Ba(BO_2)_2$ evaporation, more heat resistive composition enriched by MgO is formed.

However, estimates of the composition changes according to [36] indicate the minor effect of low-volatile components evaporation in the discussed case.

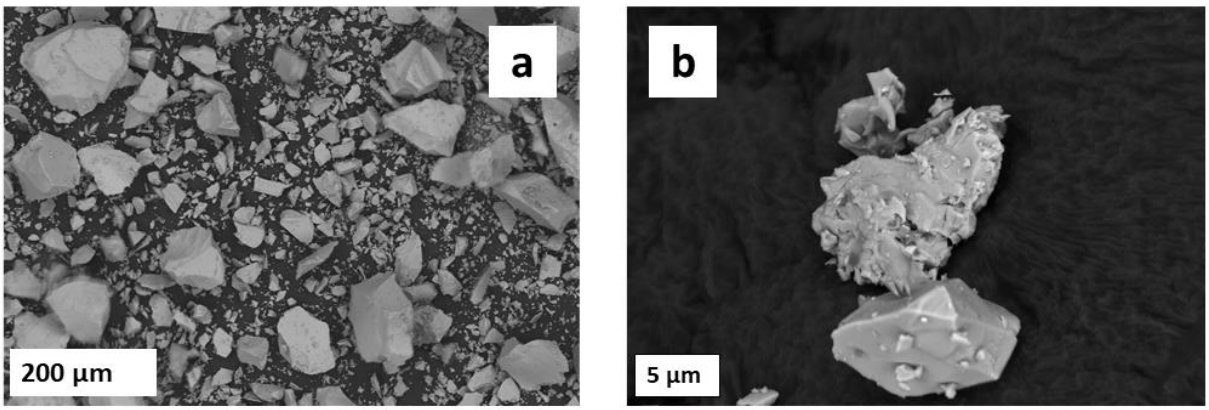

Fig. 2. HR-SEM photos of powdered Co-MBB glass: (a) SE mode, magnification×200, (b) magnification × 5000

YSZ ceramics manufacturing

YSZ and Co-MBB glass powders taken in a ratio of 95 and 4 wt. %, respectively, were mixed in Pulverisette 6 planetary ball mill (250 rpm for 1 hour), placed in a steel press form (∅ 50 mm, height ~ 15 mm) and subjected to isostatic cold pressuring (15 tons/cm^2 for 20 min). Resulting disks were loaded on a corundum wafer and annealed at 1500 °C for 2 hours. After cooling to room temperature, specimens for bending strength tests (4 × 5 × 45 mm beams) were cut using Isomet 4000 precision saw. The final specimen preparation step was the final material hardening by annealing at 1400 °C for 2 hours.

Structure measurements

The phase composition of powders and ceramics after the synthesis and consolidation was investigated by X-Ray diffraction analysis (XRD). The XRD patterns were registered using SHIMADZU XRD-6000 (CuK_α=1.54 Å, 2Θ=10-80º, scan speed 0.02º/min), reflexes identification was carried out using PDF-2 database (release 2021). Microstructures and the chemical compositions of glass binder powder and polished ceramics were analyzed using high resolution scanning electron microscopy (HR-SEM, Zeiss Merlin, accelerating voltage 20 eV, equipped by a console for Energy-dispersive X-ray spectroscopy, EDS). Fracture surfaces of the ceramic samples after the bending tests were also analyzed in HR-SEM (Zeiss Merlin, accelerating voltage 20 eV). Apparent density of YSZ ceramics and ceramics after the mechanical tests at 19 and 1127 °C was measured by hydrostatic weighting technique (scales RADWAG 220 c/xc, Poland). Each sample was measured in the air and then in octane. The results were averaged for 3 parallel measurements of each sample. The theoretical density of material was calculated using the rule of mixtures. The theoretical density of the cubic YSZ ceramics was taken from crystallography data to be 5.96 g/cm^3 [37] and MBBO density to be 3.67 g/cm^3 [35].

In-situ 3-point bending strength measurements at high temperatures

In-situ estimation of 3-point bending strength at high temperatures was carried out as follows. We used a laboratory homemade setup based on the principles recommended by ISO 5014:1997 (Dense and insulating shaped refractory products, Determination of modulus of rupture at ambient temperature). The recommended 3-point scheme (supports – fused silicon carbide, load – tantalum rod) was realized inside the induction heated graphite cylinder, the temperature was measured by WR5-WR20 thermocouple placed directly on one of the supports, the measurement accuracy was ± 2 °C. The applied load was measured using Megeon 4500 dynamometer placed in a cold zone, the measurement accuracy was ± 1 %. Note that the working volume of the measuring cell during the high temperature measurements was filled by an inert gas (Ar, 99.99 wt. %) to prevent the graphite cylinder and metallic pieces of the measuring cell (Ta, Mo) oxidation. The data was averaged for 5 samples.

Results and Discussion

Typical XRD patterns for the ceramics after sintering at 1500 °C for 2 hours and after the bending strength tests at 1100°C are presented in Fig. 3.

As seen from Fig. 3, YSZ ceramics after sintering corresponds to the high crystalline single phase cubic solid solution with no admixtures of the other phases. All reflexes in the XRD pattern corresponds to cubic fluorite-like structure (space group $Fm\bar{3}m$, point group 225).

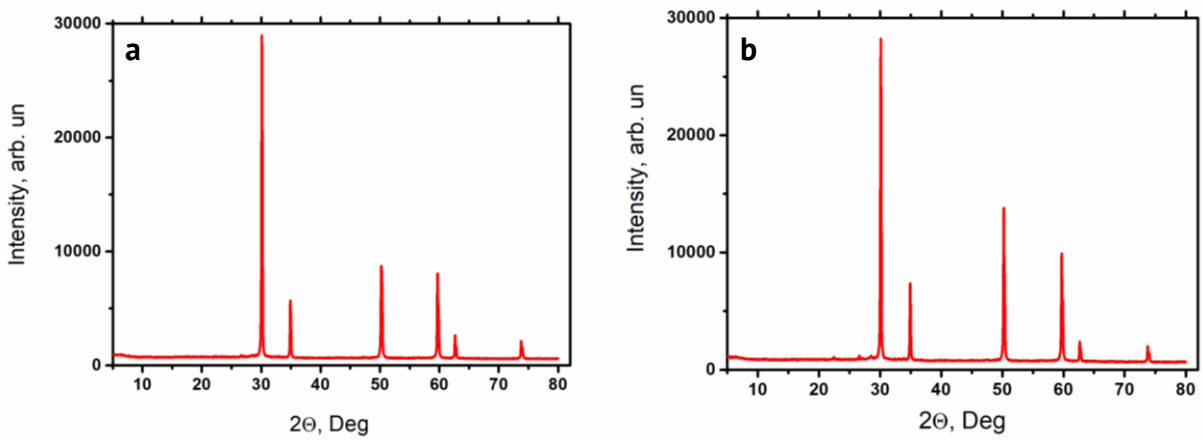

Fig. 3. XRD patterns obtained for the ceramics after sintering (a)and after bending strength tests at 1115 °C (b)

The microstructure of ceramics after sintering with Co-MMB glass binder and EDS elemental maps of Zr, Mg, Ba and O are presented in Fig. 4. Overall structure of ceramics contains some voids and pores, it is in accordance with the relative density of ceramics after sintering, being of 81.80 ± 0.11 %. The structure of the ceramics consists of well-defined grains with the typical sizes from 10 to 40 μm divided by rather thick grain boundaries (see Fig. 4(a)). Under higher magnification using the BSE mode for better phase contrast, one can see that a typical grain boundary is filled up by a transparent glassy phase. (see Fig. 4(b)). The ceramic grains are bonded together with the glassy wires.

The EDS mapping taken from the polished surface of ceramics (Figs. 4(b,c,f)) shows that zirconium is located only in the ceramics grains, whereas oxygen element is spread

between grains and grain boundaries and concentrated in the grain boundaries. Such elements as Mg and Ba are also located in grain boundaries only, corresponding to the Co-MBB glass (Figs. 4(b,c,f)). It should be noted that B is too light element to be detected by EDS, while the Co contents is too low to be detected.

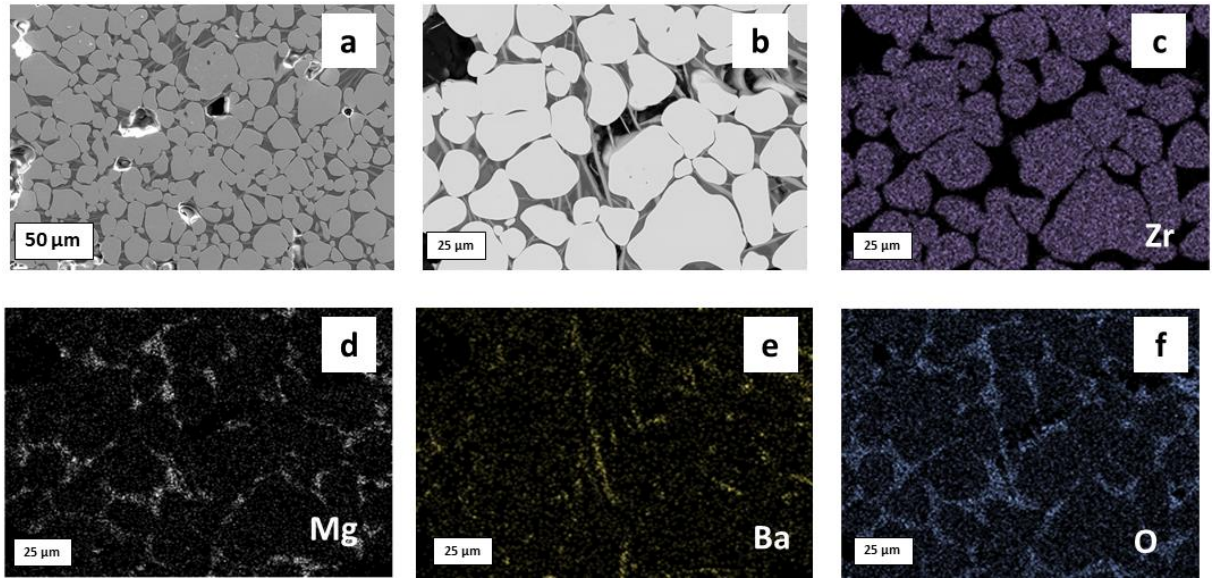

Fig. 4. HR-SEM images of (a) and (b) ceramics after sintering with Co-MMB glass binder, (c) EDS map of Zr, (d) EDS map of Mg, (e) EDS map of Ba, and (f) EDS map of O taken from HR-SEM image

Figure 5 presents the results of the bending stress tests, the temperature scheme of the test was as follows. First, reference values were obtained at room temperature (25 °C), they were compared with the data at 1000 °C. Measurements at intermediate temperatures (600 and 800 °C) provide an opportunity to understand the type of the bending strength vs temperature dependence. At the final step, the temperature was increased up to the value of the specimen break under the weight of the dynamometer without any additional load application.

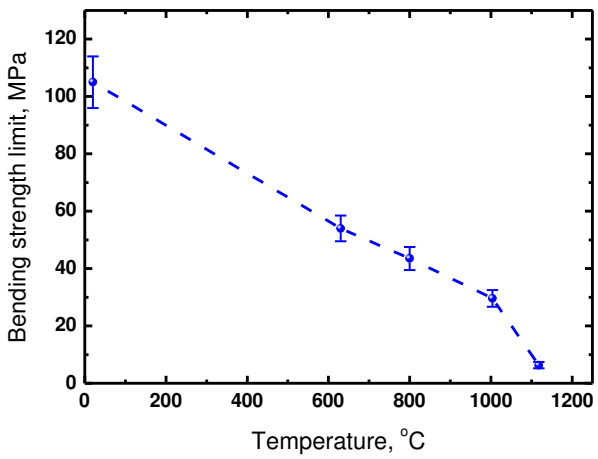

Fig. 5. Temperature dependence of the bending strength of YSZ ceramics with Co-MBB binder

As seen from the figure, the initial ultimate bending strength of the YSZ specimens studied (> 100 MPa) is typical for cubic yttria stabilized zirconia ceramics [6,38]. The evident decrease (~ 3 times) in the bending strength limit value is seen for the temperature of 1000 °C. Accounting for the data taken in the intermediate points, one could assume the linear character of the dependence. The break of the specimens under the dynamometer weight without any additional load application occurred at temperatures ~ 1115 °C.

A set of experiments was carried out to understand the above material behavior. First, the phase composition of the specimen after bending tests at high temperature was studied by XRD (Fig. 3(b)). The results, presented in Fig. 3(b), demonstrate the constancy of the YSZ matrix phase composition: the position of the reflexes obtained for the initial specimen (Fig. 3(a)) are the same as those for specimen tested at 1115 °C (Fig. 3(b)). In-situ bending test induces a slight change of the intensity of the reflexes at 2Θ = 51 and 59° in the XRD pattern for ceramics. That is likely due to the texturing of ceramics exposed to in situ 3-point bending test at high temperature.HR-SEM and fractography analysis were performed to understand the state of the glass binder phase and to characterize the nature of the specimens fracture (see Fig. 6).

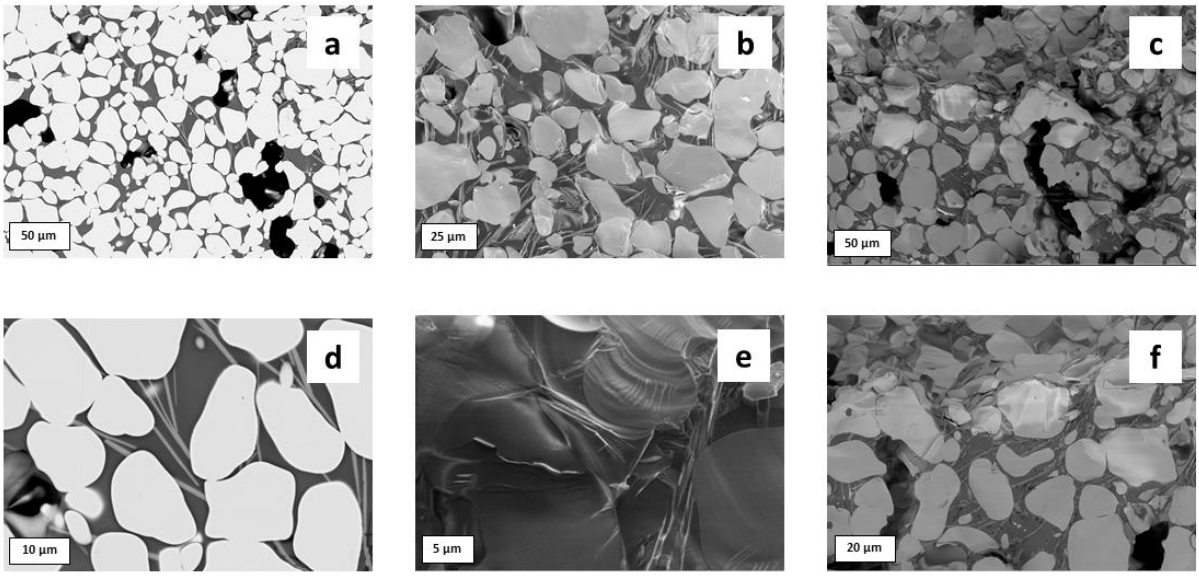

Fig. 6. HR-SEM images of (a) and (d) polished cross-section of ceramics with Co-MMB glass binder after fracture at 1115 °C in BSE mode; (b) and (e)cleavage surfaces for ceramics after mechanical tests at room temperature, SE mode (c) and (f) cleavage surfaces for ceramics after mechanical tests at 1115 °C, SE mode

The structure of YSZ ceramics after mechanical tests at 1115 °C remains unchanged (see Fig. 6(a,d)). The relative density of ceramics increases slightly up to 86.10 ± 0.07 %. The results of the fractography tests are of particular interest. Analyzing the above data, one can consider that the specimen's breakage is related to the Co-MBB glass binder state. Indeed, all cleavage surfaces are characterized by the glass binder presence and drastically differ from those typically observed for YSZ ceramics. An amorphous fracture is observed both at room and at high temperature. Upon the temperature increase, glass binder plays a key role in the bending strength decrease. Glass softening induces twice decrease in bending strength at 600 °C and its melting cause the bending strength values

drop almost to zero at 1115 °C. Indeed, according to the data on MgO-BaO-B_2O_3 phase diagram [23], the melting temperature for the compositions similar to MBB glass composition should be ~ 1170-1200 °C, similar value can be expected for the Co-MBB glass due to small amount of the cobalt oxide additive. It is worth noticing that amorphous fracture also takes place for ceramic grain. It may indicate that longer sintering time is necessary to achieve better formed structure.

In summary, the use of novel Co-MBB glass based inorganic binder is with no doubts prospective since it would allow increasing the temperature range of exploitation of the additively manufactured YSZ ceramics compared to the existing data on organic binder used for zirconia ceramics production via AM. The results obtained can be concerned asa basis for further comprehensive research including the optimization of the annealing and quenching temperatures and duration to eliminate binder predomination in the fracture; determination of the CTE of Co-MBB glass, manufacturing of YSZ ceramics via SLS and the detailed study of the structures and mechanical characteristics of such ceramics.

Conclusions

Using XRD it was shown that YSZ ceramics with the glass binder corresponds to a single phased cubic fluorite-like zirconia solid solution. Using HR-SEM and EDS mapping it was confirmed that the structure of ceramics consists of micron-sized grains separated by the thick grain boundaries filled up with the glassy binder. The relative density of ceramics increases from 81.80 ± 0.11 to 86.10 ± 0.07 % upon the testing temperature increase from room to 1115 °C with no change in the phase composition of ceramics. In-situ 3-point bending strength showed that the temperature increase induces the linear decrease of bending strength value from 104 ± 10 to 31 ± 3 MPa. Fractography tests revealed that amorphous fracture takes place at all temperature range studied, and the glass binder plays predominant role in the mechanical behavior of ceramics.

References

1. Carrette L, Friedrich KA, Stimming U. Fuel Cells: Principles, Types, Fuels, and Applications. *Chem Phys Chem*. 2000;1(4): 162–193.
2. Mahato N, Banerjee A, Gupta A, Omar Sh, Balani K. Progress in Material Selection for Solid Oxide Fuel Cell Technology: a Review. *Prog. Mater. Sci*. 2015;72: 141–337.
3. Kim J, Kim J, Yoon KJ, Son JW, Lee JH, Lee JH, Lee HW. Solid Oxide Fuel Cells with Zirconia/Ceria Bilayer Electrolytes via Roll Calendering Process. *J. Alloys Compd*. 2020;846: 156318.
4. Pesce A, Hornés A, Núñez M, Morata A, Torrella A, Tarancón A. 3D Printing the Next Generation of Enhanced Solid Oxide Fuel and Electrolysis Cells. *J. Mater. Chem. A*. 2020;8: 16926–16932.
5. Minh N.Q. Ceramic Fuel Cells. *J. Amer. Ceram. Soc*. 1993;76(3): 563–588.
6. Terauchi S, Takizawa H, Endo T, Uchida S, Terui T, Shimada M. High Ionic Conductivity and High Fracture Strength of Cubic Zirconia, (Y0.16 – xScx)Zr0.84O1.92,/Alumina Composites. *Mater. Lett*. 1995;23(4–6): 273–275.
7. Kurapova OYu, Pivovarov MM, Nikiforova KV, Konakov VG. Sensor Properties of Stabilized Zirconia Ceramics, Manufactured from Nanopowders. *Rev. Adv. Mater. Sci*. 2018;57(2): 257–261.
8. Sikarwar S, Yadav BC, Singh S, Dzhardimalieva GI, Pomogailo SI, Golubeva ND, Pomogailo AD. Fabrication of Nanostructured Yttria Stabilized Zirconia Multilayered Films and their Optical Humidity Sensing Capabilities Based on Transmission. *Sens Actuators B Chem*. 2016;232: 283–291.
9. Roitero E, Reveron H, Gremillard L, Garnier V, Ritzberger C, Chevalier J. Ultra-Fine Yttria-Stabilized Zirconia for Dental Applications: A Step Forward in the Quest Towards Strong, Translucent and Aging Resistant Dental Restorations. *J Eur Ceram Soc*. 2023;43(7): 2852–2863.

10. Khajavi P, Xu Y, Frandsen HL, Chevalier J, Gremillard R, Kiebach R, Hendriksen PV. Tetragonal Phase Stability Maps of Ceria-Yttria Co-Doped Zirconia: From Powders to Sintered Ceramics. *Ceram Int.* 2020;46(7): 9396–9405.
11. Pakseresht A, Sharifianjazi F, Esmaeilkhanian A, Bazli L, Nafchi MR, Bazli M, Kirubaharan K. Failure Mechanisms and Structure Tailoring of YSZ and New Candidates for Thermal Barrier Coatings: A Systematic Review. *Mater Des.* 2022;222: 111044.
12. Fournier S, Chevalier J, Baeza GP, Chaput Ch, Louradour E, Sainsot Ph, Cavoret J, Reveron H. Ceria-Stabilized Zirconia-Based Composites Printed by Stereolithography: Impact of the Processing Method on the Ductile Behaviour and its Transformation Features. *J Eur Ceram Soc.* 2023;43(7): 2894–2906.
13. Chevalier J, Loh J, Gremillard L, Meille S, Adolfson E. Low-Temperature Degradation in Zirconia with a Porous Surface. *Acta Biomater.* 2011;7(7): 2986–2993.
14. Chevalier J. What Future for Zirconia as a Biomaterial? *Biomaterials.* 2006;27(4): 535–543.
15. Chevalier J, Gremillard L, Virkar AV, Clarke DR. The Tetragonal-Monoclinic Transformation in Zirconia: Lessons Learned and Future Trends. *J. Amer. Ceram. Soc.* 2009;92(9): 1901–1920.
16. Zhou J, Zhang J, Zhong Z. Mechanical Properties of Yttria-Stabilized Zirconia: A Study by ReaxFF Molecular Dynamics Simulations. *Mechanics of Materials*. 2020;149: 103542.
17. Cousland GP, Cui XY, Smith AE, Stampfl APJ, Stampfl CM. Mechanical Properties of Zirconia, Doped and Undoped Yttria-Stabilized Cubic Zirconia from First-Principles. *J. Phys. Chem. Solids*. 2018;122: 51–71.
18. Fregeac A, Ansart F, Selezneff S, Estournès C. Relationship Between Mechanical Properties and Microstructure of Yttria Stabilized Zirconia Ceramics Densified by Spark Plasma Sintering. *Ceram Int.* 2019;45(17): 23740–23749.
19. Giraud S, Canel J. Young's Modulus of Some SOFCs Materials as a Function of Temperature. *J. Eur. Ceram. Soc.* 2008;28(1): 77–83.
20. Kushi T, Sato K, Unemoto A, Hashimoto Sh, Amezawa K, Kawada T. Elastic Modulus and Internal Friction of SOFC Electrolytes at High Temperatures under Controlled Atmospheres. *J. Power Sources*. 2011;196(19): 7989–7993.
21. Kulyk V, Duriagina Z, Kostryzhev A, Vasyliv B, Vavrukh V, Marenych O. The Effect of Yttria Content on Microstructure, Strength, and Fracture Behavior of Yttria-Stabilized Zirconia. *Materials.* 2022; 15(15): 5212.
22. Ren X, Pan W. Mechanical Properties of High-Temperature-Degraded Yttria-Stabilized Zirconia. *Acta Mater.* 2014;69: 397–406.
23. Jang BK, Lee JH, Fisher CAJ. Mechanical Properties and Phase-Transformation Behavior of Carbon Nanotube-Reinforced Yttria-Stabilized Zirconia Composites. *Ceram. Int.* 2021;47(24): 35287–35293.
24. Zhang J. Thermal Cycling Effect on Mechanical Properties of Yttria-Stabilized Tetragonal Zirconia. *Key Eng Mater.* 2013;538: 121–124.
25. Zhang X, Wu X, Shi J. Additive Manufacturing of Zirconia Ceramics: a State-of-the-Art Review. *J Mat. Res. Tech.* 2020;9(4): 9029–9048.
26. Golubev SN, Kurapova OYu, Archakov IYu, Konakov VG. Characterization of a High Temperature Ceramics Produced via Two-Step Additive Manufacturing. *Open Ceramics*. 2021;7: 100165.
27. Wang L, Yu H, Hao Z, Tang W, Dou R. Investigating the Effect of Solid Loading on Microstructure, Mechanical Properties, and Translucency of Highly Translucent Zirconia Ceramics Prepared via Stereolithography-Based Additive Manufacturing. *J. Mech. Behav. Biomed. Mater*. 2023;144: 105952.
28. Shao H, Zhao D, Lin T, He J, Wu J. 3D Gel-Printing of Zirconia Ceramic Parts. *Ceram Int.* 2017;43(16): 13938–13942.
29. Kuscer D, Stavber G., Trefalt G, Kosec M. Formulation of an Aqueous Titania Suspension and its Patterning with Ink-Jet Printing Technology. *J. Amer. Ceram. Soc.* 2012;95(2): 487–493.
30. Huang S, Huang S, Ye Ch, Zhao H, Fan Z, Wei Q. Binder Jetting Yttria Stabilized Zirconia Ceramic with Inorganic Colloid as a Binder. *Advances in Applied Ceramics*. 2019;118(8): 458–465.
31. Özkol E. Rheological Characterization of Aqueous 3Y-TZP Inks Optimized for Direct Thermal Ink-Jet Printing of Ceramic Components. *J Amer Ceram Soc.* 2013;96(4): 1124–1130.
32. Hayashi H, Saitou T, Maruyama N, Inaba H, Kawamura K, Mori M. Thermal Expansion Coefficient of Yttria Stabilized Zirconia for Various Yttria Contents. *Solid State Ion.* 2005;176(5–6): 613–619.
33. Kurapova OY, Glumov OV, Lomakin IV, Golubev SN, Pivovarov MM, Krivolapova JV, Konakov VG. Microstructure, Conductivity and Mechanical Properties of Calcia Stabilized Zirconia Ceramics Obtained from Nanosized Precursor and Reduced Graphene Oxide Doped Precursor Powders. *Ceram. Int.* 2018;44(13): 15464–15471.
34. Kurapova OY, Konakov VG. Phase Evolution in Zirconia Based Systems. *Rev. Adv. Mater. Sci.* 2014;36(2): 177–190.
35. Fomenko G, Nosenko A, Goleus V, Ilchenko N, Amelina A. Glass Formation and Properties of Glasses in Mgo-Bao-B_2O_3 System. *Chemistry & Chemical Technology*. 2015;9(4): 463-466.
36. Archakov IYu. *Evaporation of Borosilicate Glasses. PhD Thesis.* Institute for Silicate Chemistry RAS; 1993. (In Russian)

37. Glukharev A, Glumov O, Temnikova M, Shamshirgar AS, Kurapova O, Hussainova I, Konakov V. YSZ-rGO Composite Ceramics by Spark Plasma Sintering: The Relation Between Thermal Evolution of Conductivity, Microstructure and Phase Stability. *Electrochim. Acta*. 2021;367: 137533.
38. Abraham I, Gritzner G. Mechanical Properties of Doped Cubic Zirconia Ceramics. *J. Mat. Sci Lett*. 1993;12: 995–997.

About Authors

Peter Maniakin
Bachelor Student (Peter the Great St. Petersburg Polytechnic University, St. Petersburg, Russia)

Sergei G. Shalagaev
Engineer (Glass and Ceramics, LTD, St. Petersburg, Russia)

Ivan Yu. Archakov Sc
Candidatre of Chemical Sciences
Senior Reseahcer (Institute for Problems of Mechanical Engineering RAS, St. Petersburg, Russia)

Yaroslav V. Konakov Sc
Junior Reseahcer (Peter the Great St. Petersburg Polytechnic University, St. Petersburg, Russia),
Researcher (Institute for Problems in Mechanical Engineering RAS, St. Petersburg, Russia)

Olga Yu. Kurapova Sc
Candidatre of Chemical Sciences
Associate Professor (St. Petersburg State University, St. Petersburg, Russia),
Senior Researcher (Institute for Problems in Mechanical Engineering RAS, St. Petersburg, Russia)

Vladimir G. Konakov Sc
Doctor of Chemical Sciences
Professor (Peter the Great St. Petersburg Polytechnic University, St. Petersburg, Russia),
General Director (Glass and Ceramics, LTD, St. Petersburg, Russia),
Senior Researcher (Institute for Problems in Mechanical Engineering RAS, St. Petersburg, Russia)

MATERIALS PHYSICS AND MECHANICS RESEACH ARTICLE

Submitted: February 16, 2023 Revised: February 29, 2023 Accepted: March 23, 2024

Effect of femtosecond irradiation on the luminescence of $CsPbI_3$ perovskite crystals in borogermanate glass

A.L. Losin, A.N. Babkina ✉, R.D. Kharisova, K.S. Zyryanova, A.D. Dolgopolov, M.M. Sergeev,

ITMO University, St. Petersburg, Russia

✉ babkina.anastasya@bk.ru

ABSTRACT

The article demonstrates femtosecond-laser-induced crystallization of CsPbI3 perovskite nanocrystals in borogermanate glass with no additional heat treatment. With an increase in the laser radiation power, the mean size of the precipitated crystals increases, which leads to the luminescence redshift from 660 up to 700 nm and its width decrease from 60 down to 35 nm. An increase in the mean size of CsPbI3 nanocrystals is also accompanied by an increase in the size of the laser exposure modified region. The appearance of CsPbI3 after irradiation with without additional heat treatment indicates the prospects for using this material for the repeated optical information recording.

KEYWORDS

cesium lead iodide perovskite • borogermanate glass • femtosecond irradiation • laser-induced crystallization

Acknowledgements. *This research was supported by Russian Science Foundation (Agreement #19-72-10036).*

Citation: A.L. Losin, A.N. Babkina, R.D. Kharisova, K.S. Zyryanova, A.D. Dolgopolov, M.M. Sergeev. Effect of femtosecond irradiation on the luminescence of CsPbI3 perovskite crystals in borogermanate glass. *Materials Physics and Mechanics*. 2024;52(2): 57–62.
http://dx.doi.org/10.18149/MPM.5222024_7

Introduction

Cesium lead halide ($CsPbX_3$) quantum dots (QDs) have attracted big attention because of their remarkable optical properties, such as size-dependent emission wavelengths, narrow emission spectra and high photoluminescence quantum yields [1–5]. They possess great potential applications in light-emitting diodes, lasers, solar cells and photodetectors. The propensity of lead-cesium halide nanocrystals to atmospheric air oxidation and low-temperature phase transitions led to the idea of their stabilization in a polymer [6–8] or glassy matrix [9–12]. Traditionally for glass-ceramics, isothermal heat treatment at temperatures exceeding glass transition temperature is a favorable way to realize controllable nucleation and volume nanocrystal growth in glass greed. This is the way when the optical properties of QDs can be guaranteed for a long-term period. On the other hand, femtosecond laser [13,14], due to its short pulse width and high peak power, can induce high transient temperature field, which is enough for the nuclei formation of QDs. Nonlinear absorption process happens while the fs laser interacts with the glass matrix, leading to the destruction of the glass network and the redistribution of atoms at the laser focal area, which is beneficial for ion migration to form nanocrystals and for the reduction in crystallization temperature. A promising application of laser crystallization of a glass matrix is the optical recording and storage of information with the spatial selectivity up to nanoscale [15–17]. However, in most studies [13,14], to obtain perovskite nanocrystals in a glass matrix after femtosecond irradiation, it is necessary to carry

out additional heat treatment, which makes this method unsuitable for single-stage information recording.

Here, the luminescent properties of $CsPbI_3$ nanocrystals, obtained by laser-induced crystallization in borogermanate glass, are demonstrated.

Materials and Methods

The initial glass matrix had the following composition: 6.67 ZnO-5.81 Na_2O-31.3 B_2O_3-50.53 GeO_2 mol. %. The synthesis was carried out in air atmosphere at a temperature of 950 °C for 30 min using closed quartz crucibles [18,19]. For the subsequent nucleation of $CsPbI_3$ perovskite nanocrystals, $CsCO_3$, PbO and KI were added to the batch composition. The luminescence spectra were studied with a Renishaw inVia Raman Microscope of 100–7000 cm^{-1} working range at room temperature with the excitation wavelengths of 633 and 514 nm and 20× build-in lens. Laser-driven crystallization was obtained by ANTAUS femtosecond laser (AVESTA, operating wavelength of 1030 nm, pulse duration of 224 fs, pulse repetition rate of 50 and 100 kHz, pulse energy from 0.58 to 2.57 uJ, the pulse quantity in the irradiated region from 500 to 500,000). The laser beam was focused by the microscope objective lens with an N.A. of 0.4.

Results and Discussion

Insert in Fig. 1 shows photograph of the patterns obtained by femtosecond laser irradiation of glasses under study, whose ring-shaped prints are quite characteristic [20,21]. An optical breakdown zone is observed in the center of the ring: in the region of the laser beam waist, nonlinear multiphoton absorption occurred, due to which the local volume of glass was intensely heated, and thus expanded, creating stresses and leading to the destruction of the material [20]. The dark region, the size of which is designated as *d*, determines the temperature zone within which color centers were formed in the glass matrix due to the breaking of O-Ge-O bonds [22]. Due to the high contrast of this area with the neighboring one, using a Carl Zeiss microscope and built-in software, we determined the size *d*. Based on this size, we calculated the area of the modification zone *S* (Fig. 1), taking it to be ideally spherical as a first approximation. Further studies of the luminescent properties showed that $CsPbI_3$ nanocrystals were formed at the edges of this region. The largest light modified area indicated a change in the density and refractive index of the material without the formation of nanocrystals. Figure 1 shows the dependence of the modified area *S*, within which the nanocrystals were formed, on the number of pulses at different pulse energies E_p. When the number of pulses was less than 50,000, the modified area increased significantly; with a further increase in the number of pulses up to 500,000, the modified area increased only twofold. If we trace the dependence of the modified area on the pulse energy, it will be close to a linear function, in which the proportionality coefficient will depend on the exposure time (that is, the number of pulses).

The initial glass did not possess luminescence but contained all the components necessary for the formation of $CsPbI_3$ crystals. After femtosecond irradiation along the inner edge of the dark modified region, the size of which is shown in Fig. 1, red luminescence was detected. Figure 2 shows the luminescence spectra obtained after different laser exposure time (a) and with different pulse energy (b). Luminescence spectra were recorded under 514 nm laser excitation through the optical system of a microscope with a lens ×50. The luminescence maximum located in the region of 660–695 nm and the FWHM varied within 35-60 nm, which is typical for $CsPbI_3$ perovskite nanocrystals in glass [23,24]. As the pulse energy and their

number decreased, the luminescence spectrum shifted towards short wavelengths and widens. The luminescence intensity increased with increasing exposure time and pulse energy, however, since the optical design of the microscope is not intended for absolute measurement of intensity, but only relative, all spectra in Fig. 2 are shown normalized.

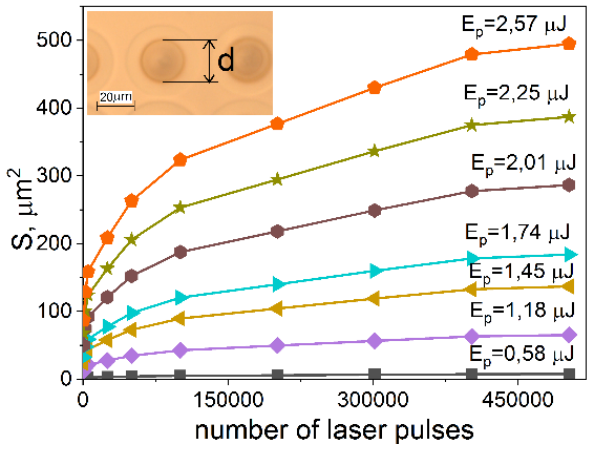

Fig. 1. The area of the modified region with nucleated $CsPbI_3$ QDs (*S*) vs. number of fs laser pulses at different pulse energy E_p; the insert: determining the size d of the modified area

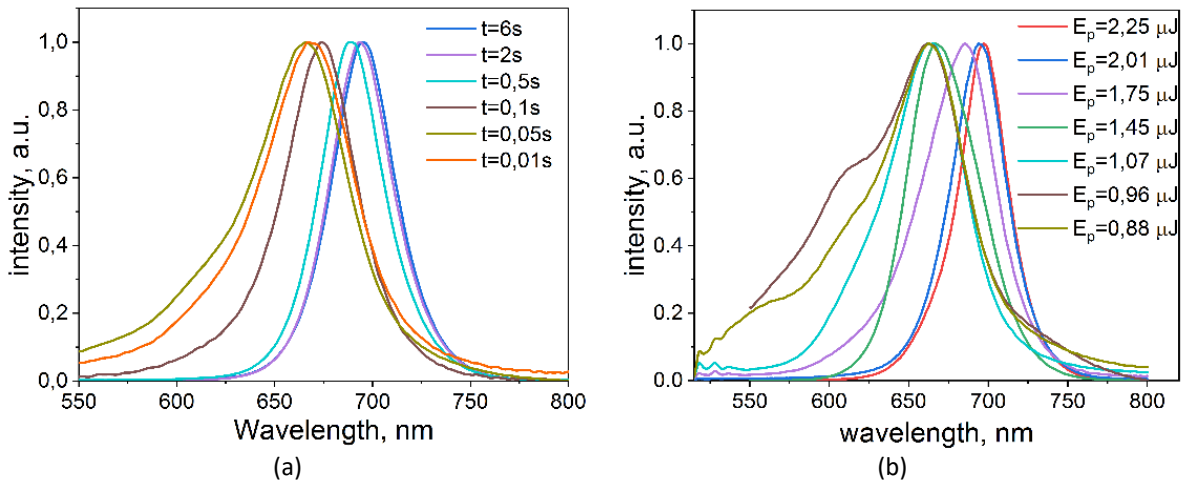

Fig. 2. Luminescence spectra of $CsPbI_3$ QDs in borogermanate glass obtained after fs laser exposure with different duration at E_p=2.57 μJ (a), and at different pulse energy for duration of 10 s (b)

While using the maximum pulse energy (Fig. 2(a)), during the exposure time decrease from 10 to 0.01 seconds, the luminescence band maximum shifted from 695 to 666 nm, and the luminescence FWHM increased from 37 to 59 nm. Such transformations of the luminescence spectrum of semiconductor crystals indicate the presence of a size effect: with an increase in the mean size of QDs, the luminescence spectrum shifted to long wavelengths and vice versa [25–27]. The peculiarity of the crystal nucleation in glass meant that with a decrease in the mean size of crystals' ensemble, its size dispersion broadened, along with which the luminescence band width increased [25]. This means that with an increase in the laser exposure energy, the mean size of the crystals increased. For the shortest exposure time, the second luminescence band appeared near 610 nm. Figure 3 shows that the main changes in the luminescence spectrum occurred in the pulse number range up to 50,000, as in the case

of the modified area in Fig. 1. When the number of pulses was exceeded, the FWHM and the luminescence maximum location remained practically unchanged.

When the pulse energy changes (Fig. 2(b)), the transformation of the luminescence spectrum turned out to be more complicated. Quantitative changes (of location and FWHM) had the same range as in the first case. However, when small pulse energies were used, additional bands clearly appeared in the luminescence spectrum: at 610 and 560 nm. Their appearance may indicate that, in this case, the total radiation energy transferred to the material was insufficient for the formation of large crystals; therefore, instead of them, small crystals and clusters were formed in the glass structure, which can play a role of the nuclei of the crystalline phase [25–27] and can have luminescence in shorter wavelengths, but with bigger FWHM.

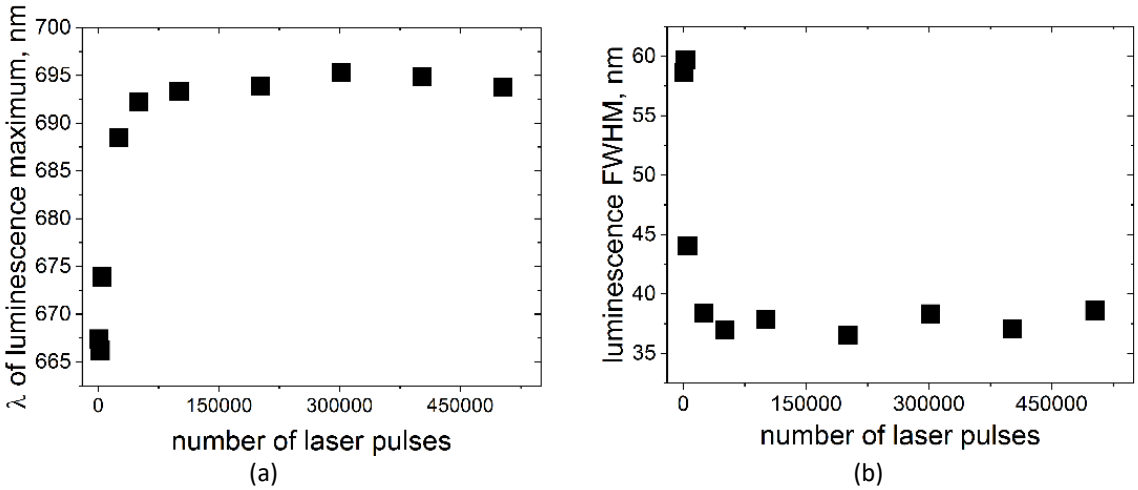

Fig. 3. Dependence of the maximum location (*a*) and FWHM (*b*) of $CsPbI_3$ QDs' luminescence on the number of fs laser pulses (E_p=2.57 μJ)

An increase in laser exposure energy led to an increase in the size of the glass modified zone and the volume of the material, from which diffusion of cesium, lead, and iodine ions occurred for the subsequent formation of crystals during the cooling after laser exposure. It has been shown [28–30] that perovskite crystals precipitated only during the femtosecond laser exposure and the subsequent heat treatment of glass. This was since, during laser irradiation, perovskite crystals were formed in the glass matrix; however, a large number of defects in them led to nonradiative transfer of excitation and hence luminescence quenching. Subsequent heat treatment led to the relaxation of defects, the reduction of the nonradiative channel, and the appearance of luminescence of perovskite crystals. In our case, luminescence of perovskite $CsPbI_3$ nanocrystals was observed immediately after laser exposure, which is more promising for repeated recording and storage of information in glass using principles of local crystallization.

Conclusions

Femtosecond-laser-induced crystallization of $CsPbI_3$ perovskite nanocrystals in borogermanate glass with no additional heat treatment was demonstrated. With an increase in the laser radiation energy, the mean size of the precipitated crystals increased, which led to the luminescence redshift from 660 up to 700 nm and FWHM decrease from 60 down to 35 nm. The absence of subsequent heat treatment to obtain the luminescence of crystals was promising for the development of materials for repeated optical recording of information.

References

1. Protesescu L, Yakunin S, Bodnarchuk MI, Krieg F, Caputo R, Hendon CH, Yang RX, Walsh A, Kovalenko MV. Nanocrystals of Cesium Lead Halide Perovskites (CsPbX3, X = Cl, Br, and I). *Nano Lett*. 2015;15(6): 3692–3696.
2. Kovalenko MV, Protesescu L, Bodnarchuk MI. Properties and potential optoelectronic applications of lead halide perovskite nanocrystals. *Science*. 2017;358(6364): 745–750.
3. Li X, Cao F, Yu D, Chen J, Sun Z, Shen Y, Zhu Y, Wang L, Wei Y, Wu Y, Zeng H. All Inorganic Halide Perovskites Nanosystem: Synthesis, Structural Features, Optical Properties and Optoelectronic Applications. *Small*. 2017;13(9): 1603996.
4. Swarnkar A, Marshall AR, Sanehira EM, Chernomordik BD, Moore DT, Christians JA, Chakrabarti T, Luther JM. Quantum dot–induced phase stabilization of alpha-CsPbI3 perovskite for high-efficiency photovoltaics. *Science*. 2016;354(6308): 92–95.
5. Eperon GE, Paternò GM, Sutton RJ, Zampetti A, Haghighirad AA, Cacialli F, Snaith HJ. Inorganic caesium lead iodide perovskite solar cells. *J. Mater. Chem. A*. 2015;3(39): 19688–19695.
6. Xuan T, Xie RJ. Recent processes on light-emitting lead-free metal halide perovskites. *Chem. Eng. J.* 2020;393: 124757.
7. Lin YH, Qiu ZH, Wang SH, Zhang XH, Wu SF. All-inorganic RbxCs1-xPbBrI2 perovskite nanocrystals with wavelength-tunable properties for red light-emitting. *Inorg. Chem. Commun*. 2019;103: 47–52.
8. Pathak S, Sakai N, Wisnivesky Rocca Rivarola F, Stranks SD, Liu J, Eperon GE, Ducati C, Wojciechowski K, Griffiths JT, Haghighirad AA, Pellaroque A, Friend RH, Snaith HJ. Perovskite Crystals for Tunable White Light Emission. *Chem. Mater*. 2015;27(23): 8066–8075.
9. Ai B, Liu C, Wang J, Xie J, Han J, Zhao X. Precipitation and Optical Properties of CsPbBr3 Quantum Dots in Phosphate Glasses. *J. Am. Ceram. Soc*. 2016;99(9): 2875–2877.
10. Yuan S, Chen D, Li X, Zhong J, Xu X. In Situ Crystallization Synthesis of CsPbBr3 Perovskite Quantum Dot-Embedded Glasses with Improved Stability for Solid-State Lighting and Random Upconverted Lasing. *ACS Appl. Mater. Interfaces*. 2018;10(22): 18918–18926.
11. Lin M, Zhang X, Guo L, Zhang Y, Song R, Xu S, Xu S, Zhu H, Cheng C, Cao Y, Wang Y, Chen B. Blue and green light exciton emission of chloro-brominated perovskite quantum dots glasses. *Opt. Mater*. 2021;122(PB): 111654.
12. Li S, Nie L, Ma S, Yao G, Zeng F, Wang XY, Sun C, Hu G, Su Z. Environmentally friendly CsPbBr3 QDs multicomponent glass with super-stability for optoelectronic devices and up-converted lasing. *J. Eur. Ceram. Soc*. 2020;40(8): 3270–3278.
13. Sun K, Tan D, Fang X, Xia X, Lin D, Song J, Lin Y, Liu Z, Gu M, Yue Y, Qiu J. Three-dimensional direct lithography of stable perovskite nanocrystals in glass. *Science*. 2022;375(6578): 307–310.
14. Teng Y, Zhou J, Lin G, Luo F, Zhou S, Qiu J. Recent Research Progress on Femtosecond Laser Induced Microstructures in Glasses. *Int. J. Optomechatronics*. 2012;6(2): 179–187.
15. Lipatiev AS, Fedotov SS, Lotarev S V., Lipateva TO, Shakhgildyan GY, Sigaev VN. Single-Pulse Laser-Induced Ag Nanoclustering in Silver-Doped Glass for High-Density 3D-Rewritable Optical Data Storage. *ACS Appl. Nano Mater*. 2022;5(5): 6750–6756.
16. Zhestkij N, Efimova A, Rzhevskiy S, Kenzhebayeva Y, Bachinin S, Gunina E, Sergeev M, Dyachuk V, Milichko VA. Reversible and Irreversible Laser Interference Patterning of MOF Thin Films. *Crystals*. 2022;12(6): 846.
17. Veiko VP, Kudryashov SI, Sergeev MM, Zakoldaev RA, Danilov PA, Ionin AA, Antropova TV, Anfimova IN. Femtosecond laser-induced stress-free ultra-densification inside porous glass. *Laser Phys. Lett*. 2016;13(5): 055901.
18. Shirshnev PS, Spiridonov VA, Panov DI, Shirshneva-Vaschenko EV, Gafarova AR, Eremina RM, Romanov AE, Bougrov VE. The influence of gamma rays radiation on optically induced luminescence of copper-containing potassium-lithium-borate glass. *Materials Physics and Mechanics*. 2019;42(2): 198–203.
19. Shirshnev PS, Snezhnaia ZG, Shirshneva-Vaschenko EV, Romanov AE, Bougrov VE. Relation of the optical properties of boron copper-containing glasses on the concentration of lithium. *Materials Physics and Mechanics*. 2018;40(1): 78–83.
20. Kostyuk GK, Sergeev MM, Yakovlev EB. The processes of modified microareas formation in the bulk of porous glasses by laser radiation. *Laser Phys.* 2015;25(6): 066003.
21. Yu B, Chen B, Yang X, Qiu J, Jiang X, Zhu C, Hirao K. Study of crystal formation in borate, niobate, and titanate glasses irradiated by femtosecond laser pulses. *J. Opt. Soc. Am. B*. 2004;21(1): 83–87.
22. Sigaev VN, Savinkov VI, Lotarev S V., Shakhgildyan GY, Lorenzi R, Paleari A. Spatially selective Au nanoparticle growth in laser-quality glass controlled by UV-induced phosphate-chain cross-linkage. *Nanotechnology*. 2013;24(22): 225302.
23. Ke F, Wang C, Jia C, Wolf NR, Yan J, Niu S, Devereaux TP, Karunadasa HI, Mao WL, Lin Y. Preserving a robust CsPbI3 perovskite phase via pressure-directed octahedral tilt. *Nat. Commun*. 2021;12(1): 461.
24. Sun C, Wang X, Xu Y, Lu W, Teng X, Fu G, Yu W. Physical origins of high photoluminescence quantum yield in α-CsPbI3 nanocrystals and their stability. *Appl. Surf. Sci*. 2020;508: 145188.
25. Ekimov A. Growth and optical properties of semiconductor nanocrystals in a glass matrix. *J. Lumin*. 1996;70(1–6): 1–20.
26. Gurevich S, Ekimov A, Kudryavtsev I, Gandaisb M, Wangb Y. CdS nanocrystal growth in thin silica films : evolution of size distribution function. *J. Cryst. Growth*. 1998;184–185: 360–364.
27. Yamanaka K, Edamatsu K, Itoh T. Quantum-size effects on the exciton states of CuCl nanocrystals. *J. Lumin*. 1998;76–77: 256–259.

28. Huang X, Guo Q, Kang S, Ouyang T, Chen Q, Liu X, Xia Z, Yang Z, Zhang Q, Qiu J, Dong G. Three-Dimensional Laser-Assisted Patterning of Blue-Emissive Metal Halide Perovskite Nanocrystals inside a Glass with Switchable Photoluminescence. *ACS Nano*. 2020;14(3): 3150–3158.
29. Sun K, Li X, Tan D, Jiang H, Xiong K, Zhang J, Xu B, Xiao Z, Li Z, Qiu J. Pure Blue Perovskites Nanocrystals in Glass: Ultrafast Laser Direct Writing and Bandgap Tuning. *Laser Photonics Rev*. 2023;17(5): 2200902.
30. Huang X, Guo Q, Yang D, Xiao X, Liu X, Xia Z, F Fan, Qiu J, Dong G. Reversible 3D laser printing of perovskite quantum dots inside a transparent medium. *Nat. Photonics*. 2020;14(2): 82–88.

About Author

Arthur L. Losin Sc
Master Student (ITMO University, St. Petersburg, Russia)

Anastasiia N. Babkina Sc
Candidate of Physical and Mathematical Sciences
Associate Professor (ITMO University, St. Petersburg, Russia)

Rufina D. Kharisova Sc
PhD Student (ITMO University, St. Petersburg, Russia)

Ksenia S. Zyryanova Sc
Lead Engineer (ITMO University, St. Petersburg, Russia)

Arthur D. Dolgopolov
PhD Student (ITMO University, St. Petersburg, Russia)

Maksim M. Sergeev Sc
Candidate of Physical and Mathematical Sciences
Associate Professor (ITMO University, St. Petersburg, Russia)

MATERIALS PHYSICS AND MECHANICS RESEACH ARTICLE

Submitted: November 27, 2023 Revised: December 13, 2023 Accepted: March 11, 2024

Finite element analysis of elastic properties of metamaterials based on triply periodic minimal surfaces

A.I. Borovkov [1], L.B. Maslov [1,2], M.A. Zhmaylo [1] ✉, F.D. Tarasenko [1], L.S. Nezhinskaya [1],

[1] Peter the Great St. Petersburg Polytechnic University, St. Petersburg, Russia

[2] Ivanovo State Power Engineering University n.a. V.I. Lenin, Ivanovo, Russia

✉ zhmaylo@compmechlab.com

ABSTRACT

The paper considers models of porous structures based on triply periodic minimal surfaces, which are an example of additively produced metamaterials of a new topological class. A numerical technology for the construction of metamaterial periodicity cell based on surface structures is developed, which ensures the periodic boundary conditions fulfilment on finite element meshes. The elastic properties of metamaterials have been calculated by the method of direct numerical homogenization at the periodicity cell meso-level. The dependences of the effective properties on the volume fraction of the metamaterial solid phase are revealed and it is noted that their proper description requires an orthotropic material model. It is shown that the considered types of metamaterials demonstrate strongly nonlinear dependence of elastic properties on the relative density or volume fraction of the solid phase of the metamaterial. The curvature of the curve is more pronounced for values of relative density less than 50 %, which may indicate a pronounced influence of the topological characteristics of the cell on the behaviour of the metamaterial at the meso-level. When analysing the Poisson's ratios, a significant variation in their behaviour for different types of metamaterials is observed. The reason for this phenomenon may be the more pronounced influence of the unit cell topology on the transverse deformations. The consequence of this phenomenon is the apparent existence of stationary points corresponding to the maximum or minimum achievable values of the Poisson's ratio, which can be useful in problems where its value has a significant influence on the global result.

KEYWORDS

metamaterials • porous structures • finite element analysis • homogenization • periodic cell• elastic moduli

Acknowledgements. *This work has been supported by the Russian Science Foundation grant No. 23-19-00882, https://rscf.ru/project/23-19-00882/.*

Citation: Borovkov AI, Maslov LB, Zhmaylo MA, Tarasenko FD, Nezhinskaya LS. Finite element analysis of elastic properties of metamaterials based on triply periodic minimal surfaces. *Materials Physics and Mechanics*. 2024;52(2): 63–81.
http://dx.doi.org/10.18149/MPM.5222024_8

Introduction

The concept of "metamaterials" has emerged relatively recently to denote a new promising class of artificial porous structures that can be produced using additive manufacturing technologies. It can be said that the precursors of modern metamaterials produced on 3D printers using selective laser melting technologies [1] were foamy highly porous polymeric materials of low and ultralow density with random distribution of voids and material in the volume, known since the end of the previous century [2,3].

The characteristic features of modern metamaterials are the possibility of designing structures with specific mechanical [4,5], acoustic [6], electromagnetic [7], poroelastic [8],

biophysical [9,10] and other material properties, which are determined by the type and parameters of the internal structure of a typical repeating unit cell forming the metamaterial. Moreover, by changing the characteristics of the cell, it becomes possible to control the effective physical and mechanical properties of the structure in any spatial direction to create so-called gradient metamaterials [11].

An actual direction of research in the field of mechanics of metamaterials is the study of dependence of macroscopic physical and mechanical properties of a periodic structure of a metamaterial on topological parameters of this structure at the meso-level of the periodicity cell. The main purpose of such studies is to investigate and develop methods of metamaterial design for given operating conditions, as a rule, by varying topological parameters and their distribution in accordance with the obtained dependences. For example, in [12,13], models and samples with a unique combination of parameters and shape of the periodic structure are presented, providing effective mechanical properties close to bone tissue.

If we exclude from consideration porous materials with irregular distribution of pore channels, the existing models of metamaterials as periodic structures can be divided into two main groups differing by the type of characteristic basic elements forming the periodicity cell of the metamaterial. The first group includes metamaterials whose representative volume element, or periodicity cell, is formed from beams or rod elements [14]. Such structures were inspired by the crystal structures of metals and, often, repeat some form of spatial symmetry: volume-centred lattice (VCC), face-centred cubic lattice (FCC), hexagonal closely packed (HCP) and others. The second group includes metamaterials whose periodicity cell is a shell structure and is based on complex curved surfaces of a given thickness [15].

For “beam” metamaterials, the issue of the influence of topological properties on quasi-static mechanical properties is represented by a broad front of studies, where typical periodicity cells are considered and the influence of the filling density on the effective properties is studied. The works use both analytical models, such as Euler-Bernoulli [16] or Timoshenko [17] rod models, which allow predicting macroscopic elastic properties without virtual tests, and direct numerical homogenisation based on the finite element method (FEM) implemented in commercial software tools [18–20], to calculate the elastic properties of metamaterials.

Prototypes of metamaterials based on surface elements have appeared relatively recently and immediately gained popularity among researchers due to their advantages over metamaterials based on rod elements in a number of specific applications, where a developed internal structure formed by a branched system of interconnected pore channels is required without abrupt changes in their curvature. Metamaterials based on triply periodic minimal surfaces (TPMS) have taken a special place among them [21]. TPMS represent a set of periodically repeating implicit surfaces with zero mean curvature, which means local minimisation of the surface area for a three-dimensional region with some given boundary. The metamaterial based on TPMS’s consists of infinite, non-overlapping shells of a given thickness, repeating in the directions of three coordinate axes with a given frequency.

Due to the large specific area of internal surfaces, TPMS-metamaterials can be used as energy absorbers (kinetic, thermal, acoustic wave energy, microwave electromagnetic

waves), chemical microreactors, membrane devices, and heat-generating elements [21]. Currently, the use of such metamaterials in the field of biomedical applications as bone scaffold or implant is being actively studied. This is due to the fact that for effective osteointegration, artificial bone tissue substitutes should possess a branched system of open-type pore channels for migration and transformation of active cells into bone substance [22], but, at the same time, have sufficient strength to ensure the functionality of organs, especially the human musculoskeletal apparatus [23]. The use of metamaterials of this type has potential advantages over the "bar" type due to the larger area of internal surfaces with a curvature close to the curvature of the trabecular bone tissue structure having a branched system of pore channels [24,25], which is necessary to ensure effective regeneration of biological tissue in the inner space of the scaffold [26].

Among the basic parameters of metamaterials related to various physical applications, studies of mechanical characteristics have received the most attention in the publications. Whether TPMS-based porous structures are used as bone scaffolds, energy absorbers or heat exchangers, the determination of basic mechanical characterisation is required to ensure the reliability of the structures. Young's and shear moduli, Poisson's ratios, especially in the case of anisotropy of elastic properties, are the main mechanical parameters that are the subject of studies [27].

Porous structures can be considered as a special kind of composite material with solid material phase and air phase [28]. Consequently, the Hashin-Strikman upper boundary can be effectively applied to evaluate the mechanical properties of TPMS's. It is shown that, compared to lattice structures, the value of the bulk modulus of elasticity of metamaterials based on TPMS is much closer to the theoretical limit [29].

The effective, or relative, density, which is related to the porosity or volume content of the material, acts as the main integral characteristic that determines the geometrical features of the metamaterial. In this regard, there are a number of studies devoted to the evaluation of this influence. The essence of the studies is to determine the relationship between the effective characteristics (elastic moduli and ultimate stresses) and the relative density also on the basis of scaling laws [30]. According to numerical calculations using FEM and full-scale compression tests, there is a monotonic smooth dependence of the effective elastic moduli on the relative density of the metamaterial [31,32].

It is worth noting that different metamaterials in general and TPMS-based metamaterials in particular can have the same relative density, but show different effective properties. This effect is due to the fact that relative density is not an exhaustive characteristic, and the properties depend on other topological parameters as well. The influence of topological parameters describing triply periodic minimal surfaces on elastic moduli and degree of anisotropy was investigated in [33]. According to the study, it was shown that the elastic modulus and anisotropic properties can be controlled simultaneously by varying different unit cell parameters.

In addition to the analysis of effective elastic properties, significant research attention is paid to the issues of static strength and loss of stability of metamaterials, which is essential for lattice structures formed by beam elements operating in compression [34]. Methods for non-topological optimization of metamaterials to ensure a given strength at minimum weight of the lattice structure are also being developed [35], in particular for biomedical applications of metamaterials [36].

The numerical algorithms for parametric optimization of the lattice structure proposed in [35] were developed in [37] for a special type of metamaterial based on a basic cell containing a pore of varying elliptical shape and orientation. The proposed technique demonstrated its success on the example of the stem of a hip joint endoprosthesis, allowing to reduce the volume of material by 9-11 % depending on the type of implant while maintaining the strength of the structure.

Despite the fact that the studies demonstrate the high potential of the described structures [38], the degree of study of such metamaterials in the context of the previously described issues is much lower in comparison with the "beam" type of cells for a number of reasons: non-triviality of creating parameterised geometrical models, complexity of additive manufacturing, limited number of basic geometrical parameters to be varied.

The paper will consider computer models of metamaterials having periodicity cells with internal structure formed by shells based on thrice periodic minimal surfaces. Using the method of direct finite-element homogenisation, the effective elastic properties of the developed metamaterial models will be calculated depending on the characteristic parameters of their internal structure.

Materials and methods

Theoretical aspects of homogenization technique

Homogenisation is a method of estimating equivalent macroscopic properties, where a relatively homogeneous material is obtained from a heterogeneous material, and the properties of the homogeneous material are globally the same as those of the heterogeneous material. Such properties of the metamaterial are called effective properties. The results obtained for one cell can be generalised for the whole material due to its periodic structure.

The stress and strain values averaged over the elementary representative element are defined by the formulas:

$$\langle\sigma_{ij}\rangle = \frac{1}{V}\int_V \sigma_{ij}dV,\ \langle\varepsilon_{ii}\rangle = \frac{1}{V}\int_V \varepsilon_{ii}dV,\ \langle\gamma_{ij}\rangle = \frac{1}{V}\int_V \gamma_{ij}dV, \quad (1)$$

where V are the volume of the representative volume element (RVE).

The stresses and strains averaged over a representative volume element in points of a porous material, which is considered as a homogeneous continuous medium, as a result of homogenisation are related by the equations of the generalised Hooke's law written in the principal axes of material symmetry X, Y, Z of the stress and strain tensors:

$$\begin{aligned}
&E_x\langle\varepsilon_{xx}\rangle = \langle\sigma_{xx}\rangle - \nu_{xy}\langle\sigma_{yy}\rangle - \nu_{xz}\langle\sigma_{zz}\rangle,\\
&E_y\langle\varepsilon_{yy}\rangle = -\nu_{yx}\langle\sigma_{xx}\rangle + \langle\sigma_{yy}\rangle - \nu_{yz}\langle\sigma_{zz}\rangle,\\
&E_z\langle\varepsilon_{zz}\rangle = -\nu_{zx}\langle\sigma_{xx}\rangle - \nu_{zy}\langle\sigma_{yy}\rangle + \langle\sigma_{zz}\rangle, \quad (2)\\
&G_{xy}\langle\gamma_{xy}\rangle = \langle\sigma_{xy}\rangle,\\
&G_{yz}\langle\gamma_{yz}\rangle = \langle\sigma_{yz}\rangle,\\
&G_{xz}\langle\gamma_{xz}\rangle = \langle\sigma_{xz}\rangle,
\end{aligned}$$

here E_x, E_y, E_z are effective Young's moduli of the elementary cell; ν_{xy}, ν_{yx}, ν_{yz}, ν_{zy}, ν_{xz} and ν_{zx} are effective Poisson's ratios; G_{xy}, G_{yz} and G_{xz} are effective shear moduli.

Compliance matrix $[C]$, which defines the relation between stresses and strains, can be written in the following way according to Eq. (2):

$$[C] = \begin{pmatrix} \frac{1}{E_x} & -\frac{\nu_{yx}}{E_y} & -\frac{\nu_{zx}}{E_z} & 0 & 0 & 0 \\ -\frac{\nu_{xy}}{E_x} & \frac{1}{E_y} & -\frac{\nu_{zy}}{E_z} & 0 & 0 & 0 \\ -\frac{\nu_{xz}}{E_x} & -\frac{\nu_{yz}}{E_y} & \frac{1}{E_z} & 0 & 0 & 0 \\ 0 & 0 & 0 & \frac{1}{G_{xy}} & 0 & 0 \\ 0 & 0 & 0 & 0 & \frac{1}{G_{yz}} & 0 \\ 0 & 0 & 0 & 0 & 0 & \frac{1}{G_{xz}} \end{pmatrix}. \tag{3}$$

Apart from the Eq. (2), Hooke's law can be written in the form more familiar to continuum mechanics as an expression of stress through strain:

$$\begin{pmatrix} \langle\sigma_{xx}\rangle \\ \langle\sigma_{yy}\rangle \\ \langle\sigma_{zz}\rangle \\ \langle\sigma_{xy}\rangle \\ \langle\sigma_{yz}\rangle \\ \langle\sigma_{xz}\rangle \end{pmatrix} = \begin{pmatrix} D_{11} & D_{12} & D_{13} & 0 & 0 & 0 \\ D_{21} & D_{22} & D_{23} & 0 & 0 & 0 \\ D_{31} & D_{32} & D_{33} & 0 & 0 & 0 \\ 0 & 0 & 0 & D_{44} & 0 & 0 \\ 0 & 0 & 0 & 0 & D_{55} & 0 \\ 0 & 0 & 0 & 0 & 0 & D_{66} \end{pmatrix} \begin{pmatrix} \langle\varepsilon_{xx}\rangle \\ \langle\varepsilon_{yy}\rangle \\ \langle\varepsilon_{zz}\rangle \\ \langle\gamma_{xy}\rangle \\ \langle\gamma_{yz}\rangle \\ \langle\gamma_{xz}\rangle \end{pmatrix}, \tag{4}$$

where $[D]$ is a stiffness matrix corresponding to 4th rank the elastic moduli tensor, which is inverse to the compliance matrix:

$$[D] = \begin{pmatrix} D_{11} & D_{12} & D_{13} & 0 & 0 & 0 \\ D_{21} & D_{22} & D_{23} & 0 & 0 & 0 \\ D_{31} & D_{32} & D_{33} & 0 & 0 & 0 \\ 0 & 0 & 0 & D_{44} & 0 & 0 \\ 0 & 0 & 0 & 0 & D_{55} & 0 \\ 0 & 0 & 0 & 0 & 0 & D_{66} \end{pmatrix}, [D] = [C]^{-1}. \tag{5}$$

Six numerical tests are required to determine the independent constants: three in uniaxial tension and three in shear. The average stresses for numerical homogenisation can be found as the ratio of the reaction force F_k applied to the face of the unit cell to its area S:

$$\langle\sigma_{ij}^{k}\rangle = \frac{F_k}{S} \tag{6}$$

where $i, j \in \{x, y, z\}, k \in \{x, y, z, xy, yz, xz\}$.

The index k in Eq. (6) corresponds to the experiment performed: X-stretching along the *X*-axis, Y-stretching along the *Y*-axis, Z-stretching along the *Z*-axis, XY-shear in the *XY*-plane, YZ-shear in the *YZ*-plane, XZ-shear in the *XZ*-plane. When considering each experiment separately, the Eq. (6) will take a simplified form, where $\langle\sigma_{ij}^{x}\rangle, \langle\sigma_{ij}^{y}\rangle, \langle\sigma_{ij}^{z}\rangle$ are averaged stress values for the cases of uniaxial tension along *X*, *Y*, and *Z* axes correspondingly, $\langle\sigma_{ij}^{xy}\rangle, \langle\sigma_{ij}^{yz}\rangle, \langle\sigma_{ij}^{xz}\rangle$ are averaged stress values for the cases of shear in *XY*, *YZ* and *ZX* planes correspondingly (here $i, j \in \{x, y, z\}$). As a result of application of Eqs. (4) and (6), the following expressions can be formulated:

$$A\begin{pmatrix}D_{11}\\D_{21}\\D_{31}\\0\\0\\0\end{pmatrix}=\begin{pmatrix}\langle\sigma_{xx}^{x}\rangle\\\langle\sigma_{yy}^{x}\rangle\\\langle\sigma_{zz}^{x}\rangle\\0\\0\\0\end{pmatrix},\ A\begin{pmatrix}D_{12}\\D_{22}\\D_{32}\\0\\0\\0\end{pmatrix}=\begin{pmatrix}\langle\sigma_{xx}^{y}\rangle\\\langle\sigma_{yy}^{y}\rangle\\\langle\sigma_{zz}^{y}\rangle\\0\\0\\0\end{pmatrix},\ A\begin{pmatrix}D_{13}\\D_{23}\\D_{33}\\0\\0\\0\end{pmatrix}=\begin{pmatrix}\langle\sigma_{xx}^{z}\rangle\\\langle\sigma_{yy}^{z}\rangle\\\langle\sigma_{zz}^{z}\rangle\\0\\0\\0\end{pmatrix},\tag{7a}$$

$$A\begin{pmatrix}0\\0\\0\\D_{44}\\0\\0\end{pmatrix}=\begin{pmatrix}0\\0\\0\\\langle\sigma_{xy}^{xy}\rangle\\0\\0\end{pmatrix},\ A\begin{pmatrix}0\\0\\0\\0\\D_{55}\\0\end{pmatrix}=\begin{pmatrix}0\\0\\0\\0\\\langle\sigma_{yz}^{yz}\rangle\\0\end{pmatrix},\ A\begin{pmatrix}0\\0\\0\\0\\0\\D_{66}\end{pmatrix}=\begin{pmatrix}0\\0\\0\\0\\0\\\langle\sigma_{xz}^{xz}\rangle\end{pmatrix},\tag{7b}$$

where A is a value of longitudinal strain along one of the main orthotropy axes or value of transverse shear strain in one of the main orthotropy planes; hereinafter we will take the value of $A = 0.001$.

Based on the results of six experiments, according to relations (7a) and (7b), we obtain the unknown components of the stiffness matrix D_{ij}. Then we determine the compliance matrix by Eq. (5), after which all unknown elastic constants can be determined using Eq. (3):

$$\begin{aligned}&E_x=\frac{1}{C_{11}},E_y=\frac{1}{C_{22}},E_z=\frac{1}{C_{33}},\\&G_{xy}=\frac{1}{C_{44}},G_{yz}=\frac{1}{C_{55}},G_{xz}=\frac{1}{C_{66}},\\&\nu_{xy}=-\frac{C_{21}}{C_{11}},\nu_{xz}=-\frac{C_{31}}{C_{11}},\nu_{yz}=-\frac{C_{32}}{C_{22}}.\end{aligned}\tag{8}$$

Due to the fact that the metamaterial is a periodic structure, numerical experiments should be carried out with boundary conditions different from the traditional ones. Periodic boundary conditions sufficiently describe the three-dimensional symmetry of the structure, and also provide a more adequate description of deformations, since they reflect the direct influence of deformation of the cell under consideration on its neighbours.

The periodic boundary conditions represent the same displacements of each pair of nodes on opposite faces of a periodic cell of size $L_x \times L_y \times L_z$. Three tensile tests and three shear tests are considered sequentially to determine the material parameters under the boundary conditions described above.

For the numerical uniaxial tensile tests along the *X*, *Y* and *Z* axes, the following periodicity boundary conditions must be satisfied on pairs of opposite sides of the representative element, respectively.

Tension along the *X*-axis:

$$\mathbf{u}|_{x=0}-\mathbf{u}|_{x=L_x}=A\mathbf{i},\mathbf{u}|_{y=0}-\mathbf{u}|_{y=L_y}=0,\mathbf{u}|_{z=0}-\mathbf{u}|_{z=L_z}=0.\tag{9a}$$

Tension along the *Y*-axis:

$$\mathbf{u}|_{x=0}-\mathbf{u}|_{x=L_x}=0,\mathbf{u}|_{y=0}-\mathbf{u}|_{y=L_y}=A\mathbf{j},\mathbf{u}|_{z=0}-\mathbf{u}|_{z=L_z}=0.\tag{9b}$$

Tension along the *Z*-axis:

$$\mathbf{u}|_{x=0}-\mathbf{u}|_{x=L_x}=0,\mathbf{u}_{y=0}-\mathbf{u}|_{y=L_y}=0,\mathbf{u}|_{z=0}-\mathbf{u}|_{z=L_z}=A\mathbf{k}.\tag{9c}$$

here $\mathbf{u}$ is a displacement vector for the RVE; $\mathbf{i},\mathbf{j},\mathbf{k}$ are orts of the coordinate system corresponding to axes *X*, *Y*, *Z*.

To perform three shear tests in the *XY*, *YZ* and *XZ* planes, the periodic boundary conditions on pairs of opposite sides of the representative element will take the following form.

Shear in the *XY*-plane:

$$\mathbf{u}|_{x=0} - \mathbf{u}|_{x=L_x} = A\mathbf{j}, \mathbf{u}|_{y=0} - \mathbf{u}|_{y=L_y} = A\mathbf{i}, \mathbf{u}|_{z=0} - \mathbf{u}|_{z=L_z} = 0. \quad (10a)$$

Shear in the *YZ*-plane:

$$\mathbf{u}|_{x=0} - \mathbf{u}|_{x=L_x} = 0, \mathbf{u}|_{y=0} - \mathbf{u}|_{y=L_y} = A\mathbf{k}, \mathbf{u}|_{z=0} - \mathbf{u}|_{z=L_z} = A\mathbf{j}. \quad (10b)$$

Shear in the *ZX*-plane:

$$\mathbf{u}|_{x=0} - \mathbf{u}|_{x=L_x} = A\mathbf{k}, \mathbf{u}_{y=0} - \mathbf{u}|_{y=L_y} = 0, \mathbf{u}|_{z=0} - \mathbf{u}|_{z=L_z} = A\mathbf{i}. \quad (10c)$$

The presented algorithm is implemented in the EasyPBC plug-in [39] for the finite element analysis software package Abaqus CAE, where all the necessary calculations were performed. The work of the plug-in consists in defining sets of nodes on opposite faces of the periodicity cell and sequential application of periodic boundary conditions (9) and (10) to them. Consecutive numerical solutions of three uniaxial tensile problems along each of the coordinate axes and three pure shear problems in each of the coordinate planes are then carried out. Schemes of the problems for tension along the *Z* coordinate axis and shear in the *YZ* coordinate plane are shown in Fig. 1.

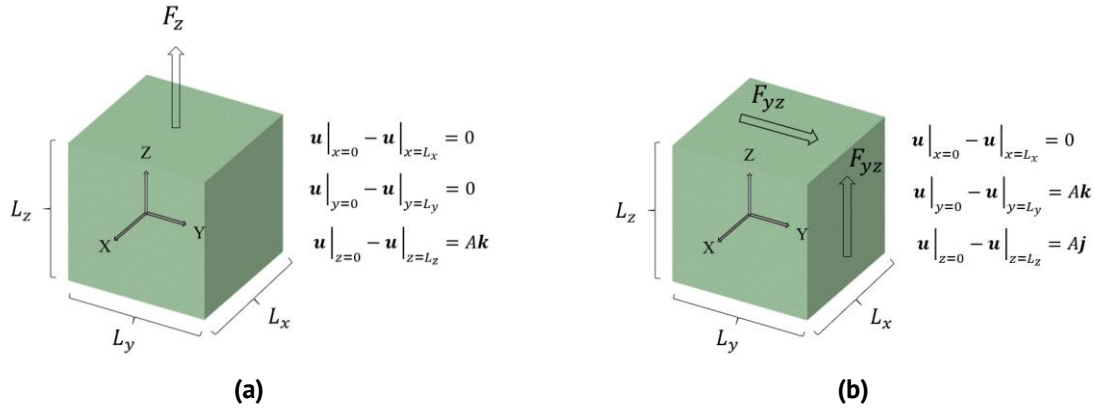

(a) **(b)**

Fig. 1. Problem statements of uniaxial tension along the *Z*-axis (a) and shear in the *YZ*-plane (b) to perform homogenization

After the calculations at the meso-level of the elementary representative volume, the effective elastic characteristics of the metamaterial according to Eq. (8) are calculated from the obtained stress values (7) and given deformations.

Triply periodic minimal surfaces

In this paper we consider nine well-known types of triply periodic minimal surfaces described by functions $F(x, y, z)$ [40] (Table 1).

Geometrical models of elementary cells of metamaterial based on TPMS are developed under the assumption that the interface surface of solid material and air of inhomogeneous structure is described by an implicit equation of the following form $F(x, y, z) = C$.

Table 1. Parameters of triply periodic minimal surfaces

Name	Surface shape	Mathematical expression $F(x, y, z)$
Fischer Koch	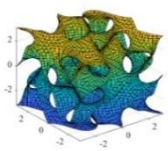	$sin(\omega_x x)\, cos(\omega_y y)\, cos(2\omega_z z) + cos(2\omega_x x) sin(\omega_y y) cos(\omega_z z) + cos(\omega_x x) cos(2\omega_y y) sin(\omega_z z)$
Gyroid	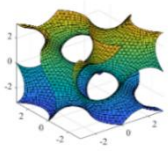	$cos(\omega_x x)\, sin(\omega_y y) + sin(\omega_x x)\, cos(\omega_z z) + cos(\omega_y y)\, sin\,(\omega_z z)$
Lidinoid	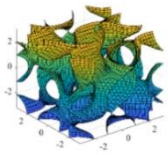	$sin(\omega_x x) sin(2\omega_y y) cos(\omega_z z) + sin(2\omega_x x) cos(\omega_y y) sin(\omega_z z) - cos(2\omega_y y) cos(2\omega_z z) + cos(\omega_x x) sin(\omega_y y) sin(2\omega_z z) - cos(2\omega_x x) cos(2\omega_y y) - cos(2\omega_x x) cos(2\omega_z z)$
Neovius	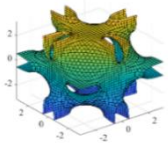	$4cos(\omega_x x) cos(\omega_y y) cos(\omega_z z) + 3(cos(\omega_x x) + cos(\omega_y y) + cos(\omega_z z))$
Primary IWP	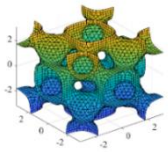	$4cos(\omega_x x) cos(\omega_y y) cos(\omega_z z) - (cos(2\omega_x x) cos(2\omega_y y) + cos(2\omega_x x) cos(2\omega_z z) + cos(2\omega_y y) cos(2\omega_z z))$
Schwarz D	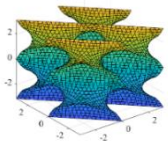	$sin(\omega_x x) sin(\omega_y y) sin(\omega_z z) + sin(\omega_x x) cos(\omega_y y) cos(\omega_z z) + cos(\omega_x x) sin(\omega_y y) cos(\omega_z z) + cos(\omega_x x) cos(\omega_y y) sin(\omega_z z)$
Schwarz P	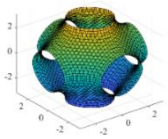	$cos(\omega_x x) + cos(\omega_y y) + cos(\omega_z z)$
Secondary IWP	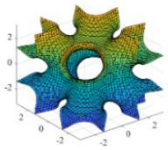	$2(cos(\omega_x x) cos(\omega_y y) + cos(\omega_x x) cos(\omega_z z) + cos(\omega_y y) cos(\omega_z z)) - (cos(2\omega_x x) + cos(2\omega_y y) + cos(2\omega_z z))$
Split P	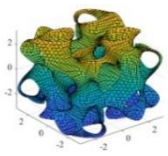	$-0{,}2(cos(2\omega_x x)\, cos(2\omega_y y) + cos(2\omega_x x)\, cos(2\omega_z z) + cos(2\omega_y y)\, cos(2\omega_z z)) + sin(2\omega_x x) cos(\omega_y y) sin(\omega_z z) - 0{,}4(cos(2\omega_x x) + cos(2\omega_y y) + cos(2\omega_z z)) + cos\,(\omega_x x) sin\,(\omega_y y) sin\,(2\omega_z z)) + 1{,}1(sin(\omega_x x)\, sin(2\omega_y y)\, cos(\omega_z z))$

The constant C allows to vary the ratio of solid material to air in the structure and serves as a parameter determining the volume fraction of the unit cell. By assuming the condition $F(x, y, z) > C$ or $F(x, y, z) < C$, we can switch between considering only one part of the porous material, namely the solid phase or air [41]. At $C = 0$ values of the volumes of solid material and air in the unit cell are equal to each other.

The influence of constant C on the surface appearance is explained in Fig. 2 at fixed repetition frequencies along the coordinate axes for two typical Fischer Koch and Schwarz P TPMS's. It can be observed that varying the constant between 0 and 0.5 changes the characteristic dimensions of the surface structures without changing the topology. However, when C approaches 1, the initial topology (at $C = 0$) changes significantly, including the fact that it may become unsuitable for construction of a metamaterial model.

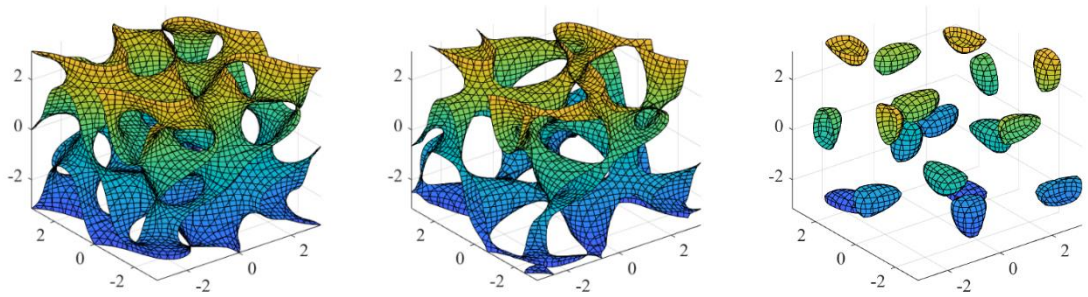

$\boldsymbol{C = 0,\ \omega_x = \omega_y = \omega_z = 1}$ $\boldsymbol{C = 0.5,\ \omega_x = \omega_y = \omega_z = 1}$ $\boldsymbol{C = 1,\ \omega_x = \omega_y = \omega_z = 1}$

(a)

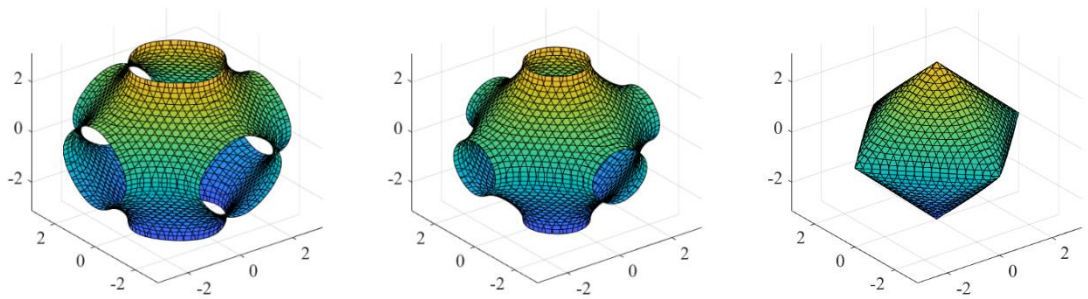

$\boldsymbol{C = 0,\ \omega_x = \omega_y = \omega_z = 1}$ $\boldsymbol{C = 0.5,\ \omega_x = \omega_y = \omega_z = 1}$ $\boldsymbol{C = 1,\ \omega_x = \omega_y = \omega_z = 1}$

(b)

Fig. 2. Surface structures of Fischer Koch (a) and Schwarz P (b) TPMS types at different values of constant C and fixed repetition rate

The frequencies ω_x, ω_y and ω_z in the arguments of the equations of the triply periodic surface structures determine the spatial step along the corresponding coordinates. This makes it possible to fit a different number of surfaces into the periodicity cell of the metamaterial, thus changing the volume fraction or density of the material (Fig. 3). The frequency expressions have the following form:

$$\omega_x = \frac{2\pi}{L_x}, \omega_y = \frac{2\pi}{L_y}, \omega_z = \frac{2\pi}{L_z}, \tag{11}$$

where L_x, L_y, L_z are lengths of the sides of a parallelepiped defining the elementary representative cell of the metamaterial.

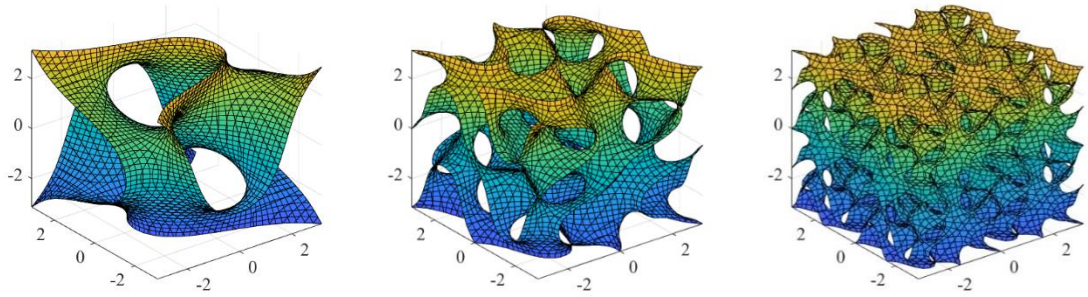

$C = 0,\ \omega_x = \omega_y = \omega_z = 0.5$ $C = 0,\ \omega_x = \omega_y = \omega_z = 1$ $C = 0,\ \omega_x = \omega_y = \omega_z = 2$

Fig. 3. Surface structures based on Fischer Koch TPMP's at different values of repetition rate and fixed constant $C = 0$

Due to the analytical expressions, the range, curvature and period of the TPMS can be easily controlled. In addition, complex calculations such as logic value, modulation and convolution can also be realised on the basis of functions describing the TPMS.

Finite element modelling of unit cells of metamaterials

The finite element model of a periodicity cell of a metamaterial based on TPMS should be constructed in such a way that the nodes of three-dimensional finite elements on the opposite faces of the cell coincide at parallel transfer of the cell along the coordinate axes by the value of the linear size of the cell. This is necessary to ensure correct formulation of periodic boundary conditions [39]. In the algorithm developed by us, the coincidence of opposite faces is ensured by duplicating three mutually perpendicular faces of the unit cell with subsequent joining of the inner surface of the surface structure. The use of this approach is caused by the unavailability of solid-state geometry of the initial TPMS-based unit cells and the absence of geometrically identical faces opposite to each other.

Let us consider more in detail the algorithm for constructing the metamaterial periodicity cell model based on a triply periodic minimal surface of the Fischer Koch type, which is required for finite element analysis. Let the volume fraction of the material, or relative density, be equal to 0.5.

Altair Sulis software [42] allows to select the desired type of surface structure, set the dimensions of the unit cell of the metamaterial based on the selected type of TPMS and the value of the volume fraction of the solid phase (Fig. 4).

The next step is to export the obtained geometry to a file of standard geometric surface description format STL (stereolithography), which can be opened by CAD software. In particular, we used the CAD package of direct geometric modelling Ansys SpaceClaim [43] for further geometry processing and preparation of the 3D solid model. In the environment of SpaceClaim, by intersecting surface structures with a 5 × 5 × 5 mm cube, the required solid-state periodicity cell of the considered metamaterial was obtained (Fig. 5). In addition, three faces of the unit cell parallel to the three coordinate planes were identified, which is related to the setting periodic boundary conditions in finite element calculations.

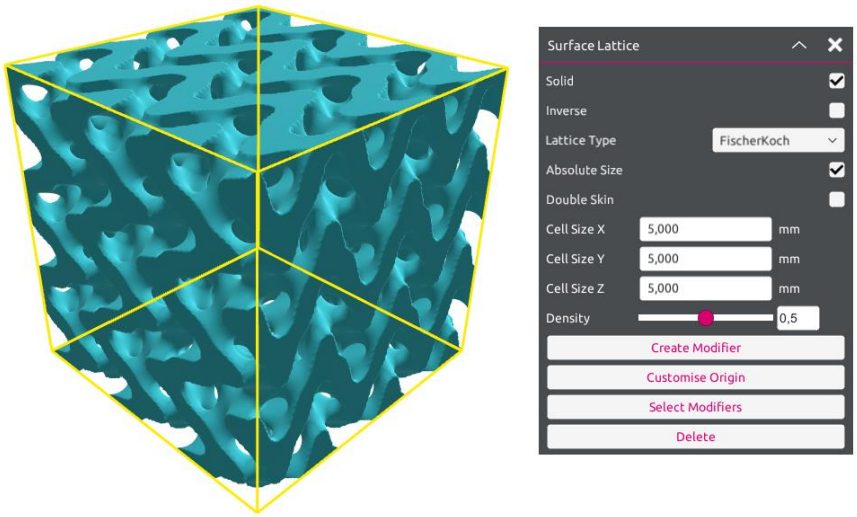

Fig. 4. The structure consisting of 3×3×3 elementary cells of metamaterial with the size of 5×5×5 mm, developed in Altair Sulis software on the basis of Fischer Koch surface cell with the volume fracture of solid phase equal to 0.5

The obtained model (Fig. 5) in a standard solid modelling format is exported to a finite element analysis package. In our case, the Abaqus CAE [44] was used. In Abaqus CAE, using virtual topology and setting the number of elements on the edges of the geometry, it is possible to ensure the coincidence of element nodes on the edges when duplicating the faces, which allows to guarantee the correct connection of opposite faces for subsequent work with periodic boundary conditions. The solid-air interface surface is then added to the unit cell faces in SpaceClaim (Fig. 6).

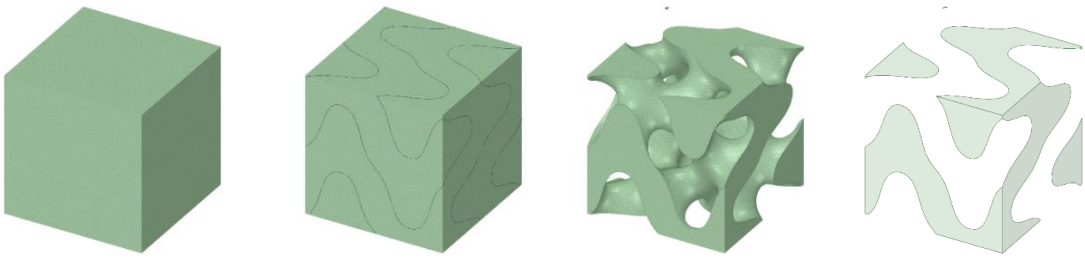

Fig. 5. Scheme of preparing the periodicity unit cell faces of metamaterial based on Fischer Koch surface structure with solid phase volume content of 0.5

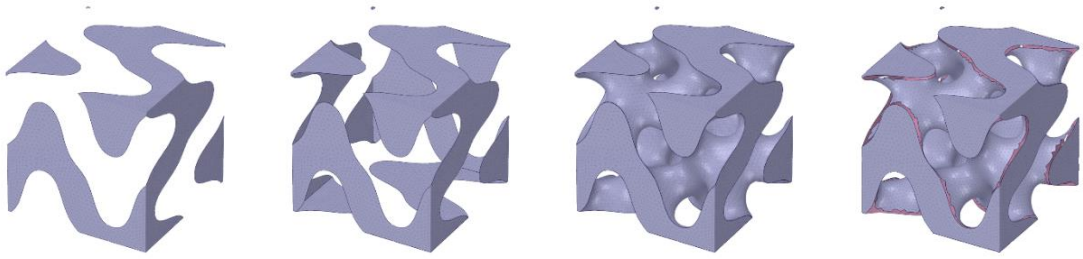

Fig. 6. Steps of construction of periodicity cell of metamaterial based on Fischer Koch surface structure with volume fraction of solid phase phase equal to 0.5

Then in Autodesk Meshmixer [45] we invert the normals of the duplicated faces and remove the elements of the inner surface close to the outer faces of the cell. Finally, in Altair SimLab software [46] we mesh the faces and the interface surface by adding elements according to the existing nodes. As a result of these operations, we obtain the volumetric mesh geometry of the unit cell of the metamaterial, the coincidence of the opposite sides of which guarantees the possibility of correct imposition of periodicity conditions between the nodes of the finite element mesh (Fig. 6).

Using the described algorithm, finite element models of metamaterial periodicity unit cells were developed for the considered surface types (Table 1). The overall dimensions of elementary cells of each type were taken as 5 × 5 × 5 mm. For each type of surface structures, five options of the models were constructed with the range of volume fractions varied from 0.1 to 0.9 with a fixed step of 0.2.

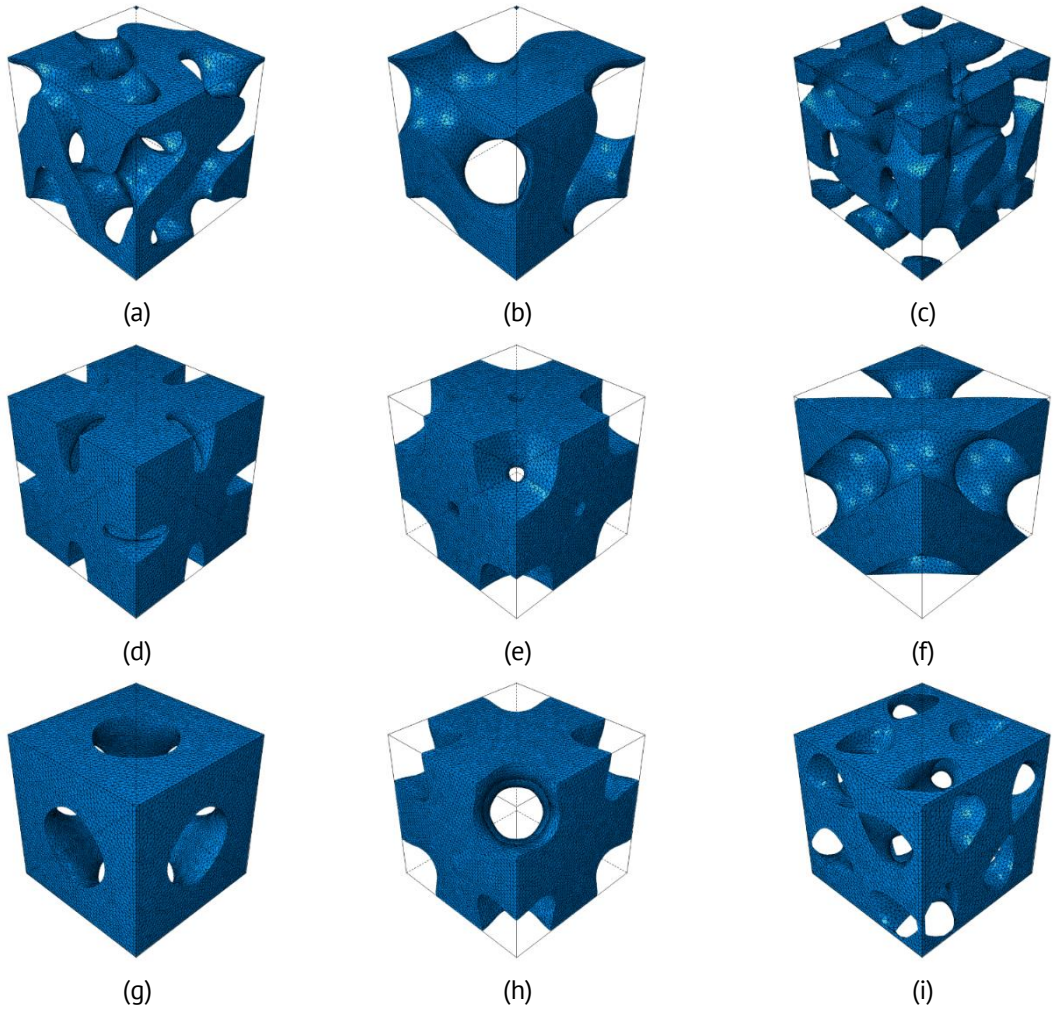

Fig. 7. Finite element models based on TPMS's with the volume fraction value of 0.5: (a) Fischer Koch; (b) Gyroid; (c) Lidinoid; (d) Neovius; (e) Primary IWP; (f) Schwarz D; (g) Schwarz P; (h) Secondary IWP; (i) Split P

Three-dimensional numerical models of periodicity cells are formed by tetrahedral linear finite elements with the first order of displacement interpolation. The characteristic side size of the finite element is 0.1 mm. The quantitative characteristics of the developed

finite element models for the case of material volume fraction equal to 0.5 are listed in Table 2, and their shape is shown in Fig. 7.

Table 2. Characteristics of the developed finite element models

Type of the unit cell	Number of elements	Number of nodes
Fischer Koch	226 999	46 101
Gyroid	237 683	46 134
Lidinoid	308 027	65 490
Neovius	236 782	48 042
Primary IWP	277 099	54 197
Schwarz D	231 803	45 569
Schwarz P	225 452	43 865
Secondary IWP	219 745	43 874

For the formulation of problems of the theory of elasticity, it is necessary to specify the material properties. In the present work, surface-type metamaterials made of isotropic aluminium are considered. The material parameters of the solid phase and air used in the calculation are presented in Table 3.

Table 3. Material properties of the solid phase and air

Material type	Young's modulus, MPa	Shear modulus, MPa	Poisson's ratio	Density, g/cm^3
Aluminium	78 670	29 700	0.32	2.67
Air	1	0.385	0.3	0.0012

Results and Discussion

This section presents the results of calculation of the elastic constants of all types of metamaterials using the direct numerical homogenisation method when varying the degree of filling of the structural unit cell with solid material.

For clarity, as an example of solving problems with periodic boundary conditions, Fig. 8 shows the results of the stress-strain state of a Fischer Koch-type unit cell at a material volume fraction value of 0.5 in tension along the *Z*-axis with boundary conditions (9b) and shear in the *YZ*-plane with boundary conditions (10c).

To analyse the effective elastic properties of the metamaterial formed by different types of elementary cells on the basis of TPMS obtained from the results of numerical homogenisation, we present comparative graphs that reflect the dependences of mechanical properties on the volume fraction of the solid phase (Fig. 9). The graphs of Young's moduli and shear moduli are given in relative units with respect to the modulus of the base material forming the solid phase of the metamaterial.

The calculations resulted in the same values of effective Young's moduli along the coordinate axes, shear moduli and Poisson's ratios in the coordinate planes. Therefore, Fig. 9 shows plots of Young's moduli along arbitrary coordinate axis, shear moduli and Poisson's ratios in arbitrary coordinate planes. The equality of Young's moduli, shear moduli and Poisson's ratios in the principal axes does not mean that the metamaterial is isotropic, since the metamaterial inherits the properties of material symmetry, which should lead to the syngonic material behaviour with cubic symmetry. Below this issue will be considered in more detail.

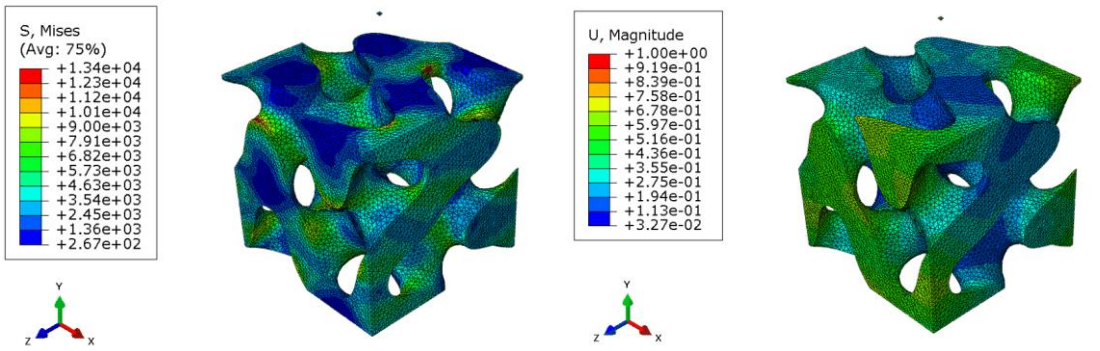

(a)

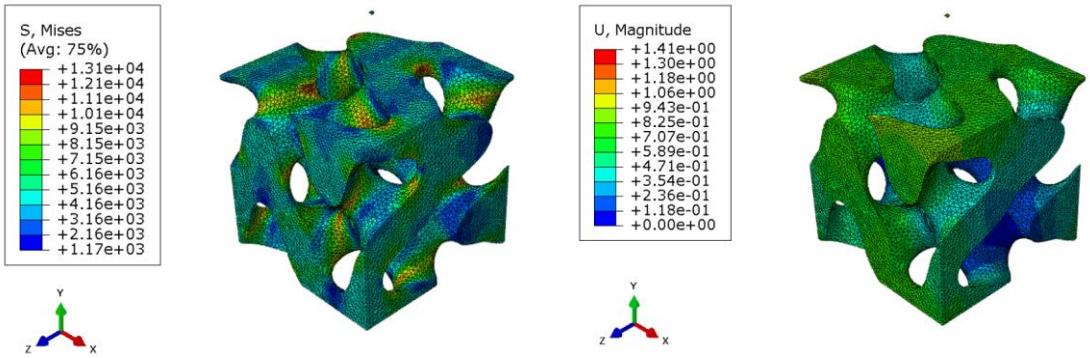

(b)

Fig. 8. Equivalent stresses (left) and total displacement (right) under uniaxial tension along the *Z*-axis (a) and shear in the *YZ*-plane (b) at the meso-level of a metamaterial based on a Fischer Koch surface structure with a volume fraction of 0.5

The dependences of Young's moduli (Fig. 9(a)) and shear moduli values (Fig. 9(b)) are qualitatively similar for each type of elementary cells of the metamaterial. At the material volume fraction of 0.0, the diagrams reflect the values of mechanical characteristics of air, while at the volume fraction of 1.0 they coincide with the values of elastic moduli of aluminium. As the volume fraction of the solid phase of the metamaterial increases, the values of Young's and shear moduli grow and tend to the values of elastic properties of the base material.

The intensity of change in mechanical properties at the same rate of change in volume fraction is different for each cell type. It is interesting to mention that the Neovius and Lidinoid cell types show a minimum growth of Young's modulus in the first third of the volume fraction range, which is explained by the lack of cohesion of the cell geometry at the described values of the effective density of the metamaterial.

Note that all the considered types of metamaterials show strongly nonlinear dependence of elastic properties on relative density, which differs from simple formulas, for example, in the mechanics of mixtures. Moreover, the curvature is more pronounced for values of relative density less than 0.5. This may indicate a more significant influence of the topological characteristics of the cell on its behaviour compared to their influence in the case of high relative density, where the mechanical properties of the basic material are the prevailing factor. It can be concluded that for problems with relative density close to 1.0 the question of choosing a particular type of cell is not so relevant, and that in a comparative study of different topological characteristics the results obtained for small values of relative density will be more indicative.

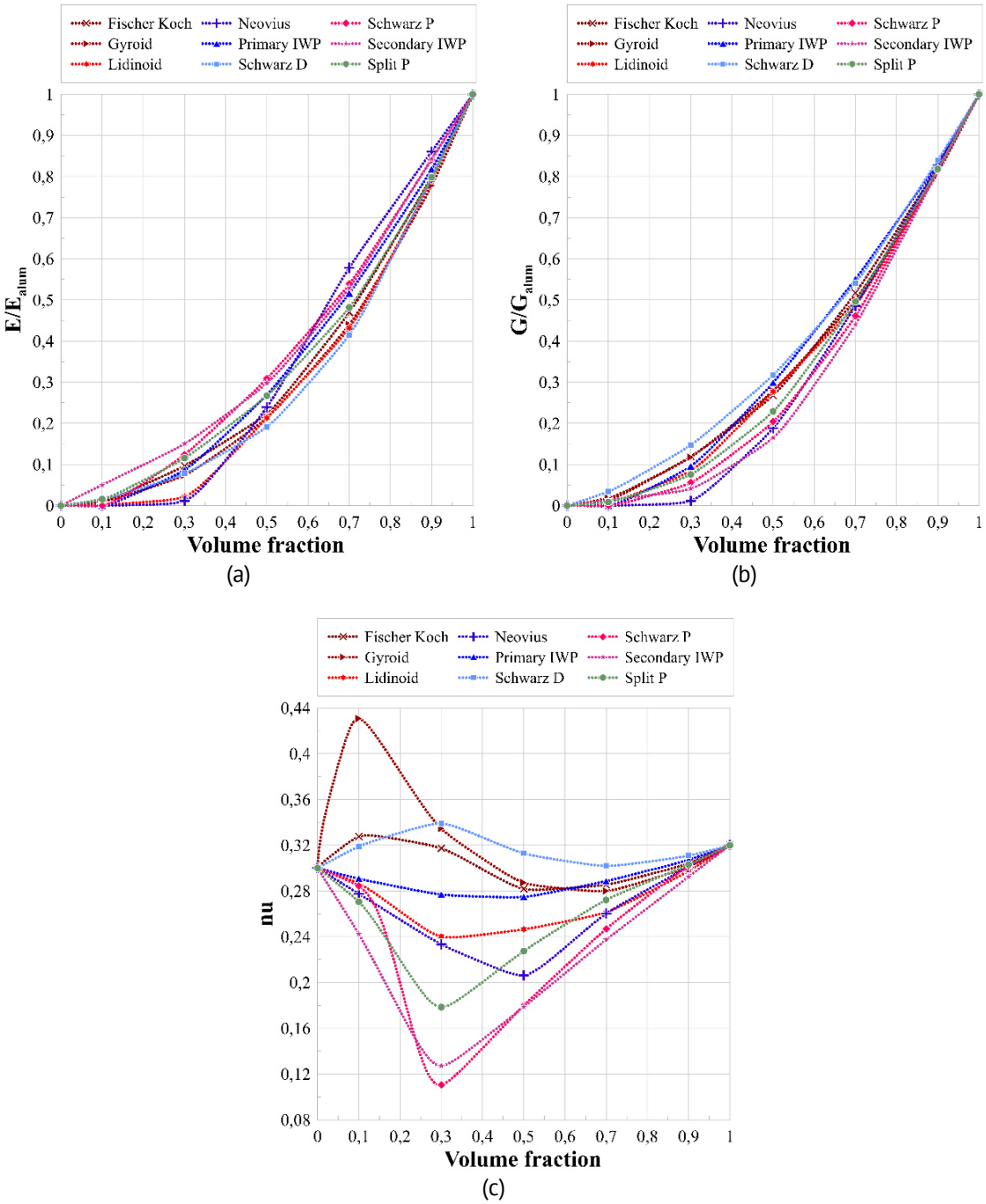

Fig. 9. Dependences of effective elastic constants of metamaterial based on nine types of surface structures on the volume content of solid phase: (a) Young's moduli; (b) shear moduli; (c) Poisson's ratios

When analysing the dependences of Poisson's ratio values (Fig. 9(c)), much less consistency in the qualitative behaviour of the plots for different types of metamaterials is observed. For values of the volume fraction greater than 0.5, a general tendency for the final value to tend to the value of the constant for the solid material is revealed. The reasons for such an effect were discussed earlier. At the same time, the values of the constant in the range of volume fraction 0.1-0.5 are non-monotonic. The reason for this phenomenon may be a more pronounced influence of the topology of the unit cell on the transverse deformations. The consequence of this phenomenon is the apparent presence of stationary points corresponding to the maximum or minimum achievable values of the

Poisson's ratio, which can be useful in problems where its value has a significant influence on the global result. It can also be noticed that Gyroid, Fischer Koch, Schwarz P unit cells at medium values of effective density show a larger value of Poisson's ratio in comparison with the value of Poisson's ratio of air and other types of unit cells with a much smaller value of this dimensionless characteristic.

The graphs shown in Fig. 9 may give a wrong idea about the isotropy of the effective properties of the obtained metamaterials. To assess the degree of anisotropy and to check the relationship of mechanical properties between each other, we determine from the available values of Young's modulus and shear modulus the value of Poisson's ratio for each unit cell in accordance with the classical formula for an isotropic continuous medium: $\nu = \frac{E}{2G} - 1$. The results of the calculations are presented in Fig. 10.

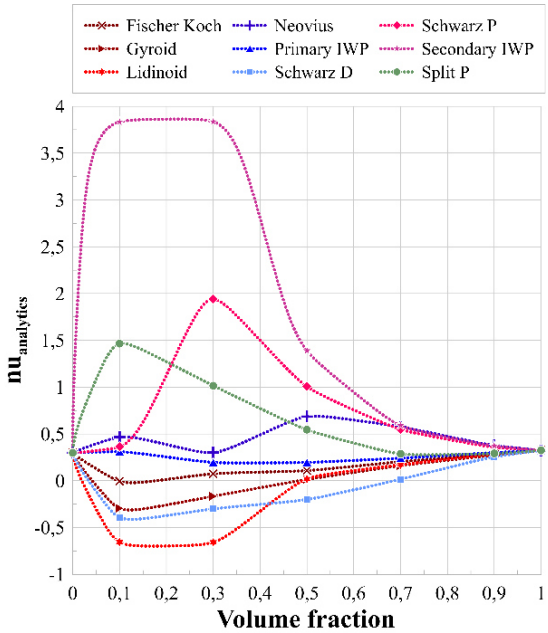

Fig. 10. Dependences of the effective Poisson's ratios calculated by the isotropic continuum model formula on the volume fraction of the solid phase of the metamaterial

The graphs (Fig. 10) clearly show that the obtained analytical values according to the classical formula of the isotropic material model both qualitatively and quantitatively differ from the calculated parameters. This means that the hypothesis of the syngonic material behaviour with cubic symmetry implemented into orthotropic model of the metamaterial is confirmed, because despite the equality of Young's moduli and shear moduli in the directions of the three principal axes, the basic relation about the relation between these constants for an isotropic material is not fulfilled. At the same time, the coincidence of the values of elastic moduli along the three principal axes can be explained by the order of spatial symmetry of the unit cell of the metamaterial on the basis of the considered types of surface structures.

Conclusion

The presented work considers models of metamaterials based on triply periodic minimal surfaces, which is a popular and rational direction in digital materials science. A computerized technique for constructing periodicity cells of metamaterials as representative volume elements of specific heterogeneous media is proposed.

The boundary value problems for uniaxial tension and pure shear for calculating the stress-strain state of the selected representative volume elements taking into account periodic boundary conditions are formulated and finite element models are developed.

Using a direct numerical homogenization method at the meso-level of the periodicity cell, the elastic properties of metamaterials are calculated. A number of assumptions about the relationship between mechanical properties and the topology parameters of the basic cells of TPMS-metamaterials, such as the type of unit cell and the volume fraction of the material, have been verified. Dependences of effective properties on volume fraction of solid material are revealed and it is noted that for their correct description, due to syngonic material behaviour with cubic symmetry, application of orthotropic material model is required. It is shown that the considered types of surface metamaterials exhibit strongly nonlinear dependence of elastic properties on the relative density or volume fraction of the solid phase of the metamaterial. The analysis of Poisson's ratios shows a significant difference in their behaviour for different types of metamaterials, which may be caused by a more pronounced influence of the unit cell topology on the transverse deformations.

The conducted study of dependences should allow to create TPMS-materials with specific mechanical properties necessary for the development of modern promising and advanced industrial products, including medical applications.

References

1. Popovich AA, Sufiiarov VS, Borisov EV, Polozov IA, Masaylo DV. Design and manufacturing of tailored microstructure with selective laser melting. *Materials Physics and Mechanics*. 2018;38(1): 1–10.
2. Torquato S, Gibiansky L, Silva M, Gibson L. Effective mechanical and transport properties of cellular solids. *Int. J. Mech. Sci.* 2000;40(1): 71–82.
3. Christensen RM. Mechanics of cellular and other low-density materials. *Int. J. Sol. Struct.* 2000;37(1–2): 93–104.
4. de Jonge CP, Kolken HMA, Zadpoor AA. Non-Auxetic Mechanical Metamaterials. *Materials.* 2019;12(4): 635.
5. Kolken HMA, Zadpoor AA. Auxetic Mechanical Metamaterials. *RSC Advances*. 2017;7: 5111–5129.
6. Comi C, Moscatelli M, Marigo JJ. Two scale homogenization in ternary locally resonant metamaterials. *Materials Physics and Mechanics*. 2020;44(1): 8–18.
7. Walser RM. Electromagnetic Metamaterials. *Proceedings of SPIE. Complex Mediums II: Beyond Linear Isotropic Dielectrics*. 2001;4467: 1–15.
8. Maslov LB. Study of vibrational characteristics of poroelastic mechanical systems. *Mechanics of Solids*. 2012;47(2): 221–233.
9. Zadpoor AA. Design for additive bio-manufacturing: from patient-specific medical devices to rationally designed meta-biomaterials. *Int. J. Mol. Sci*. 2017;18(8): 1607.
10. Maslov LB. Mathematical model of bone regeneration in a porous implant. *Mechanics of Composite Materials*. 2017;53(3): 399–414.
11. Fousová M, Vojteěch D, Kubásek J, Jablonská E, Fojt J. Promising characteristics of gradient porosity Ti-6Al-4V alloy prepared by SLM process. *J. Mech. Behav. Biomed. Mater*. 2017;69: 368–376.
12. Bobbert FSL, Janbaz S, Zadpoor AA. Towards deployable meta-implants. *Journal of Materials Chemistry. B.* 2018;6(21): 3449–3455.

13. Kolken HM, Janbaz S, Leeflang SM, Lietaert K, Weinans HH, Zadpoor AA. Rationally designed meta-implants: a combination of auxetic and conventional meta-biomaterials. *Mater. Horiz*. 2018;5(1): 28–35.
14. Hanks B, Berthel J, Frecker M, Simpson TW. Mechanical properties of additively manufactured metal lattice structures: data review and design interface. *Addit. Manuf*. 2020;35: 101301.
15. Feng J, Fu J, Shang C, Lin Z, Li B. Porous scaffold design by solid T-splines and triply periodic minimal surfaces. *Comput. Methods Appl. Mech. Eng*. 2018;336: 333–352.
16. Zadpoor AA, Hedayati R. Analytical relationships for prediction of the mechanical properties of additively manufactured porous biomaterials. *J. Biomed. Mater. Res. Part A*. 2016;104(12): 3164–3174.
17. Hedayati R, Sadighi M, Mohammadi-Aghdam M, Zadpoor A. Mechanical properties of regular porous biomaterials made from truncated cube repeating unit cells: analytical solutions and computational models. *Mat. Sci. Eng*. 2016;60: 163–183.
18. Vlădulescu F, Constantinescu DM. Lattice structure optimization and homogenization through finite element analyses. *Proceedings of the Institution of Mechanical Engineers, Part L: Journal of Materials: Design and Applications*. 2020;234: 1490–1502.
19. Ravari MK, Kadkhodaei M, Badrossamay M, Rezaei R. Numerical investigation on mechanical properties of cellular lattice structures fabricated by fused deposition modelling. *Int. J. Mech. Sci*. 2014;88: 154–161.
20. Zhmaylo M, Maslov L, Borovkov A, Tarasenko F. Finite element homogenization and experimental evaluation of additively manufactured lattice metamaterials. *J. Braz. Soc. Mech. Sci. Eng*. 2023;45: 299.
21. Feng JW, Fu JZ, Yao XH, He Y. Triply periodic minimal surface (TPMS) porous structures: from multi-scale design, precise additive manufacturing to multidisciplinary applications. *Int. J. Extrem. Manuf*. 2022;4: 022001.
22. Mitrofanov AV, Maslov LB, Mizonov VE. A stochastic model of cell transformations at bone tissue regeneration. *Rus. J. Biomech*. 2021;25(1): 41–54.
23. Maslov LB, Dmitryuk AY, Zhmaylo MA, Tarasenko FD, Kovalenko AN. Strength analysis in a hip endoprosthesis made of polymeric material. *Rus. J. Biomech*. 2022;26(4): 14–28.
24. Chikova TN, Kichenko AA, Tverier VM, Nyashin YI. Biomechanical modelling of trabecular bone tissue in remodelling equilibrium. *Rus. J. Biomech*. 2018;22(3): 245–253.
25. Kichenko AA. Cancellous bone tissue remodelling: mathematical modelling. *Rus. J. Biomech*. 2019;23(3): 284–304.
26. Maslov LB. Biomechanical model and numerical analysis of tissue regeneration within a porous scaffold. *Mechanics of Solids*. 2020;55(7): 1115–1134.
27. Callens SJP, Arns CH, Kuliesh A, Zadpoor AA. Decoupling minimal surface metamaterial properties through multi-material hyperbolic tilings. *Adv. Funct. Mater*. 2021;31: 2101373.
28. Maslov LB. Dynamic Model of a Periodic Medium with Double Porosity. *Mechanics of Solids*. 2018;53(2): 184–194.
29. Deng B, Cheng GJ. Soap film inspired mechanical metamaterials approaching theoretical bound of stiffness across full density range. *Mater. Horiz*. 2021;8: 987–996.
30. Maskery I, Sturm L, Aremu AO, Panesar A, Williams CB, Tuck CJ, Wildman RD, Ashcroft IA, Hague RJM. Insights into the mechanical properties of several triply periodic minimal surface lattice structures made by polymer additive manufacturing. *Polymer*. 2018;152: 62–71.
31. Lee DW, Khan KA, Abu Al-Rub RK. Stiffness and yield strength of architectured foams based on the Schwarz primitive triply periodic minimal surface. *Int. J. Plast*. 2017;95: 1–20.
32. Al-Ketan O, Soliman A, Al-Qubaisi AM, Abu Al-Rub RK. Nature-inspired lightweight cellular co-continuous composites with architected periodic gyroidal structures. *Adv. Eng. Mater*. 2018;20: 1700549.
33. Feng J, Liu B, Lin Z, Fu J. Isotropic porous structure design methods based on triply periodic minimal surfaces. *Mater. Des*. 2021;210: 110050.
34. Akifyev KN, Kharin NV, Statsenko EO, Sachenkov OA, Bolshakov PV. Pilot study of lattice endoprosthesis buckling by compression in-situ using X-ray tomography. *Rus. J. Biomech*. 2023;27(4): 32–39.
35. Bolshakov P, Raginov I, Egorov V, Kashapova R, Kashapov R, Baltina T, Sachenkov O. Design and optimization lattice endoprosthesis for long bones: manufacturing and clinical experiment. *Materials*. 2020;13(5): 1185.
36. Kharin N, Bolshakov P, Kuchumov AG. Numerical and Experimental Study of a Lattice Structure for Orthopedic Applications. *Materials*. 2023;16(2): 744.
37. Bolshakov P, Kuchumov AG, Kharin N, Akifyev K, Statsenko E, Silberschmidt V. Method of computational design for additive manufacturing of hip endoprosthesis based on basic-cell concept. *Int. J. Numer. Meth. Biomed. Engng*. 2024;40(3): 3802.

38. Montazerian H, Davoodi E, Asadi-Eydivand M, Kadkhodapour J, Solati-Hashjin M. Porous scaffold internal architecture design based on minimal surfaces: a compromise between permeability and elastic properties. *Mater. Des*. 2017;126: 98–114.
39. Omairey SL, Dunning PD, Sriramula S. Development of an ABAQUS plugin tool for periodic RVE homogenisation. *Engineering with Computers*. 2019;35: 567–577.
40. Karakoç A. RegionTPMS – Region based triply periodic minimal surfaces (TPMS) for 3-D printed multiphase bone scaffolds with exact porosity values. *SoftwareX*. 2021;16: 100835.
41. Al-Ketan O, Abu Al-Rub RK. MSLattice: A free software for generating uniform and graded lattices based on triply periodic minimal surfaces. *Mat. Design. Process. Comm*. 2020: 205.
42. *Design software for additive manufacturing*. Available from: https://gen3d.com [Accessed 1 June 2023].
43. *Ansys SpaceSlaim. 3D Modeling Software*. Available from: https://www.ansys.com/products/3d-design/ansys-spaceclaim [Accessed 1 June 2023].
44. *Abaqus CAE. A powerful standalone interface*. Available from: https://www.simuleon.com/simulia-abaqus/abaqus-cae [Accessed 1 June 2023].
45. *Autodesk Meshmixer. Free software for making awesome stuff*. Available from: https://www.meshmixer.com [Accessed 1 June 2023].
46. *Multiphysics Workflows with CAD Associativity | Altair SimLab*. Available from: https://altair.com/simlab [Accessed 1 June 2023].

About Author

Aleksey I. Borovkov Sc
Candidate of Technical Sciences, Associate Professor
Vice-rector for Digital Transformation (Peter the Great St. Petersburg Polytechnic University, St. Petersburg, Russia)

Leonid B. Maslov Sc
Doctor of Physical and Mathematical Sciences, Associate Professor
Lead Researcher (Peter the Great St. Petersburg Polytechnic University, St. Petersburg, Russia)
Lead Researcher (Ivanovo State Power Engineering University n.a. V.I. Lenin, Ivanovo, Russia)

Mikhail A. Zhmaylo Sc
Master of Science
Lead Engineer (Peter the Great St. Petersburg Polytechnic University, St. Petersburg, Russia)

Fedor D. Tarasenko Sc
Master of Science
Lead Engineer (Peter the Great St. Petersburg Polytechnic University, St. Petersburg, Russia)

Liliya S. Nezhinskaya Sc
Bachelor of Science
Engineer (Peter the Great St. Petersburg Polytechnic University, St. Petersburg, Russia)

MATERIALS PHYSICS AND MECHANICS RESEACH ARTICLE

Submitted: October 30, 2023 Revised: November 9, 2023 Accepted: December 11, 2024

Brittle vs ductile fracture behavior in ceramic materials at elevated temperature

S.A. Krasnitckii [1,2] ✉, **A.G. Sheinerman** [3], **M.Yu. Gutkin** [3],

[1] ITMO University, St. Petersburg, Russia

[2] St. Petersburg State University, St. Petersburg, Russia

[3] Institute for Problems of Mechanical Engineering RAS, St. Petersburg, Russia

✉ Krasnitsky@inbox.ru

ABSTRACT

An intergranular crack initiated at a pore located in a triple junction of grain boundaries in a ceramic material is considered in order to investigate the brittle versus ductile fracture in different temperature ranges. The critical fracture stress and critical dislocation slip stress are estimated in dependence on temperature for the case of Al_2O_3 ceramics. The temperature dependless local stresses in vicinity of blunt cracks and a triangular-shaped pore are calculated by the finite element method. The provided analysis reveals the favorability of the fracture scenarios upon the temperature conditions and bluntness of a crack tip as well.

KEYWORDS

ceramic materials • pore •crack • intergranular fracture •dislocation emission • finite element simulation

Acknowledgements. *This work was supported by the Russian Science Foundation (grant No. 23-19-00236).*

Citation: Krasnitckii SA, Sheinerman AG, Gutkin MYu. Brittle vs ductile fracture behavior in ceramic materials at elevated temperature. *Materials Physics and Mechanics*. 2024;52(2): 82–89.
http://dx.doi.org/10.18149/MPM.5222024_9

Introduction

Due to relatively high melting point and ability to arouse plastic deformation at elevated temperatures, the ceramic materials are widely used in modern industry [1–3]. The mechanical properties as well as the fracture tolerance of these materials are strongly determined by the temperature range of the operational conditions [4,5]. Commonly, the brittle behavior of fracture is expected to experience at relatively low temperatures while the ductile one occurs at relatively high temperatures. The first scenario stems from the propagation of cracks whereas the second one is accompanied with activation of dislocation glide and grain boundary (GB) sliding. In particular, the dislocation emission from the crack tip can significantly inhibit the crack growth due to blunting of the crack tip.

The problem of brittle-to-ductile transition has been long studied in literature [6]. For instance, some studies [7–11] were focused on the influence of GBs on the dislocation emission, other works [12–14] concerned with the effect of crack blunting on the material toughening and research [15–17] examined the critical condition of the GB sliding. However, the aforementioned models did not consider the brittle vs ductile response to the increment of mechanical properties of the materials under temperature increase. The analysis of the occurrence of either brittle or ductile behaviors of ceramics with regard to the temperature conditions seem to be an essential issue that could be ascertained

through thorough investigation of the critical conditions for both crack propagation and dislocation emission as well as stress concentration effects associated with cracks.

In our previous research, the stress concentration induced by triangular-shaped pores [18] and inhomogeneities [19] in ceramics was investigated by both the perturbation technique and finite element method. It was demonstrated that the first-order semi-analytical solution is in a good agreement with the results of finite element simulations. Besides, a finite element simulation was employed in [20] to reveal the favorability of various crack configurations in a ceramic composite containing a lamellar inhomogeneity viz. crack initiation in the matrix, in the inhomogeneity and at the interface. It was shown that, in the case of relatively rigid inhomogeneities, the crack initiation is more feasible in the matrix region near the interface, in contrast to the case of relatively soft inhomogeneities, when the cracks are expected to occur either in the inhomogeneity or at the interface.

This work is aimed at analyzing the favorability of failure scenarios considering the intergranular fracture initiated on a pore at a triple junction (TJ) of GBs in a monolithic ceramics. The GBs are assumed to be the preferred pathways for crack propagation. In doing so, we investigate the critical conditions for crack cleavage and dislocation slip with respect to the temperature, implement the finite element simulation to determine stress concentration effects due to both rounded triangular pore and elliptical crack, and exhibit the preferred fracture scenarios in dependence of the temperature and geometric parameters of the problem. It is worth noting that this study considers the plasticity through the dislocation mechanisms and does not concern other mechanisms such as the GB sliding.

Model

Consider a pore located in an equilibrium TJ of GBs in a ceramic material exerted by axial loading S_0 (see Fig. 1(a)). The following failure scenarios can be expected: (i) intergranular fracture due to crack initiation at the pore and subsequent growth along the GB, (ii) ductile fracture due to dislocation nucleation on either the crack or the pore. The preference of these scenarios is mainly determined by both local stresses prescribed by the pore or crack geometry and temperature conditions defining the critical cleavage stress for crack propagation and the critical stress for dislocation nucleation.

According to [21], the critical cleavage stress (theoretical strength) for crack advance can be estimated as follows:

$$S_c = \sqrt{\frac{E\gamma}{x_0}}, \tag{1}$$

where E is the Young modulus, γ is the specific surface energy, and x_0 is the interatomic distance of the material. Generally speaking, the values of material parameters E and γ are strongly defined by the temperature of a sample. For instance, Nie et al [22] investigated the Young modulus of α-Al_2O_3 ceramics at high temperatures by applying the impulse excitation technique and the static three- and four-point bending tests. They demonstrated that the elastic modulus of alumina at first slowly decreased from 20 to 1000 °C and then rapidly dropped with the increase in temperature from 1000 to 1300 °C. The results of these measurements are given in Table 1.

Table 1. Temperature dependence of the Young modulus of α-Al_2O_3 ceramics [22]

Temperature, °C	20	400	600	800	1000	1100	1200	1300
Young modulus, GPa	282	269	250	235	195	132	88	27

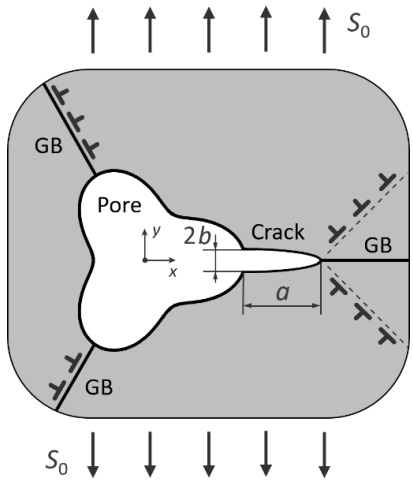

Fig. 1. Various scenarios of microfracture: the intergranular fracture due to the crack initiation at the TJ pore and the ductile fracture due to dislocation emission from the pore and the crack tip

As for the specific surface energy γ, the experiments [23] and theoretical modelling [24] clearly indicate its linear decrease in ceramics when the temperature increases from 0 K to the melting point. For α-Al_2O_3 ceramics, the following approximation is valid:

$$\gamma = \gamma_0 - \beta T, \quad (2)$$

where the temperature T is given in K, $\beta \approx 0.83$ mJ/(m^2 K) and $\gamma_0 \approx 2138$ mJ/m^2.

In addition, the interatomic distance x_0 in the α-Al_2O_3 ceramics can be estimated as ~ 0.25 nm over the wide range of temperatures.

To evaluate the critical stress for dislocation slip in dependence on temperature in the α-Al_2O_3 ceramics, the following empirical formulas can be employed [25]:

$$\ln \tau_{cb} = \ln \tau_{0b} - 0.0052T, \quad (3)$$

where τ_{cb} is a critical shear stress for basal dislocation slip, τ_{0b} = 109 GPa, and T is given in K.

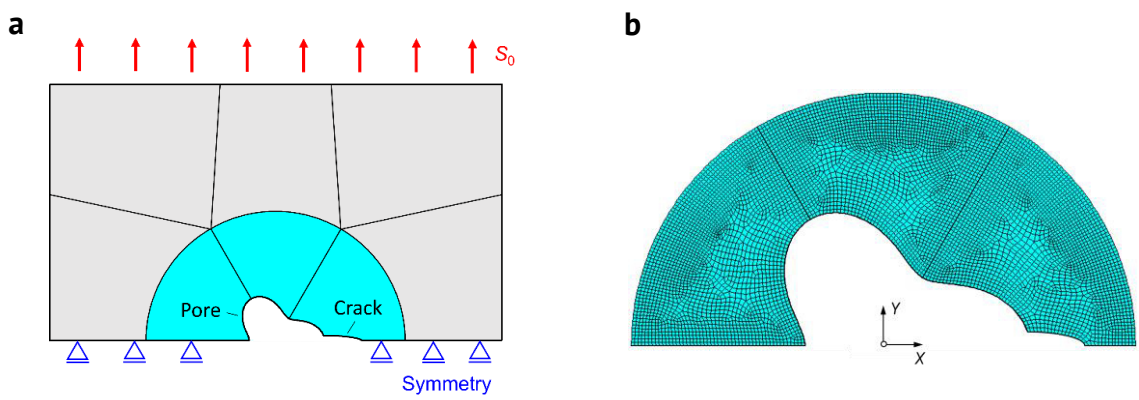

Fig. 2. (a) The finite element model of a ceramic material containing a triangular-shaped pore and an elliptical crack. The prescribed boundary conditions are shown. (b) The magnified inset highlights the irregular finite element mesh in vicinity of the pore and the crack for $\varepsilon = 0.3$

The local stress associated with the geometrical aspects of the crack and the pore can be calculated within finite element simulations. A 2D finite element model of a ceramic material containing a triangular-shaped pore and an elliptical crack has been prepared in a commercial software as shown in Fig. 2. The rounded triangular shape of three-fold symmetry of the pore is prescribed by the following analytical equations [18,19]:

$$x = (R_0 + \varepsilon \cos 3\theta) \cos\theta, \quad (4)$$

$$y = (R_0 + \varepsilon \cos 3\theta) \sin\theta, \quad (5)$$

where (x,y) are the coordinates of the pore boundary, θ is the polar angle, and the parameter ε describes the maximum deviation of pore boundary from the circle of radius R_0.

The crack shape is treated as an elliptical one with semi-axes a and b. The radius of the crack tip can be determined as follows $\rho = b^2 / a$. The model is built up from 2D plane elements containing 8 nodes to better approximate the pore and crack geometry. The top of the model is loaded by an external pressure S_0, while the bottom is fixed in the y-direction due to the symmetry of the problem under consideration. The size of the model is considered to be big enough to neglect the shielding effects of the external boundaries. The material is supposed to be linearly elastic and isotropic, determined by the Young modulus E according to Table 1 and the Poisson ratio $\nu = 0.25$.

Results

The derived temperature dependences of the critical stress for crack propagation (Eq. 1) and the critical stress of dislocation nucleation (Eq. 3) for the case of α-Al_2O_3 ceramics are shown in Fig. 3. The latter stress is expressed through the equivalent tensile stress as follows: $S_{db} = 2\tau_{cb}$. As is seen from Fig. 3, the critical stresses decrease when the temperature increases. Moreover, at relatively low temperatures, the critical cleavage stress S_c is much lower than the critical stress for dislocation generation S_{db}, i.e. the material tends to the brittle fracture. On the contrary, at relatively high temperatures, the critical cleavage stress exceeds the critical stress of dislocation slip, i.e. the ductile fracture is expected. It is worth noting that, in the case of α-Al_2O_3 ceramics, the threshold temperature T_1 takes a value close to 300 K (T_1 ~ 20 °C). Besides, the cleavage stress S_c estimated at 0 K takes a value close to 48.9 GPa shown by density functional calculations [26].

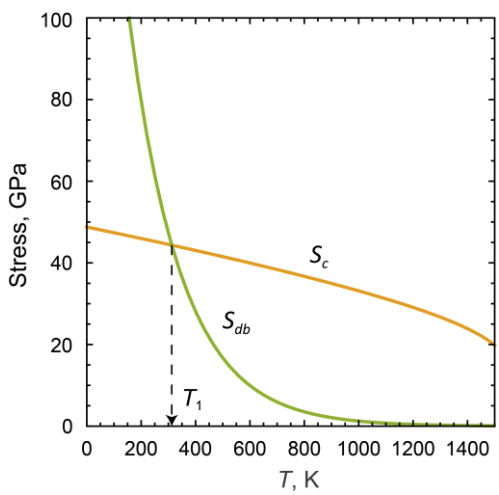

Fig. 3. Dependence of the critical cleavage stress S_c and the critical stress of dislocation slip S_{db} on the temperature for α-Al_2O_3 ceramics

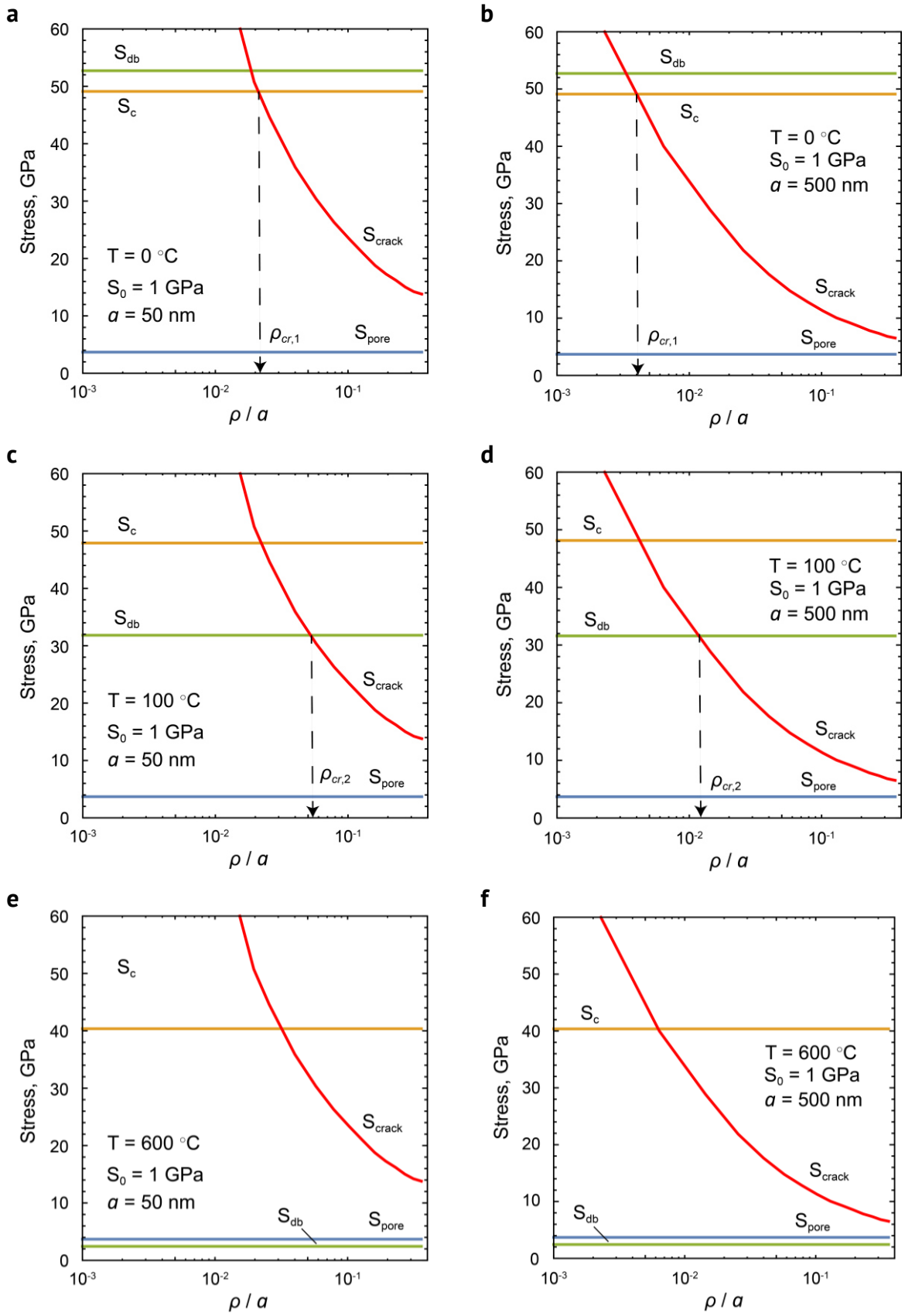

Fig. 4. Maximum local stress in vicinities of the crack tip, S_{crack}, and the rounded triangular pore, S_{pore}, under the uniaxial tensile stress S_0 = 1 GPa vs the crack tip radius to crack length ratio ρ / a at a / R_0 = 1/2 and crack lengths 50 (a,c,e) and 500 nm (b,d,f) for the three different temperatures: (a,b) 0, (c,d) 100, and (e,f) 600 °C

Thus, the cracks tend to propagate if the temperature is less than the threshold one that is T_1. Otherwise, one can expect the emission of dislocations from the crack with subsequent blunting of its tip at elevated temperatures, when $T > T_1$. This phenomenon can lead to significant decrease of local stress in the crack tip, thus suppressing the brittle behavior of cracks.

Taking into account the above theoretical analysis, some numerical calculations have been carried out to demonstrate the impact of the crack and pore geometry on the local stress concentration. Figure 4 depicts the local stress calculated by the finite element simulation at the elliptic crack and the rounded triangle pore in dependence on the normalized crack tip radius ρ / a. The following failure scenarios are elucidated below.

(i) *Brittle fracture*. This scenario is attributed to relatively low temperatures when the critical stress of dislocation slip S_{db} is higher than the critical cleavage stress S_c. As is seen from Fig. 4(a,b), for $T < T_1$, the local stress at the crack tip, S_{crack}, exceeds the critical cleavage stress S_c for relatively sharp cracks with $\rho < \rho_{cr,1}$. It means that these cracks have a tendency to advance provoking the brittle fracture. On the contrary, the local stress influenced by the blunting is not high enough to exert the crack propagation if the crack tip radius ρ exceeds the critical one $\rho_{cr,1}$, $\rho > \rho_{cr,1}$. On the other hand, the local stress at the pore is considerably lower than that at the crack tip and does not depend on the crack length.

(ii) *Quasi-brittle fracture*. In contrast to the previous scenario, the critical stress for the dislocation slip activation is lower than the critical cleavage stress ($T > T_1$), i.e. the dislocation emission becomes the most favorable mechanism. Fig. 4(c,d) shows that the local stress at the crack tip S_{crack} can be high enough to provide the dislocation emission that is accompanied by the crack tip blunting when $\rho < \rho_{cr,2}$. One can expect that S_{crack} decreases due to the blunting process as long as the radius of the crack tip reaches its critical value $\rho_{cr,2}$. The cracks with tip radius $\rho > \rho_{cr,2}$ are unable to either propagate or emit dislocations until the external tensile stress S_0 gets a necessary level. The local stress at the pore S_{pore} remains so low that the pore can not emit dislocations.

(iii) *Ductile fracture*. In the case of relatively high temperatures ($T > 500$ °C), the critical stress of dislocation slip becomes so low that the pore is enabled to emit dislocations as is seen from Fig. 4(e,f). It means that the fracture fashion in monolithic ceramic materials at elevated temperatures can be largely determined by the dislocation emission from pre-existing pores.

It is worth noting that the local stress in vicinity of relatively small cracks (of length $a = 50$ nm) is essentially influenced by the concentration effect of the triangular-shaped pore while the relatively large cracks (of length $a = 500$ nm) are not responsive to the pore effect. As a result, small cracks have a tendency to accelerate the evolution process through either growing or blunting.

Conclusions

In this study, different failure scenarios in monolithic ceramics at evaluated temperatures have been elucidated. In doing so, a Mode I crack initiated at a triple-junction pore under uniaxial tensile stress has been considered. The critical stresses for crack cleavage and dislocation emission have been derived for the case of α-Al_2O_3 ceramics with regard to the temperature. The finite element analysis incorporating both the elliptical shape of the crack and rounded triangle shape of the pore has been employed to determine the local stress concentration effects. It has been assumed that the cracks tend to propagate

when the maximum local stress exceeds the critical cleavage stress whereas the dislocation emission occurs when the maximum local stress attains the critical stress of dislocation slip. As a result, the following failure scenarios with respect to the temperature and defect geometry are suggested. It is shown that, at relatively low temperatures ($T < T_1$), the critical fracture stress is less than that for dislocation slip. In this case, the local stress at the crack tip is sufficient to provoke the cleavage if the crack tip is sharp enough, $\rho < \rho_{cr,1}$. This fracture fashion is considered as a brittle failure. In the range of medium temperatures ($T > T_1$), the dislocation emission precedes cleavage as the critical stress of dislocation slip becomes lower than the critical fracture stress. As a result, the multiple emission of dislocations from the tip converts a sharp crack into the blunt one until the crack tip radius ρ takes its critical value $\rho_{cr,2}$. The cracks with tip radii $\rho > \rho_{cr,2}$ are able to advance only when the temperature and the loading conditions are changed. This fracture fashion is treated as quasi-brittle failure. At elevated temperatures ($T > 500$ °C), the critical stress for dislocation emission becomes lower than the maximal local stress at the triangular-shaped pore. It means that the dislocation emission from the pore is the most favorable response to external loading. In this case, the significant plastic deformation preceding the failure is expected.

Thus, it has been shown that the preference of the considered fracture scenarios in a ceramic material is determined by temperature range and geometrical parameters of pre-existing pores and cracks. Another important finding is that the significant plasticity of ceramics at elevated temperatures can be explained in terms of dislocation emission from the pre-existing pores.

References

1. Simonenko EP, Simonenko NP, Sevastyanov VG, Kuznetsov NT. ZrB 2/HfB 2–SiC Ultra-High-Temperature Ceramic Materials Modified by Carbon Components: The Review. *Russian Journal of Inorganic Chemistry*. 2018;63: 1772–1795.
2. Savino R, Mungiguerra S, Martino GD. Testing ultra-high-temperature ceramics for thermal protection and rocket applications. *Advances in Applied Ceramics*. 2018;117(1): 9–18.
3. Fahrenholtz WG, Hilmas GE. Ultra-high temperature ceramics: Materials for extreme environments. *Scripta Materialia*. 2017;129: 94–99.
4. Faoite D, Browne DJ, Chang-Díaz FR, Stanton KT. A review of the processing, composition, and temperature-dependent mechanical and thermal properties of dielectric technical ceramics. *Journal of Materials Science*. 2012;47: 4211–4235.
5. Zapata-Solvas E, Jayaseelan DD, Lin HT, Brown P, Lee WE. Mechanical properties of ZrB2-and HfB2-based ultra-high temperature ceramics fabricated by spark plasma sintering. *Journal of the European Ceramic Society*. 2013;33(7): 1373–1386.
6. Ovidko IA. Micromechanics of fracturing in nanoceramics. *Philosophical Transactions of the Royal Society A: Mathematical, Physical and Engineering Sciences*. 2015;373(2038): 20140129.
7. Bobylev SV, Mukherjee AK, Ovidko IA. Emission of partial dislocations from amorphous intergranular boundaries in deformed nanocrystalline ceramics. *Scripta Materialia*. 2009;60(1): 36–39.
8. Ovidko IA, Sheinerman AG. Grain size effect on crack blunting in nanocrystalline materials. *Scripta Materialia*. 2009:60(8): 627–630.
9. Zeng XH, Hartmaier A. Modeling size effects on fracture toughness by dislocation dynamics. *Acta Materialia*. 2010;58(1): 301–310.
10. Armstrong RW. Material grain size and crack size influences on cleavage fracturing. *Philosophical Transactions of the Royal Society A: Mathematical, Physical and Engineering Sciences*. 2015;373(2038): 20140124.
11. Reiser J, Hartmaier A. Elucidating the dual role of grain boundaries as dislocation sources and obstacles and its impact on toughness and brittle-to-ductile transition. *Scientific Reports*. 2020;10(1): 2739.

12. Beltz GE, Lipkin DM, Fischer LL. Role of crack blunting in ductile versus brittle response of crystalline materials. *Physical Review Letters*. 1999;82(22): 4468.
13. Fischer LL, Beltz GE. The effect of crack blunting on the competition between dislocation nucleation and cleavage. *Journal of the Mechanics and Physics of Solids*. 2001;49(3): 635–654.
14. Ovidko IA, Skiba NV, Sheinerman AG. Influence of grain boundary sliding on fracture toughness of nanocrystalline ceramics. *Physics of the Solid State*. 2008;50: 1261–1265.
15. Ovidko IA, Sheinerman AG. Ductile vs. brittle behavior of pre-cracked nanocrystalline and ultrafine-grained materials. *Acta Materialia*. 2010;58(16): 5286–5294.
16. Sheinerman AG, Ovidko IA. Grain boundary sliding and nanocrack generation near crack tips in nanocrystalline metals and ceramics. *Materials Physics and Mechanics*. 2010;15(1/2): 37–46.
17. Sheinerman AG, Morozov NF, Gutkin MY. Effect of grain boundary sliding on fracture toughness of ceramic/graphene composites. *Mechanics of Materials*. 2019:137: 103126.
18. Vakaeva AB, Krasnitckii SA, Smirnov A, Grekov, MA, Gutkin MY. Stress concentration and distribution at triple junction pores of three-fold symmetry in ceramics. *Reviews on Advanced Materials Science*. 2018;57(1): 63–71.
19. Vakaeva AB, Krasnitckii SA, Grekov MA, Gutkin MYu. Stress field in ceramic material containing threefold symmetry inhomogeneity. *Journal of Materials Science*. 2020;55(22): 9311–9321.
20. Ignateva EV, Krasnitckii SA, Sheinerman AG, Gutkin MYu. The finite element analysis of crack tolerance in composite ceramics. *Materials Physics and Mechanics*. 2023:51(2): 21–26.
21. Anderson TL. *Fracture mechanics: fundamentals and applications*. CRC press; 2017.
22. Nie GL, Bao YW, Wan DT, Tian Y. Measurement of the high temperature elastic modulus of alumina ceramics by different testing methods. *Key Engineering Materials*. 2018;768: 24–30.
23. Cheng T, Fang D, Yang Y. The temperature-dependent surface energy of ceramic single crystals. *Journal of the American Ceramic Society*. 2017;100(4): 1598–1605.
24. Weirauch DA, Ownby PD. Application of the Zisman critical surface tension technique to ceramic surfaces at high temperature. *Journal of Adhesion Science and Technology*. 1999;13(11): 1321–1330.
25. Lagerlöf KPD, Heuer AH, Castaing J, Rivière JP, Mitchell TE. Slip and twinning in sapphire (α-Al2O3). *Journal of the American Ceramic Society*. 1994;77(2): 385–397.
26. Huang HY, Wu M. First principles calculations of hydrogen-induced decrease in the cohesive strength of α-Al2O3 single crystals. *Computational Materials Science*. 2012;54: 81–83.

About Authors

Stanislav A. Krasnitckii Sc
Candidate of Physical and Mathematical Sciences
Associate Professor (ITMO University, St. Petersburg, Russia)
Researcher (St. Petersburg State University, St. Petersburg, Russia)

Alexander G. Sheinerman Sc
Doctor of Physical and Mathematical Sciences
Lead Researcher (Institute for Problems in Mechanical Engineering RAS, St. Petersburg, Russia)

Mikhail Yu. Gutkin Sc
Doctor of Physical and Mathematical Sciences
Head of Department, Principal Researcher (Institute for Problems in Mechanical Engineering RAS, St. Petersburg, Russia)

MATERIALS PHYSICS AND MECHANICS RESEACH ARTICLE

Submitted: April 8, 2023 Revised: April 30, 2023 Accepted: April 4, 2024

Studies of trapezoidal panels under thermo-mechanical load: a nonlinear dynamic analysis

E. Kumari [1] ✉, **S. Lal** [2],

[1] MBM University, Jodhpur, India

[2] Rajasthan Technical University, Kota, India

✉ emarti.me@mbm.ac.in

ABSTRACT

Large amplitude flexural and vibration behavior of trapezoidal panels with sixteen node degenerated shell element are studied under thermo-mechanical load. The finite element formulation has been done considering the first-order shear deformation theory with incorporation of Von Karman's geometric nonlinearity, and the governing equations are solved using energy and conservation time integration scheme (combination of trapezoidal and three-point Euler backward method). The efficacy of the method is checked for nonlinear static and dynamic responses of both trapezoidal plate and curved panel. The effect of cord to span ratio (c/a), radius to span ratio (R/a), boundary conditions and stacking sequence on the nonlinear dynamic response of trapezoidal panels are also investigated under thermo-mechanical load. Moreover, new results for nonlinear dynamic response of trapezoidal panels under step thermal load with and without radial pressure are also presented and that will be important outcomes for the scientific community.

KEYWORDS

trapezoidal panels • finite element method • laminated composite • thermo-mechanical • nonlinear dynamic

Citation: Kumari E, Lal S. Studies of trapezoidal panels under thermo-mechanical load: a nonlinear dynamic analysis. *Materials Physics and Mechanics*. 2024;52(2): 90–105.
http://dx.doi.org/10.18149/MPM.5222024_10

Introduction

The laminated trapezoidal panels widely used in the various industries like aeronautical (wing panels, tail panels), ship hulls, automobile and defence industries etc., due to its flexible, high strength to weight ratio, and superior corrosion resistance. This type of thin-wall structures are subjected to step thermal and mechanical load, hence the nonlinear dynamic behaviour of trapezoidal flat and curved panels is an important matter of concern to design sustainable structures. The studies of nonlinear dynamic response of laminated trapezoidal panels under step thermal load with and without mechanical load is very important, hence it is investigated.

Srinivasan and Babu [1] investigated the free vibration and flutter characteristics of laminated quadrilateral plates. The transverse vibrational frequencies and mode shapes characteristics of symmetric trapezoidal plates were analysed by implementing the superposition method [2]. Ng and Das [3] studied the linear free vibration and buckling behaviour of skew plates under in-plane forces by applying Galerkin's variational method. The linear vibration frequencies of composite triangular and trapezoidal shells was examined by employing shallow shell theory with Ritz method [4]. Han and Petyt [5,6] studied the linear vibration behaviour of composite plates of rectangular shape using *p*-version FEM (Finite Element Method) under no load and harmonic plane wave incident

normal to plate surface; respectively. Vibration characteristics of continuous rectangular plates were analysed by using a discrete method [7]. Kumar *et al.* [8] elaborated the linear free vibrational behaviour of composite skew panels employing FEM with high order shear deformation based on the C_0 continuity.

Malekzadeh [9] investigated large amplitude free vibration characteristics of laminated skew thin plates by employing differential quadrature (DQ) method.

Gupta and Sharma [10] calculated the frequencies of clamped-simply supported trapezoidal plates having linearly varying thickness in the presence of thermal gradient by applying Rayleigh-Ritz method. Nguyen-Minh *et al.* [11] illustrated the free vibration characteristics of trapezoidal and sinusoidal corrugated panels using homogenization method with first order shear deformation theory. It was considered a cell-based smoothed Mindlin plate element for linear dynamic analysis. Rout *et al.* [12] studied the free vibration characteristics of doubly curved composite panels under thermal loading by employing FEM with consideration of higher-order shear deformation theory. Liu *et al.* [13] conducted experiments on six different shape aluminium plates and applied unified coordinate transformation method with Lagrange interpolation method to study the in-planer free vibration behaviour of arbitrarily shaped plates. Authors compared the analytical (two-dimensional spectral-Chebyshev polynomial) and experimental results with available numerical results for clamped and cantilever boundary conditions. Niu and Yao [14] carried out the linear and nonlinear vibrational analysis of composite tapered flat graphene platelet and curved panels under transverse excitations. Li and Cheng [15] studied the vibration characteristics pre-twisted rotation blades using shallow shell theory. It was considered the centrifugal force and Coriolis acceleration due to rotation of blade and observed the effect of spring stiffness variation, thickness variation of cantilever plate.

Dou *et al.* [16] investigated the shear buckling behaviour of corrugated isotropic plates using FEM based ANSYS R113.0 software. Franzoni *et al.* [17] experimentally studied the buckling behaviour of unstiffened laminated cylindrical shells; and compared the presented experimental results with numerical results obtained by ABQUAS 6.16. Magnucka-Blandzi [18,19] formulated the multi-layered beam and trapezoidal plate using Hamilton's principle to study the stability and vibrational behaviour of thin-walled structure, and compared the presented analytical results with numerical results. Watts *et al.* [20] used the element free Galerkin method to investigate the dynamic instability characteristics of shear deformable trapezoidal plate under non-uniform compressive loads. It was derived the governing equations by employed the Hamilton's principle and Mathieu-Hill type ordinary differential equations and solved by Bolotin's method to analyse the dynamic instability. Linear and nonlinear static and dynamic responses of folded structures, rectangular and trapezoidal curved panels were investigated [21–27] by using the FEM based first-order shear deformation theory with incorporating the von-Karman's kinematic geometric nonlinearity. The linear vibration behaviour of functionally graded plates resting on elastic foundation was studied by Kumar *et al.* [28] using higher-order shear deformation theory. Recently, in [29–32] it was investigated the stability characteristics of structures in the presence of thermal environment.

From the literature review, it is observed that the large amplitude flexural vibration behaviour of composite trapezoidal panels is scarce. Therefore, the dynamic characteristic of trapezoidal panels subjected to thermo-mechanical loading is illustrated here. In this

communication, the authors employed the finite element method using a degenerated shell element to study the large amplitude flexural vibration behaviour of laminated composite trapezoidal panels under mechanical load in the presence of a thermal environment.

Mathematical Modelling

FEM Formulations

A schematic representation of shell element geometry is presented in Fig. 1, it is having sixteen nodes and five degrees of freedom at each node (u_1^k, u_2^k, u_2^k, α_k and β_k) is used here to modelling the composite trapezoidal panels. The global geometrical coordinates x_i, I = 1, 2, 3 and displacement components u_i, i = 1, 2, 3 along the unit vectors V_1^k, V_2^k and V_n^k as represented in the Fig. 1 [33].

$$x_i = \sum_{k=1}^{16} N_k\, x_i^k + \frac{t}{2}\sum_{k=1}^{16} hN_k\, {}^{t}V_{ni}^k, \tag{1}$$

$$u_i = \sum_{k=1}^{16} N_k\, u_i^k + \frac{t}{2}\sum_{k=1}^{16} hN_k V_{ni}^k, \tag{2}$$

where, N_k is an interpolation function associated with the node k = 1, 16; x_i^k is the global coordinates of the node k, i = 1, 2, 3; ${}^{t}V_{ni}^k$ is normal to the shell mid-surface at node k; $V_{ni}^k = {}^{t}V_{ni}^k - {}^{0}V_{ni}^k$ stores the addition in the direction cosines of ${}^{0}V_{ni}^k$.

$$\Delta V_n^k = -{}^{t}V_2^k \alpha_k + {}^{t}V_1^k \beta_k \tag{3}$$

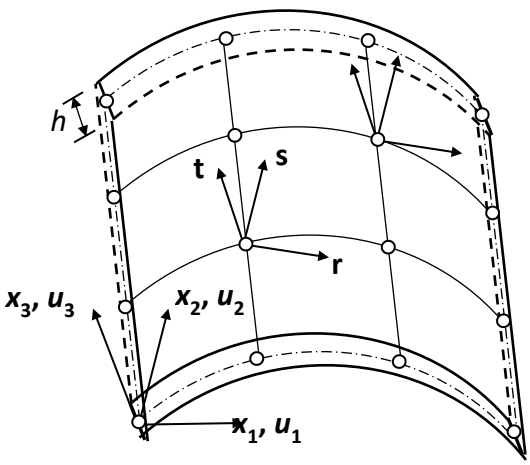

Fig. 1. Schematic diagram of 16-node shell element

The alteration in the direction cosines of the shell element (ΔV_n^k) shall be demonstrated as a nodal rotations (α_k and β_k) about two unit vectors ${}^{t}V_1^k$ and ${}^{t}V_2^k$ at the time t as [33–35].

The strain tensors ($\varepsilon_{ij} = e_{ij} + \eta_{ij}$) may be written as linear strains (e_{ij}) and nonlinear strains (η_{ij}) in terms of displacement components (u_i, i = 1, 2, 3):

$$e_{ij} = \frac{1}{2}(u_{i,j} + u_{j,i}) \text{ and } \eta_{ij} = \frac{1}{2}u_{k,i}u_{k,j};\ i, j, k = 1, 2, 3. \tag{4}$$

Firstly, the strain components are determined by direct interpolation at the Gaussian points, and it is called direct strains ε_{ij}^{DI}. Thereafter, the shear strains & direct strain

components are further interpolated at the trying points to eliminate the spurious membrane and computed the assumed strains may be written as:

$$\varepsilon_{ij}^{AS}(r,s) = \sum_{k=1}^{n_{ij}} N_k^{ij}(r,s)\varepsilon_{ij}^{DI}(r,s), \tag{5}$$

here, $N_k^{ij}(r,s)$ represents the interpolation functions or shape functions (polynomials in isoparametric coordinate systems r and s) associated with the strain component ε_{ij}at trying point k and n_{ij} is the number of trying points (adopted from Bathe [33]).

The σ_{ij} is thermo-elastic stress component in a lamina which having ply-orientation (θ) with unit vector V_1^k will be written as:

$$\begin{Bmatrix} \sigma_{11} \\ \sigma_{22} \\ \sigma_{33} \\ \sigma_{23} \\ \sigma_{13} \\ \sigma_{12} \end{Bmatrix} = \begin{bmatrix} \bar{Q}_{11} & \bar{Q}_{12} & 0 & 0 & 0 & \bar{Q}_{16} \\ \bar{Q}_{21} & \bar{Q}_{22} & 0 & 0 & 0 & \bar{Q}_{26} \\ 0 & 0 & 0 & 0 & 0 & 0 \\ 0 & 0 & 0 & \bar{Q}_{44} & \bar{Q}_{45} & 0 \\ 0 & 0 & 0 & \bar{Q}_{54} & \bar{Q}_{55} & 0 \\ \bar{Q}_{61} & \bar{Q}_{62} & 0 & 0 & 0 & \bar{Q}_{66} \end{bmatrix} \begin{Bmatrix} \varepsilon_{11} - \alpha_{11}\Delta T \\ \varepsilon_{22} - \alpha_{22}\Delta T \\ \varepsilon_{33} \\ \varepsilon_{23} \\ \varepsilon_{13} \\ \varepsilon_{12} - \alpha_{12}\Delta T \end{Bmatrix} \tag{6}$$

where, $\bar{Q}_{ij}$is the plane stress-reduced stiffness matrix of the laminates at h from the natural x-axis may be written by:

$$\bar{Q}_{11} = Q_{11}\cos^4\theta + 2(Q_{12} + 2Q_{66})\sin^2\theta\cos^2\theta + Q_{22}\sin^4\theta,$$
$$\bar{Q}_{12} = (Q_{11} + Q_{22} - 4Q_{66})\sin^2\theta\cos^2\theta + Q_{12}(\sin^4\theta + \cos^4\theta),$$
$$\bar{Q}_{22} = Q_{11}\sin^4\theta + 2(Q_{12} + 2Q_{66})\sin^2\theta\cos^2\theta + Q_{22}\cos^4\theta,$$
$$\bar{Q}_{16} = (Q_{11} - Q_{12} - 2Q_{66})\sin\theta\cos^3\theta + (Q_{12} - Q_{22} + 2Q_{66})\sin^3\theta\cos\theta,$$
$$\bar{Q}_{26} = (Q_{11} - Q_{12} - 2Q_{66})\sin^3\theta\cos\theta + (Q_{12} - Q_{22} + 2Q_{66})\sin\theta\cos^3\theta,$$
$$\bar{Q}_{66} = (Q_{11} + Q_{22} - 2Q_{12} - 2Q_{66})\sin^2\theta\cos^2\theta + Q_{66}(\sin^4\theta + \cos^4\theta),$$
$$\bar{Q}_{44} = Q_{44}\cos^2\theta + Q_{55}\sin^2\theta,\ \bar{Q}_{45} = (Q_{55} - Q_{44})\cos\theta\sin\theta,$$
$$\bar{Q}_{55} = Q_{55}\cos^2\theta + Q_{44}\sin^2\theta,$$

where, $Q_{11} = \frac{E_1}{1-\nu_{12}\nu_{21}}$; $Q_{12} = \frac{\nu_{12}E_2}{1-\nu_{12}\nu_{21}}$; $Q_{22} = \frac{E_2}{1-\nu_{12}\nu_{21}}$; $Q_{66} = G_{12}$; $Q_{44} = G_{23}$; $Q_{55} = G_{13}$; α_{ij} is the transformation of thermal coefficients and it can be written by:

$$\alpha_{11} = \alpha_L\cos^2\theta + \alpha_T\sin^2\theta;\ \alpha_{22} = \alpha_L\sin^2\theta + \alpha_T\cos^2\theta;\ \alpha_{12} = (\alpha_L - \alpha_T)\cos\theta\sin\theta.$$

The E_1, E_2 and E_3 in above equations are young's modulus along longitudinal, transverse and normal directions respectively; G_{23}, G_{13} and G_{12} are shear modulus in the *2-3* plane, *1-3* plane and *1-2* plane respectively; $\nu_{23} = \nu_{13} = \nu_{12}$ is the Poisson's ratio; and α_L and α_T are thermal expansion coefficient along with the longitudinal and transverse direction; $\Delta T = T - T_0$ is the change in temperature from room temperature T_0.

Anisotropic case reduced to isotropic: $E_1 = E_2 = E_3 = E$; $\nu_{12} = \nu_{13} = \nu_{23} = \nu$ and $\alpha_L = \alpha_T = \alpha$.

Governing equation of motion for nonlinear dynamic analysis

The nonlinear equation of motion for dynamic analysis of isotropic and laminated composite trapezoidal panels under thermo-mechanical loading condition can be written as:

$$[M]\{\ddot{\delta}\} + [K_L + K_{NL1}(\delta) + K_{NL2}(\delta,\delta)]\{\delta\} = \{F_M\} + \{F_T\}. \tag{7}$$

Here, $[M]$ is the mass matrix; $[K_L]$ is the linear stiffness matrix; $[K_{NL1}]$ and $[K_{NL2}]$ are the nonlinear stiffness matrix; $\{\delta\}$ and $\{\ddot{\delta}\}$are the displacement and acceleration vector of degrees of freedom; $\{F_M\}$ and $\{F_T\}$ are the nodal load vectors due to radial pressure and thermal load; respectively.

Solution procedure

Nonlinear static analysis. The equation (7) will be employed to investigate the linear and nonlinear bending and vibrational analysis by neglecting the appropriate terms.

The governing equation for nonlinear bending analysis may be expressed as:

$$[K_L + K_{NL1}(\delta) + K_{NL2}(\delta,\delta)]\{\delta\} = \{F_M\} + \{F_T\}. \tag{8}$$

The Newton Raphson iterative scheme is used to solve the Eq. (8) for nonlinear static analysis of trapezoidal panels.

Residual force:

$$\{\Delta F^i\} = \left[K_L + K_{NL1}(\delta^i) + K_{NL2}(\delta^i,\delta^i)\right]\{\delta^i\} - \{F_M\} - \{F_T\}, \tag{9}$$

$$\left[K_T^i\right]\{\Delta\delta^{i+1}\} = \{\Delta F^i\}, \tag{10}$$

$$\{\delta^{i+1}\} = \{\delta^i\} + \{\Delta\delta^{i+1}\}, \tag{11}$$

where, $[K_T]$ is tangent stiffness matrix and "i" (i = 1, 2, 3, ...) is the number of iterations.

The iteration process is repeated until the difference between $\{\delta^i\}$ and $\{\delta^{i+1}\}$ becomes smaller than error tolerance (ε = 0.001) as discussed by Maleki and Tahani [37]. In this investigation an error criteria is taken by:

$$\sqrt{\frac{\sum_{J=1}^{NP}\left|\delta_J^{i+1} - \Delta\delta_J^{i+1}\right|^2}{\sum_{J=1}^{NP}\left|\Delta\delta_J^{i+1}\right|^2}} \le \varepsilon, \tag{12}$$

where N_P is number of unknowns.

Linear vibration analysis. Linear free vibration frequencies of trapezoidal panel are determined by neglecting appropriate terms in Eq. (7), equation of motion is written as follows:

$$[M]\{\ddot{\delta}\} + [K_L]\{\delta\} = \{0\}. \tag{13}$$

Here, displacement $\{\delta\}$ vector is assumed to be function of simple harmonic motion$\{\delta\} = A\,sin\,\omega_i\,t$; $\{\ddot{\delta}\} = -A\omega_i^2\,sin\,\omega_i\,t$; i = 1,2,3.....n (n = degree of freedom of the panel). By using Eq. (13) calculated the natural frequencies of the trapezoidal panels.

Nonlinear dynamic analysis. The nonlinear dynamic analysis of trapezoidal panel is obtained by solving Eq. (7) with the defined initial conditions.

$$\{\delta(0)\} = \{a\} \text{ and } \quad \{\dot{\delta}(0)\} = \{b\}. \tag{14}$$

The energy and momentum conservation implicit time integration method [30] has been used here to solve the equation of motion (7) for the nonlinear dynamic response of trapezoidal panels under thermo-mechanical load.

The velocity and acceleration at each time step ($t + \Delta t$) may be written as:

$$\dot{\delta}_{(t+\Delta t)} = \frac{1}{\Delta t}\delta_{(t)} - \frac{4}{\Delta t}\delta_{(t+\Delta t/2)} + \frac{3}{\Delta t}\delta_{(t+\Delta t)}, \tag{15}$$

$$\ddot{\delta}_{(t+\Delta t)} = \frac{1}{\Delta t}\dot{\delta}_{(t)} - \frac{4}{\Delta t}\dot{\delta}_{(t+\Delta t/2)} + \frac{3}{\Delta t}\dot{\delta}_{(t+\Delta t)}. \tag{16}$$

By substituting Eqs. (15), (16) into Eq. (7), we obtain:

$$\left[\frac{9}{\Delta t^2}M + K_T\right]\Delta\delta^i = F_{(t+\Delta t)} - (K_L + K_{NL})\delta_{(t+\Delta t)}^{(i-1)}\frac{1}{\Delta t}\dot{\delta}_{(t)} -$$
$$-M\left[\frac{9}{\Delta t^2}\delta_{(t+\Delta t)}^{(i-1)} - \frac{12}{\Delta t^2}\delta_{(t+\Delta t/2)} + \frac{3}{\Delta t^2}\delta_{(t)} - \frac{4}{\Delta t}\dot{\delta}_{(t+\Delta t/2)} + \frac{1}{\Delta t}\delta_{(t)}\right]. \tag{17}$$

Incremental displacement is updated at each sub-step using Eq. (11).

Results and Discussion

Geometrical model design

The schematic diagram of the trapezoidal (symmetric and unsymmetrical) flat and curved panels is shown in Fig. 2 with fiber orientation.

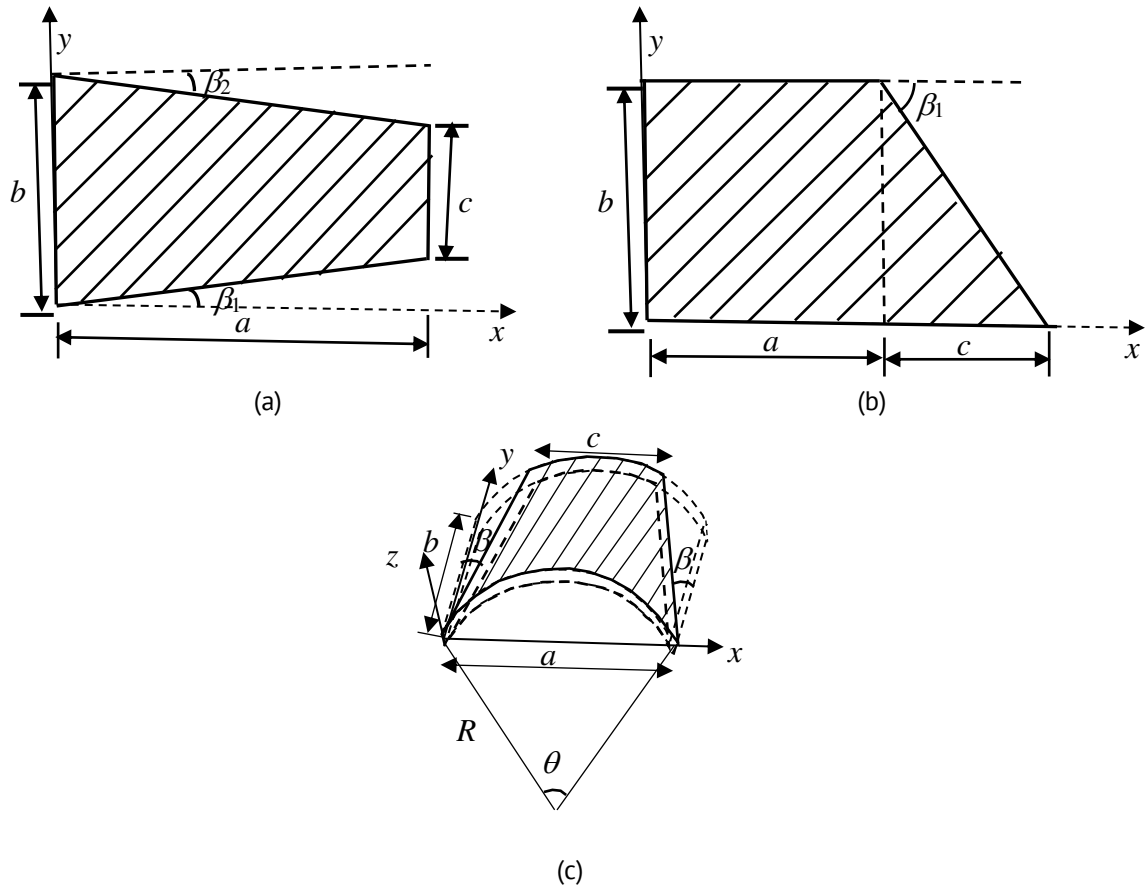

Fig. 2. Schematic representation of geometry with fibre-orientation of laminated (a) symmetric trapezoidal plate, (b) unsymmetrical trapezoidal plate, and (c) symmetric trapezoidal curved panel

Boundary conditions

The following boundary conditions are considered which are expressed in Table 1.

Table 1. Boundary conditions of various cases and their degree of freedom

S. No.	Boundary conditions	Degree of freedom restrained
1	Simply supported (*SSSS*)	
	Case 1	$u_l = u_t = u_3 = 0$; *along all edges*
	Case 2	$u_l = u_3 = \beta_t = 0$; at $x = 0, a$ and; $u_t = u_3 = \alpha_l = 0$; at $y = 0, b$
2	Clamped (*CCCC*)	$u_l = u_t = u_3 = \alpha_l = \beta_t = 0$; along all edges
3	CSCS	$u_l = u_t = u_3 = \alpha_l = \beta_t = 0$ at $y = 0, b$; $u_l = u_3 = \beta_t = 0$ at $x = 0, a$
4	*SCSF*	$u_l = u_t = u_3 = 0$; at $x = 0, a$; $u_l = u_t = u_3 = \alpha_l = \beta_t = 0$ at $y = 0$

Model validation

The following material properties of isotropic and laminated composite trapezoidal panels have been used to solve the equations:
1) For the Isotropic panels: $E = 1 \times 10^6$ N/m^2, $\nu = 0.3$, $\rho = 1.0$ kg/m^3, $\alpha = 1 \times 10^{-6}$ /°C.
2) For the Laminated composite panels: $E_1 = 53.8$ GPa, $E_2 = E_3 = 17.9$ GPa, $G_{23} = G_{13} = G_{12} = 8.68$ GPa, $\nu_{23} = \nu_{13} = \nu_{12} = 0.25$, $\rho = 1600$ kg/m^3, $\alpha_L = 6.3 \times 10^{-6}$ /°C, $\alpha_T = 20.5 \times 10^{-6}$ /°C, where, E_1, E_2, and E_3 denoted for young's modulus along longitudinal, transverse and normal direction; G_{23}, G_{13} and G_{12} are presented the shear modulus in $y - z$ plane, x - z plane and x - y plane respectively; ν_{23}, ν_{13} and ν_{12} are the Poisson's ratios; ρ is the density of used material; α_L and α_T are represents the thermal expansion along longitudinal and transverse directions; respectively.

Convergence Study

Linear bending and vibration analysis. First, examined the accuracy of developed FORTRAN code and evaluated the efficacy of degenerated sixteen node shell elements for linear vibration and bending analysis of symmetric and unsymmetrical trapezoidal flat panels as presented in the Tables 2 and 3, respectively.

The non-dimensional natural frequencies ($\varpi_i = (\omega_i a^2/\pi^2)\sqrt{\rho h/D}$; $i = 1,5$; ω_i is natural frequency in rad/sec; $D = Eh^3/12(1-\nu^2)$ is flexural rigidity of structure) of simply supported (case 1) and clamped isotropic symmetric trapezoidal are compared as given in Table 2 with available published results Watts *et al.* [20], Chopra and Durvasula [38] and Kitipornchai *et al.* [39] for various chord-to-span ratios (c/a = 0.2, 0.4, 0.6). Firstly, convergence study is performed for converge numerical results considering 2×2 and 4×4 mesh size. It is noticed that 4×4 mesh size results are matched very well with Galerkin method [38], Rayleigh-Ritz method [39] and meshless method [20]. Thereafter, percentage of errors are also examined for the isotropic ($\nu = 0.3$) symmetric trapezoidal flat panel (a/b = 1, and b/h = 100), and it is found that percentage of error is less than 0.1 and 0.2 % for fully clamped and simply supported panels, respectively. After mesh convergence, it is noticed that 4×4 mesh size is suitable for converged results. Moreover, also plotted the vibration mode shapes for an isotropic clamped symmetric trapezoidal flat panels (a/b = 1, b/h = 100, c/a = 0.6) and schematically shown in Fig. 3.

Then, the non-dimensional central deflection of simply supported (case 1) isotropic (ν=0.3) and laminated composite (cross-ply $[0°/90°]_S$ and angle-ply $[45°/-45°]_S$) moderately thick (a/h = 20) and thin (a/h = 100, 500) unsymmetrical trapezoidal (b/c = 1) flat panel are presented in Table 3 for different aspect ratios such as a/b = 1.0, 1.2, 1.4, 1.6, 1.8, and 2.0. The study is also compared the presented numerical and analytical results through Galerkin method published by Saadatpour and Azhari [36] for thin (a/h = 500) isotropic unsymmetrical trapezoidal plate. As concerned with error analysis, the root-mean-square error (RMSE) is evaluated and observed very small (0.0006120) as given in Table 3, it is concluded that the proposed model is given results with accuracy and found validated. So the author can use this model for future study. Moreover, the new results for static behaviour of cross-ply and angle-ply laminated unsymmetrical trapezoidal flat panels (a/b = 1, b/c = 1, β_2 = 0°, a/h = 20, 100, 500) under uniformly distributed load is presented in Table 3, considering following material properties: $E_1/E_2 = 25$, $G_{12} = G_{13} = 0.5E_2$, $G_{23} = 0.2E_2$, $\nu_{12} = 0.25$.

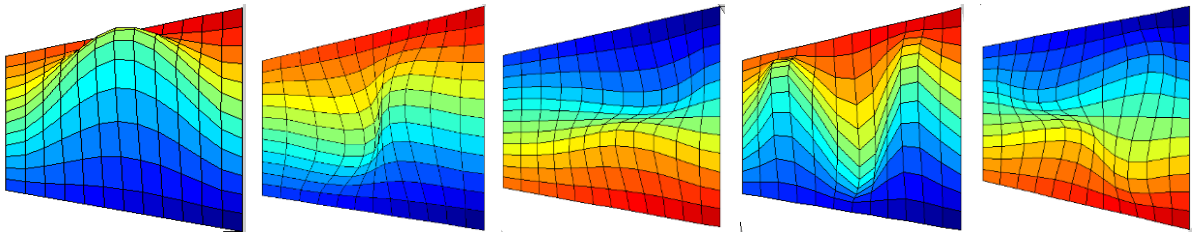

ϖ_1= 4.8063 ϖ_2= 8.4791 ϖ_3= 10.6156 ϖ_4= 14.2566 ϖ_5 = 14.7674

Fig. 3. First five vibrational mode shapes of an isotropic (ν = 0.3) clamped (*CCCC*) symmetric trapezoidal flat panel (*a/b* = 1, *b/h* = 100, *c/a* = 0.6)

Table 2. Non-dimensional natural frequencies ($\varpi_i = (\omega_i a^2/\pi^2)\sqrt{\rho h/D}; i = 1,5$) of a thin isotropic ($\nu$ = 0.3) trapezoidal plates (*a/b* = 1, *a/h* = 100)

Boundary conditions	***c/b***	**Normalized Natural frequency (ϖ)**		ϖ_1	ϖ_2	ϖ_3	ϖ_4	ϖ_5
SSSS (Case 1)	0.2	Present (FEM)	2 × 2	3.8344	8.2064	9.9940	14.8149	17.6728
			4 × 4	3.8151	8.0417	9.7639	13.6335	16.6335
		Chopra and Durvasula [38] (Galerkin Method)		3.8242	8.0707	9.7898	13.664	16.681
		Kitipornchai *et al.* [39] (Rayleigh-Ritz method)		3.8212	8.0728	9.7850	13.6748	16.6673
		Watts *et al.* [20] (Meshless method)		3.8291	8.0972	9.8081	13.7556	16.6910
	0.4	Present	2 × 2	3.1213	6.5321	8.5318	12.2655	13.8010
			4 × 4	3.1136	6.4522	8.3839	11.4693	13.3454
		Chopra and Durvasula [38]		3.1200	6.472	8.402	11.494	13.388
		Kitipornchai *et al.* [39]		3.1204	6.4727	8.3992	11.4933	13.3813
		Watts *et al.* [20]		3.1248	6.4861	8.4192	11.5220	13.4065
	0.6	Present	2 × 2	2.5971	5.7182	7.1772	10.8938	11.3703
			4 × 4	2.5934	5.6584	7.0794	10.6436	10.6798
		Chopra and Durvasula [38]		2.5977	5.67	7.091	10.656	10.710
		Kitipornchai *et al.* [39]		2.5977	5.6697	7.0904	10.6535	10.7076
		Watts *et al.* [20]		2.6004	5.6760	7.1053	10.6694	10.7324
CCCC	0.2	Present	2 × 2	7.4148	13.5881	17.1105	22.4752	27.3439
			4 × 4	7.2074	12.6375	14.8186	19.3755	23.0853
		Kitipornchai *et al.* [39]		7.2195	12.6609	14.8419	19.3154	23.0600
		Watts *et al.* [20]		7.2312	12.6798	14.9139	19.3719	23.1247
	0.4	Present	2 × 2	5.9607	10.1901	14.3788	18.2722	21.1821
			4 × 4	5.8630	9.9000	12.6365	15.5891	18.5473
		Kitipornchai *et al.* [36]		5.8721	9.9195	12.6607	15.6043	18.5838
		Watts *et al.* [20]		5.8839	9.9418	12.7294	15.6686	18.6473
	0.6	Present	2 × 2	4.8474	8.6882	11.7737	16.0929	16.9832
			4 × 4	4.8063	8.4791	10.6156	14.2566	14.7674
		Kitipornchai *et al.* [39]		4.8129	8.4954	10.6362	14.2726	14.8026
		Watts *et al.* [20]		4.8247	8.5200	10.6929	14.3362	14.8773

Percentage of error is less than 0.2 % for simply supported and fully clamped trapezoidal panels with Galerkin method [38], Rayleigh-Ritz method [39] and meshless method [20]

Table 3. The non-dimensional central deflection of simply supported (case 1) and for unsymmetrical trapezoidal plates (b/c = 1, β_2 = 0°)

a/b	**Isotropic (ν = 0.3) unsymmetrical trapezoidal plate** ($\bar{w} = 10^3 \times wD/q_0b^4$)							
	Moderately thick trapezoidal plate *a/h* = 20			**Thin trapezoidal plate *a/h* = 500**				
	Present study			**Present study**			[36]	RSME
	2 × 2	**4 × 4**	**6 × 6**	**2 × 2**	**4 × 4**	**6 × 6**	8 × 8	
1.0	4.1892	4.2415	4.2665	4.0592	4.0626	4.0628	4.062	1.35E-07
1.2	5.0202	5.0906	5.1206	4.8492	4.8219	4.8217	4.821	1.667E-07
1.4	5.7572	5.8423	5.8752	5.4944	5.4606	5.4631	5.466	2.52E-07
1.6	6.4005	6.4922	6.5260	6.0055	5.9756	5.9847	6.000	1.707E-05
1.8	6.9559	7.0441	7.0771	6.3918	6.3755	6.3942	6.437	0.0001602
2.0	7.4286	7.5052	7.5363	6.6743	6.6761	6.7059	6.787	0.0006120
	Laminated composite unsymmetrical trapezoidal plate ($\bar{w} = 10^3 \times wE_2h^3/q_0b^4$)							
	Cross-ply [0°/90°/90°/0°]			**Angle-ply [45°/-45°/-45°/45°]**				
	***a/h* = 20**	***a/h* = 100**	***a/h* = 500**	***a/h* = 20**	***a/h* = 100**	***a/h* = 500**		
1.0	7.7473	6.8360	6.7981	6.4028	4.9037	4.7477		
1.2	8.5401	7.1120	7.0457	8.3839	6.1497	5.9266		
1.4	9.2115	7.1720	7.0509	10.4757	7.4711	7.1708		
1.6	9.8598	7.1733	6.9657	12.5825	8.8101	8.4242		
1.8	10.5214	7.1375	6.8353	14.6259	10.0658	9.8512		
2.0	11.2070	7.0687	6.6712	16.5652	11.1619	10.5685		

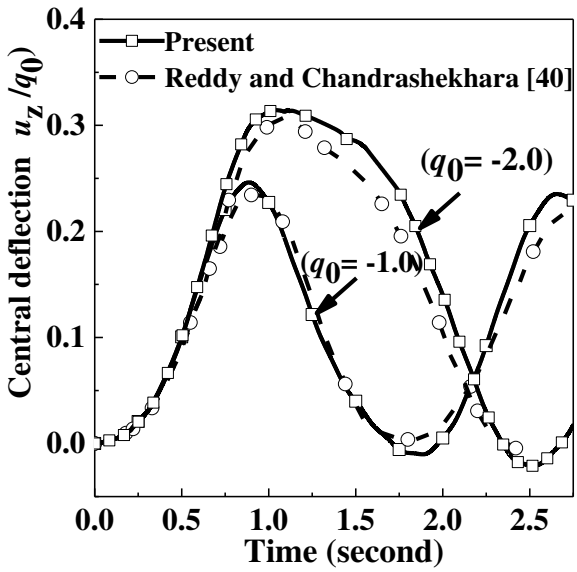

Fig. 4. Geometrical nonlinear dynamic response of simply supported (*Case* 4) laminated [90°/0°] double curved panel under external pressure (q_0 = -1 and -2)

Nonlinear dynamic response. The nonlinear dynamic response of cross-ply [90°/0°] spherical panel (a/b = 1, a/h = 100, h = 1, R/a = 10, R_1, = R_2 = R) under radial pressure (q_0 = -1, -2) is shown in Fig. 4 considering simply supported (case 2) boundary conditions. Here, employed the energy and momentum conservation implicit time integration scheme proposed by Bathe [41] to solve nonlinear governing equations. The linear vibration frequency (ω) of spherical panel is 3.697 radian/ second and time period (T_L) is 1.69921 second, time step is taken Δt = 0.01 second for geometric nonlinear dynamic

response of spherical panel. The presented numerical results are validated with available published results of Reddy and Chandrashekhara [40] for nonlinear transient response of spherical panel, and it is noticed that the presented results have good combination with [40].

Results and Discussions

Linear vibration analysis of laminated panel. Next, the linear non-dimensional vibration frequencies ($\varpi_i = (\omega_i b^2/h)\sqrt{\rho/E_2}; i = 1,4$; ω_i is the circular frequency of composite panel) of simply supported (case 1) four-layer cross-ply $[0°/90°]_S$ and angle-ply $[45°/-45°]_S$ laminated composite unsymmetrical trapezoidal flat panels (b/c = 1, β_2 = 0°) is presented in Table 4 for moderately thick (a/h = 20) and thin (a/h = 100, 500) panels considering various aspect ratios for example a/b = 1.0, 1.2, 1.4, 1.6, 1.8 and 2.0. It is found that as increases the aspect ratio from a/b = 1.0 to 2.0, reduces the non-dimensional vibration frequencies (ϖ_i, i = 1, 4) for moderately thick (a/h = 20) and thin ($a/h \geq 100$) laminated trapezoidal panels.

Table 4. Non-dimensional fundamental frequency ($\varpi_i = (\omega_i b^2/h)\sqrt{\rho/E_2}; i = 1,4$) of simply supported (case 1) laminated composite unsymmetrical trapezoidal flat panels (b/c = 1, β_2 = 0°). Considering following material properties: E_1/E_2 = 25, $G_{12} = G_{13} = 0.5E_2$, $G_{23} = 0.2E_2$, ν_{12} = 0.25

a/h	a/b	Cross-ply $[0°/90°]_S$				Angle-ply $[45°/-45°]_S$			
		ϖ_1	ϖ_2	ϖ_3	ϖ_4	ϖ_1	ϖ_2	ϖ_3	ϖ_4
20	1.0	14.1929	25.9700	42.8389	48.4354	15.5091	30.4996	37.7022	48.1889
	1.2	13.4606	22.5612	39.2109	40.0881	13.5271	26.7153	32.2003	42.8126
	1.4	12.8997	20.2908	33.6547	36.6220	12.0772	23.2938	28.9447	38.2665
	1.6	12.3903	18.6256	29.3614	33.8671	11.0027	20.5636	26.6167	33.4631
	1.8	11.8984	17.2962	26.1164	31.4063	10.1949	18.4462	24.6956	29.2651
	2.0	11.4198	16.1731	23.5614	29.2088	9.5712	16.7754	22.9688	26.1155
100	1.0	15.1803	27.8593	53.9085	54.5452	17.8542	35.6111	47.0191	59.2310
	1.2	14.8428	24.8708	46.2017	53.5380	15.9418	32.3890	41.4478	54.9092
	1.4	14.7253	23.2124	40.7507	53.1872	14.4519	29.1601	38.2372	50.4681
	1.6	14.6297	22.1063	36.9479	52.7870	13.2918	26.3510	36.1501	45.9961
	1.8	14.5283	21.2615	34.1292	50.9178	12.4266	24.1580	34.5387	42.0954
	2.0	14.4272	20.5796	31.9784	46.7551	11.8054	22.4992	33.0892	39.1361
500	1.0	15.2259	27.9478	54.5568	54.8481	18.1603	36.0162	47.9907	60.1180
	1.2	14.9180	25.0153	46.6159	54.4707	16.2578	32.9332	42.4182	56.0401
	1.4	14.8607	23.4804	41.3221	54.4656	14.7703	29.8055	39.1841	51.7491
	1.6	14.8369	22.5338	37.6429	54.4527	13.6104	27.0374	37.1119	47.3796
	1.8	14.8015	21.8338	34.9227	52.9022	12.7531	24.8724	35.5583	43.5889
	2.0	14.7585	21.2691	32.9115	49.2364	12.1496	23.2509	34.2033	40.7276

Then, the non-dimensional fundamental vibration frequencies of five-layered laminated cross-ply and angle-ply composite trapezoidal curved (shown in Fig. 2(d)) panels (a/b = 1, a/h = 200 and R/a = 5) is given in Table 5 for various boundary conditions for example *CCCC*, *SSSS* case 2, *SCSF*. It is identified that by increasing the span to cord ratio (c/a = 0.2, 0.4, 0.6, 0.8, 1.0) reduces the vibration frequencies for different boundary conditions i.e. fully clamped (*CCCC*), simply supported (*SSSS* case 2), and *SCSF* boundary conditions. Trend of numerical results of cross-ply and angle-ply laminated composite trapezoidal curved panel is qualitatively similar, but the vibration frequency of cross-ply laminated panel (c/a = 0.2) is higher side compare to angle-ply composite panels for the

case *CCCC*, *SCSF* boundary conditions; whereas, vibration frequency of regular shape (c/a = 1.0) panel is lower side for same case.

Table 5. Non-dimensional fundamental frequency ($\varpi_i = (\omega_i b^2/h)\sqrt{\rho/E_2}; i = 1,4$) of laminated composite symmetric trapezoidal curved (shown in Fig. 2(c)) panels (a/b = 1, a/h = 200 and R/a = 5)

Boundary conditions	c/a	Cross-ply [0°/90°/0°/90°/0°]				Angle-ply [45°/-45°/45°/-45°/45°]			
		ϖ_1	ϖ_2	ϖ_3	ϖ_4	ϖ_1	ϖ_2	ϖ_3	ϖ_4
CCCC	0.2	56.9120	65.0013	69.8813	89.0529	50.2041	61.5680	65.1301	85.0165
	0.4	54.2965	57.0587	62.7385	76.3326	47.2894	53.1792	57.5156	72.9480
	0.6	49.3405	51.9792	58.8479	65.5270	45.1230	45.4688	54.0883	64.1960
	0.8	42.2670	49.6560	56.7027	56.8583	39.7326	43.3319	52.6230	57.8579
	1.0	37.2144	46.6908	52.5165	55.2854	36.4844	41.1807	51.8634	54.3969
SSSS (case 2)	0.2	33.1823	53.1264	55.1647	73.3451	33.5581	52.1432	54.7831	73.3753
	0.4	27.9279	44.6200	48.3694	61.2444	28.0481	45.0114	47.7857	63.0979
	0.6	24.4497	40.9825	42.1846	54.9163	26.4124	37.4097	46.1345	54.3952
	0.8	23.7298	31.7367	42.7446	43.4487	27.5925	29.2541	46.0690	46.4634
	1.0	22.9628	24.3950	37.3112	43.9925	22.0271	29.4154	37.6981	43.1123
SCSF	0.2	50.2155	55.3062	63.2162	76.5029	47.6864	48.9190	56.8211	70.8112
	0.4	43.5048	53.5984	58.0567	63.5551	41.6769	45.8360	50.0730	58.3954
	0.6	36.3518	48.4946	51.2879	54.3916	32.4765	43.0491	46.0196	47.7162
	0.8	27.7035	39.8012	46.9176	50.5925	24.3752	38.1959	41.8596	44.3402
	1.0	21.9335	37.4441	38.4618	44.9045	20.7230	30.5711	39.8556	41.9476

Nonlinear dynamic response under thermal load. Next, the nonlinear static and dynamic responses of fully clamped (*CCCC*) cross-ply [0°/90°/0°/90°/0°] laminated composite trapezoidal curved panels (a/b = 1, a/h = 200, R/a = 5) under thermal load ΔT °C is plotted in Fig. 5 with outward and inward deformed shapes at time t = 0.563 second and 1.034 second, respectively.

The geometrical nonlinear dynamic responses: transverse central deflection (u_3/h) versus time is shown in Fig. 5(a) for clamped laminated trapezoidal panel for various cord-to-span ratios at thermal load (ΔT = 100 °C, at Room Temp. T_R = 20 °C) considering time step size Δt = 0.01 second. The natural frequency (ω_n) and time period (T_L) of these selected panels (a/b = 1, a/h = 200 and R/a = 5) with cord to span ratio c/a = 0.2, 0.4, 0.6, 0.8, 1.0 are ω_n = 4.8732, 4.6329, 4.4499, 3.8328 and 3.2067 radian/second; T_L = 1.2893, 1.3562, 1.412, 1.6392 and 1.9593 second; respectively. It is seen that as increases the cord-to-span ratio 0.2 to 1.0 then the time period of cycle T_L increases 1.2893 second to 1.9593 second. It is noticed that, the vibration amplitude increases with the increase in cord-to-span ratio. Moreover, nonlinear static response of trapezoidal panel for various cord to span ratios i.e. c/a = 0.2, 0.4, 0.6, 0.8, 1.0 at various temperatures ΔT = 0 to 1200 °C is shown in Fig. 5(b). It is noticed that central deflection (u_3/h) increases with increase in cord-to-span ratio, therefore thermal load carrying capacity is reduces. This occurs due to change in structural stiffness of trapezoidal panels.

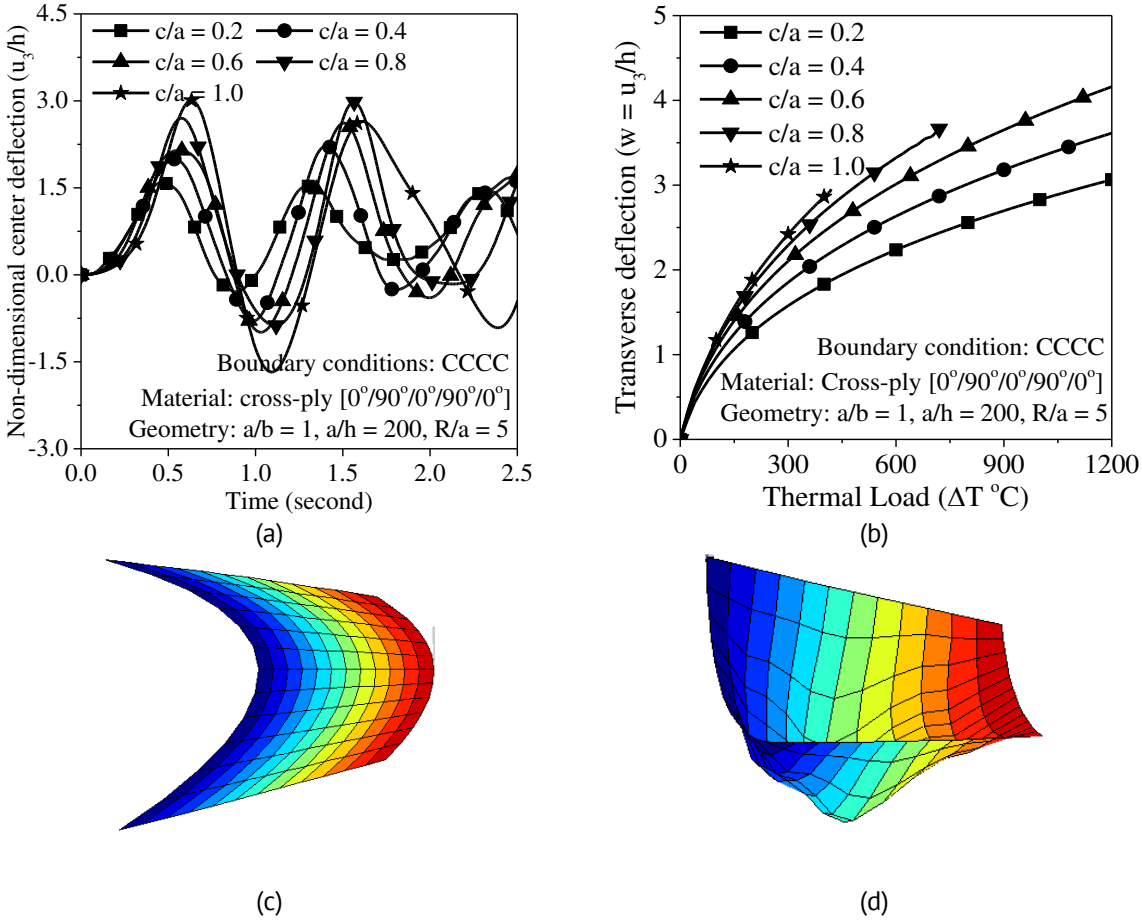

Fig. 5. Nonlinear static and dynamic response of clamped (*CCCC*) cross-ply [0°/90°/0°/90°/0°] composite trapezoidal panel (as given in Fig. 2(c)) under thermal environment (ΔT °C) considering various chord to span ratios: (a) nonlinear dynamic response at thermal load (ΔT =100 °C, at Room Temp. T_R = 20 °C); (b) nonlinear static response; (c) deformed shape of panel (c/a = 0.6) at time t = 0.563 second; (d) deformed shape of panel (c/a = 0.6) at time t = 1.034 second

Effect of boundary conditions on nonlinear dynamic response. Further, the effect of various boundary conditions such as: *CCCC*, *CSCS*, *SSSS* case 2 and *SCSF* has been investigated on nonlinear bending and transient responses of cross-ply [0°90°/0°/90°/0°] composite trapezoidal curved panels (a/b = 1, a/h = 200, c/a = 0.6 and R/a = 5) under thermal environment ΔT °C. The transient response of trapezoidal curved panel (R/a = 5, c/a = 0.6) under thermal load ΔT = 100 °C is presented in Fig. 6(a), whereas nonlinear bending response is given in Fig. 6(b) for various boundary conditions. It is noticed that thermal load carrying capacity of simply supported panel is much lower than the clamped trapezoidal panel. Also plotted the deformation shapes of trapezoidal curved panel at thermal load ΔT = 200 °C in Fig. 6 for various boundary conditions.

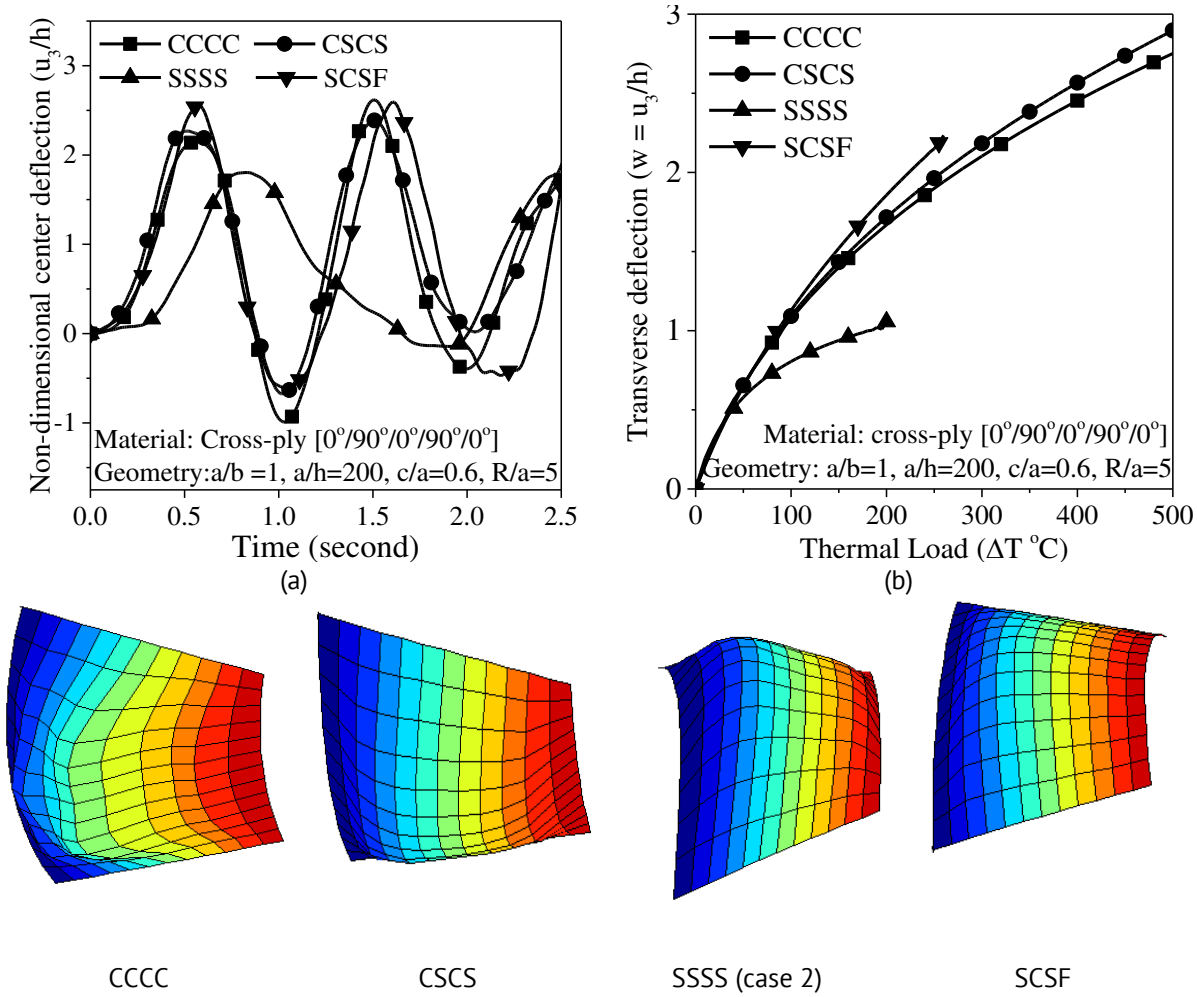

Fig. 6. Nonlinear dynamic and static response of cross-ply [0°/90°/0°/90°/0°] laminated composite trapezoidal curved panel under thermal load (ΔT °C at room temperature T_R = 20 °C) considering different boundary conditions with deformation shapes at ΔT = 200 °C

Nonlinear dynamic response under thermo-mechanical load. Next, studied the effect of intensity of thermal load (ΔT), cord-to-span ratio (c/a), radius-to-span ratio (R/a) and boundary conditions on the geometric nonlinear dynamic behaviour of fully clamped (*CCCC*) five-layered [45°/-45°/45°/-45°/45°] composite trapezoidal curved panel (a/b = 1, a/h = 200, h = 1) in presence of mechanical load (q_0 = 10 kN/m^2) ; and nonlinear dynamic response verses time is shown in Fig. 7. It is seen that by increasing intensity of thermal load from ΔT = 25 °C to 150 °C in the presence of constant radial pressure (q_0 = 10 kN/m^2) increases the non-dimensional transverse deformation u_3/h = 1.75 to 3.692 and time period of cycle is reduces from t = 1.382 second to 0.97 second as given in Fig. 7(a). Further, it is observed that by increasing the cord-to-span ratio (c/a) from 0.2 to 1.0 increases the non-dimensional central deflection (u_3/h) from 2.216 to 4.109, and structures vibration frequency reduces as the cyclic time increases from 0.926 second to 1.236 second as presented in Fig. 7(b) at thermal load (ΔT = 100 °C) and mechanical load (q_0 = 10 kN/m^2). Then, effect of radius-to-span ratio (R/a = 4, 5, 8, 10 and 12) changing from deep shell (R/a = 4) to shallow shell (R/a = 12) on nonlinear transient characteristics of angle-ply laminated trapezoidal curved panel subjected to thermal ΔT = 100 °C and mechanical load q_0 = 10 kN/m^2 is investigated

in Fig. 7(c); it is found that trend of dynamic response is qualitatively similar as change in the cord to span ratios c/a = 0.2, to 1.0. Moreover, the same problem is investigated for fully clamped (CCCC), simply supported-clamped-free (SCSF), and simply supported (SSSS case 1 and SSSS case 2) composite trapezoidal curved panel subjected to thermal loading with radial pressure. The transient response of a symmetric trapezoidal cylindrical panel for four different boundary conditions is presented in Fig. 7(d).

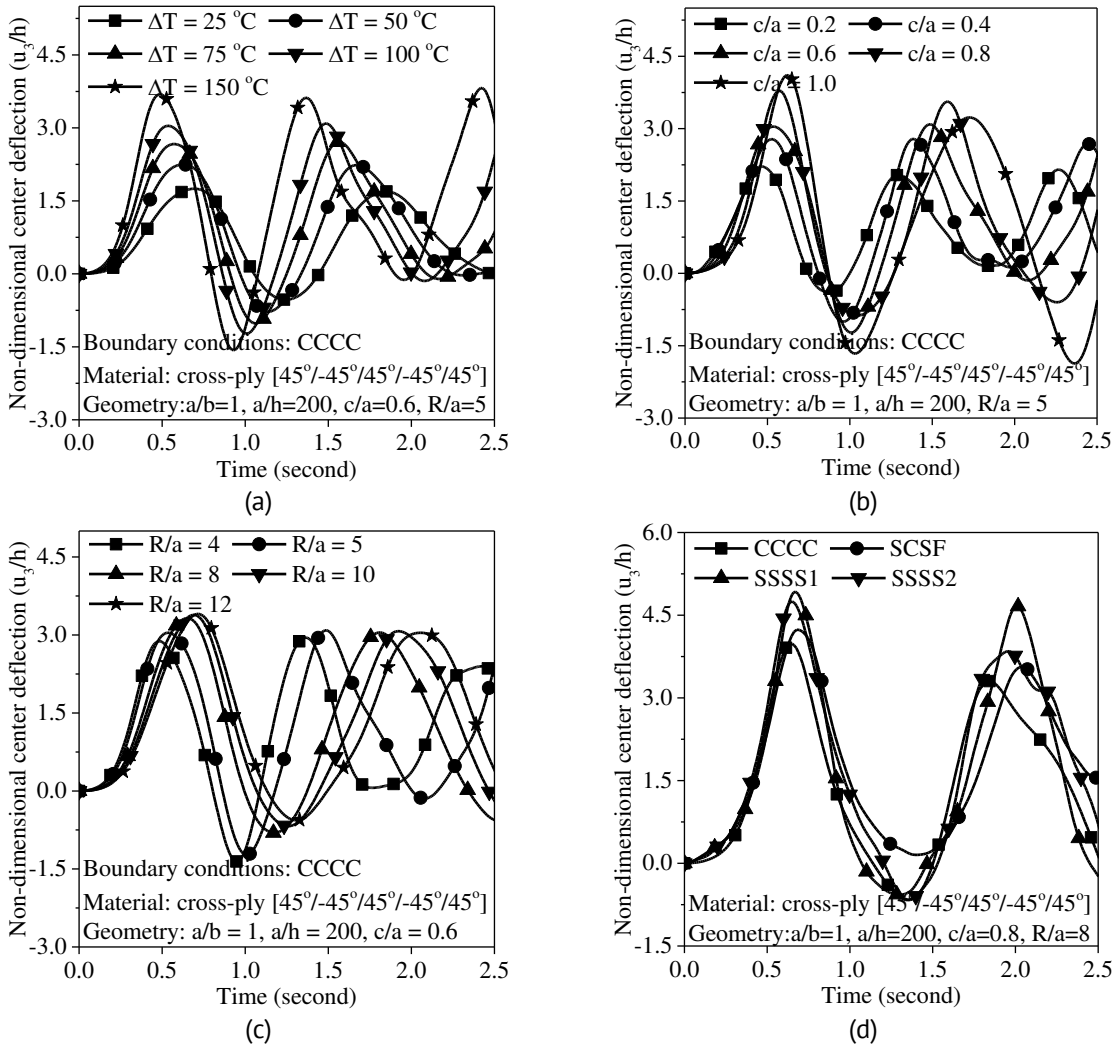

Fig. 7. Nonlinear dynamic response of angle-ply [45°/-45°/45°/-45°/45°] laminated composite trapezoidal curved panel to present the effect of (a) intensity of thermal load (ΔT °C), (b) cord to span ratio, (c) radius to span ratio and (d) boundary conditions considering four different cases in the presence of radial pressure q_0 = 10 kN/m^2

Conclusion

Geometrical nonlinear bending and flexural vibration characteristics of laminated composite trapezoidal curved panels are investigated here under thermal environment in the absence and presence of radial pressure. First, examined the accuracy of in-house FORTRAN code and validated the present numerical results of linear bending, linear vibration and geometric nonlinear dynamic response with available published results, it is found that, error is less than 0.02 percent or under the limit. Thereafter, new results for

future research on the geometric nonlinear vibration characteristics of symmetric trapezoidal panels under thermal shock in the presence of mechanical load are presented. Here, investigated the effect of cord to span ratios (*c/a*), radius to span ratios (*R/a*), boundary conditions and stacking sequence on the nonlinear bending and dynamic response of composite trapezoidal cylindrical panels subjected to different heating rates (thermal shock loading) with and without mechanical load.

The vibration frequencies of trapezoidal cylindrical panel will increase with increase in intensity of thermal (ΔT = 25, 50, 75, 100 and 150 °C) and mechanical load (q_0 = 10 kN/m^2), whereas the vibration frequencies are of cross-ply and angle-ply laminated composite panels will reduce with increase in cord to span ratio from 0.2 to 1.0 and radius-to-span ratio (*R/a* = 4, 5, 8, 10 and 12); and magnitude of central deflection (u_3/h) is increase with incremental change is thermal load (ΔT); cord-to-span ratio; and radius-to-span ratio. This occurs due to reduction in structural stiffness of trapezoidal panel with incremental change in load intensity, cord-to-span ratio and radius-to-span ratio.

References

1. Srinivasan RS, Babu BJC. Free vibration and flutter of laminated quadrilateral plates. *Computers & Structures*. 1987;27(2): 297–304.
2. Saliba HT. Transverse free vibration of fully clamped symmetrical trapezoidal plates. *Journal of Sound and Vibration*. 126(2), 237–247.
3. Ng SSF, Das B. Free vibration and buckling analysis of clamped skew sandwich plates by the Galerkin method. *Journal of Sound and Vibration*. 1986;107(1): 97–106.
4. Qatu MS. Natural vibration of free, laminated composite triangular and trapezoidal shallow shells, *Composite Structures*. 1995;31(1): 9–19.
5. Han W, Petyt M. Linear vibration analysis of laminated rectangular plates using the hierarchical finite element method—I. Free vibration analysis. *Computers & Structures*. 1996;61(4): 705–712.
6. Han W, Petyt M. Linear vibration analysis of laminated rectangular plates using the hierarchical finite element method—II. Forced vibration analysis. *Computers & Structures*. 1996;61(4): 713–724.
7. Huang M, Ma XQ, Sakiyama T, Matsuda H, Morita C. Free vibration analysis of continuous rectangular plates. *Journal of Sound and Vibration*. 2010;329(4): 485–496.
8. Kumar A, Bhargava P, Chakrabarti A. Vibration of laminated composite skew hypar shells using higher order theory. *Thin-Walled Structures*. 2013;63: 82–90.
9. Malekzadeh P. A differential quadrature nonlinear free vibration analysis of laminated composite skew thin plates. *Thin-Walled Structures*. 2007;45(2): 237–250.
10. Gupta AK, Sharma S. Effect of thermal gradient on vibration of non-homogeneous orthotropic trapezoidal plate of linearly varying thickness. *Ain Shams Engineering Journal*. 2013;4(3): 523–530.
11. Nguyen-Minh N, Tran-Van N, Bui-Xuan T, Nguyen-Thoi T. Free vibration analysis of corrugated panels using homogenization methods and a cell-based smoothed Mindlin plate element (CS-MIN3). *Thin-Walled Structures*. 2018;124: 184–201.
12. Rout M, Hota SS, Karmakar A. Thermoelastic free vibration response of graphene reinforced laminated composite shells. *Engineering Structures*. 2019;178: 179–190.
13. Liu T, Wang Q, Qin B, Wang A. Free in-plane vibration of plates with arbitrary curvilinear geometry: Spectral-Chebyshev model and experimental study. *Thin-Walled Structures*. 2022;170: 108628.
14. Niu Y, Yao M. Linear and nonlinear vibrations of graphene platelet reinforced composite tapered plates and cylindrical panels. *Aerospace Science and Technology*. 2021;115: 106798.
15. Li C, Cheng H. Free vibration analysis of a rotating varying-thickness-twisted blade with arbitrary boundary conditions. *Journal of Sound and Vibration*. 2021;492: 115791.
16. Dou C, Jiang ZQ, Pi YL, Guo YL. Elastic shear buckling of sinusoidally corrugated steel plate shear wall. *Engineering Structures*. 2016;121: 136–146.
17. Franzoni F, Odermann F, Lanbans E, Bisagni C, Arbelo MA, Degenhardt R. Experimental validation of the vibration correlation technique robustness to predict buckling of unstiffened composite cylindrical shells. *Composite Structures*. 2019;224: 111107.

18. Magnucka-Blandzi E, Walczak Z, Jasion P, Wittenbeck L. Buckling and vibrations of metal sandwich beams with trapezoidal corrugated cores–the lengthwise corrugated main core. *Thin-Walled Structures*. 2017;112: 78–82.
19. Magnucka-Blandzi E, Walczak Z, Wittenbeck L, Jasion P, Rodak M, Szyc W, Lewiński J. Stability and vibrations of a metal seven-layer rectangular plate with trapezoidal corrugated cores. *Thin-Walled Structures*. 2017;114: 154–163.
20. Watts G, Kumar R, Patel SN, Singh S. Dynamic instability of trapezoidal composite plates under non-uniform compression using moving kriging based meshfree method. *Thin-Walled Structures*. 2021;164: 107766.
21. Kumari E, Lal S. Nonlinear Bending Analysis of Trapezoidal Panels under Thermo-Mechanical Load. *Forces in Mechanics*. 2022;8: 100097.
22. Kumari E, Saxena D. Buckling analysis of folded structures. *Materials Today: Proceedings*. 2021;43: 1421–1430.
23. Kumari E. Free vibration analysis of rotating laminated composite plate type blades with variable thickness. *Materials Today: Proceedings*. 2021;43: 1762–1773.
24. Kumari E. Dynamic response of composite panels under thermo-mechanical loading. *Journal of Mechanical Science and Technology*. 2022;36(8): 3781–3790.
25. Kumari E, Singha MK. Nonlinear response of laminated panels under blast load. *Procedia Engineering*. 2017;173: 539–546.
26. Kumari E, Singh J, Kasera G. Analysis of piston of internal combustion engine under thermo-mechanical load. *International Research Journal on Advanced Science Hub*. 2021;3: 11–18.
27. Sharma M, Kumari E, Meena PM. A parametric study to improve the heat transfer of solar air heater through CFD analysis. *Journal of Mechanical and Construction Engineering*. 2022;2: 1–17.
28. Kumar V, Singh SJ, Saran VH, Harsha SP. Vibration response of exponentially graded plates on elastic foundation using higher-order shear deformation theory. *Indian Journal of Engineering & Material Sciences*. 2022;29: 181–188.
29. Govindaraj T, Mahendran C, Manikandan VS, Archana J, Navaneethan M. Enhanced visible-light-driven photocatalytic activity of Ce doped WO3 nanorods for Rhodamine B dye degradation. *Materials Letters*. 2021;305: 130705.
30. Kumar A, Mariappan CR. A new biocompatible phosphate free mesoporous calcium borosilicate glass-ceramics for medical application. *Materials Letters*. 2021;305: 130752.
31. Panfilov P, Panfilov GP, Zaytsev D. Deformation behavior of polycrystalline rhenium under shear testing at room temperature. *Materials Letters*. 2020;277: 128379.
32. Myslyvchenko O, Bondar A, Petyukh V, Tikhonova I, Tsyganenko N. Structure of orthorhombic martensite in the Ti92. 5Nb5Mo2. 5 alloy, its deformation and thermal stability. *Materials Letters*. 2020;277: 128267.
33. Bathe KJ. *Finite Element Procedures*. Prentice-Hall of India; 1997.
34. Ko Y, Lee PS, Bathe KJ. The MITC+ shell element and its performance. *Computers & Structures*. 2016;169: 57–68.
35. Ko Y, Lee PS, Bathe KJ. The MITC+ shell element in geometric nonlinear analysis. *Computers & Structures*. 2017;185: 1–14.
36. Saadatpour MM, Azhari M. The Galerkin method for static analysis of simply supported plates of general shape. *Computers & Structures*. 1998;69(1): 1–9.
37. Maleki S, Tahani M. Non-linear analysis of moderately thick laminated plates and shell panels under thermo-mechanical loadings. *ZAMM-Journal of Applied Mathematics and Mechanics*. 2012;92(8): 652–667.
38. Chopra I, Durvasula S. Vibration of simply-supported trapezoidal plates I. Symmetric trapezoids. *Journal of Sound and Vibration*. 1971;19(4): 379–392.
39. Kitipornchai S, Xiang Y, Liew KM, Lim MK. A global approach for vibration of thick trapezoidal plates. *Computers & Structures*. 1994;53(1): 83–92.
40. Reddy JN, Chandrashekhara K. Geometrically non-linear transient analysis of laminated, doubly curved shells. *International Journal of Non-Linear Mechanics*. 1985;20(2): 79–90.
41. Bathe KJ. Conserving energy and momentum in nonlinear dynamics: a simple implicit time integration scheme. *Computers & Structures*. 2007;85(7-8): 437–445.

About Author

Kumari Emarti Sc
PhD, Assistant Professor (MBM University, Jodhpur, India)

Lal Shiv Sc
PhD, Associate Professor (Rajasthan Technical University, Kota, India)

MATERIALS PHYSICS AND MECHANICS RESEACH ARTICLE

Submitted: December 17, 2023 Revised: January 29, 2024 Accepted: February 12, 2024

Study of the melting nanocrystalline aluminum by the molecular dynamics method

G.M. Poletaev [1]✉, A.A. Sitnikov [1], V.I. Yakovlev [1], V.Yu. Filimonov [1,2], D.V. Novoselova [3],

[1] Polzunov Altai State Technical University, Barnaul, Russia

[2] Institute for Water and Environmental Problems SB RAS, Barnaul, Russia

[3] Kuzbass Institute of the Federal Penitentiary Service of Russia, Novokuznetsk, Russia

✉ gmpoletaev@mail.ru

ABSTRACT

Using molecular dynamics simulation, a study of the melting of aluminum with a nanocrystalline structure obtained as a result of severe plastic deformation was conducted. It is shown that the melting of nanocrystalline aluminum begins at a lower temperature than monocrystalline aluminum. The higher the density of grain boundaries and other defects, and, accordingly, the higher the excess energy, the lower the melting temperature. In the presence of defects, melting proceeds heterogeneously and begins primarily from the grain boundaries and free surface. In a pure crystal that did not contain any defects or free surface, melting in the model proceeded homogeneously. When studying recrystallization in nanocrystalline aluminum, it was found that its intensity is greatly influenced by the free surface: the restructuring of the structure near it occurred faster than in the bulk of the material.

KEYWORDS

molecular dynamics • melting • nanocrystalline structure • recrystallization

Acknowledgements. *The study was supported by Ministry of Science and Higher Education of the Russian Federation (FZMM-2023-0003).*

Citation: Poletaev GM, Sitnikov AA, Yakovlev VI, Filimonov VYu, Novoselova DV. Study of the melting nanocrystalline aluminum by the molecular dynamics method. *Materials Physics and Mechanics*. 2024;52(2): 106–113. http://dx.doi.org/10.18149/MPM.5222024_11

Introduction

In recent decades, much attention has been paid to ultrafine-grained and especially nanocrystalline materials, which include polycrystals with an average grain size of less than 100 nm. They have unusual physical and mechanical properties, associated mainly with a large volume fraction of grain boundaries compared to the usual coarse-grained state [1–4]. They are obtained by different methods, including intense plastic deformation, sintering of nanopowders, condensation from the gas phase, etc. A common property of nanocrystalline materials is a high degree of nonequilibrium structure and large values of excess, or stored, energy [1–4].

One of the examples of the manifestation of excess energy in nanocrystalline materials, apparently, should be considered the experimentally observed decrease in the ignition temperature of the high-temperature synthesis reaction during the production of intermetallic compounds after preliminary mechanical activation treatment of the initial mixture of powders [5–10]. As a result of such processing, the initial mixture is subjected to intense mechanical action, as a result of which a nanocrystalline structure with a high

concentration of structural defects is often formed in metals [8–10]. Under normal conditions, the ignition temperature coincides with the melting temperature of aluminum, but after mechanical activation treatment it decreases significantly [5–10]. Among the main reasons for this decrease are the relatively high values of excess energy due to the high concentration of grain boundaries and other defects in the mixture after mechanical activation, the high diffusion mobility of atoms in nanocrystalline materials, as well as a possible decrease in the melting point of nanocrystalline aluminum compared to conventional coarse-crystalline aluminum.

As for the latter, in [11–14], using computer modeling, it has been shown that melting is not a homogeneous process, it begins, as a rule, from free surfaces and grain boundaries. In this case, the melting of the structure near the interfaces began in the mentioned works at lower temperatures than for a pure crystal. The nanocrystalline structure has a relatively high proportion of nonequilibrium grain boundaries, which, obviously, should be reflected in the overall melting process and the temperature at which the phase transition begins. When studying phase transitions in nanoparticles [15–17], we actually observed a noticeable decrease in the melting temperature of metal particles with a nanocrystalline structure.

This work is devoted to the study, using molecular dynamics simulation, of the melting of aluminum with a nanocrystalline structure obtained as a result of severe plastic deformation. The effect of excess energy on the melting temperature was considered. The melting mechanism was studied under conditions of the presence and absence of a free surface along with grain boundaries. The work also considered the influence of the initial excess energy and free surface on the intensity of recrystallization.

Description of the model

To describe interatomic interactions in the molecular dynamics model, the EAM potential from [18] was used, where it was obtained based on comparison with experimental data and *ab initio* calculations of various properties of aluminum. This potential well reproduces a wide range of mechanical and structural-energetic properties [18–20]. It has proven itself in various molecular dynamics studies and has been successfully tested in modeling various processes, including melting, crystallization and self-diffusion in the melt [18–24]. This potential has been repeatedly used to simulate the melting of aluminum [22–24]. It reproduces this phase transition quite well and gives a melting temperature relatively close to the reference value – 990 K for an ideal crystal with a free surface [22,23].

The computational cell had the shape of a parallelepiped with dimensions of 14.3, 14.0 and 11.7 nm at 0 K along the *x*, *y*, *z* axes, respectively (Fig. 1) and contained 124416 atoms. The initial structure corresponded to an ideal fcc aluminum crystal (Fig. 1(a)). To obtain a nanocrystalline structure containing a high density of defects, intense plastic deformation was simulated. Intense deformation was carried out by alternating uniaxial compression and tension by 15 % along all three axes, followed by shear deformation also alternately along all axes by 15 %. During deformation, the temperature of the computational cell increased. To avoid its melting and recrystallization, the computational cell was sharply cooled after each stage of deformation.

Figure 1(b) shows the structure of the computational cell after deformation using a crystalline phase visualizer based on the CNA (Common Neighbor Analysis) method [25]. As can be seen, it contains a high density of defects and a large number of small grains.

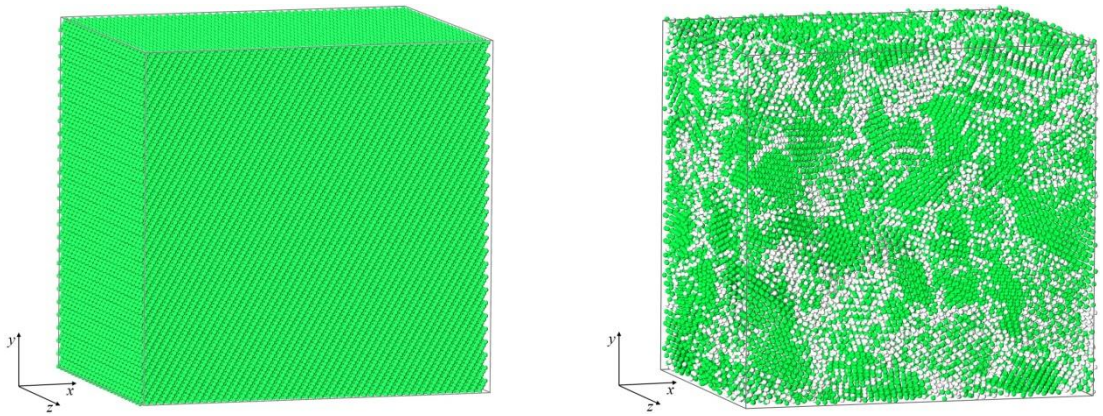

(a) (b)

Fig. 1. Obtaining an initial deformed structure: a) starting computational cell; b) the cell after severe plastic deformation. Atoms whose immediate environment corresponds to the first coordination sphere of the crystal lattice are colored green; white atoms – the crystal lattice has not been identified

In this work, three variants of the nanocrystalline structure were considered, which were obtained as a result of relaxation of the structure shown in Fig. 1(b), for 200 ps at different temperatures: 500, 600 and 700 K (Fig. 2). During the relaxation process, the concentration of defects and the number of grains decreased, and their average size increased. Excess, or stored, energy was estimated as the difference between the average potential energies of an atom in the structure under consideration and in an ideal crystal. That is, this is the energy that can be released during the restructuring of the structure into an ideal crystal, per one atom. For the computational cells shown in Fig. 2, the stored energy was equal to 0.14, 0.10 and 0.08 eV, respectively, for the structures in Fig. 2.

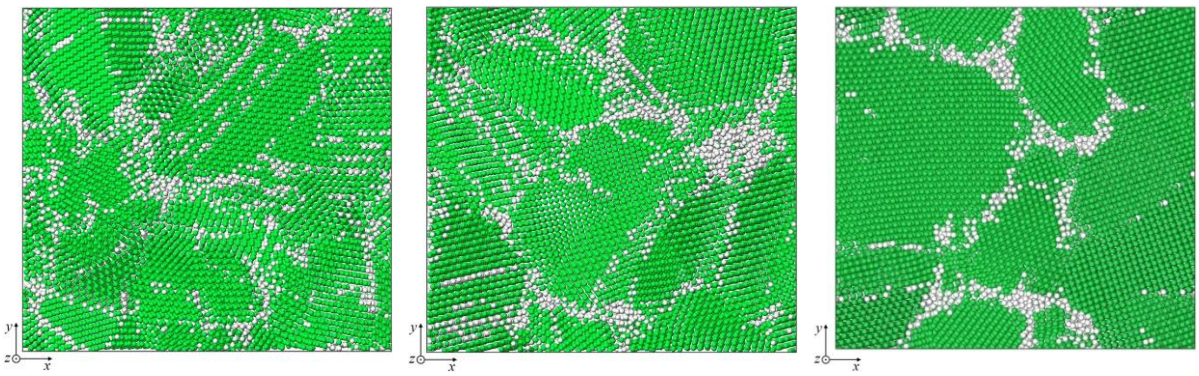

(a) (b) (c)

Fig. 2. Sections of the considered computational cells obtained as a result of relaxation for 200 ps at different temperatures: (a) 500 K; (b) 600 K; (c) 700 K

For comparison, computational cells containing a free surface and without it were considered. In the second case, periodic boundary conditions were used along all axes; in the first case, free conditions were used at the ends along the x-axis, that is, a free surface was simulated. In both cases, the NPT canonical ensemble was simulated using the Nose-Hoover thermostat. The time integration step was 2 fs.

To determine the melting point, the method of gradual heating was used to plot the dependence of the average potential energy of atoms on temperature [12,26–28]. Heating was carried out at a rate of 10^{12} K/s. At lower speeds, the results were strongly influenced by recrystallization, which was especially intense at temperatures close to the melting point. On the other hand, at higher heating rates it was more difficult to determine the melting point.

Results and Discussion

Figure 3 shows the dependences of the average atomic energy on temperature for the nanocrystalline structures under consideration when heated at a constant rate of 10^{12} K/s in the absence and presence of a free surface. For comparison, curves (indicated by number 4) obtained by heating an ideal crystal are shown.

The melting temperature of the crystal in the absence of a surface and any defects (curve 4 in Fig. 3(a)) turned out to be significantly higher (1140 K) than the melting temperatures found for the other structures under consideration. In this case, the melting process proceeded homogeneously, that is, almost simultaneously throughout the entire volume of the computational cell, and therefore the increase in atomic energy at the moment of melting appears sharper in Fig. 3(a) compared to other cases.

If there were grain boundaries or surfaces in the computational cell, melting began at them, after which the liquid-crystal interface moved away from the defects into the rest of the volume. The crystal-liquid front, as is known, moves with a finite speed that depends on temperature and, as a rule, amounts to several tens of meters per second [29,30].

Figure 3 clearly shows that the melting point of aluminum with a nanocrystalline structure is lower than that of monocrystalline aluminum. Moreover, the higher the defect density, the smaller the grain size and the higher the stored energy, the lower the melting temperature. This dependence manifested itself to a greater extent in the absence of a free surface (Fig. 3(a)). In the case of the presence of a surface, the melting temperatures of the considered variants of the structures turned out to be close, which, firstly, is explained by the large contribution of the surface as an additional site of initiation of melting, and, secondly, by more intense recrystallization in comparison with cells without a surface. Due to the recrystallization, the average energy of atoms initially decreased with increasing temperature. For structures with a higher density of grain boundaries and other defects, and correspondingly containing more stored energy, recrystallization, as can be seen from the graphs in Fig. 3, proceeded more intensely.

Figure 4 shows sections of nanocrystalline aluminum with a structure corresponding to Fig. 2(c) (3 in Fig. 3(b)), in the presence of a surface at different moments of the melting process. The figure clearly shows that melting begins at the boundaries of grains and the surface, that is, where the atoms are in shallower potential wells compared to an ideal crystal.

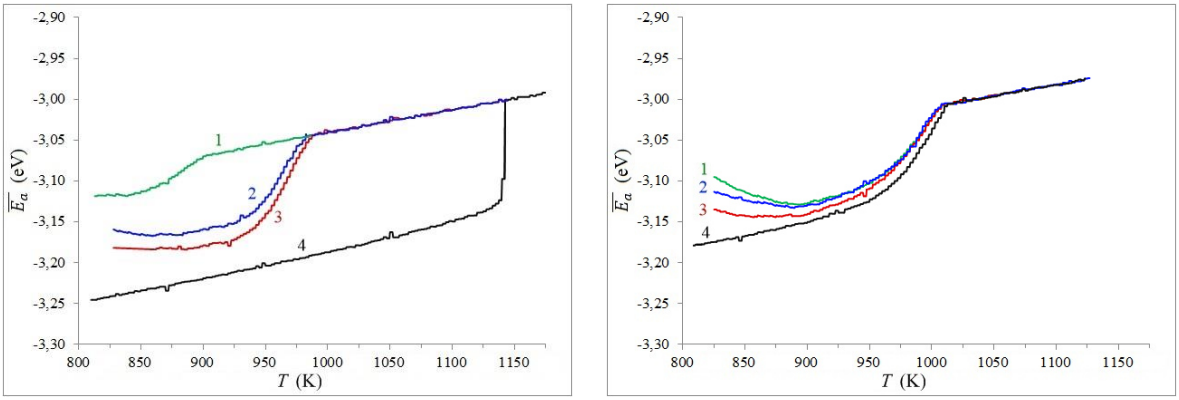

(a) (b)

Fig. 3. Dependences of the average potential energy of atoms on temperature during heating at a rate of 10^{12} K/s under conditions without (a) and in the presence of a free surface (b). 1, 2, 3 – dependencies for cells with structures shown in Fig. 2(a-c), respectively; 4 – for an ideal crystal

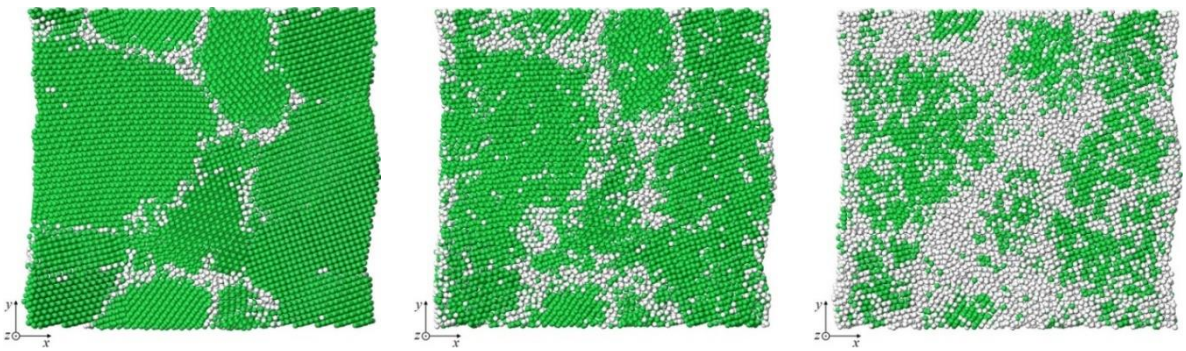

(a) (b) (c)

Fig. 4. Melting from grain boundaries and surface: (a) initial structure; (b) at a temperature of 950 K at a time of 5 ps; (c) at a temperature of 970 K at a time of 10 ps

However, not all grain boundaries are equally likely to initiate melting. As it turned out, this depends on the energy of boundary formation, that is, again on the stored energy. For example, in the case of boundaries with low formation energy, that is, low-angle boundaries with a high density of coinciding nodes, special boundaries, and especially twins, melting occurs less intensely than at other boundaries.

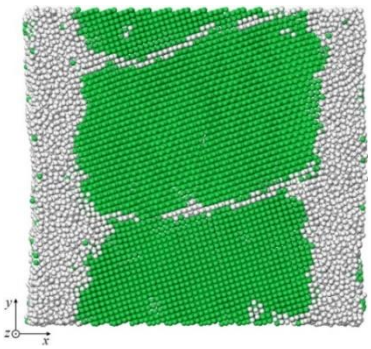

Fig. 5. Melting from the surface in the presence of low-energy grain boundaries

For a computational cell with a low-energy grain boundary, a relatively small difference in the average atomic energy from the average atomic energy in a cell without defects was characteristic. In addition, when using the crystalline phase visualizer for such boundaries, the number of atoms whose environment did not correspond to the crystal (white atoms in the figures) was noticeably smaller than in the case of high-angle boundaries. Figure 5 shows an example where it is clearly visible that the melting front comes from the free surface (left and right), while two low-energy boundaries remain almost unmolten.

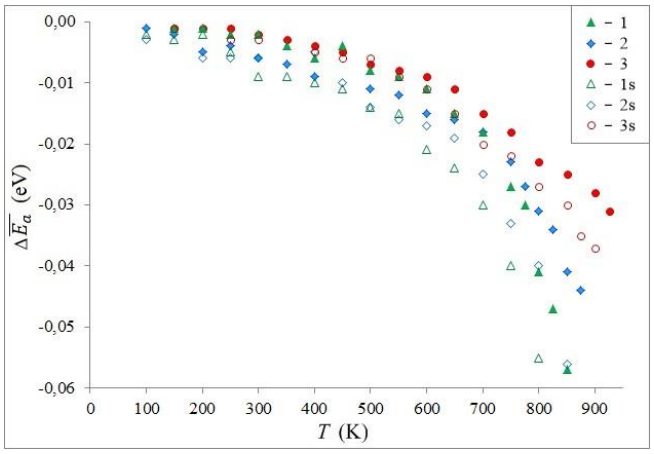

Fig. 6. Dependence of the change in the average energy of an atom during relaxation for 200 ps on temperature. Filled markers - when there is no surface, unfilled - when there is a free surface. The numbering of markers coincides with the numbering of curves in Fig. 3

When simulating heating, intense recrystallization was observed, during which a decrease in the concentration of defects and grain growth occurred. We conducted an additional study of the decrease in stored energy in the cells under consideration during relaxation at different temperatures. The results are shown in Fig. 6. Based on the research data, one can judge the stability of the nanocrystalline structure depending on various factors. So, first of all, with increasing temperature and, especially when approaching the melting temperature, recrystallization occurs more intensely. Secondly, a structure that initially has a higher excess energy, that is, containing more nonequilibrium defects, is reconstructed faster. In addition, we noticed a significant influence of the free surface. In its presence, recrystallization proceeded relatively more intensely (open markers in Fig. 6), which is apparently explained by the contribution of surface diffusion, which, as is known, proceeds faster than in the bulk.

Conclusions

Using molecular dynamics simulation, a study of the melting of aluminum with a nanocrystalline structure obtained as a result of severe plastic deformation was conducted. It is shown that the melting of nanocrystalline aluminum begins at a lower temperature than monocrystalline aluminum. Moreover, the higher the density of grain boundaries and other defects, and, accordingly, the higher the excess energy, the lower the melting temperature. In the presence of defects, melting proceeds heterogeneously

and begins primarily from the grain boundaries and free surface, after which the melting front moves towards the rest of the volume. In a pure crystal that did not contain any defects or free surface, melting in the model proceeded homogeneously and began at a temperature significantly higher (150 K) than in the case of the presence of grain boundaries or surfaces.

Grain boundaries with relatively low energy of formation (i.e., high density of coincident nodes) are less likely to initiate melting than high-angle boundaries.

When studying recrystallization in nanocrystalline aluminum, it was found that it occurs more intensely as the temperature approaches the melting point, as well as when it contains a larger number of nonequilibrium defects. In addition, the free surface had a significant effect on the intensity of recrystallization. The restructuring of the structure near it occurred faster than in the bulk of the material.

References

1. Gleiter H. Nanostructured materials: Basic concepts and microstructure. *Acta Materialia*. 2000;48(1): 1–29.
2. Meyers MA, Mishra A, Benson DJ. Mechanical properties of nanocrystalline materials. *Progress in Materials Science*. 2006;51: 427–556.
3. Kumar KS, Van Swygenhoven H, Suresh S. Mechanical behavior of nanocrystalline metals and alloys. *Acta Materialia*. 2003;51: 5743–5774.
4. Fraga MA. Nanostructured Materials. *MRS Bulletin*. 2020;45: 867–868.
5. Shkodich NF, Rogachev AS, Vadchenko SG, Sachkova NV, Chassagnon R. Reactivity of mechanoactivated Ni-Al blends. *International Journal of Self-Propagating High-Temperature Synthesis*. 2012;21(2): 104–109.
6. Maglia F, Milanese C, Anselmi-Tamburini U, Doppiu S, Cocco G, Munir ZA. Combustion synthesis of mechanically activated powders in the Ta-Si system. *Journal of Alloys and Compounds*. 2004;385: 269–275.
7. Maglia F, Milanese C, Anselmi-Tamburini U. Combustion synthesis of mechanically activated powders in the Nb-Si system. *Journal of Materials Research*. 2002;17(8): 1992–1999.
8. Rogachev AS, Shkodich NF, Vadchenko SG, Baras F, Kovalev DY, Rouvimov S, Nepapushev AA, Mukasyan AS. Influence of the high energy ball milling on structure and reactivity of the Ni + Al powder mixture. *Journal of Alloys and Compounds*. 2013;577: 600–605.
9. Filimonov VY, Loginova MV, Ivanov SG, Sitnikov AA, Yakovlev VI, Sobachkin AV, Negodyaev AZ, Myasnikov AY. Peculiarities of phase formation processes in activated Ti+Al powder mixture during transition from combustion synthesis to high-temperature annealing. *Combustion Science and Technology*. 2020;192(3): 457–470.
10. Loginova MV, Yakovlev VI, Filimonov VY, Sitnikov AA, Sobachkin AV, Ivanov SG, Gradoboev AV. Formation of structural states in mechanically activated powder mixtures Ti+Al exposed to gamma irradiation. *Letters on Materials*. 2018;8(2): 129–134.
11. Phillpot SR, Lutsko JF, Wolf D, Yip S. Molecular-dynamics study of lattice-defect-nucleated melting in silicon. *Physical Review B*. 1989;40: 2831.
12. Xiao S, Hu W, Yang J. Melting behaviors of nanocrystalline Ag. *Journal of Physical Chemistry B*. 2005;109: 20339–20342.
13. Xiao S, Hu W, Yang J. Melting temperature: from nanocrystalline to amorphous phase. *Journal of Chemical Physics*. 2006;125: 184504.
14. Noori Z, Panjepour M, Ahmadian M. Study of the effect of grain size on melting temperature of Al nanocrystals by molecular dynamics simulation. *Journal of Materials Research*. 2015;30: 1648–1660.
15. Poletaev GM, Bebikhov YV, Semenov AS. Molecular dynamics study of the formation of the nanocrystalline structure in nickel nanoparticles during rapid cooling from the melt. *Materials Chemistry and Physics*. 2023;309: 128358.
16. Poletaev G, Gafner Y, Gafner S, Bebikhov Y, Semenov A. Molecular dynamics study of the devitrification of amorphous copper nanoparticles in vacuum and in a silver shell. *Metals*. 2023;13(10): 1664.
17. Poletaev GM, Gafner YY, Gafner SL. Molecular dynamics study of melting, crystallization and devitrification of nickel nanoparticles. *Letters on Materials*. 2023;13(4): 298–303.
18. Zope RR, Mishin Y. Interatomic potentials for atomistic simulations of the Ti-Al system. *Physical Review B*. 2003;68: 024102.

19. Kim Y-K, Kim H-K, Jung W-S, Lee B-J. Atomistic modeling of the Ti-Al binary system. *Computational Materials Science.* 2016;119: 1–8.
20. Pei Q-X, Jhon MH, Quek SS, Wu Z. A systematic study of interatomic potentials for mechanical behaviours of Ti-Al alloys. *Computational Materials Science*. 2021;188: 110239.
21. Poletaev GM. Self-diffusion in liquid and solid alloys of the Ti-Al system: molecular-dynamics simulation. *Journal of Experimental and Theoretical Physics*. 2021;133(4): 455–460.
22. Poletaev GM, Bebikhov YV, Semenov AS, Sitnikov AA, Yakovlev VI. Molecular dynamics study of the dissolution of titanium nanoparticles in aluminum. *Materials Physics and Mechanics*. 2023;51(5): 9–15.
23. Poletaev GM, Bebikhov YV, Semenov AS, Sitnikov AA. Molecular dynamics investigation of the effect of the interface orientation on the intensity of titanium dissolution in crystalline and amorphous aluminum. *Journal of Experimental and Theoretical Physics*. 2023;136(4): 477–483.
24. Levchenko EV, Ahmed T, Evteev AV. Composition dependence of diffusion and thermotransport in Ni-Al melts: a step towards molecular dynamics assisted databases. *Acta Materialia*. 2017;136: 74–89.
25. Tsuzuki H, Branicio PS, Rino JP. Structural characterization of deformed crystals by analysis of common atomic neighborhood. *Computer Physics Communications*. 2007;177: 518–523.
26. Nguyen TD, Nguyen CC, Tran VH. Molecular dynamics study of microscopic structures, phase transitions and dynamic crystallization in Ni nanoparticles. *RSC Advances*. 2017;7: 25406–25413.
27. Safaei A, Attarian Shandiz M, Sanjabi S, Barber ZH. Modeling the melting temperature of nanoparticles by an analytical approach. *The Journal of Physical Chemistry C*. 2008;112: 99–105.
28. Gafner Y, Gafner S, Redel L, Poletaev G. Estimation of the structure of binary Ag-Cu nanoparticles during their crystallization by computer simulation. *Journal of Nanoparticle Research*. 2023;25: 205.
29. Chan W-L, Averback RS, Cahill DG, Ashkenazy Y. Solidification velocities in deeply undercooled silver. *Physical Review Letters.* 2009;102: 095701.
30. Zhang HY, Liu F, Yang Y, Sun DY. The molecular dynamics study of vacancy formation during solidification of pure metals. *Scientific Reports*. 2017;7: 10241.

About Authors

Gennady M. Poletaev Sc
Doctor of Physical and Mathematical Sciences
Head of Department (Polzunov Altai State Technical University, Barnaul, Russia)

Alexander A. Sitnikov Sc
Doctor of Technical Sciences
Director of the industrial implementation complex of applied research and development (Polzunov Altai State Technical University, Barnaul, Russia)

Vladimir I. Yakovlev Sc
Candidate of Technical Sciences
Leading Researcher (Polzunov Altai State Technical University, Barnaul, Russia)

Valeriy Yu. Filimonov Sc
Doctor of Physical and Mathematical Sciences
Professor (Polzunov Altai State Technical University, Barnaul, Russia)
Leading Researcher (Institute for Water and Environmental Problems SB RAS, Barnaul, Russia)

Darya V. Novoselova Sc
Candidate of Physical and Mathematical Sciences
Assistant Professor (Kuzbass Institute of the Federal Penitentiary Service of Russia, Novokuznetsk, Russia)

MATERIALS PHYSICS AND MECHANICS RESEACH ARTICLE

Submitted: November 14, 2023 **Revised: December 18, 2023** **Accepted: April 24, 2024**

Stability analysis of solid morphology incorporating surface elasticity and surface tension

G.M. Shuvalov ✉, **S. A. Kostyrko**,

St. Petersburg State University, St. Petersburg, Russia

✉ g.shuvalov@spbu.ru

ABSTRACT

This paper is primarily focused on exploring the morphological instability conditions inherent in nanostructured solid surfaces. Employing the constitutive equations of Gurtin–Murdoch model, we examine how surface elasticity and surface tension exert their influence on surface relief formation. Within this framework, we posit that the surface instability of the solid surface is instigated by surface diffusion processes propelled by the nuanced interplay of surface and bulk energy across the undulated surface. To distinguish the strain field along the undulated surface, we navigate the solution space of the plane elasticity problem, accounting for plane strain conditions. Our investigation tracks the linearized evolution of the surface, capturing the change in the amplitude of surface perturbations with time. Thus, the presented linear stability analysis sheds light on the precise conditions that initiate the early-stage increase in surface relief amplitude. This nuanced exploration provides not only a theoretical foundation, but also practical insights into the intricate mechanisms governing the morphological stability of nanostructured solid surfaces.

KEYWORDS

morphological stability • surface elasticity • surface diffusion • plane strain

Acknowledgements. *The author acknowledges the support of the Russian Science Foundation under grant number 22-11-00087, https://rscf.ru/en/project/22-11-00087/*

The article was prepared based on the report presented at the Symposium "Micromechanics of Functional Materials" at the XIII All-Russian Congress on Theoretical and Applied Mechanics.

Citation: Shuvalov GM, Kostyrko SA. Stability analysis of solid morphology incorporating surface elasticity and surface tension. *Materials Physics and Mechanics*. 2024;52(2): 114–122.
http://dx.doi.org/10.18149/MPM.5222024_12

Introduction

The study of nanostructured materials is important for the development of modern electronic and optoelectronic devices. The roughness of free surfaces and interfacial boundaries has a significant effect on optical properties [1,2]. It is also used to enhance the coupling between electronic circuit components when creating flexible electronics [3]. Additionally, the formation of the surface relief can be applied to produce quantum dots [4]. However, the created relief may be unstable and evolve during the manufacture and operation of devices. Morphological instability can lead to decreased reliability or functionality of the devices based on patterned structures, especially in applications where high levels of mechanical stress are present. Stress concentrations at valley regions of an undulated surface can aid the nucleation of defects [5,6]. Therefore, in addition to other processes [7–9], morphological instability is one of the key factors in the stress-assisted degradation of materials. This highlights the significance of understanding the self-organization of solid surfaces.

Mullins [10] conducted pioneering research on the morphological instability of free solid surfaces influenced by surface diffusion, particularly observing the formation of surface grooves at the grain boundaries of a heated polycrystal. Later studies revealed the morphological instability of the stressed solid bodies due to diffusion perturbations with wavelengths exceeding a critical value [11]. The determination of this critical wavelength is based on the ratio between the surface energy and the energy of elastic deformation calculated on the surface.

A series of studies were conducted to analyze the stability of free and interfacial surfaces in solids with different topological defects [12–14]. However, in most works dedicated to studying surface/interface morphological instability, the influence of surface and interface elasticity was neglected, as it was considered to be small compared to bulk elastic behavior. Nevertheless, in nanostructured materials, the ratio of surface to volume increases, which leads to an increase in the influence of surface deformation [15]. So, to accurately predict the conditions under which morphological instability occurs, we need to take surface elasticity into account.

In this paper, we examine the phenomenon of surface nanosized relief instability, considering its surface elastic properties and surface tension. Our study is based on the complete model of surface elasticity developed by Gurtin and Murdoch [16] and the Asaro–Tiller–Grinfeld model of morphological instability [11,17,18].

Problem formulation

We consider film coating under plane strain loading (Fig. 1). It is assumed that the film thickness significantly exceeds the surface relief period. Therefore, we neglect the deformation of the substrate and the interfacial boundary and come to the 2D elastic problem for a homogeneous half-plane B with a curvilinear boundary S, which profile is described by an arbitrary periodic function f:

$$S = \{z: z \equiv \zeta = x_1 + i\varepsilon(\tau)f(x_1)\},\ \ B = \{z: x_2 < \varepsilon(\tau)f(x_1)\},\ \ z = x_1 + ix_2,\ \ i^2 = -1,$$
$$f(x_1) = f(x_1 + a),\ \ \max|f(x_1)| = a,\ \ \ \varepsilon(\tau) = \frac{A(\tau)}{a}\forall\,\tau,\ \ A(0) = A_0. \tag{1}$$

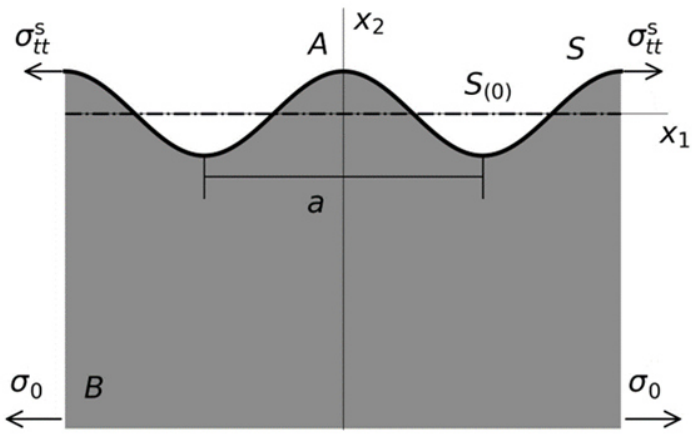

Fig. 1. The model of a solid with a slightly undulated surface

According to the principles of Gurtin–Murdoch surface elasticity theory, the surface domain is considered as an exceptionally thin layer that firmly adheres to the bulk without any slipping. The continuity of displacements across the surface region is provided by the following conditions:

$$u_s(\zeta) = u(\zeta), \quad \zeta \in S, \tag{2}$$

where $u^s = u_1^s + iu_2^s$, $u = u_1 + iu_2$; u_1^s, u_2^s and u_1, u_2 are the displacements of the surface and bulk phases along Cartesian axes x_1 and x_2.

The mechanical equilibrium conditions on a curved solid surface are captured by the generalized Young–Laplace equations [19]:

$$\sigma(\zeta) = \gamma_0\kappa + \left[M\kappa\mathrm{Re}\frac{\partial u}{\partial\zeta} + \gamma_0\mathrm{Im}\left(\frac{\partial^2 u}{\partial\zeta^2}e^{i\alpha_0}\right)\right] + i\left[M\mathrm{Re}\left(\frac{\partial^2 u}{\partial\zeta^2}e^{i\alpha_0}\right) - \gamma_0\kappa\mathrm{Im}\frac{\partial u}{\partial\zeta}\right], \tag{3}$$

where $\sigma(\zeta) = \sigma_{nn}(\zeta) + i\sigma_{nt}(\zeta)$ is the complex stress vector, σ_{nn} and σ_{nt} are the components of bulk stress tensor, defined in the Cartesian coordinates (n, t) ($\boldsymbol{n}$ is a normal to S), γ_0 is residual surface stress (surface tension), $M = \lambda_s + 2\mu_s$ is surface stiffness, λ_s and μ_s are the Lame parameters for the surface domain, κ is the local curvature of S, α_0 is the angle between the tangent to S and x_1-axis at the point ζ.

The boundary conditions at infinity are defined as

$$\lim_{x_2\to-\infty}\omega = \lim_{x_2\to-\infty}\sigma_{22} = \lim_{x_2\to-\infty}\sigma_{12} = 0, \lim_{x_2\to-\infty}\sigma_{11} = \sigma_0, \tag{4}$$

where ω is the rotation angle, σ_{ij} $(i, j = \{1,2\})$ are components of stress tensor in Cartesian coordinates (x_1, x_2) and the longitudinal stress σ_0 may means either misfit stress or mechanical loading.

As it was mentioned in introduction, the surface profile of a stressed solid may change under the influence of surface diffusion due to nonuniform distribution of chemical potential. So, the surface atoms are moving from a region with high chemical potential to a region with a lower one, i.e. atomic flow along the surface is proportional to the gradient of chemical potential. According to [18], the chemical potential is defined as the sum of bulk strain elastic energy and surface energy. The mass conservation law leads to the following differential equation, which describes the change of surface profile $g(x_1, \tau) = \varepsilon(\tau)f(x_1)$ over the time [18,20]:

$$\frac{\partial g(x_1,\tau)}{\partial\tau} = K_s h(x_1,\tau)\frac{\partial^2}{\partial s^2}[U(\zeta,\tau) - \kappa(\zeta,\tau)U_s(\zeta,\tau)], \; K_s = D_s C_s \Omega^2/(k_b T), \tag{5}$$

where U is the strain elastic energy density and U_s is the surface energy, h is the metric coefficient, D_s is the self-diffusivity coefficient; C_s is the number of diffusing atoms per unit area; k_b is the Boltzmann constant, T is the absolute temperature; and s is arc length along S.

To prevent or minimize morphological instability in stressed films, it is crucial to consider various factors such as the elastic properties of bulk and surface phases, the stress levels, and the shape of the initial surface profile. In this paper, our attention was directed towards the examination of the conditions that facilitate the occurrence of morphological instability.

Linear stability analysis

To integrate the evolution equation (5) and establish the stability conditions for a stressed solid surface, we must first calculate the elastic strain energy U and the surface energy U_s. It is important to note that the effect of surface elasticity was assumed to be insignificant in previous studies dedicated to investigating the morphological instability of the surface

microrelief. However, to accurately predict the instability conditions for a stressed surface with nanosized relief, it is essential to consider the effect of surface elasticity.

The elastic strain energy U and the surface energy U_s can be expressed as follows [21]:

$$U = \left(\frac{1}{2}\lambda + \mu\right)\left((\varepsilon_{tt})^2 + (\varepsilon_{nn})^2\right) + \lambda\varepsilon_{nn}\varepsilon_{tt} + 2\mu(\varepsilon_{nt})^2, \tag{6}$$

$$U_s = \gamma_0 + \left(\frac{1}{2}\lambda_s + \mu_s\right)(\varepsilon_{tt}^s)^2, \tag{7}$$

where ε_{ij} are the components of bulk and surface stress tensors, respectively, defined in the Cartesian coordinates (n, t) ($\boldsymbol{n}$ is a normal to S), and λ and μ are the Lame constants of the solid B.

Therefore, in order to integrate (5), we have to obtain the stress-strain state near the undulated surface. To achieve this, we solve the corresponding plane strain problem for a homogeneous elastic half-plane with a curved boundary (1) – (4), using the original approach suggested in [19,22].

Here we consider a weak undulation of the surface relief ($\varepsilon \ll 1$), and therefore we calculate components of the strain tensors of the bulk and surface phases as well as metric coefficient h and the surface curvature κ using the linear approximation of the boundary perturbation method [19]:

$$\varepsilon_{ij} = \varepsilon_{ij(0)} + \varepsilon\varepsilon_{ij(1)},\ \varepsilon_{tt}^s = \varepsilon_{tt(0)}^s + \varepsilon\varepsilon_{tt(1)}^s, \tag{8}$$

$$\kappa(x_1, \tau) = \varepsilon(\tau)f''(x_1), \quad h(x_1, \tau) = 1, \tag{9}$$

where a prime denotes the derivative with respect to the argument.

Substituting Eqs. (6) – (9) into (5), and integrating over the interval $[0;\ x_0]$ ($x_0 \in [0, a/2]$ and $f(x_0) = 0$), we receive an ordinary differential equation that reveals the variation of surface relief amplitude with time:

$$\begin{aligned}\frac{dA(\tau)}{d\tau}\int_0^{x_0} f(x_1)dx_1 = \frac{A(\tau)K_s}{2}\int_0^{x_0}\frac{d^2}{dx_1^2}\Big[\lambda\left(\varepsilon_{tt(0)}\varepsilon_{nn(1)}(x_1) + \varepsilon_{tt_0}\varepsilon_{nn(1)}(x_1)\right) + \\ + \left(\frac{1}{2}\lambda + \mu\right)\left(2\varepsilon_{tt(0)}\varepsilon_{tt(1)}(x_1) + 2\varepsilon_{nn(0)}\varepsilon_{nn(1)}(x_1)\right) + 4\mu\varepsilon_{nt(0)}\varepsilon_{nt(1)}(x_1) - \\ - f''(x_1)\left(\gamma_0 + \left(\frac{1}{2}\lambda_s + \mu_s\right)\left(\varepsilon_{tt(0)}^s\varepsilon_{tt(0)}^s\right)\right)\Big]\,dx_1.\end{aligned} \tag{10}$$

We seek the functions $\varepsilon_{ij(1)}$, $\varepsilon_{tt(1)}^s$ in the form of a Fourier series with unknown coefficients P and Q:

$$\varepsilon_{ij(1)} = \sum_{k=1}^{\infty}\left[P_{(\varepsilon_{ij})k}\sin(b_k x_1) + Q_{(\varepsilon_{ij})k}\cos(b_k x_1)\right], \tag{11}$$

$$\varepsilon_{tt(1)}^s = \sum_{k=1}^{\infty}\left[P_{(\varepsilon_{tt}^s)k}\sin(b_k x_1) + Q_{(\varepsilon_{tt}^s)k}\cos(b_k x_1)\right], \tag{12}$$

where $b_k = 2\pi k/a$.

In the present paper, we do not give explicit expressions for these functions due to their tremendous size, but they can be found using the original algorithm, presented in [19].

The Fourier series approximation is also utilized to represent the known function $f(x_1)$, which describes the surface profile:

$$f(x_1) = \sum_{k=1}^{\infty} R_k\cos(b_k x_1), \quad R_k = \frac{2}{a}\int_{-a/2}^{a/2} f(x_1)\cos(b_k x_1)\,dx_1. \tag{13}$$

The solution of the elasticity problem gives the unknowns components of surface and bulk strain tensors required to determine the amplitude as a function of time. Due to the enormous size of the explicit solution of evolution equation, we write it in the following form:

$$\ln\left(\frac{A(\tau)}{A_0}\right) = \frac{K_s}{J_f}\sum_{k=1}^{\infty} V_k\,k^{-1}\sin(b_k x_0)\,\tau,\ J_f = \sum_{k=1}^{\infty} R_k k^{-1}\sin(b_k x_0). \tag{14}$$

where functions $V_k = V_k(a, \lambda, \mu, \lambda_s, \mu_s, \gamma_0, \sigma_0, R_k)$ are known functions depending on the physical and geometrical parameters of the problem but are not presented here because of their cumbersomeness.

Numerical results

As per the findings of experimental research, it has been determined that the diverse relief configurations, encompassing a cusp-like relief and a smoothly undulated relief, may be occurred in the process of surface rearrangement because of morphological instability. The following function is used to investigate the impact of surface profiles on morphological instability:

$$f(x_1) = -\frac{a}{d}\left[\mathrm{Im\ ctg}\left(\frac{\pi x_1}{a} - iy\right) - 1\right], \quad d = \mathrm{Im\ ctg}\,(iy) + 1, \tag{15}$$

where the parameter $y \in (0, +\infty)$ defines the shape of surface profile. We take $y = 2$ for the smoothly undulated surface, and y = 0.7 for cusp-like relief.

For example, we use following bulk Lame parameters for isotropic solid: λ =58.17 GPa, μ =26.13 GPa. Also, we set surface stiffness $M =$ 6.099 N/m and surface tension $\gamma_0 = 1$ N/m, which correspond to aluminum surface Lame parameters calculated in [23] using molecular dynamics. As the thin film systems are often subjected to large stress, typically in giga-Pascal range [5], we consider the values of σ_0 in the range from 1 to 2 GPa.

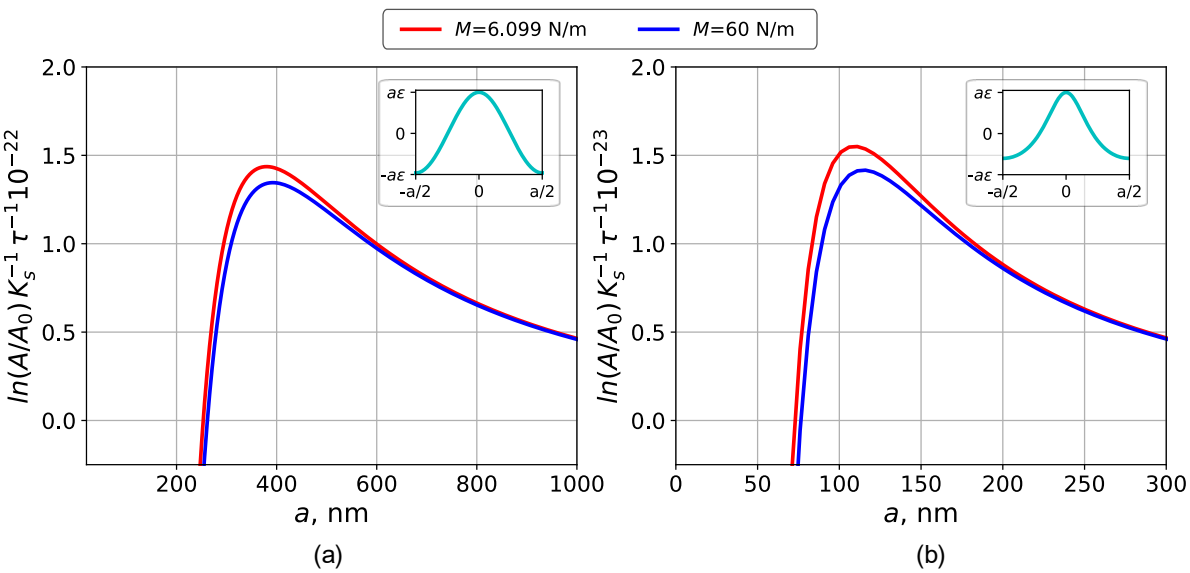

Fig. 2. The dependence of normalized amplitude changes $A(\tau)/A_0$ on the perturbation wavelength a for surface profile parameters y = 2 (a) and y = 0.7 (b)

Figure 2 shows the dependence of the normalized amplitude changes $A(\tau)/A_0$ of the surface relief on the perturbation wavelength a for $\sigma_0 = 1$ GPa, different surface stiffness values $M = \{6.099, 60\}$ N/m (red and blue lines, respectively) and surface profiles with y = 2 (a) and y = 0.7 (b). The abscissas of the intersections of the x-axis and each line lead to the determination of the critical undulation wavelengths a_{cr} corresponding to the thermodynamic equilibrium. If the wavelength of initial undulation $a \in (0, a_{cr})$, the surface relief amplitude will decrease with time, and vice versa, surface undulation will grow in the

case $a \in (a_{cr}, \infty)$. The critical perturbation wavelength a_{cr} for the considered parameters and for the case, when surface elasticity is neglected ($M = 0$), are presented in the Table 1.

Table 1. The critical wavelength a_{cr} of considered system for various parameters

Surface stiffness M, N/m	6.099	60	0
Shape parameter a_{cr}, nm			
y = 2	253.3	261.6	252.3
y = 0.7	72.8	76.5	72.2

Figures 3–5 demonstrate the dependence of critical undulation wavelength a_{cr} on surface stiffness M, surface tension γ_0 and misfit stress σ_0. A succinct examination of the results is presented in the conclusions. It is noteworthy that these findings are in good agreement with the outcomes of previous studies where the simplified Gurtin-Murdoch model was considered omitting the normal component of the surface gradient of the displacement field [24,25]. From the results of current study, it follows that accounting of this term doesn't affect the critical value of perturbation wavelength found within the linear analysis of morphological stability. The main goal of linear stability analysis is to predict the conditions under which changes in morphology might occur. Nonetheless, it's worth noting that linear stability analysis is limited to minor changes in surface profile amplitude. To examine how the surface changes over longer periods, it's essential to take into account the nonlinear terms in the surface evolution equation. By keeping terms up to a certain order in the perturbation expansion, we can grasp the behavior at higher amplitudes when cusp-like grooves appear. However, higher amplitudes of undulation profile may significantly amplify the misfit stresses and lead to the nucleation of dislocations [5,6]. The generation of dislocations lowers the local strain energy in the surface layer decreasing the driving force behind relief formation [26].

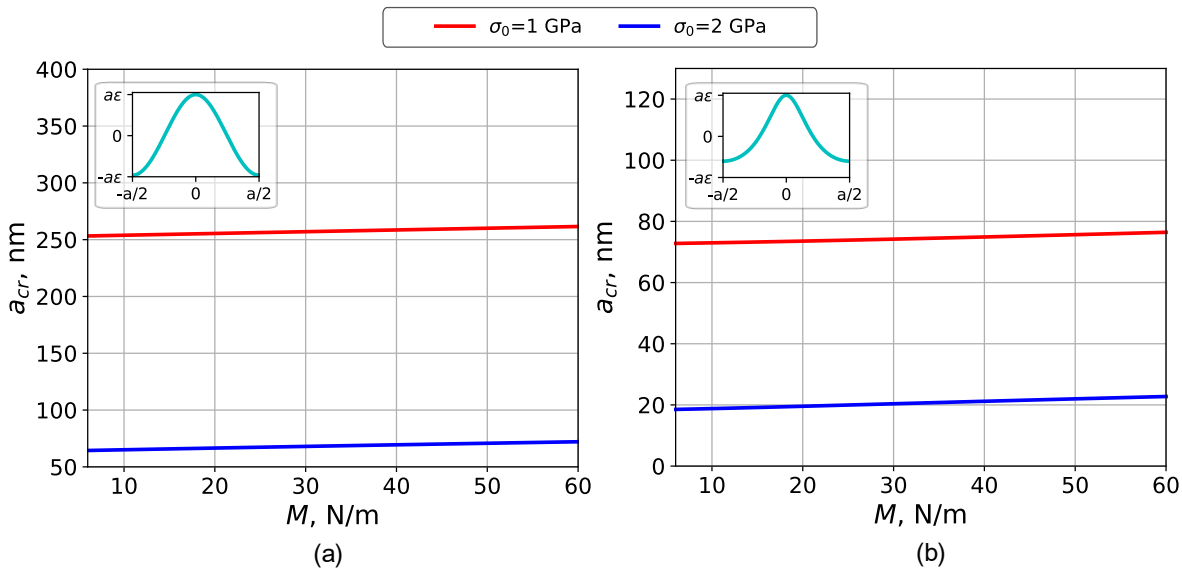

Fig. 3. The effect of surface stiffness M on critical undulation wavelength a_{cr} for surface profile parameters y = 2 (a) and y = 0.7 (b)

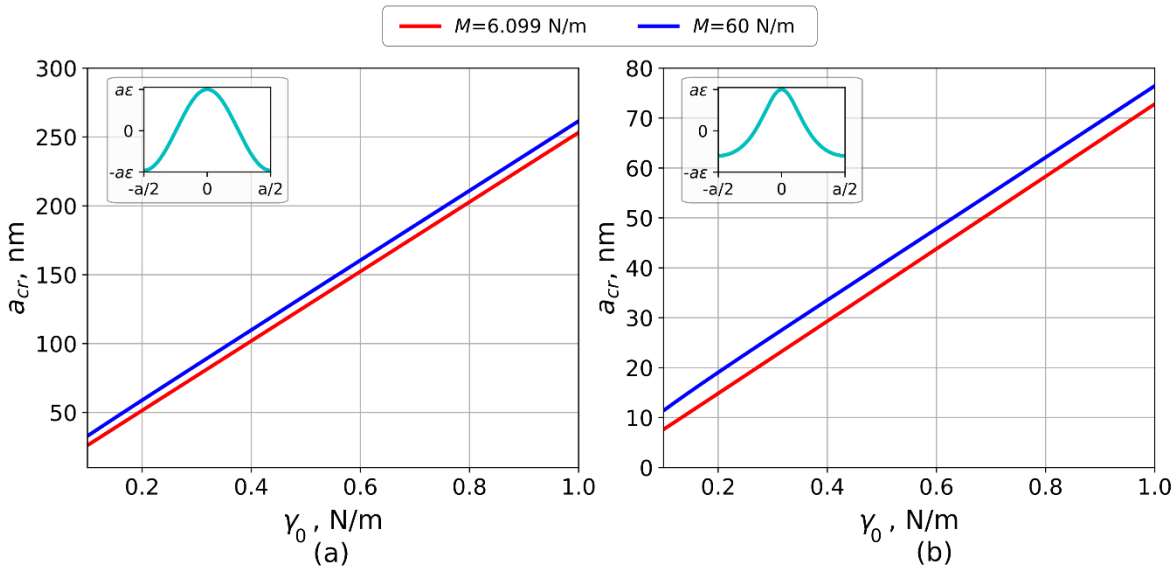

Fig. 4. The effect of surface tension γ_0 on critical undulation wavelength a_{cr} for surface profile parameters y = 2 (a) and y = 0.7 (b)

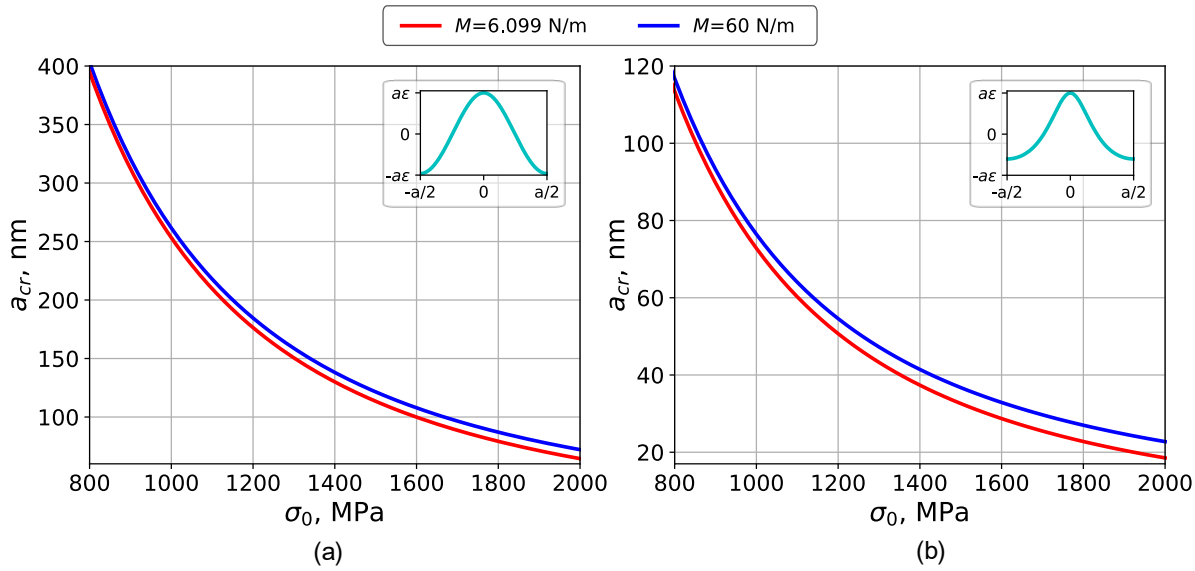

Fig. 5. The effect of longitudinal stress σ_0 on critical undulation wavelength a_{cr} for surface profile parameters y = 2 (a) and y = 0.7 (b)

Conclusions

In this paper, we investigate the joint effect of surface elasticity, tension and shape on the morphological instability in nanopatterned solid films based on Gurtin – Murdoch theory of surface elasticity and the Asaro – Tiller – Grinfeld model of morphological instability. In line with [18], the morphological instability of the film surface results from surface diffusion driven by variations in surface and bulk energy along the undulated solid surface.

Assuming that the film thickness is significantly greater than the initial surface relief wavelength, we defined the elastic strain energy and the surface energy from the solution of the elastic problem for a homogeneous elastic half-plane with curved boundary under plane strained conditions. The solution of the linearized evolution equation allowed us

to determine the amplitude of arbitrary periodic surface relief as a function of time. The critical conditions that correspond to surface morphological instability are determined through the analysis of this solution.

We investigated the dependence of the critical undulation wavelength on the misfit stress, surface tension, surface stiffness and the shape of the initial surface relief, and based on the obtained data, we have come to the following conclusions:

– an increase in the curvature radius of the initial surface profile, surface stiffness, surface tension, and a decrease in longitudinal stress result in an augmentation of the critical perturbation wavelength.

– a decrease in the influence of surface stiffness is observed with an increase in surface tension as well as in curvature radius of the initial surface profile, and a decrease in longitudinal stress.

References

1. Kim S, Kim SM, Park HH, Choi DG, Jung JV, Jeong JH, Jeong JR. Conformally direct imprinted inorganic surface corrugation for light extraction enhancement of light emitting diodes. *Optics Express*. 2012;20(5): A713-A721.
2. Vasiliev OS, Ruzankina J, Tarasov SS. The relationship of the geometric parameters of the surface with its properties (optical, emission, tribological). *Journal of Physics: Conference Series*. 2019;1410: 012174.
3. Lacour SP, Wagner S, Huang ZY, Suo Z. Stretchable gold conductors on elastomeric substrates. *Applied Physics Letters*. 2003;82(15): 2404.
4. Aqua JN, Xu X. Growth of quantum dots on pit-patterns. *Surface Science*. 2015;639: 20-24.
5. Gao H, Nix WD. Surface roughening of heteroepitaxial thin films. *Annual Review of Material Science*. 1999;29: 73-209.
6. Goldthorpe IA, Marshall AF, McIntyre PC. Synthesis and strain relaxation of Ge-core/Si-shell nanowire arrays. *Nano Letters*. 2008;8(11): 4081-4086.
7. Evstafeva I, Pronina Y. On the mechanochemical dissolution of shells and its temperature dependence: Discussion of different models. *International Journal of Engineering Science*. 2023;190: 103889.
8. Javanbakht M, Ghaedi MS. Phase field approach for void dynamics with interface stresses at the nanoscale. *International Journal of Engineering Science*. 2020;154: 103279.
9. Krasnitckii SA, Gutkin MY, Kolesnikova AL, Romanov AE. Formation of a pore as stress relaxation mechanism in decahedral small particles. *Letters on Materials*. 2022;12(2): 137-141.
10. Mullins WW. Theory of thermal grooving. *Journal of Applied Physics*. 1957;28(3): 333-339.
11. Asaro RJ, Tiller WA. Interface morphology development during stress-corrosion cracking: Part I. Via surface diffusion. *Metallurgical and Materials Transactions B*. 1972;3: 1789-1796.
12. Duan HL, Weissmuller J, Wang Y. Instabilities of core – shell heterostructured cylinders due to diffusions and epitaxy: spheroidization and blossom of nanowires. *Journal of the Mechanics and Physics of Solids*. 2008;56(5): 1831-1851.
13. Wang W, Suo Z. Shape change of a pore in a stressed solid via surface diffusion motivated by surface and elastic energy variation. *Journal of the Mechanics and Physics of Solids*. 1997;45(5): 709-729.
14. Schmidt V, McIntyre PC, Gösele U. Morphological instability of stress-strained core-shell nanowires. *Physical Review B*. 2008;77(23): 235302.
15. Shuvalov GM, Vakaeva AB, Shamsutdinov DA, Kostyrko SA. The effect of nonlinear terms in boundary perturbation method on stress concentration near the nanopatterned bimaterial interface. *Vestnik of Saint Petersburg University. Applied Mathematics. Computer Science. Control Processes.* 2020;16(2): 165-176.
16. Gurtin ME, Murdoch AI. Surface stress in solids. *International Journal of Solids and Structures*. 1978;14(6): 431-440.
17. Grinfeld M. Instability of the equilibrium of a nonhydrostatically stressed body and a melt. *Fluid Dynamics*. 1987;22: 169-173.
18. Freund LB. Evolution of waviness on the surface of a strained elastic solid due to stress-driven diffusion. *International Journal of Solids and Structures*. 1995;32(6-7): 911-923.

19. Kostyrko S, Grekov M, Altenbach H. Stress distribution at the wavy surface of a solid incorporating surface stresses and surface tension. In: Altenbach H, Bauer SM, Belyaev AK, Indeitsev DA, Matveenko VP, Petrov YV. (eds.) *Advances in Solid and Fracture Mechanics*. Cham: Springer; 2022. p.151-166.
20. Kostyrko SA, Shuvalov GM. Surface elasticity effect on diffusional growth of surface defects in strained solids. *Continuum Mechanics and Thermodynamics*. 2019;31: 1795-1803.
21. Ru CQ: Simple geometrical explanation of Gurtin-Murdoch model of surface elasticity with clarification of its related versions. *Science China Physics, Mechanics & Astronomy*. 2010;53: 536-544.
22. Kostyrko S, Grekov M, Altenbach H. Stress concentration analysis of nanosized thin-film coating with rough interface. *Continuum Mechanics and Thermodynamics*. 2019;31: 1863-1871.
23. Miller RE, Shenoy VB. Size-dependent elastic properties of nanosized structural elements. *Nanotechnology*. 2000;11: 139-147.
24. Shuvalov G, Kostyrko S. On the role of interfacial elasticity in morphological instability of a heteroepitaxial interface. *Continuum Mechanics and Thermodynamics*. 2021;33(5): 2095-2107.
25. Shuvalov GM, Kostyrko SA. Stability analysis of nanoscale surface patterns in ultrathin film coating. *Materials Physics and Mechanics*. 2022;48(2): 232-241.
26. Gao H, Ozkan CS, Nix DW, Zimmerman JA, Freund LB. Atomistic models of dislocation formation at crystal surface ledges in Si1-xGex/Si(100) heteroepitaxial thin films. *Philosophical Magazine A*. 1999;79(2), 349-370.

About Author

Gleb M. Shuvalov Sc
Candidate of Physical and Mathematical Sciences
Associate Professor (St. Petersburg State University, St. Petersburg, Russia)

Sergey A. Kostyrko Sc
Candidate of Physical and Mathematical Sciences
Associate Professor (St. Petersburg State University, St. Petersburg, Russia)

Submitted: September 26, 2023 **Revised: November 30, 2023** **Accepted: December 15, 2023**

Thermal transformation and mechanical properties of high-temperature-resistant matrix based polyetherketones

A.S. Shabaev [1], K.T. Shakhmurzova [1], A.A. Zhansitov [1], A.L. Slonov [1], I.N. Fomicheva [2], I.V. Dolbin [1] ✉, S.Yu. Khashirova [1],

[1] Kh.M. Berbekov Kabardino-Balkarian State University, Nalchik, Russia

[2] Tula State University, Tula, Russia

✉ i_dolbin@mail.ru

ABSTRACT

Of the entire variety of polyaryletherketones, the most promising representatives of this class of polymers with high thermal and mechanical properties (polyether ether ketone, polyether ketone ketone) were studied in this work. The dependence of the rate of thermal decomposition on the structure was revealed, and the temperature-time ranges for the onset of gas evolution were shown. The order of destruction of the main polymer chain depending on temperature has been established. Due to the complexity of processing this class of polymers into products, the possibilities of changing the temperatures of phase transitions were shown in order to improve the technological conditions of processing without loss of performance characteristics. Comparative studies of the kinetics of the release of the main gaseous degradation products for polyether ether ketones from various manufacturers were carried out. The influence of hydrogen formed during the destruction process on the rate of decomposition of polymers is shown, and the dependences of the formation of carbon oxide and carbon dioxide on the structure and manufacturer of polymer materials are revealed. It has been established that polyether ether ketone has slightly higher mechanical properties compared to polyether ketone ketone, which is associated with the lower crystallinity of the latter due to the content of a comonomer with an irregular structure - isophthaloyl chloride.

KEYWORDS

polyether ether ketone • synthesis • processing• heat resistance • mechanical properties

Acknowledgements. *The study was carried out with the financial support of the Tula Region Committee for Science and Innovation under Agreement No. 10 dated 07.09.2022 "Development of a highly efficient import-substituting technology for the production of high-tech polyesterketonketone with a long service life".*

Citation: Shabaev AS, Shakhmurzova KT, Zhansitov AA, Slonov AL, Fomicheva IN, Dolbin IV, Khashirova SY. Thermal transformation and mechanical properties of high-temperature-resistant matrix based polyetherketones. *Materials Physics and Mechanics*. 2024;52(2): 123–132.
http://dx.doi.org/10.18149/MPM.5222024_12

Introduction

Polyaryletherketones (PEK) represent a group of aromatic polyethers possessing a ketone moiety, exhibiting exceptional resistance to high temperatures [1–9]. The enduring fascination with this particular polymer category arises from their ability to meet the most up-to-date demands for the performance characteristics of contemporary polymer materials, while also potentially serving as a binding agent in the fabrication of revolutionary polymer composite materials (PCM) [10–20].

The choice of matrix directly affects the physical, mechanical, and technical characteristics of the final product, as well as the manufacturing process itself. Among

these characteristics, thermal properties play a crucial role as they not only influence the properties of the resulting product, but also determine its reliability and operational range. In this context, the thermal changes of polyetherketones of various structures utilized in industry as part of PCM should be considered.

To date, several types of polyaryletherketones are known: polyether ether ketone (PEEK), polyether ether ether ketone (PEEEK), polyether ether ketone ether ketone (PEEKEK), polyether ketone (PEK), polyether ether ketone ketone (PEEKK), polyether ketone ether ketone ketone (PEKEKK), polyether ketone ketone (PEKK) (Table 1).

Table 1. The main representatives of a number of polyaryletherketones

Name of the polymer	Polymer structure
Polyetherketone (PEK)	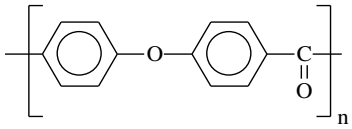
Polyether ether ketone (PEEK)	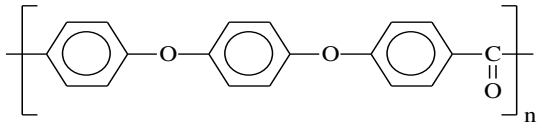
Polyether ketone ketone (PEKK)	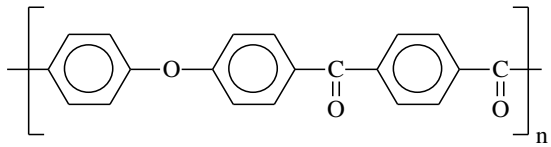
Polyether ether ketone ketone (PEEKK)	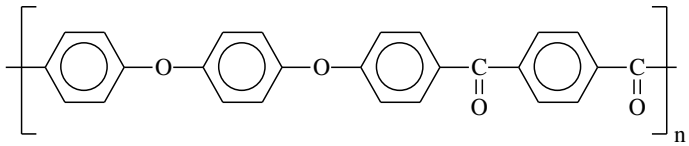
Polyether ketone ether ketone ketone (PEKEKK)	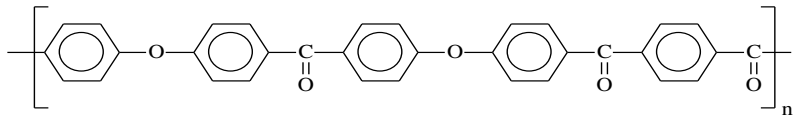
Polyether ether ether ketone (PEEEK)	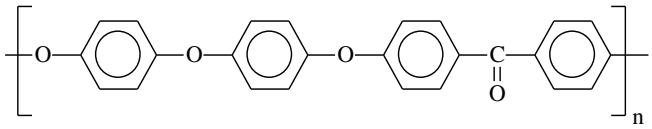

The composition of ether and carbonyl groups dictates the properties of the polymers listed in the table. Hence, as the concentration of carbonyl groups escalates, there is a corresponding elevation in the melting and glass transition temperatures (Table 2).

The level of crystallinity greatly influences impact strength, elasticity, and chemical resistance. The processing of PEK poses challenges due to its high melting point and melt viscosity. To achieve the desired operating characteristics, it is necessary to plan the processing operations that result in the appropriate level of crystallinity for PEK.

Polyetheretherketones (PEEK) have gained popularity due to their enhanced recyclability from melting, thanks to the inclusion of carbonyl and two ether linkages. In previous studies [21–23], researchers investigated the patterns of thermal degradation in polyetheretherketones with different structures and developed strategies for thermal

decomposition. The thermal degradation of polyether ketones was found to initiate with the breakage of the ketone group, and in the case of a diane fragment, with the separation of the methyl group and a simple ether bond (Fig. 1).

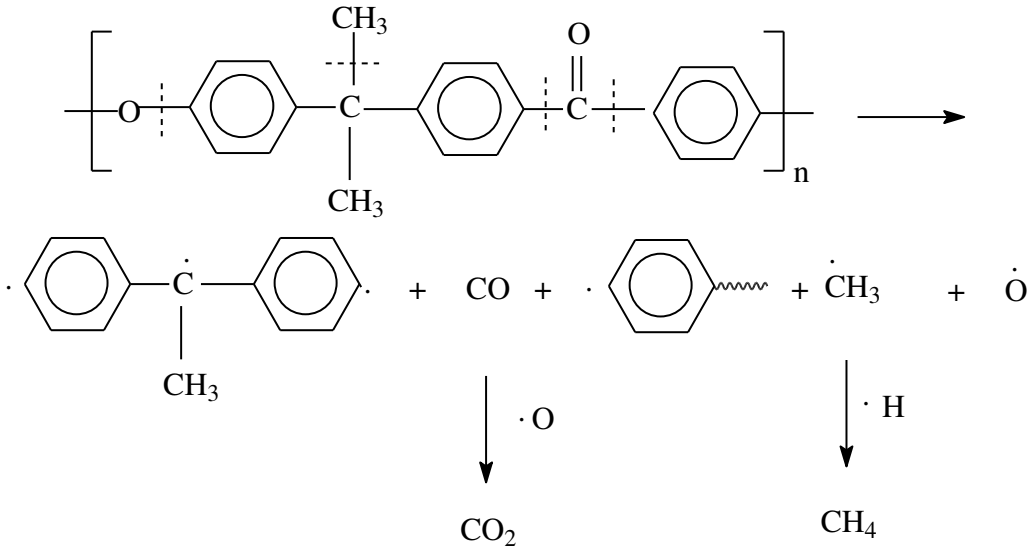

Fig. 1. Scheme of thermal decomposition of polyether ketones

Table 2. Values of melting and glass transition temperatures for various PEK [15]

Polyethylene	Concentration of ketone groups, %	T_m, °C	T_g, °C
Substituted polyphenyleneoxide	0	285	110
PEEEK	25	324	129
PEEK	33	335	141
PEK	37,5	337	144
PEEKEK	40	345	148
PEK	50	365	152
PEEKK	50	365	150
PEK	57	374 (416)	157 (160)
PEKEKK	60	384	160
PEKK	67	391	165

The discovery of water during the pyrolysis processes, which had a significant impact on the degradation of polymer materials, was a prominent characteristic observed in nearly all studies conducted on polyaryletherketones.

Polyarylates, polyether sulfones, and polyimides are the most susceptible to thermohydrolysis of all known heat-resistant polymers [24,25]. When these polymers are pyrolyzed in a humid atmosphere, the start of breakdown changes to lower temperatures by 50-100 °C. According to studies on the influence of water, drying modes of polyether ketones on their thermal and physico-mechanical properties [26,27], polymer thermos hydrolysis processes significantly worsen both the physico-mechanical and thermal properties of the products obtained. Simple ether groups are the most vulnerable to the impact of water.

Polyether ketones are typically processed into products in air at temperatures ranging from 360 to 420 °C. It is not always possible to keep the required qualities of items under such extreme circumstances. When researching the thermos-oxidative degradation of polyether ketones [28], it was discovered that PEEK thermos-oxidation begins around 325 °C and is followed by the loss of ketone groups. A rise in temperature causes parts of the benzene ring to oxidize. The authors were able to realize the potential of directional management of the depth of thermo-oxidative transformations for its processing without risk of deterioration of the major technical and operational properties with the aid of various stabilizers.

To ease processing, it is feasible to adjust both the melting point and the glass transition temperature in the synthesis of PEKK using isophthaloyl chloride. Furthermore, this substance has a high affinity for the tissues of live creatures and may be employed as an implant.

The goal of this work is to synthesize and investigate the thermal characteristics of PEKK and PEEK across a wide temperature range.

Methods

The study's subjects were the polyether ketone (PEKK) and polyether ether ketone (PEEK) of the following structure created at Kh.M. Berbekov Kabardino-Balkarian State University, Center for Advanced Materials and Additive Technologies (Fig. 2).

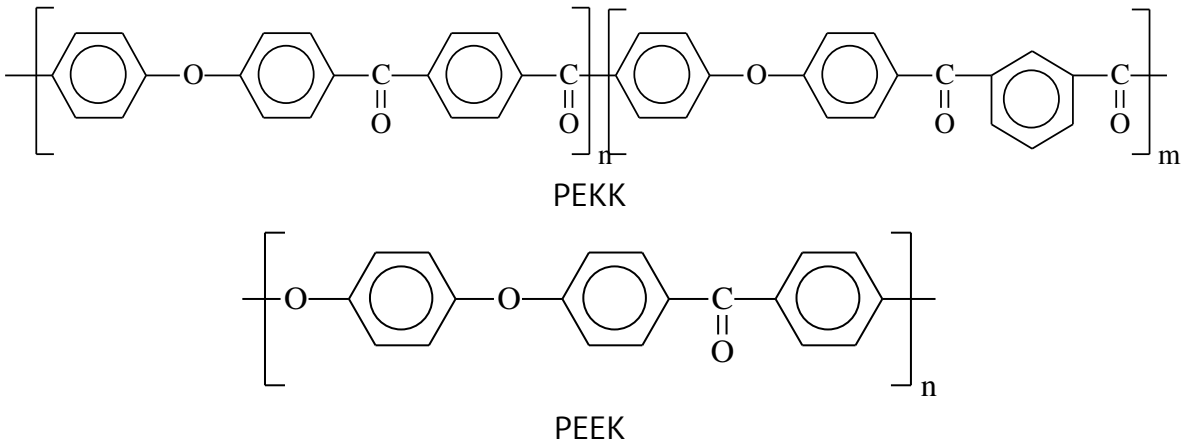

Fig. 2. Participation of atomic hydrogen in the destruction of the ketone group

Polyether ether ketone (PEKK) was synthesized via a low-temperature polycondensation process of electrophilic substitution via the Friedel-Crafts reaction. A glass reactor with a mechanical stirrer and a hydrogen chloride output was filled with diphenyl ether (DFE), terephthaloyl chloride (TPH), isophthaloyl chloride (IFX), a dispersant, and 1,2-dichloroethane. Lithium chloride, benzoin acid (BC), and guanidine methacrylate (MAG) were studied as dispersing chemicals. The reaction mixture was chilled to -20 °C before gradually adding aluminum chloride. After 1 hour, the temperature was gradually increased (0 °C – 30 min, 10 °C – 30 min) to 23-40 ± 2 °C, and the synthesis was completed in 7-20 hours. Depending on the synthesis conditions

used, the polymer precipitated from the solution over time in the form of a polymer gel or individual particles. Following synthesis, 1,2-dichloroethane with a portion of aluminum chloride was filtered from the polymer mass and subjected to regeneration, and PEKK was decompexed from the catalyst with a 3 % hydrochloric acid solution, and the resulting polymer powder was repeatedly washed with hot distilled water until a negative reaction to chlorine ions was observed. For 12 hours, the purified PEK was dried in a vacuum drying chamber at 120 °C.

The nucleophilic substitution procedure was used to synthesize polyether ether ketone (PEEK) via high-temperature polycondensation. 1,4-dihydroxybenzene 33.03 g (0.3 mol), 65.46 g (0.3 mol) 4,4'-difluorobenzophenone, 24.88 g (0.18 mol) potassium carbonate, 19.08 g (0.18 mol) sodium carbonate, and 300 g diphenyl sulfone. The reaction mass is heated to 320 °C for 2 hours and then continuously agitated in an inert gas current for 5 hours. The polymer is cooled to 250 °C and released into a metal pallet at the end of the synthesis. The cooled monolithic mass is crushed and washed with hot distilled water and acetone. For 12 hours, the powder is dried in a vacuum drying cabinet at 120 °C.

Thermogravimetric measurements were made on a Perkin-Elmer TGA-4000 derivatograph in an environment of air and nitrogen at a heating rate of 5 degrees/min. The principal gaseous pyrolysis products were analyzed using a gas chromatograph "Tsvet-800" equipped with a thermal conductivity detector, as described in [29]. The glass transition, melting, and crystallization temperatures were obtained using differential scanning calorimetry on a Perkin Elmer DSC 4000 equipment in an inert medium ranging from 30 to 370 °C, with a scanning speed of 10 °C/min. The study was based on the values of the glass transition and melting temperatures obtained during the second heating of the sample.

Results and Discussion

Figure 3 shows thermogravimetric weight loss curves for PEKK (1) and PEEK (2) in air. The study of the provided curves revealed that the temperatures for 2.5 and 10 wt. % loss for PEKK are 458, 513, and 537 °C, respectively, which is somewhat lower than for PEEK, which is 538, 553, and 561 °C. Nonetheless, the weight loss rate with PEEK is substantially greater and comprises three distinct phases (Fig. 4).

The maximal rate of weight loss for PEKK is significantly higher than for PEEK (619 and 567 °C, respectively). Given these findings, it can be hypothesized that PEKK decomposition happens by the normal homolytic break of the main polymer chain (a minor rate of weight loss), whereas PEEK breakdown occurs via a radical chain, which sometimes increases the rate of decomposition. Studies using differential scanning calorimetry are presented in Table 3.

Table 3. Values of glass transition, melting and crystallization temperatures

Sample	T_g, °C	T_m, °C	T_{cr}, °C
PEKK	170	338	254
PEEK	147	348	306

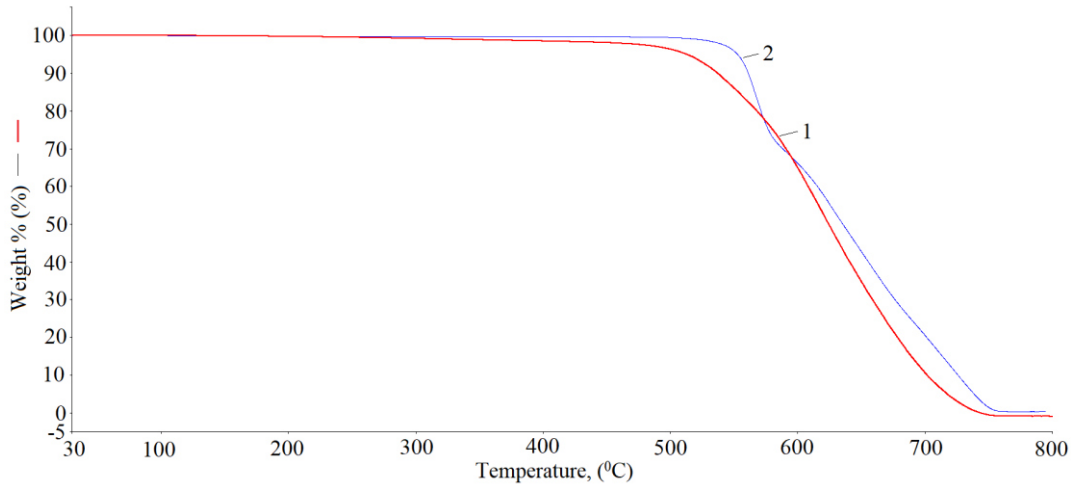

Fig. 3. Curves of weight loss in the air: 1 – PEKK, 2 – PEEK

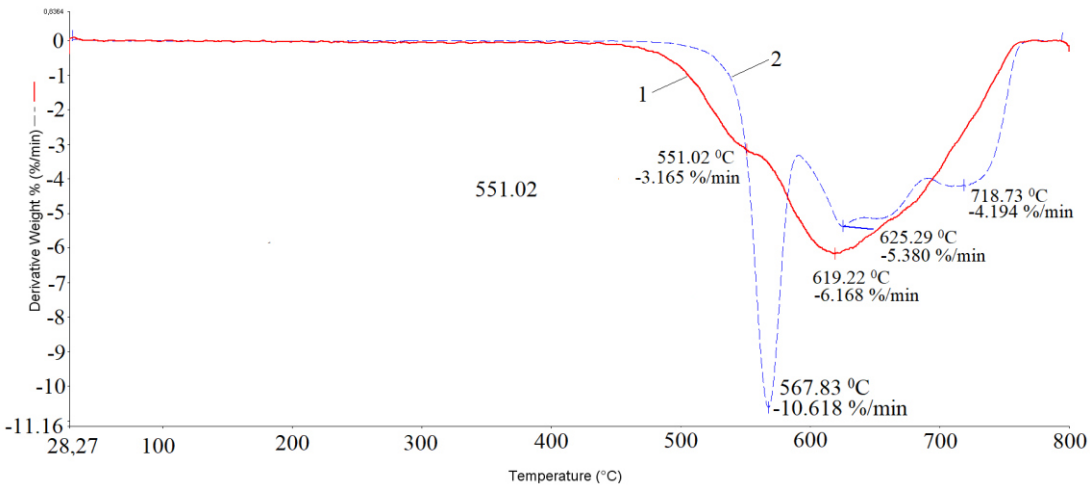

Fig. 4. The dependence of the rate of weight loss on temperature: 1 – PEKK, 2 – PEEK

Based on the results presented in Table 3, we can conclude that PECK has more comfortable conditions for processing into products, which compensate for the lower temperatures at which weight loss begins.

Comparative investigations of the kinetics of the production of the main gaseous degradation products for PEKK produced in KBSU (PEKK-1) (1), PEKK brand CC-5801 (PEKK-2) (2) (China), and PEEK 450 P produced by Victrex (3) (Great Britain) were carried out using gas chromatography in a wide temperature range. The pyrolysis time was 30 minutes at all temperatures. For each temperature, a new sample of 20 mg was obtained.

No substantial quantities of hydrogen were discovered in any samples at temperatures ranging from 250 to 400 °C, which is most likely due to branching and crosslinking processes (Fig. 5). The hydrogen output for samples PEKK-2 and PEEK increases by an order of magnitude when the temperature is raised compared to PEKK-1.

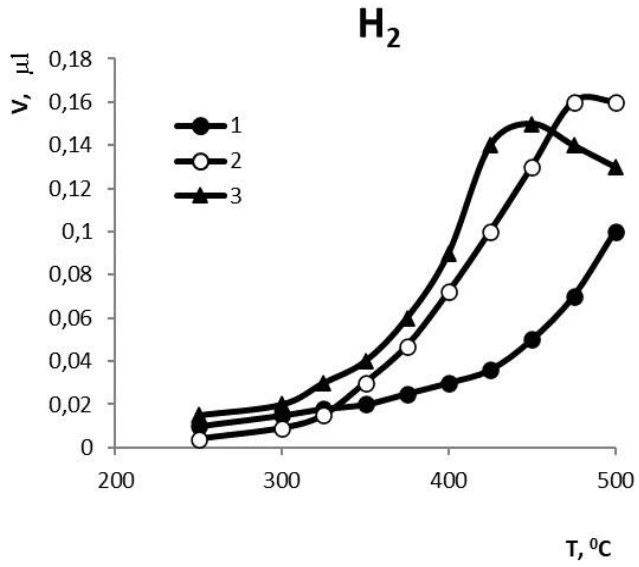

Fig. 5. Kinetic curves of hydrogen formation: 1 – PEKK-1, 2 – PEKK-2, 3 – PEEK

It decreases at temperatures over 450 °C, which is connected with its participation in subsequent polymer degradation processes, transforming homolytic decay into radical chain decay, which has a particular impact on the rate of mass loss for PEEK (Fig. 4).

Figure 6 depicts how active atomic hydrogen contributes to the breakdown of the ketone group by producing phenolic radicals, which also contribute to an increase in the rate of polymer decomposition.

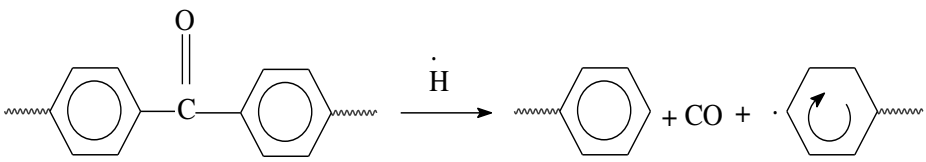

Fig. 6. Scheme of the influence of atomic hydrogen on the destruction of ketones

The presence of carbon monoxide in the breakdown products shows that the ketone group has been destroyed. However, carbon dioxide is found in the breakdown products in addition to CO (Fig. 7).

In [30], it was shown that the emergence of carbon dioxide with CO suggests that, at higher temperatures, the breaking of the simple ether link in the polymer happens concurrently with the release of oxygen, oxidizing CO to to CO_2.

The figures show that the quantities of CO_2 for PEKK (1) are almost the same as the amounts of CO. The amount of carbon dioxide increases dramatically in sample (3), which has two simple ether groups in the structure, which is consistent with the results of the work [19]. The unusually high quantity of CO_2 observed in sample 2 is unknown. This is either the consequence of certain impurities remaining after synthesis or the breakdown of numerous stabilizers, plasticizers, and other additives added to the structure.

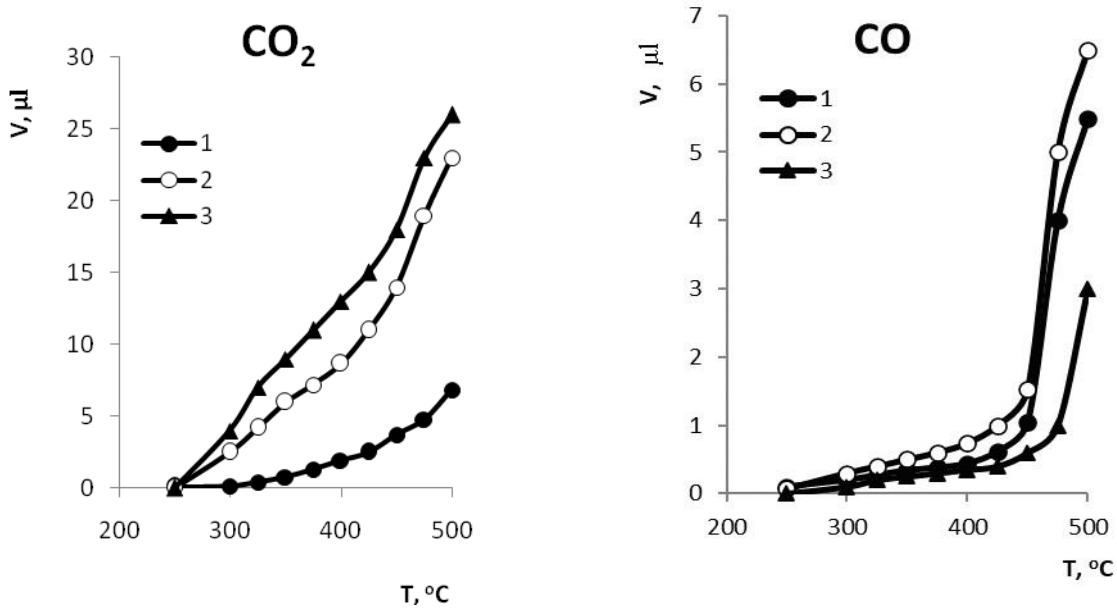

(a) (b)

Fig. 7. Kinetic curves of CO_2 (a) and CO (b) formation: 1 – PEKK-1, 2 – PEKK-2, 3 – PEEK

In general, the revealed patterns indicate the possibility of directional regulation of the depth of thermal degradation processes of matrix with a decrease in phase transformation temperatures (T_{st}, T_m, T_{cr}) without risk of deterioration of the main technological and operational characteristics. The mechanical properties of polyaryletherketones were also investigated. The main properties are shown in Table 4.

Table 4. Mechanical properties of polyaryletherketones

Sample	E_{fl}, GPa	E_{ten}, GPa	σ_{yield}, MPa	σ_{ten}, MPa	ε, %
PEEK 450 P	3.74	2.98	117.0	98.2	120.0
PEKK CC-5801	3.17	2.66	77.4	61.5	22.6
PEKK KBSU	3.0	2.74	-	75.5	4.4

E_{fl} is the flexural modulus, E_{ten} is the tensile modulus, σ_{ten} is the tensile strength, σ_{yield} is the yield point, ε is the elongation at break.

A comparison of the mechanical properties of the studied polyaryletherketones showed that they all have a high range of mechanical characteristics. At the same time, it can be noted that PEEK has higher strength and elastic modulus then PEKK. Apparently, PEEK has superior properties due to its higher crystallinity, since the studied PEKK brands contain isophthaloyl chloride as a comonomer and resulting structure has a lower crystallization rate and degree of crystallinity, which causes lower mechanical properties. A significant difference in the properties of synthesized and industrial PEKK is the higher plasticity of the latter. The synthesized PEKK has a significantly lower elongation and does not exhibit a yield point, i.e., has a brittle character of destruction.

Conclusions

Thus, the conducted studies show that PEKK, due to its high thermal stability, good mechanical properties and lower melting point than PEEK, is a promising material for use as a for composite materials. A matrix based on PEKK is most suitable for creating various products, including implants for living organisms.

References

1. Bühler KU. *Spezialplaste*. Berlin: Akademic Verlag; 1978.
2. Mikhailin YA. *Heat-resistant polymers and polymer materials*. St. Petersburg: Profession; 2006. (In-Russian)
3. Korshak VV. *Chemical structure and temperature characteristics of polymers*. Moscow: Nauka; 1970. (In-Russian)
4. Baur E, Osswald TA, Rudolph N, Saechtling H. (eds.) *Saechtling Kunststoff Taschenbuch*. Carl Hanser Verlag GmbH & Co. KG; 2013.
5. Barvinsky IA, Barvinskaya IE. *Handbook of injection molding thermoplastic materials*. Moscow: 2018. (In-Russian)
6. Sheremetyev SV, Sergeeva EA, Bakirova IN, Zenitova LA, Abdullin ISh. The use of polyetheretherketones in medicine and other industries. Review. *Bulletin of Kazan Technological University*. 2012;15(20): 164–167. (In-Russian)
7. Harris JE, Robenson LM. Blends of poly(aryl ether ketones). In: *Multiphase Macromol. Syst.: Proc. Int. Symp. 14th Bienn. Meet. Div. Polym. Sci. Amer. Chem. Soc., San Diego, Calif., Nov. 19-23, 1988*. New York; 1989. p.519–546.
8. Werdingen W. High temperature performing plastics. *Automot*. 1991;44(11): 757–762.
9. Kuperman AM, Lebedeva OV, Puchkov LV, Zelensky ES, Gorbatkina YuA, Berlin AA. Reinforced plastics based on thermoplastic matrix. *Plasticheskie massy*. 1992;5: 9–10. (In-Russian).
10. Clavijo S, Membrives F, Boccaccini AR, Santillan MJ. Characterization of Polyetheretherketone Particle Suspensions for Electrophoretic Deposition. *J. Appl. Polym. Sci.* 2014;131(20): 40953.
11. Zhang G, Liao H L, Coddet C. Chapter 19 - Friction and wear behavior of PEEK and its composite coatings. *Tribology and Interface Engineering Series*. 2008;55: 458–482.
12. Small G. Outstanding physical properties make PEEK ideal for sealing applications. *Sealing Technology*. 2014;2014(4): 9–12.
13. Salamov AKh, Mikitaev AK, Beev AA, Beeva DA, Kumysheva YuA. Polyether etherketones (PEEC) as representatives of aromatic polyarylene etherketones. *Fundamental research*. 2016;1-1: 63–66. (In-Russian)
14. Yang D, Cao Y, Zhang Z, Yin Y, Li D. Effects of crystallinity control on mechanical properties of 3D-printed short-carbon-fiber-reinforced polyether ether ketone composites. *Polymer Testing*. 2021;97: 107149.
15. Murray BR, Doyle A, Feerick PJ, Semprimoschnig COA, Leen SB, Ó Brádaigh CM. Rotational moulding of PEEK polymer liners with carbon fifiber/PEEK over tape-placement for space cryogenic fuel tanks. *Mater. Des*. 2017;132: 567–581.
16. Zhang Y, Tao W, Zhang Y, Tang L. Continuous carbon fiber/crosslinkable poly(ether ether ketone) laminated composites with outstanding mechanical properties, robust solvent resistance and excellent thermal stability. *Compos. Sci. Technol*. 2018;165: 148–153.
17. Monich PR, Henriques B, Novaes de Oliveira AP. Mechanical and biological behavior of biomedical PEEK matrix composites: a focused review. *Mater. Lett*. 2016;185: 593–597.
18. Shakhmurzova KT, Zhansitov AA, Kurdanova ZhI, Baykaziev AE, Salamov AKh, Khashirova SYu. Synthesis and characterization of copolyesteretherketone based on 1,4-dihydroxybenzene and 4,4-dihydroxydiphenyl. *Proceedings of the Kabardino-Balkarian State University*. 2016;6(3): 67–69. (In-Russian)
19. Rival G, Paulmier T, Dantras E. Influence of electronic irradiations on the chemical and structural properties of PEEK for space applications. *Polym. Degrad. Stabil*. 2019;168: 108943.
20. Sun W, Chen T, Liu X, Jiao Y, Zhu Y, Ye J. Microstructure-armored surface and its tribological effects on ultralow-wear PEEK/PTFE composites. *Polymer*. 2024;291: 126599.
21. Kirin BS, Kuznetsova KR, Petrova GN, Sorokin AE. Comparative analysis of the properties of polyetheretherketones of domestic and foreign production. *Proceedings of VIAM*. 2018;5(65): 34–43. (In-Russian)
22. Shabaev AS, Zhansitov AA, Kurdanova ZI, Kuchmenova LKh, Khashirova SYu. Investigation of thermal and thermo-oxidative degradation of poly(ether ether ketone) by gas chromatography. *Chin. J. Chromatogr*. 2018;36(4): 395–399.
23. Khakyasheva EV, Shabaev AS, Khashirova SYu. The effect of PEEK drying modes on its thermal stability. *Proceedings of the Kabardino-Balkarian State University*. 2018;8(3): 68–72. (In-Russian)
24. Saechtling H, Oberbach K. (eds.) *Kunststoff – Taschenbuch. 27 Ausgabe*. Munchen: Hanser Fachbuch; 1999.

25. Korshak VV. *Kinetics and mechanism of formation and transformation of macromolecules*. Moscow: Nauka; 1968. (In-Russian)
26. Krasnov YeP, Savinov VM, Sokolov LB, Logunova VI, Belyakov VK, Polyakova TA. Thermal stability of polyamides in various media. *Polymer Science U.S.S.R*. 1966;8(3): 413–421.
27. Kalra S., Munjal B.S., Singh V.R., Bhattacharya B. Investigations on the suitability of PEEK material under space environment conditions and its application in a parabolic space antenna. *Advances in Space Research*. 2019;63(12): 4039–4045.
28. Shabaev AS, Khakyasheva EV, Khashirova SYu. Effect of Water on the Thermal Properties of Polyetheretherketone. *Polymer Science, Series A*. 2022;64(5): 410–414.
29. Shabaev AS, Kalazhokov ZKh, Khashirova SYu, Kalazhokov KhKh, Dolbin IV. Stability of bridging groups of polyether ether ketone during thermal destruction and exposure to ion beams. *Russian Chemical Bulletin*. 2023;72(6): 1422–1429.
30. Shabaev AS, Zhansitov AA, Khakyasheva EV, Khashirova SYu. Study of thermo-oxidative transformations of unstabilized and stabilized poly(ether ether ketone). *Polymer Science, Series B*. 2019;61(5): 582–588.

About Authors

Al'bert S. Shabaev Sc
PhD in Chemistry
Senior Researcher (Kh.M. Berbekov Kabardino-Balkarian State University, Nalchik, Russia)

Kamila T. Shakhmurzova Sc
PhD in Chemistry
Senior Researcher (Tula State University, Tula, Russia)

Azamat A. Zhansitov Sc
PhD in Chemistry
Senior Researcher (Tula State University, Tula, Russia)

Azamat L. Slonov Sc
PhD in Technical Sciences
Senior Researcher (Tula State University, Tula, Russia)

Irina N. Fomicheva Sc
Junior Researcher (Tula State University, Tula, Russia)

Igor V. Dolbin Sc
PhD in Chemistry
Senior Researcher (Kh.M. Berbekov Kabardino-Balkarian State University, Nalchik, Russia)

Svetlana Yu. Khashirova Sc
Doctor of Chemical Sciences, Professor
Vice-Rector for Research (Kh.M. Berbekov Kabardino-Balkarian State University, Nalchik, Russia)

Submitted: January 27, 2023 Revised: May 25, 2023 Accepted: July 31, 2023

Effect of plasticizers of different polarity on dynamic mechanical properties of butyl rubber

V.V. Avdonin ✉ [1], **O.I. Tarasova** [2], **Yu.V. Yurkin** [2],

[1] National Research Ogarev Mordovia State University

[2] Vyatka State University, Kirov, Russia

✉ avdoninvalerii@bk.ru

ABSTRACT

The article presents the results of studies of the influence of the concentration of three types of plasticizers with different percentages on the dynamic mechanical properties of mixtures based on elastomer: butyl rubber (BR) / industrial oil, BR/chlorinated paraffin, BR/dioctyl phthalate. Plasticizers were taken in a ratio of 20 to 40% by volume. The leading research methods were a comparative analysis of the temperature-frequency dependence of the loss tangent and the elastic modulus, obtained by the method of dynamic mechanical analysis (DMA). The developed compositions of the composite material were tested by IR spectroscopy. It has been established that in order to obtain self-adhesive composite materials with high damping properties, a plasticizer-industrial oil with a minimum content of 40 % should be used. Based on the conducted studies, it was proved that when plasticizers of various types and polarities are introduced into butyl rubber, the properties of the compositions change depending on the concentration of the plasticizer, the molecular structure and the forces of intermolecular interaction. It was revealed by infrared spectroscopy that no chemical interaction occurs in the polymer matrix of butyl rubber, on the grounds that the influence of the components on the intensity or magnitude of the peak is not traced.

KEYWORDS

elastic modulus • mechanical loss tan δ • temperature • butyl rubber (BR) • plasticizers • industrial oil (IO) chlorinated paraffin (CP) • dioctyl phthalate (DOP)

Acknowledgements. *The authors acknowledge a financial support of this work by the Russian Science Foundation, project No 21-79-00301, https://rscf.ru/project/21-79-00301/.*

Citation: Avdonin VV, Tarasova OI, Yurkin YV. Effect of plasticizers of different polarity on dynamic mechanical properties of butyl rubber *Materials Physics and Mechanics*. 2024;52(2): 133–141. http://dx.doi.org/10.18149/MPM.5222024_14

Introduction

Increased levels of harmful noises and vibrations can have undesirable effects on humans and structures in general. Using materials with high damping properties is an effective method for reducing noise and vibration. Analysis of different vibration-damping materials indicates that the highest damping characteristics are found in materials containing polymers [1–3], which can undergo significant reversible deformations at low stresses [4]. Vibration absorption (damping) is a method for reducing vibration by inducing internal friction processes in the structure, dissipating vibration energy by irreversibly transforming it into heat during deformation occurring in materials [5]. The measure of vibration damping is the mechanical loss tangent (tan δ), which is a characteristic of the lag between strain and stress, damping materials must meet the requirement that tan $\delta > 0.3$ [6–8].

As a rule, rubbers are used as a basis for composite materials with vibration-damping properties [7,9–12] since their glass transition temperature lies in the region of negative temperatures. The properties of polymer composite materials are also influenced by plasticizing additives introduced into the polymer to reduce the glass transition temperature, to expand the temperature range of the highly elastic state of the polymer and to improve machinability. Esters of aliphatic and aromatic carboxylic acids, polyesters, epoxidized compounds, synthetic and vegetable oils are most commonly used [13]. Various types of oils are commonly used as plasticizers for composite vibration-damping materials based on BR [14,15].

The mechanism of plasticization is considered in [3,5,16], finding the main factors influencing the plasticizing efficiency: the amount of plasticizer introduced into the polymer, the chemical structure of the polymer and plasticizer, their thermodynamic compatibility, volume, shape and size of plasticizer molecules, ability for conformational transformations (flexibility of polymer molecules). Processes of molecular dispersion, transformations in the structure of the mixture and variations in molecular mobility occur upon contact of the polymer with the plasticizer, affecting such characteristics as glass transition temperature (T_c), flow temperature (T_τ), dynamic modulus (E'), mechanical loss tangent (tan δ) and others.

From a physicochemical standpoint, the thermodynamic affinity of polymers is characterized by the amount of mutual solubility. The ability of polymers to swell or dissolve in different solvents depends on the structure of the molecules. The swelling and solubility of a polymer in a particular solvent depend on the interactions of functional groups or atoms, forming bonds producing stable complexes of polymer macromolecules with solvent molecules. As a liquid plasticizer penetrates into the polymer phase, its molecular or colloidal dispersion can occur (Fig. 1).

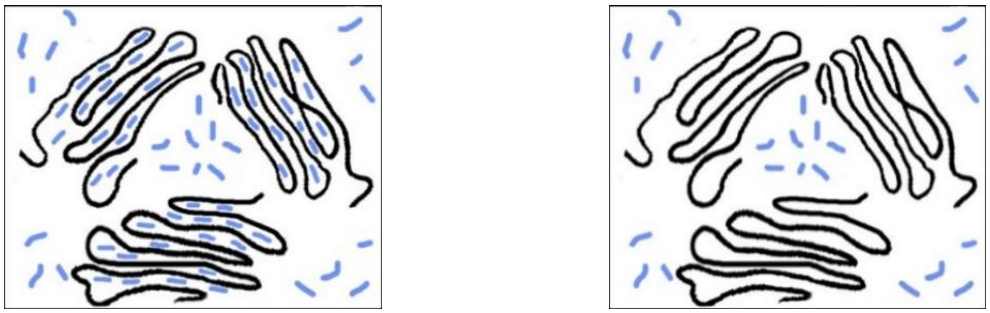

(a) (b)

Fig. 1. Scheme of plasticizer interaction: a) molecular dispersion (intrastructural plasticization); colloidal dispersion (interstructural plasticization)

Earlier studies have accumulated knowledge on the mechanism of plasticization, when the properties of composites change depending on their polarity. Figure 1(a) shows a strong intermolecular interaction of plasticizer molecules with polymer macromolecules, plasticizer molecules penetrate into any supramolecular structures, gradually destroying them. The polymer macromolecules in the plasticizer solution are shaped like unfolded loose coils. The polymer is the dispersion medium under colloidal dispersion (Fig. 1(b)), and the plasticizer is the dispersed phase [17]. The molecules are simply embedded between individual polymer chains and destroy polymer-polymer interactions without penetrating inside. Depending on the quality of the solvent, the polymer macromolecules in the solution are shaped as more folded Gaussian coils, rather

than unfolded loose coils, since there is virtually no interaction with the solvent [18]. Such a physical interaction differs from a chemical one in that old chemical bonds do not break and new ones do not form, but forces of attraction or repulsion arise due to interactions between molecules. Intermolecular interactions (between electrically neutral molecules or atoms) were first considered by Van der Waals in 1873.

Analysis of the literature data allowed to determine the composition of the structure-forming materials used for damping composite materials and establish that there are practically no studies investigating the mechanisms behind the influence that varying the concentration of plasticizers (industrial oil (IO), chlorinated paraffin (CP) and dioctyl phthalate (DOP)) has on the elastic and relaxation properties of BR-based composite materials in a wide temperature range. For comparison, consider three different types of plasticizers, differing in their properties: non-polar, polar and weakly polar, since the properties of the compositions vary depending on the polarity of the plasticizers [19,20]. Some molecules do not have polar bonds, because the electron charge is the same on both atoms, therefore, these are non-polar molecules [21]. Polarity has a direct relationship with such quantity as compatibility, understood as the ability to 'dissolve' at the molecular level. Polymer mixtures are divided into compatible, those with limited compatibility, and incompatible. The solubility parameters of the materials (Table 1) allow to assess the compatibility of the mixture components with respect to non-polar butyl rubber.

Table 1. Solubility parameters of materials used [22]

Parameter	BR	IO	CP	DOP
Solubility, kJ/(cm^3)$^{0.5}$	16.6	16.1	19.5	18.2

The solubility parameter for butyl rubber was calculated in accordance with Hoy [20]. The parameters for BR and IO have similar values, therefore, they can be assumed to be compatible (*miscible, with complete mutual solubility*), interphase interactions consisting of formation of chemical bonds are absent in them [18,23]. Similarly, it can be assumed that CP is incompatible, and DOP is a weakly compatible plasticizer with BR.

Reviewing studies by Russian and foreign scholars on the processes of structure formation, development of compositions and technologies for fabricating building materials and polymer-based products, we found that experimental studies were not carried out, despite the nature of plasticiser influence, the dynamic and mechanical characteristics of various BR-based plasticizers were not considered. Our goal was thus to identify the influence of different types of plasticizers on the dynamic characteristics of a composite material based on BR in a wide temperature and frequency range, depending on the concentration of the plasticizer.

Materials and Methods

Materials

The base polymer chosen for obtaining composite materials was BR-1675N grade butyl rubber (Arsenal Kama, Russia). To reduce the viscosity of the specimens, improve machinability and damping properties of BR-based composite materials, plasticizers were introduced at a 60 / 40 % by volume: non-polar industrial oil I-40 (IO), GOST 20799-880

(Rosneft, Russia); polar chlorinated paraffin CP-470 (CP) TU 2493-379-05763441-2002 (JSC Acoustic, Russia); weakly polar dioctyl phthalate (DOP) GOST 8728-88 (BinaGroup, Russia).

Preparation of composites

The composites were prepared using a laboratory mixer with Z-shaped rotating blades at a temperature of 80 °C for 1 hour. The specimens were prepared by milling. The grades and ratios of the components are given in Table 2.

Table 2. Grades and ratios of structure-forming components

	Volume fraction, %			Mass fraction, g	
No.	Grade	BR	plasticizer	BR	plasticizer
1	BR	100	0	64.4	0
2	BM-20	80	20	51.52	12.6
3	BM-30	70	30	45.08	18.9
4	BM-40	60	40	38.64	25.2
5	BM-50	50	50	32.2	31.5
6	BX-20	80	20	51.52	17.29
7	BX-30	70	30	45.08	25.94
8	BX-40	60	40	38.64	34.58
9	BD-20	80	20	51.52	13.78
10	BD-30	70	30	45.08	20.66
11	BD-40	60	40	38.64	27.55

The mass content was calculated based on the data for the true density of plasticizers: 0.900 g/cm^3 for IO; 1.235 g/cm^3 for CP; 0.984 g/cm^3 for DOP.

Methods

1. Dynamic mechanical analysis was carried out with a Netzsch DMA242 analyzer (Netzsch, Germany) for specimens shaped as 2 mm thick disks, which corresponds to ASTM D4065-12 *Standard Practice for Plastics: Dynamic Mechanical Properties: Determination and Report of Procedures*. The temperatures in the tests ranged from -80 to +40 °C, with a heating rate of 2 °/min. The mixtures were studied at a frequency of 1, 10, 100 Hz.
2. Spectral analysis was performed with an Infralum FT-801 FTIR spectrometer in the range of 400–4000 cm^{-1} at ambient temperatures from 18 to 25 °C, recording the absorption spectra of the specimens.

Results and Discussion

Figure 2 shows the variation in the dynamic elastic modulus (E') and the mechanical loss tangent (tan δ) of composites with three different types of plasticizers (CP, IO, DOP) at a concentration of 20 %. It can be observed from the DMA curves in this temperature range that the elastic modulus for all three plasticizers decreases monotonically with increasing temperature, becoming the most pronounced at 1000 MPa for BR modified with chloroparaffin, exhibiting an average value of 800 MPa for the composite with dioctyl phthalate, and reaching the lowest value at 100 MPa for the composite with industrial oil (comparison of all three composites was performed in the temperature range from -80 to

+40 °C). The value of tan δ has an extreme character, with the the peak on the graph corresponding to the transition of the material from a glassy to a highly elastic state. The peaks of tan δ have the following values: 1.6 at a temperature of -60 °C for CP; 1.6 at -57 °C for IO, 1.39 at -55 °C for DOP. The maximum value of the loss tangent (the main characteristic of vibration damping) is found in mixtures with CP and IO. Increasing the vibrational frequency by an order of magnitude leads to a shift in all curves towards an increase in temperature by approximately the same values, 16–17 degrees.

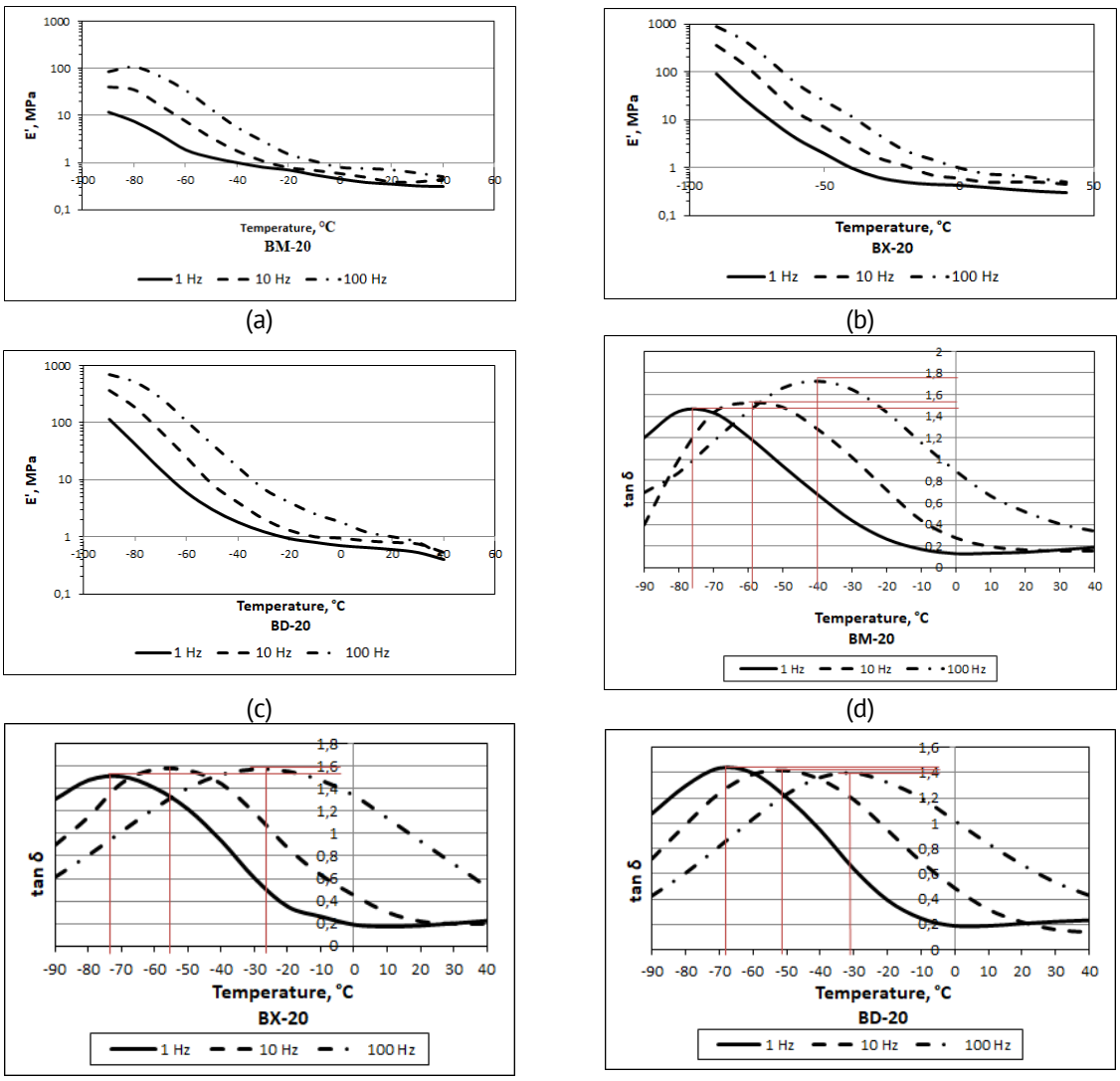

Fig. 2. Dependences of *E'* and tan δ on temperature for: BM-20 (a,b), BX-20 (c,d), BD-20 (e,f) (with a volume fraction of BR/plasticizer 80/20 at frequencies of 1 Hz, 10 Hz, 100 Hz)

Increasing the concentration of the plasticizer (for example, industrial oil, Fig. 3) leads to a decrease in the glass transition temperature of the composite, manifesting as a shift of the tan δ peak towards a decrease in temperature with a simultaneous increase in the maximum tan δ value.

Graphs for the variation in the glass transition temperature (*T*c) and the maximum tan *δ* depending on the type and volume fraction of the plasticizer are shown in Fig. 4.

Analyzing the results obtained for the values of *T*c and tan *δ*, we found that an increase in tan δ and an expected decrease in *T*c occur for all studied plasticizers with an increase in the proportion of plasticizer in all mixtures with a filling from 0 to 20 %. However, further increasing the fraction of plasticizer to 40 % produces a slight increase in the *T*c of mixtures with weakly polar DOP and polar CP, while the glass transition temperature of the mixture with non-polar IO continues to decrease to -70 °C. Mixtures with DOF and CP have a slight increase in tan *δ*, and the mixture with non-polar IO exhibits a large increase in tan *δ* to 1.6 arbitrary units.

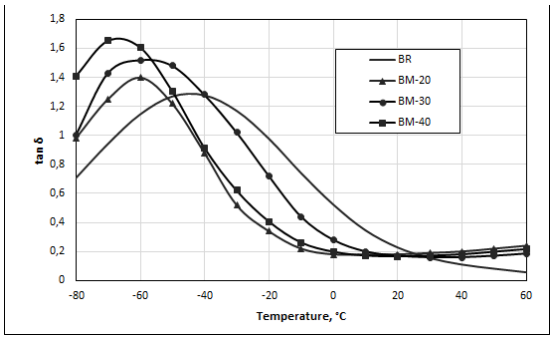

Fig. 3. Dependence of tan δ in a BR/oil mixture with different volume fractions: 100/0, 80/20, 70/30, 60/40 (vol. %) at a frequency of 10 Hz

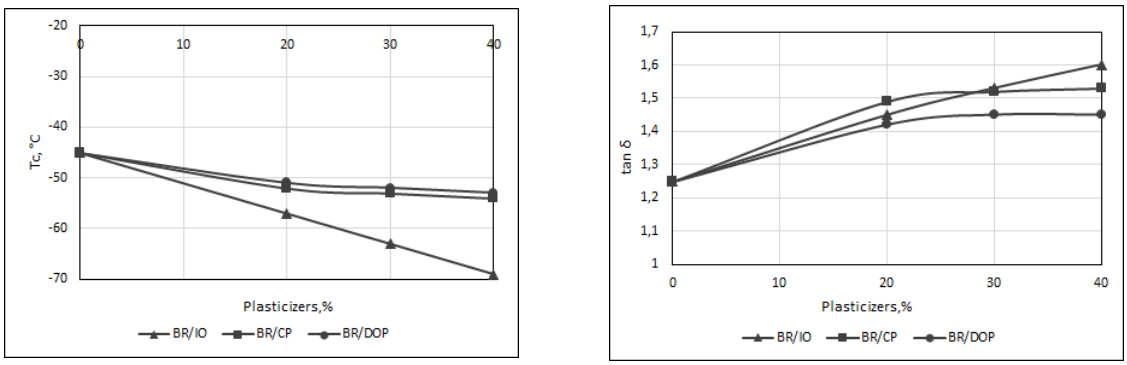

(a) (b)

Fig. 4. Variation in Tc (a) and maximum tan δ (b) for all three types of plasticizers with the concentration varied from 0 to 40 vol. %

Such an increase in tan δ can be associated with an increase in the flexibility of molecules. A true solution is spontaneously formed during the intrastructural plasticization of non-polar BC with non-polar industrial oil (Fig. 1(a)). A simplified explanation for the effect of plasticizers is that relatively small IO molecules penetrating between polymer molecules weaken intermolecular bonds and thus increase the mobility of polymer molecules. To achieve this, plasticizers must combine well with the polymer and form a stable mixture with it [24].

The main factors influencing the plasticizing efficiency are the chemical structure of the polymer and plasticizer, their thermodynamic compatibility, the volume and shape of plasticizer molecules, their capability for conformational transformations (their flexibility).

We compared the structure of butyl rubber and IO plasticizer at the molecular level for further analysis. By chemical composition, petroleum oils are a mixture of hydrocarbons with a molecular weight of 300–750, containing 20–60 carbon atoms in the molecule. Base oils consist of groups of isoparaffin, naphthenoparaffin, naphthenoaromatic and aromatic hydrocarbons with varying degrees of cyclicity. Paraffin oil is an industrial-grade oil [15]. The general chemical formula is C_nH_{2n+2}. The BR molecule is characterized by an almost complete lack of structuring, it contains a small amount of carbon–carbon double bonds and has tightly packed linear chains. The plasticization process proves the empirical like-dissolves-like rule, i.e., non-polar BR is easily dissolved in non-polar IO, which is explained by the absence of intermolecular chemical interactions between BR and IO. The dissolution of butyl rubber happens with a swelling stage, which is characterized by an increase in the mass and volume of the polymer as a result of absorption of a low-molecular-weight liquid. The molecules of the low-molecular-weight plasticizer IO in the BR chain increase the free volume and mobility of not only the main chain, but also its individual segments. As a result, the polymer swells. The plasticizer spreads the segments apart, replacing the polymer–polymer interactions with the plasticizer–polymer interaction, which means that intermolecular interactions are weakened, resulting in a decrease in Tc. Since energy is consumed for these interactions, tan δ increases, and vibration-damping properties increase accordingly.

Under colloidal dispersion, due to the presence of oxygen and chlorine in the structural formulas, DOP and CP have a higher polarity compared with IO, and, accordingly, have less compatibility with non-polar BR. Plasticization of non-polar BC with a polar plasticizer CP and a less polar DOF also proves the like-dissolves-like rule. A plasticizer with no affinity for the polymer does not spontaneously penetrate it, so there is no swelling of BR. Plasticizer molecules are located on the surface of supramolecular formations, between non-polar groups of BR macromolecules (Fig. 1(b)). The emulsion formed in the colloidal system is thermodynamically and aggregatively unstable, and therefore can become stratified. Due to high viscosity of the system, stratification occurs slowly, sometimes during storage or operation of the product. This is manifested, for example, as plasticizer droplets appearing on the surface of the product. Plasticizer molecules are located on the surface of supramolecular formations, between non-polar groups of BR macromolecules (Fig. 1(b)). The plasticizers CP and DOP act as a sort of lubricant between the BR segments. An insignificant amount of plasticizer is combined with the polymer during such plasticization; the plasticizer molecules are adsorbed (*process of spontaneous redistribution of matter*) on the surface of the interface between the structures, forming the thinnest monomolecular layers of the so-called boundary lubricant, facilitating the mobility of supramolecular structures under external mechanical action. Mixtures with DOP and CP do not increase the mobility of polymer molecules, accordingly, a small amount of energy is consumed for these interactions and a slight increase in tan δ occurs.

The spectral analysis method was used to confirm the impossibility of chemical reactions in these composite mixtures (Fig. 5). Tests of specimens by infrared spectroscopy revealed that absorption lines for superimposed curves practically coincide, the characteristic vibrations of physical groups of the BR polymer are very pronounced, and its alternating bonds appearing as its free functional groups at wavelengths of 2900 and 1400 cm^{-1} can be seen from the position of the peaks.

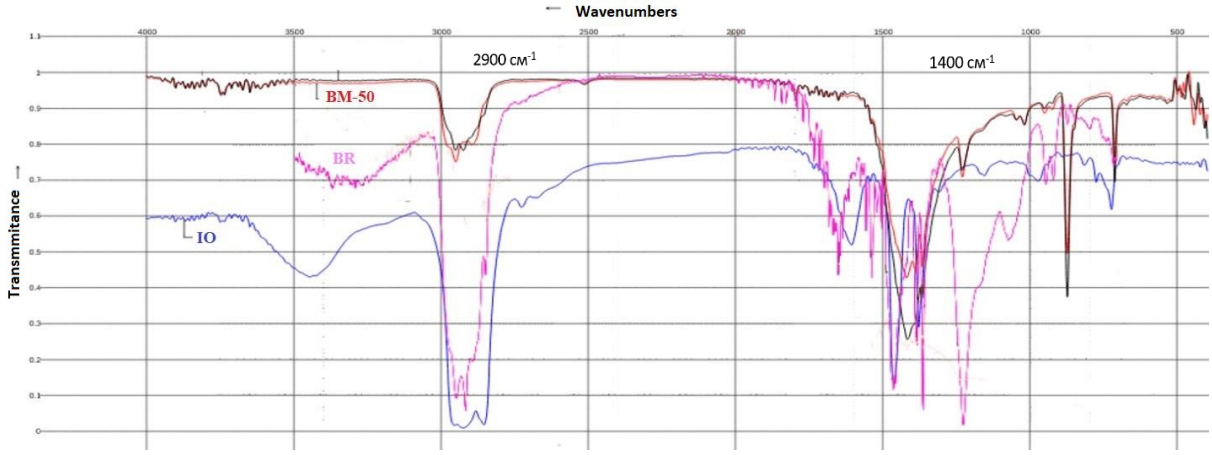

Fig. 5. Infrared spectrum of modified mixtures: pink curve corresponds to 100% BR, blue curve to 100% IO plasticizer, red curve to BM-50 (50% IO + 50% BR)

This means that the device records only the polymer matrix, no new peaks were detected, the influence of the components on the intensity or magnitude of the peak was not traced, which means that chemical interaction does not occur in the polymer matrix of butyl rubber.

Conclusion

1. We considered mixtures containing butyl rubber plasticized with either industrial oil, chlorinated paraffin, or dioctyl phthalate in different volume ratios as a polymer binder to study the effect of structure-forming components on the dynamic mechanical characteristics. Our findings indicate that all three types of plasticizers can be used to obtain a composite material with high damping properties, with an increase in the plasticizer content from 0 to 20 vol. %, while industrial oil should be used to obtain materials that are also self-adhesive, as it has the highest values of tan δ as the main measure of vibration damping, with the minimum volume content of industrial oil within 40 %. Due to limited compatibility of DOP with BR and incompatibility of CP with BR, migration can be observed in these mixtures, starting with specimens with a plasticizer content of 20–30 % and above, making them unsuitable as plasticizers for vibration-damping composite materials.
2. We confirmed that introducing plasticizers of different types and polarities into butyl rubber leads to the transformation of the structure and properties of the compositions depending on the concentration of the plasticizer, the molecular structure and the forces of intermolecular interaction. Infrared spectroscopy revealed that chemical interaction in the polymer matrix of butyl rubber does not occur, since the influence of the components on the intensity or magnitude of the peak was not traced (the appearance of new peaks was also not detected).

References

1. Yartsev BA. Composite vibration-damping structures. *Transactions of the Krylov State Research Centre*. 2019;2(388): 55-68. (In-Russian)
2. Doriomedov MS. Russian and world market of polymers composites (review). *Trudy VIAM*. 2020;6-7: 29-37. (In-Russian)
3. Erofeev V, Shafigullin L, Bobrishev A. Investigation of Noise - Vibration-Absorbing Polymer Composites Used in Construction. *IOP Conference Series: Materials Science and Engineering*. 2018;463(4): 5.

4. Mark JE, Erman B, Eirich FR. (Eds.) *Science and Technology of Rubber*. 3rd ed. Amsterdam: Elsevier; 2005.
5. Sagomonova VA, Sytnyy YuV, Kislyakova VI, Dolgopolov SS. Issledovaniye dempfiruyushchikh svoystv vibropogloshchayushchikh materialov na osnove termoelastoplastov. *Aviatsionnyye materialy i tekhnologii*. 2014;S3: 5-10. (In-Russian)
6. Volotskoy AN, Yurkin YuV, Avdonin VV. Issledovaniye tangensa ugla mekhanicheskikh poter i prochnosti vibropogloshchayushchikh materialov na osnove etilenvinilatsetata, modifitsirovannykh kauchukami. *Inzhenernyy vestnik Dona*. 2019;8(59): 35. (In-Russian)
7. Menson Dzh, Sperling L. *Polimernyye smesi i kompozity*. Moscow: Khimiya; 1979. (In-Russian)
8. Li Z, Lu X, Tao G, Guo J, Jiang H. Damping elastomer with broad temperature range based on irregular networks formed by end-linking of hydroxyl-terminated poly(dimethylsiloxane). *Polymer Engineering and Science*. 2015;56(1): 97–102.
9. Sheng Z, Yang S, Wang J, Lu Y, Tang K, Song S. Preparation and properties analysis of chlorinated butyl rubber (CIIR)/Organic diatomite damping composites. *Materials*. 2018;11(2172): 14.
10. Chung DDL. Review. Materials for vibration damping. *Journal of Materials Science*. 2001;36: 5733–5737.
11. Genkina YuM. Oils-fillers of synthetic rubbers and rubbers that meet REACH requirements for the Russian market. In: *4th International Conference CREON Rubbers*. 2009. p.1–16.
12. Murtazina LI, Garifullin AR, Nikultsev IA, Fatkhullin RF, Akhmedyanova RA, Miloslavskiy DG, Galimzyanova RYu, Khakimullin YuN. Regulirovaniye svoystv neotverzhdayemykh germetikov na osnove etilenpropilendiyenovogo kauchuka plastifikatorami. *Vestnik Kazanskogo tekhnologicheskogo universiteta*. 2014;17(9): 119–122. (In-Russian)
13. Irzhak VI. *Arkhitektura polimerov*. Nauka; 2012. (In-Russian)
14. Savchenkov VP, Artamonova TA, Savchenkova GA. *Vibratsionnyy blok №. 36869U1*. (Rossiya). Prioritet 27.12.2010. 2011.
15. He X, Qu M, Shi X. Damping properties of ethylene-vinylacetate rubber/polylactic acid blends. *Journal of Materials Science and Chemical Engineering*. 2016;4: 15–22.
16. Barshteyn RS, Kirolovich VI, Nosovskiy YuYe. *Plastifikatory dlya polimerov*. Moskva: Izd-vo Khimiya; 1982. (In-Russian)
17. Yershova OV, Ivanovskiy SK, Chuprova LV, Bakhayeva AN. Sovremennyye kompozitsionnyye materialy na osnove polimernoy matritsy. *Penzenskiy mezhdun. zhurnal prikl. i fund. issl*. 2015;4: 14–18. (In-Russian)
18. Tager AA. *Fiziko-khimiya polimerov*. Moskva: Nauchnyy mir; 2007. (In-Russian)
19. Wypych G. *Handbook of plasticizers*. Toronto: ChemTec Publishing; 2004.
20. Khannimulin YuN, Lisanevich MS, Galimzyanova RYu. *Monografiya. Neotverzhdayemyye germetiziruyushchiye kompozitsii na osnove butilkauchuka*. Kazanskiy natsionalnyy issledovatelskiy tekhnicheskiy universitet. Kazan: KNITU; 2017. (In-Russian)
21. McKeen LW. *Film Properties of Plastics and Elastomers*. Elsevier; 2017.
22. Volotskoy AN, Yurkin YuV, Chekasov VD, Avdonin VV, Mansurova IA. Otsenka vliyaniya polyarnosti plastifikatora na dinamicheskiye svoystva polimernykh materialov na osnove etilen vinilatsetata. *Vestnik BGTU im. V.G. Shukhova*. 2018;9: 15–23. (In-Russian)
23. Vadetskiy YuV. *Neftegazovaya entsiklopediya. V 3-kh tomakh*. Moskovskoye otd. "Neft i gaz"; 2002. (In-Russian)
24. Kuleznev VN, Shershnev VA. *Chemistry and physics of polymers*. Saint Petersburg: Doe; 2021. (In-Russian)

About Author

Valeriy V. Avdonin Sc
Candidate of Technical Sciences
Associated Professor (National Research Ogarev Mordovia State University)

Olga I. Tarasova
Master of Sciences
Senior Lecturer (Vyatka State University, Kirov, Russia)

Yu.V. Yurkin Sc
Candidate of Technical Sciences
Head of the Department, Associated Professor (Vyatka State University, Kirov, Russia)

MATERIALS PHYSICS AND MECHANICS RESEACH ARTICLE

Submitted: March 9, 2024 Revised: April 4, 2024 Accepted: April 16, 2024

Modeling of hysteresis characteristics of a dilute magnetic with dipole-dipole interaction of particles

P.V. Kharitonskii [1], E.A. Setrov [2]✉, A.Yu. Ralin [3],

[1] Ioffe Institute, St. Petersburg, Russia

[2] St. Petersburg Electrotechnical University "LETI", St. Petersburg, Russia

[3] Far Eastern Federal University, Vladivostok, Russia

✉ evgensetrov@gmail.com

ABSTRACT

A modification of the method for calculating the distribution function of random fields of dipole-dipole interaction in dilute magnetics using the expansion in the Gram-Charlier series with the help of Bell polynomials has been carried out. On the basis of this method, a model has been developed that allows us to estimate the ensemble magnetisation, the volume fractions of particles in different magnetic states, the volume concentration of the ferrimagnetic and its effective spontaneous magnetisations on the basis of experimental data on hysteresis characteristics. The proposed approach allows us to take into account the particle size distribution and magnetic states. The model has several advantages, such as the possibility of taking into account the cluster distribution of particles and applicability to the limiting cases of thin layer and thin filament. Examples of partial verification of this model on objects of artificial and natural origin are given.

KEYWORDS

dilute magnetic • random fields of dipole-dipole interaction • method of moments • magnetization coercivity • lognormal distribution • magnetic states • effective spontaneous magnetization

Citation: Kharitonskii PV, Setrov EA, Ralin AYu. Modeling of hysteresis characteristics of a dilute magnetic with dipole-dipole interaction of particles. *Materials Physics and Mechanics*. 2024;52(2): 142–150. http://dx.doi.org/10.18149/MPM.5222024_15

Introduction

A considerable number of works [1–7] are devoted to the theoretical description of the processes of remanent magnetization formation in various types of magnetic materials of both natural and artificial origin. Micromagnetic modeling, of this computer simulations [8–12], widely used for the theoretical study of magnetic structures, including those taking into consideration the dipole-dipole interaction between particles [13–17], firstly, often does not take into consideration the possible chemical heterogeneity of individual particles, secondly, their distribution by size, and, accordingly, by magnetic states [18,19], and thirdly, in the case of using software, there are often computational problems associated with the huge number of particles in real objects. Joint application of the micromagnetic approach and statistical methods enables partially solving these problems. The works of the authors [7,20] show the validity of such an approach for ensembles of magnetic particles randomly scattered in a "non-magnetic" matrix (dilute magnetic).

The purpose of this work is to modify the method developed earlier [21,22] for calculating the distribution function of random fields of dipole-dipole interaction in a dilute magnetic, and to apply this method to calculate the magnetization and to estimate the effective spontaneous magnetizations and ferrimagnetic concentration in the sample.

Method of moments for a cylindrically shaped sample

To find the distribution density of the dipole-dipole interaction fields of randomly scattered magnetic dipoles, we will use the approximation that N single-domain uniaxial spherical particles of diameter d_0 with magnetic moment m are randomly located in the volume V, which create a field on a fixed particle located at the origin of coordinates [21].

The field **h** generated by the test particle,

$$\mathbf{h}(\mathbf{m},\mathbf{r}) = \frac{3(\mathbf{mr})\mathbf{r}}{r^5} - \frac{\mathbf{m}}{r^3}, \quad (1)$$

where **r** is the radius vector of the test particle. Here and further in the paper all expressions are written in the CGS system, unless otherwise specified.

By averaging the fields over all values of the magnetic moments and radius vectors, it is possible to calculate the moments of the density distribution of the random fields of the dipole-dipole interaction $w(\mathbf{h})$:

$$< h_k^n > = \frac{1}{V}\int \omega(\Omega)d\Omega \int_V h_k^n(\mathbf{m},\mathbf{r})dV, \quad (2)$$

$$\mu_n = N < h^n >, \quad (3)$$

where k is the index responsible for the projection ($k = x, y, z$), ω is the distribution density of magnetic moment orientations, and V is the volume of the sample excluding the central region with a diameter of $2d_0$.

For further analysis, the shape of a non-magnetic matrix in the form of a cylinder having height d, base radius R, and volume V was chosen (Fig. 1). This geometry allows further analyzing bulk samples as well as thin layers ($d \ll R$) and thin threads ($d \gg R$).

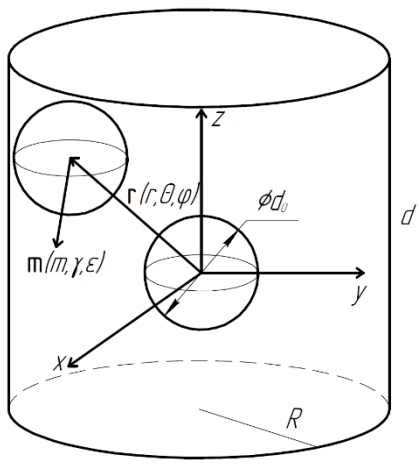

Fig. 1. Non-magnetic matrix of cylindrical shape with chaotic volume distribution of magnetic particles

The notations adopted in this model are as follows: the coordinates of the sample particle are spherical coordinates (r, θ, φ), the coordinates of the magnetic moment of the sample particle are (m, γ, ε), $\omega(\Omega) = \omega(\gamma, \varepsilon) \sin\gamma\, d\gamma\, d\varepsilon$. The two cases when the easy magnetization axes and the magnetic moments of the particles are parallel to the coordinate axes Oz and Ox (Eqs. (4) and (5), respectively) are of most interest:

$$\omega(\gamma,\varepsilon) = \frac{1}{\sin\gamma}[\alpha\delta(\gamma) + \beta\delta(\gamma-\pi)]\delta(\varepsilon), \quad (4)$$

$$\omega(\gamma,\varepsilon) = \frac{1}{\sin\gamma}[\alpha\delta(\varepsilon) + \beta\delta(\varepsilon-\pi)]\delta(\gamma-\pi/2), \quad (5)$$

where $\alpha + \beta = 1$ are the relative fractions of particles oriented along and against the direction of the coordinate axis, respectively. By substituting Eqs. (4) and (5) into Eq. (2), it is possible to analytically calculate the moments of the interaction field distribution [21]. The obtained expressions are cumbersome, but their use saves computational resources and provides an alternative to rather labor-intensive methods such as the Monte Carlo method.

There are at least two series expansions by moments of the probability density of a random normalized variable - the Gram-Charlier series expansion by orthogonal polynomials and the Edgeworth asymptotic series expansion [23]. In this paper, the Gram-Charlier series expansion is used, although the choice of the series expansion is not fundamental, since both series converge to the same values.

The Gram-Charlier series expansion of the probability density function is as follows:

$$f(x) = C_0\phi(x) + \frac{C_1}{1!}\phi'(x) + \cdots + \frac{C_n}{n!}\phi^{(n)}(x), \tag{6}$$

where $\varphi(x) = \exp(-x^2/2)/(2\pi)^{1/2}$ is the density of the standard normal distribution, $\varphi^{(n)} = (-1)^n He_n(x)\,\varphi(x)$, $He_n(x)$ is the Hermite polynomial of the nth degree, C_n are constant coefficients defined as:

$$C_n = (-1)^n \int_{-\infty}^{+\infty} He_n(x) f(x) dx. \tag{7}$$

The Hermite polynomials (in the probabilistic definition) can be found through the recurrence relation:

$$\begin{aligned} &He_0(x) = 1, \\ &He_1(x) = x, \\ &He_n(x) = x \cdot He_{n-1}(x) - (n-1) \cdot He_{n-2}(x),\ n \geq 2. \end{aligned} \tag{8}$$

Thus, it is possible to analytically find any coefficient and any term of the series expansion of $\varphi(x)$ through reduced moments:

$$\nu_k = \frac{\mu_k}{\sigma^k} = \int_{-\infty}^{+\infty} x^k f(x) dx. \tag{9}$$

This method is very convenient for analytical calculation of the coefficients and further expansion of the density into a series with a predetermined number of expansion terms. In case it is necessary to dynamically determine the number of expansion terms in the program, the numerical calculation of Eq. (9), although possible, is difficult. Therefore, in our case another approach using the Bell polynomials is chosen.

The probability density function can be defined as follows [24]:

$$f(x) = \exp\left[\sum_{r=3}^{\infty} k_r \frac{\left(-\frac{d^r}{dx^r}\right)}{r!}\right]\phi(x). \tag{10}$$

The sum under the exponent can be rewritten through the complete Bell polynomials [25]:

$$\exp\left[\sum_{r=3}^{\infty} k_r \frac{\left(-\frac{d^r}{dx^r}\right)}{r!}\right] = \sum_{n=0}^{\infty} B_n(0, 0, k_3, k_4, .., k_n) \frac{\left(-\frac{d^n}{dx^n}\right)}{n!}, \tag{11}$$

where k_n are the cumulants expressed through reduced moments by means of the incomplete Bell polynomials:

$$k_n = \sum_{i=1}^{n} (-1)^{i-1} (i-1)!\, B_{n,i}(\nu_1, \nu_2, \ldots, \nu_{n-i+1}). \tag{12}$$

The Bell polynomials can be found through the recurrence relation [26]:

$$\begin{aligned} &B_{n+1,k+1}(x_1, x_2, \ldots, x_{n-k+1}) = \sum_{i=0}^{n-k} C_n^i x_{i+1} B_{n-i,k}(x_1, x_2, \ldots, x_{n-k-i+1}), \\ &B_{0,0} = 1, \\ &B_{n,0} = 0 \text{ for } n \geq 1, \\ &B_{0,k} = 0 \text{ for } k \geq 1, \end{aligned} \tag{13}$$

where $C_n^i = n!/[i!(n-i)!]$. The complete Bell polynomials are defined through the incomplete ones as a sum:

$$B_n(x_1, x_2, \dots, x_n) = \sum_{k=1}^{n} B_{n,k}(x_1, x_2, \dots, x_{n-k+1}). \quad (14)$$

Then the density of probability distribution is expressed through cumulants as follows:

$$f(x) = \left[\sum_{n=0}^{\infty} B_n(0, 0, k_3, k_4, .., k_n) \frac{(-D)^n}{n!}\right] \phi(x). \quad (15)$$

Analytical expressions of moments (3) were previously obtained in [21]. Then the distribution density is found by Eqs. (6) or (10) with any necessary accuracy. For most problems, several first terms of the series are sufficient. Let the first unaccounted term of series (6) have the number n. Then the condition of its smallness can be written as follows:

$$\frac{1}{n!}\mu_n \ll 1 \text{ or } \frac{\mu_n}{n!\mu_2^{n/2}} \ll 1. \quad (16)$$

To estimate the accuracy, we discard the terms of order d_0/d and d_0/R in the expressions for the moments due to their smallness, then for a magnetic with volume concentration $c = Nv_0/V$ (v_0 is the particle volume) and spontaneous magnetization I_s the moments are:

$$\mu_{n,z}, \mu_{n,x} \approx 8\left(\frac{\pi}{6} I_s\right)^n c \frac{1}{n-1} \sum_{k=0}^{n} C_n^k \frac{(-3)^k}{2k+1}. \quad (17)$$

If we take μ_5 as the first discarded term, then, taking into consideration $\mu_{2,z}$, $\mu_{2,x} \approx (32/5)\cdot c\cdot(\pi I_s/6)^2$, the condition of a satisfactory approximation of the density distribution of the interaction fields will have the following form:

$$\mu_5 \ll 12400\left(\frac{\pi}{6} I_s\right)^5 c^{5/2}. \quad (18)$$

From Eq. (18) we obtain a lower limit on the range of possible volume concentrations of the magnetic, at which the remaining quantity of terms of series (6) well approximates the distribution density of the interaction fields, namely $c \gg 0.003$. Thus, for larger concentrations, the first four moments of the distribution function are sufficient. Approximate values of the moments up to the fourth order inclusive, obtained taking into account Eq. (18) from the analytical expressions given in [21], are given in Table 1.

Table 1. Analytical expressions of the first four moments of the distribution function in approximation $2R > d$ ($\mathrm{tg}\,\theta_{max} = 2R/d$ determines the maximum value of the angle θ in Fig. 1): $\langle H_i \rangle$ - mathematical expectation, σ^2 - dispersion, μ_3 and μ_4 - central moments of the corresponding orders

Moment	Orientation of the external field and easy axes	
	Parallel to the base of the cylinder (coordinate axes *Ox* or *Oy*)	Perpendicular to the base of the cylinder (coordinate axis *Oz*)
$\langle H_i \rangle$	$\frac{4\pi}{3} c I_s \left(1 - \frac{3}{2}\cdot\cos\theta_{max}\right)\zeta(x_0)$	$-\frac{8\pi}{3} c I_s \left(1 - \frac{3}{2}\cdot\cos\theta_{max}\right)\zeta(x_0)$
σ^2	$\left(\frac{4\pi}{3}\right)^2 c I_s^2 \frac{1}{10}\left[1 - \frac{45}{32}\cdot\left(\frac{d_0}{d}\right)^3\right]$	$\left(\frac{4\pi}{3}\right)^2 c I_s^2 \frac{1}{10}\left[1 - \frac{15}{4}\cdot\left(\frac{d_0}{d}\right)^3\right]$
μ_3	$\left(\frac{4\pi}{3}\right)^3 c I_s^3 \frac{1}{280}\left(1 + 10\cdot\left(\frac{d_0}{d}\right)^6\right)\zeta(x_0)$	$\left(\frac{4\pi}{3}\right)^3 c I_s^3 \frac{1}{280}\left(1 - 67\cdot\left(\frac{d_0}{d}\right)^6\right)\zeta(x_0)$
μ_4	$\left(\frac{4\pi}{3}\right)^4 c I_s^4 \frac{1}{1120}\left[1 - 20\cdot\left(\frac{d_0}{d}\right)^9\right]$	$\left(\frac{4\pi}{3}\right)^4 c I_s^4 \frac{1}{1120}\left[1 - 264\cdot\left(\frac{d_0}{d}\right)^9\right]$

In Table 1, dimensionless magnetization ζ of an ensemble of particles is equal to the difference between the relative number of magnetic moments oriented along and against external field *H* directed along the chosen axis:

$$\zeta = \alpha - \beta = \int_{-H_0}^{\infty} W(H_i - H)dH_i - \int_{-\infty}^{-H_0} W(H_i - H)dH_i, \quad (19)$$

where H_0 is the magnetization reversal field of the particle, $W(H_i - H)$ is the distribution density of the magnetostatic interaction field projections on the chosen coordinate axis, which can be expressed through $f(x)$:

$$W(H_i - H) = f(x)/\sigma, \text{ where } x = \frac{H_i - H - <H_i>}{\sigma}. \quad (20)$$

Equation (19) can be reduced to the following form:

$$\zeta(x_0) = 1 - 2\int_{-\infty}^{-x_0} f(x)dx, \text{ where } x_0 = \frac{H_0 + H + <H_i>}{\sigma}. \quad (21)$$

Expression (21) can be simplified by substituting Eqs. (6) and (15):

$$\zeta(x_0) = 1 - 2\int_{-\infty}^{-x_0} \phi(x) \sum_{n=0}^{\infty} A_n He_n(x)\, dx, \quad (22)$$

where $A_n = (-1)^n C_n/n! = B_n(0, 0, k_3, k_4, \ldots, k_n)/n!$ is a field-independent coefficient that depends only on the distribution moments. In a similar way, the functions $Z(x_0)$, independent of the distribution moments, can be introduced:

$$Z_n(x_0) = \int_{-\infty}^{-x_0} \phi(x) He_n(x) dx. \quad (23)$$

This function can be simplified to the following system:

$$Z_n(x_0) = \begin{cases} \frac{1}{2} - \frac{1}{2}\mathrm{erf}\left(\frac{x_0}{\sqrt{2}}\right), n = 0 \\ (-1)^n \phi(x_0) \cdot He_{n-1}(x_0), n \geq 1 \end{cases}, \quad (24)$$

and the magnetization is simplified to the following expression:

$$\zeta(x_0) = 1 - 2\sum_{n=0}^{\infty} A_n \cdot Z_n(x_0). \quad (25)$$

A model of interacting particles with effective spontaneous magnetization

In a real dilute magnetic, the particles are distributed by sizes and magnetic states, may have different crystallography and directions of easy axes, be chemically inhomogeneous, etc. In the case of an ensemble of stable single-domain particles, we can take a lognormal size distribution and, having estimated the average particle size, calculate the ensemble magnetization in an external field. If the dispersion of the distribution is large and the ensemble includes particles in different magnetic states, the concept of effective spontaneous magnetization, which takes into consideration possible magnetic and/or chemical inhomogeneity of the particles, can be introduced to estimate the hysteresis characteristics of the ensemble.

By using the approximation of lognormal particle distribution by volume [27,28], the fractions of particles in different magnetic states can be calculated (Fig. 2). In modeling, the range of particles is divided into 5 intervals: superparamagnetic (SP), single-domain (SD), pseudo-single-domain (PSD), and multi-domain (MD), with the range of superparamagnetic particles containing unblocked superparamagnetic ones that do not contribute to the remanent magnetization, as well as superparamagnetic particles blocked by magnetostatic interaction that contribute not only to the saturation magnetization but also to the remanent magnetization [6,29]. The probability density of the lognormal distribution is written as:

$$\varphi(x) = \frac{1}{x\sigma\sqrt{2\pi}} \exp\left(-\frac{(\ln(x-\mu))^2}{2\sigma^2}\right), \quad (26)$$

where $x = v/v_p$ is the particle volume reduced to the characteristic volume, σ is the standard deviation, and μ is the mathematical expectation of the corresponding Gaussian distribution. The fraction of particles in the volume range from x_1 to x_2 is equal to:

$$n_i = \int_{x_1}^{x_2} \varphi(x)dx \,/\, \int_{x_{\min}}^{x_{\max}} \varphi(x)dx, \tag{27}$$

where x_1 and x_2 are the lower and upper limits of the range of volumes of a group of particles in a certain magnetic state, x_{min} (d = 0) and x_{max} ($d = d_{max}$) are the minimum and maximum relative volumes of particles, respectively, and $x_2 \leqslant x_{max}$.

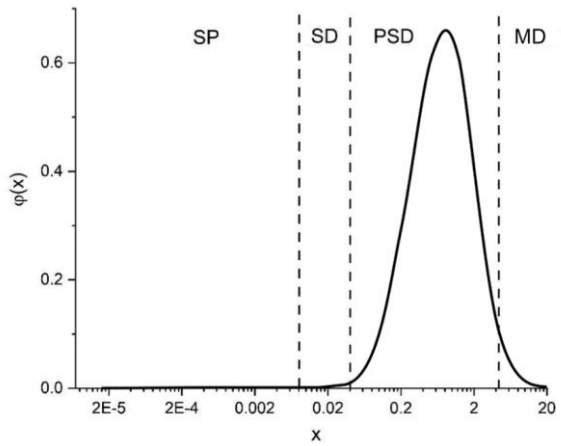

Fig. 2. Lognormal distribution of relative volumes of particles [29]

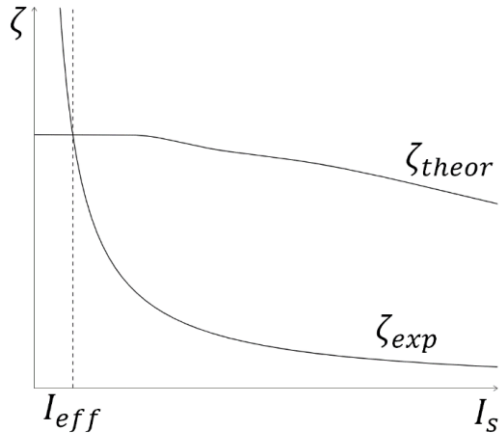

Fig. 3. Graphical determination of the value of effective spontaneous magnetization ($I_{s\,eff}$ or $I_{rs\,eff}$)

The average relative volume of each particle group is found as:

$$x_i = \int_{x_1}^{x_2} x \cdot \varphi(x)dx, \tag{28}$$

and the average absolute volume as:

$$v_i = v_p \frac{x_i}{n_i}, \tag{29}$$

where $v_p = \pi d_p^3/6$, d_p is the characteristic size of the particle.

The volume concentration of particles in each of the states is equal to:

$$c = N\frac{v_{average}}{V} = \frac{N}{V}(n_{sp}v_{sp} + n_{bsp}v_{bsp} + n_{sd}v_{sd} + n_{psd}v_{psd} + n_{md}v_{md}), \tag{30}$$

where N is the number of ferrimagnetic particles in a sample of volume V, $v_{average} = n_{sp}v_{sp} + n_{bsp}v_{bsp} + n_{sd}v_{sd} + n_{psd}v_{psd} + n_{md}v_{md}$ is the average volume of ferrimagnetic particles in various magnetic states with corresponding average volumes [6]. If the particles are grouped into clusters in the sample volume, which is essential to account for the dipole-dipole interaction, we can introduce the volume concentration of ferrimagnetic η in a cluster of volume V_{cl} and concentration of clusters c_{cl} in the sample. Then $c = \eta c_{cl}$ if the interaction between clusters can be neglected. If the interaction cannot be neglected, then, in the first approximation, we can discard the cluster distribution and consider the particle distribution to be homogeneous over the sample volume (see Eq. (30)).

To find the value of the effective spontaneous magnetization, it is necessary to bring the theoretical dimensionless magnetization determined by Eq. (25) into agreement with the experimental value:

$$\zeta_{exp} = \frac{M}{cI_s}, \tag{31}$$

where M is the saturation magnetization M_s or the saturation remanence M_{rs}, and c_s and c_{rs} are the corresponding volume concentrations of particles contributing to M_s or M_{rs}. In our model, two values correspond to the spontaneous saturation magnetization of ferroparticles: $I_{s\ eff}$ and $I_{rs\ eff}$. For chemically homogeneous particles, $I_{s\ eff}$ coincides with the spontaneous magnetization of the material, whereas for chemically inhomogeneous particles it is some averaged value. The value of $I_{rs\ eff}$ takes into consideration the magnetic and chemical heterogeneity, as well as the peculiarities of the crystallography of both individual particles and the ensemble as a whole. Besides, in our model, volume concentration c_{rs} does not include fractions of truly superparamagnetic (unblocked) and multidomain particles.

Since, in general, finding the effective spontaneous magnetizations is reduced to solving the integral equation (see Eqs. (23-25) and expressions for odd moments in Table 1), it is easier to find the solution graphically by specifying the range of possible values of I_s. The point of intersection of the theoretical ζ_{theor} (25) and experimental ζ_{exp} (31) curves provides the value of the effective spontaneous magnetization I_{eff}, corresponding to $I_{s\ eff}$ or $I_{rs\ eff}$ (Fig. 3).

The effective spontaneous magnetization by the remanence $I_{rs\ eff}$ takes into consideration the changes that occur in the magnetic state of the ensemble and its constituent particles when the external magnetic field decreases from saturation to zero. The value of $I_{rs\ eff}$ is influenced by a number of factors, namely, the distribution of particles by size and, consequently, by magnetic states, the scatter of the directions of the crystallographic axes of particles relative to the external field, and the chemical heterogeneity of the whole ensemble and individual particles. In addition, in our approximation of magnetostatic interaction due to a large number of particles, the distribution of random fields of the dipole-dipole interaction is considered unchanged, and unblocking of a part of magnetic moments of superparamagnetic particles is related only to the reduction of the external field.

To check the consistency of the values of the effective spontaneous magnetizations with the experimental data, we can use the following evaluation formula:

$$\frac{M_{rs}}{M_s} = \frac{c_{rs} I_{rs}}{c_s I_s}. \tag{32}$$

Here c_{rs} is the volume concentration of particles participating in the creation of the remanent magnetization (for simplicity we can neglect the concentrations of truly superparamagnetic and multidomain particles, see Eq. (30)); the concentration of particles contributing to the saturation magnetization, $c_s = c$.

Conclusion

The modified method for calculating the distribution function of dipole-dipole interaction fields in a dilute magnetic of cylindrical shape taking into consideration the lognormal distribution of particles by sizes (and, consequently, magnetic states) allows, on the basis of experimental values of hysteresis parameters and structural characteristics of individual particles, their clusters, and the ensemble as a whole, calculating the volume fractions of particle concentrations in different magnetic states, the volume concentration of ferrimagnetic in the sample, and its effective spontaneous magnetizations.

The approach presented in this paper has a number of advantages. In the case of chaotic distribution of magnetic particles in a “non-magnetic” matrix, the model allows

moving from micromagnetic calculations of the interaction of each of the particles with one another to the distributions of random interaction fields. In addition, due to the decomposition of the distribution function into an infinite series, any necessary accuracy can be achieved, and the moments of this function are obtained in analytical form. The model allows taking into consideration cluster distribution of particles. If the concentration of clusters is small, the dipole-dipole interaction between them can be neglected, otherwise the distribution of particles in the sample can be considered homogeneous (the entire sample is one cluster). Moreover, the choice of the cylindrical volume allows the method to be used in the limiting cases of thin threads and thin layers. The drawback of the model is the simplifying assumptions about the spherical shape of the particles and their crystallographic uniaxiality. However, this disadvantage is partially compensated by the fact that the model assumes the field of magnetization reversal of a single particle $H_0 = H_{cr}$, where H_{cr} is the experimental value of the coercivity of remanence.

Partial verification of the model described in this paper was carried out when calculating the hysteresis characteristics of objects of both artificial and natural origin [6,7,20,29,30]. To estimate the hysteresis characteristics of two-phase chemically inhomogeneous particles and their ensembles, one can use the approach developed by the authors in [6,7] and the program for micromagnetic modeling [31,32].

References

1. Shcherbakov VP, Sycheva NK. Study of Similarity between Blocking Temperature Spectra of Chemical and Thermoremanent Magnetizations by Computer Simulation. *Izv., Phys. Solid Earth*. 2019;55: 777–791.
2. Belokon V, Lapenkov R, Chibiriak E, Dyachenko O. Magnetic susceptibility of systems with different types of interactions: The random interaction fields method. *Journal of Magnetism and Magnetic Materials*. 2020;512: 167051.
3. Beguin A, Nikolaisen E, Fabian K. Micromagnetic Modeling of Thermoremanent Magnetization in Small Natural Pseudo-Single Domain Magnetite Particles. In: *EGU General Assembly 2023, Vienna, Austria, 24–28 Apr 2023*. 2023. p.EGU23-10086
4. Cortés-Ortuño D, Fabian K, De Groot LV. Mapping Magnetic Signals of Individual Magnetite Grains to Their Internal Magnetic Configurations Using Micromagnetic Models. *JGR Solid Earth*. 2022;127(5): e2022JB024234.
5. Fabian K, Shcherbakov VP. Energy barriers in three-dimensional micromagnetic models and the physics of thermoviscous magnetization. *Geophysical Journal International*. 2018;215(1): 314–324.
6. Kharitonskii P, Zolotov N, Kirillova S, Gareev K, Kosterov A, Sergienko E, Yanson S, Ustinov A, Ralin A. Magnetic granulometry, Mössbauer spectroscopy, and theoretical modeling of magnetic states of FemOn–Fem-xTixOn composites. *Chinese Journal of Physics*. 2022;78: 271–296.
7. Kharitonskii P, Sergienko E, Ralin A, Setrov E, Sheidaev T, Gareev K, Ustinov A, Zolotov N, Yanson S, Dubeshko D. Superparamagnetism of Artificial Glasses Based on Rocks: Experimental Data and Theoretical Modeling. *Magnetochemistry*. 2023;9(10): 220.
8. Abert C. Micromagnetics and spintronics: models and numerical methods. *Eur Phys. J. B*. 2019;92(6): 120.
9. Leliaert J, Mulkers J. Tomorrow's micromagnetic simulations. *Journal of Applied Physics*. 2019;125(18): 180901.
10. Donnelly C, Hierro-Rodríguez A, Abert C, Witte K, Skoric L, Sanz-Hernández D, Finizio S, Meng F, McVitie S, Raabe J, Suess D, Cowburn R, Fernández-Pacheco A. Complex free-space magnetic field textures induced by three-dimensional magnetic nanostructures. *Nat. Nanotechnol*. 2022;17(2): 136–142.
11. Fu S, Cui W, Hu M, Chang R, Donahue MJ, Lomakin V. Finite-Difference Micromagnetic Solvers With the Object-Oriented Micromagnetic Framework on Graphics Processing Units. *IEEE Trans Magn*. 2016;52(4): 7100109.
12. Bisotti MA, Cortés-Ortuño D, Pepper R, Wang W, Beg M, Kluyver T, Fangohr H. Fidimag – A Finite Difference Atomistic and Micromagnetic Simulation Package. *JORS*. 2018;6(1): 22.
13. Ambarov AV, Zverev VS, Elfimova EA. Dynamic response of interacting superparamagnetic particles with aligned easy magnetization axes. *Journal of Magnetism and Magnetic Materials*. 2020;497: 166010.
14. Ambarov AV, Zverev VS, Elfimova EA. Numerical modeling of the magnetic response of interacting superparamagnetic particles to an ac field with arbitrary amplitude. *Modelling Simul Mater Sci Eng*. 2020;28(8): 085009.

15. Komogortsev SV, Fel'k VA, Li OA. The magnetic dipole-dipole interaction effect on the magnetic hysteresis at zero temperature in nanoparticles randomly dispersed within a plane. *Journal of Magnetism and Magnetic Materials*. 2019;473: 410–415.
16. Sadat ME, Bud'ko SL, Ewing RC, Xu H, Pauletti GM, Mast DB, Shi D. Effect of Dipole Interactions on Blocking Temperature and Relaxation Dynamics of Superparamagnetic Iron-Oxide (Fe3O4) Nanoparticle Systems. *Materials*. 2023;16(2): 496.
17. Mørup S, Hansen MF, Frandsen C. Magnetic interactions between nanoparticles. *Beilstein J Nanotechnol*. 2010;1: 182–190.
18. Nigam A, Singh D, Sinha A, Sachan D, Anisha, Vishal A, Kumar D, Kumar N. Structural and magnetic properties of zinc doped nickel ferrite Ni(1−X)ZnXFe2O4 synthesized using sol-gel auto-combustion and hydrothermal methods. *Materials Physics and Mechanics*. 2021;47(3): 493–600.
19. Kumar N, Singh D, Nigam A, Rajpoot O, Kumar M, Yadav, Singh YP, Prakash PS, Singh S. Structural and magnetic properties of zinc doped copper ferrite synthesized by sol-gel and hydrothermal route. *Materials Physics and Mechanics*. 2021;47(2): 306–314.
20. Kharitonskii PV, Gareev KG, Ralin AY, Sergienko ES. Superparamagnetism of Fe3O4–Fe3 – xTixO4 Composites: Micromagnetic Modeling. *Phys. Metals Metallogr*. 2023;124(1): 46–52.
21. Al'miev AS, Ralin AYu, Kharitonskii PV. Distribution functions of dipole-dipole interaction fields in diluted magnets. *Fizika Metallov i Metallovedenie*. 1994;78(1): 28–34. (In Russian)
22. Shcherbakov VP. On the molecular field distribution function in systems with randomly distributed centres of interaction. *Phys Met Metallogr*. 1979;48: 7–10. (In Russian)
23. Cramér H. *Mathematical Methods of Statistics*. Princeton University Press; 1999.
24. Wallace DL. Asymptotic Approximations to Distributions. *Ann Math Statist*. 1958;29(3): 635–654.
25. Comtet L. *Advanced Combinatorics: The Art of Finite and Infinite Expansions*. Springer; 1974.
26. Bell ET. Exponential Polynomials. *The Annals of Mathematics*. 1934;35(2): 258.
27. Olin M, Anttila T, Dal Maso M. Using a combined power law and log-normal distribution model to simulate particle formation and growth in a mobile aerosol chamber. *Atmos Chem Phys*. 2016;16(11): 7067–7090.
28. Fujihara A, Tanimoto S, Yamamoto H, Ohtsuki T. Log-Normal Distribution in a Growing System with Weighted and Multiplicatively Interacting Particles. *J Phys Soc Jpn*. 2018;87(3): 034001.
29. Kharitonskii P, Bobrov N, Gareev K, Kosterov A, Nikitin A, Ralin A, Sergienko E, Testov O, Ustinov A, Zolotov N. Magnetic granulometry, frequency-dependent susceptibility and magnetic states of particles of magnetite ore from the Kovdor deposit. *Journal of Magnetism and Magnetic Materials*. 2022;553: 169279.
30. Sergienko E, Janson S, Kharitonskii P, Gareev K, Ilyin S, Anoshin Y, Ralin A. Magnetic Properties and Composition of Inclusions in Foraminifera Shells at the Mid-Atlantic Ridge. In: Frank-Kamenetskaya OV, Vlasov DY, Panova EG, Alekseeva TV. (Eds.) *Biogenic—Abiogenic Interactions in Natural and Anthropogenic Systems 2022*. Cham: Springer; 2023. p.153–166.
31. Kharitonskii PV, Setrov EA, Sheidaev TS. *Micromagnetic modeling of ensembles of two-phase chemically inhomogeneous nanoparticles with an infinitely thin interphase boundary*. RU2023665340 (Patent), 2023.
32. Kharitonskii PV, Setrov EA, Ralin AYu. *Modeling of magnetic hysteresis characteristics based on a model of magnetostatically interacting particles with effective spontaneous magnetization*. RU2024660027 (Patent), 2024.

About Authors

Petr V. Kharitonskii Sc
Doctor of Physical and Mathematical Sciences
Lead Researcher (Ioffe Institute, St. Petersburg, Russia)

Evgenii A. Setrov
Master Student (St. Petersburg Electrotechnical University "LETI", St. Petersburg, Russia)

Andrey Yu. Ralin Sc
Candidate of Physical and Mathematical Sciences
Associate Professor (Far Eastern Federal University, Vladivostok, Russia)

МЕХАНИКА И ФИЗИКА МАТЕРИАЛОВ

52 (2) 2024

Учредители: Санкт-Петербургский политехнический университет Петра Великого,

Институт проблем Машиноведения Российской академии наук

Издание зарегистрировано федеральной службой по надзору в сфере связи,

информационных технологий и массовых коммуникаций (РОСКОМНАДЗОР),

свидетельство ПИ №ФС77-69287 от 06.04.2017 г.

Телефон редакции

+7(812)552 77 78, доб. 224

E-mail: mpmjournal@spbstu.ru

Компьютерная верстка Л.И. Гузилова

Подписано в печать 31.05.2024 г. Формат 60x84/8. Печать цифровая
Усл. печ. л. 10,0. Тираж 100. Заказ____.

Отпечатано с готового оригинал-макета, предоставленного автором
в Издательско-полиграфическом центре Политехнического университета Петра Великого. 195251,
Санкт-Петербург, Политехническая ул., 29.
Тел.: +7(812)552 77 78, доб. 224.

MPM SCIENTIFIC JOURNAL

MPM, Vol. 52, No. 2, 2024